Computational Investigation of Noncovalent Interactions in Supramolecular Host-Guest and Amyloid-β (Aβ) Protein-Ligand Systems

A Thesis Submitted to

Indian Institute of Technology Guwahati

for the Degree of

Doctor of Philosophy

By

Haobam Kisan Singh
Roll No.176122035

Under the Supervision of

Dr. Manabendra Sarma

Department of Chemistry
Indian Institute of Technology Guwahati
Guwahati-781039, India
January 2024

Dedicated to My Family

Department of Chemistry
Indian Institute of Technology Guwahati
Guwahati-781039, India

STATEMENT

The work contained in the thesis entitled "***Computational Investigation of Noncovalent Interactions in Supramolecular Host-Guest and Amyloid-β (Aβ) Protein-Ligand Systems***" has been carried out by me at the Indian Institute of Technology Guwahati, under the supervision of Dr. Manabendra Sarma, Department of Chemistry, Indian Institute of Technology Guwahati. This work has not been submitted elsewhere for the award of any degree.

Haobam Kisan Singh
Roll No. 176122035
Department of Chemistry
Indian Institute of Technology Guwahati
Guwahati-781039, India

Dr. Manabendra Sarma

Associate Professor
Department of Chemistry
Indian Institute of Technology Guwahati
Guwahati-781039, India
Phone: +913612582318, Fax: +913612582349
Email: msarma@iitg.ac.in

CERTIFICATE

This is to certify that the work contained in the thesis entitled "***Computational Investigation of Noncovalent Interactions in Supramolecular Host-Guest and Amyloid-β (Aβ) Protein-Ligand Systems***" has been carried out by **Mr. Haobam Kisan Singh** (Roll No. 176122035) at the Indian Institute of Technology Guwahati, under my supervision. This work has not been submitted elsewhere for the award of any degree.

Dr. Manabendra Sarma

Thesis Supervisor

ACKNOWLEDGEMENT

I would like to express my gratitude to everyone who played a crucial role in the successful completion of this Doctoral thesis. Special thanks to my Ph. D. Supervisor, Dr. Manabendra Sarma for allowing me to work under his guidance. I am grateful for his constant support, encouragement, guidance, and valuable suggestions throughout my research journey.

I want to thank the members of my Doctoral Committee, Professor Aditya Narayan Panda (Chairman), Professor C. V. Sastri, and Professor Sumana Dutta, for their valuable comments, suggestions, constructive criticism, and constant encouragement.

I extend my sincere thanks to the Department of Chemistry, Indian Institute of Technology Guwahati (IITG), and other faculty members and staff. I thank the supercomputing facilities Param-Ishan IITG and Parma-Kamrupa, IITG for allowing me to conduct my research calculations. I especially want to thank Mr. Jeherul Islam and other staff members of the HPC support team for their help and co-operation throughout my Ph.D. journey.

I express my gratitude to the Indian Institute of Technology Guwahati (IITG) for their financial support and for providing a secure and pleasant working atmosphere.

I want to thank my labmates Himangshu Pratim Bhattacharyya, Bittu Lama, Niharika Keot, Upasana Nath, Monalisha Sarma, Biman Medhi, Rabu Ranjan Changmai, Shubam Kumar, Samsung Raja Daimari, Manash Pratim Sarmah, Anand Kumar Yadav, Rimi Chyrmang and Papu Kalita (alumni) for their scientific suggestion, support which played an important role in completing my work. I would like to thank Post-Doctoral Fellow Dr. Juhi Dutta for her valuable scientific suggestions. I am thankful to my seniors and friends Dr. Somorjit, Dr. Gyanendro, Dr. Gishan, Dr. Yaipharemba, Dr. Mohd Shavez, Roson, Karnajit, Hemjit, James, Badal, Suresh, Richard, Kid, Lamyanbi, Sophia, Iban, Biswanath, Banuary, Palak Mandal, and Deepak for always being there in my corner, during my research journey.

Finally, I would like to convey my deep gratitude to my family. Without their support, my studies would not be possible. I am grateful to my uncle, Joy Shaikhom, and aunt, Dr. Yumnam Surbala Devi for their constant support and bringing me in the area of research.

CONTENTS

SYNOPSIS

In the realm of chemistry, noncovalent interactions play a crucial role in supramolecular host-guest interaction, material sciences, protein-ligand binding, etc. These interactions include hydrogen bonding, π-π stacking, cation-π, anion-π, etc. The stability of various conformers is also determined by their respective engagement in these interactions. The thesis covers, using various quantum computational methods, the exploration of intramolecular and intermolecular noncovalent interactions involved in the different conformers of the supramolecular ditopic (two binding sites) receptor host 1,6-bis(2,6-bis(benzothiazol-2-yl) pyridine-4-yloxy) hexane and their complexes with resorcinol guest. Electron charge transport plays an essential role in the construction of the building blocks of organic semiconductors. Taking these concepts into consideration, we have explored the π-π interactions and electron transport in the host-guest complexes formed between three dimensions hexa-cationic host which consists of two triscationic π-electron-deficient trispyridiniumtriazine (TPZ^{3+}) units and are bridged face-to-face by three ethylene-triazole-ethylene and guest polycyclic aromatic hydrocarbons (PAH). Furthermore, we have explored the nature of the noncovalent interaction of propanediurea-based molecular clip receptor with different electron withdrawing and donating groups substituted resorcinol molecules. Our investigation has also examined the noncovalent interactions between the amino acids functionalized perylene diimide (PDI) compounds and amyloid-β (Aβ) fibrils. These fibrils are well recognized as the primary causative agents in the development of Alzheimer's disease (AD). We employed atomistic molecular dynamics (MD) simulations to conduct this study. The concise Chapter-wise outline of the thesis is summarized below.

Chapter 1: Introduction

This Chapter provides a brief overview of noncovalent interactions, incorporating an in-depth study of the diverse array of existing noncovalent interactions. The importance of noncovalent interactions and their involvement in supramolecular host-guest binding, electron transport, and ligand-amyloid-β (Aβ) fibrils protein interaction are discussed. The final part of this Chapter addresses the goals and boundaries of the work being undertaken.

Chapter 2: Methodology

This Chapter introduces fundamental quantum chemical concepts and mathematical principles for investigating noncovalent interactions. We begin by exploring the Schrödinger equation, a cornerstone of quantum mechanics. This equation provides valuable insights into the characteristics of a given system. The basic concept of Hartree-Fock (HF) Theory and Density Functional Theory (DFT) are also discussed in this Chapter. To properly define the long-range noncovalent interaction, dispersion correction is added to the standard DFT methods. The discussion for estimation of interaction energy and the benchmarking of this energy using the wavefunction-based method, the domain-based local pair natural orbital coupled cluster with singles, doubles, and perturbative triple excitations [DLPNO-CCSD(T)]. The basic concept of energy decomposition analysis (EDA) to partition the interaction energy into physically meaningful components such as electrostatic, orbital interaction, Pauli repulsion, and dispersion interactions are also explained in this Chapter. Further, the discussion of noncovalent interaction (NCI) analysis based on the reduced density gradient (RDG) is also implemented to visualize the noncovalent interaction between host and guest in complexes. In the case of amyloid-β (Aβ) fibrils protein-ligand interaction study, we have implemented molecular docking and classical molecular dynamics (MD) simulations.

Chapter 3: Torsional Rotation in Ditopic Receptor Host and its Complex Formation with Resorcinol Guest: A Computational Study

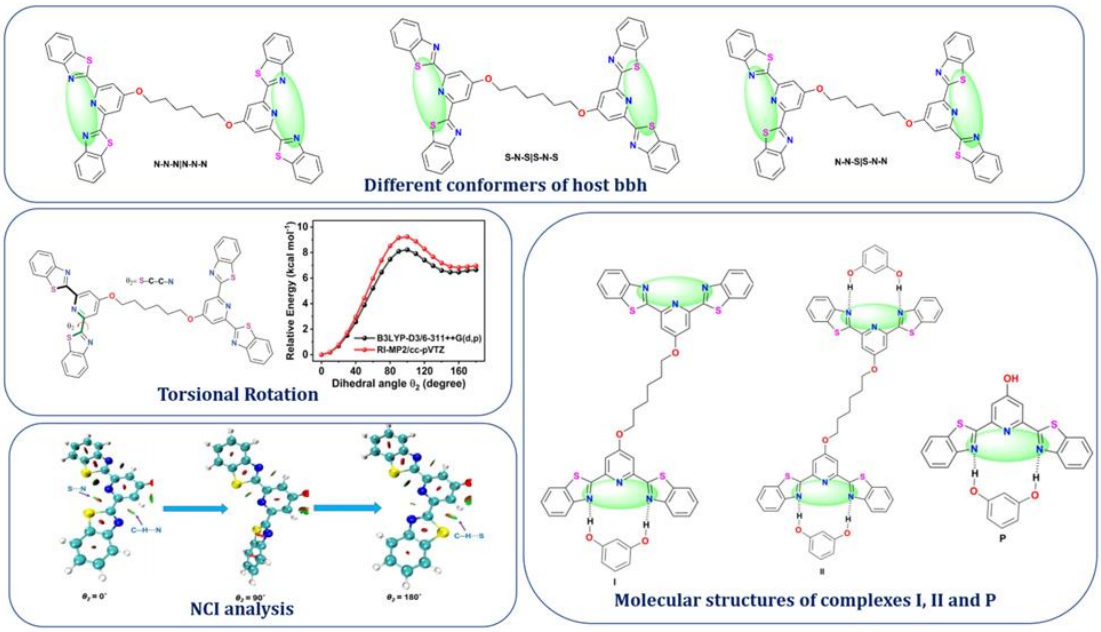

In this Chapter, we have explored the stability and torsional energy barrier of different conformers of the ditopic receptor host 1,6-bis(2,6-bis(benzothiazol-2-yl) pyridine-4-yloxy) hexane (bbh). The conformer that is accompanied by intramolecular C-H···N and C-H···S interactions is relatively more stable than the others. Due to torsional angle rotation within the host, the C-H···N and C-H···S interactions get disrupted and exhibit different binding sites for capturing guest molecules. Furthermore, to understand the interaction energy and nature of interaction in host-guest complexes I, II, and P (Prototype) formed between the host (bbh) and guest (resorcinol) were investigated by using different DFT functionals. Energy decomposition analysis (EDA) results of all the complexes revealed that the electrostatic interaction significantly contributes to the host-guest interaction energy. The noncovalent (NCI) study provides the existence of intermolecular hydrogen bonding and other weak interactions between the host and guest in complexes.

Chapter 4: Exploring π-π Interactions and Electron Transport in Complexes Involving Hexacationic Host and PAH Guest: A Promising Avenue for Molecular Devices

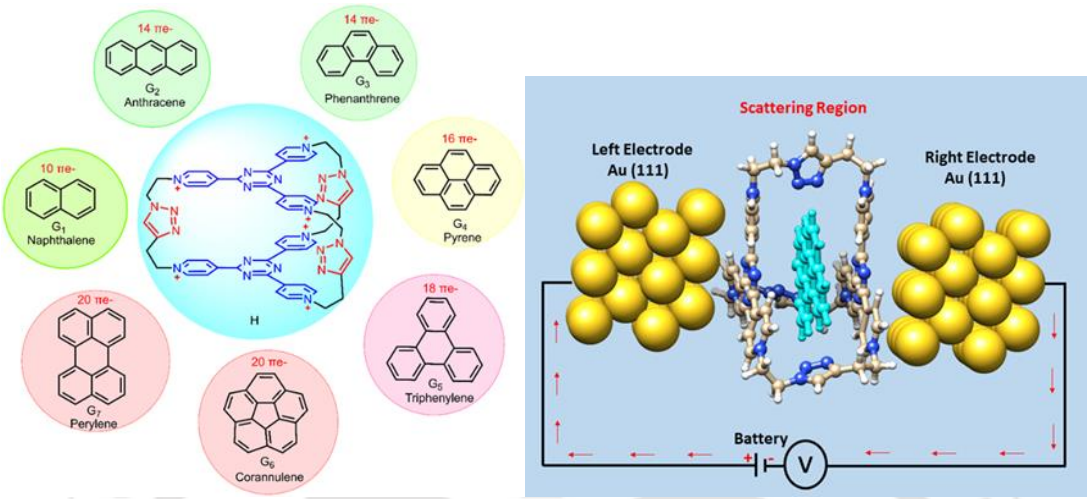

In this Chapter, we have investigated the characteristic π-π interaction and electron transport involved in the series of host-guest complexes formed between the hexacationic cage host (H) and polyaromatic hydrocarbon (PAH) guests (G1-G7) using different quantum chemical approaches. The perylene and naphthalene inclusion complexes G7⊂H and G1⊂H have the highest and lowest interaction energy values, respectively. Except for the complex G6⊂H, others follow the increase in the interaction energy values with the increase in the number of π electrons of the guest. The bowl shape geometry of the corannulene (G6) guest inside the host cavity causes the anomalous interaction energy of the G6⊂H complex. Moreover, this geometrical pose of the corannulene molecule results in improper face-to-face overlaps with the trispyridinium triazine (TPZ^{3+}) units of the host. The analysis of extended-transition-state natural orbitals for chemical valence (ETS-NOCV) provided that dispersion interaction contribution dominated in the complexes. We observed increased conductance value when guest molecules were encapsulated inside the host cavity. The complex G7⊂H shows maximum conductivity compared to others due to the maximum number of π electrons and the highest interaction energy. This work anticipated the PAH molecules embedded host-guest complex that can be utilized as molecular devices through π-π interaction and also offered new insight into the development of supramolecular devices.

Chapter 5: Insight into the Nature of Interaction between the Molecular Receptors based on Dimethylpropanediurea and Resorcinol derivatives

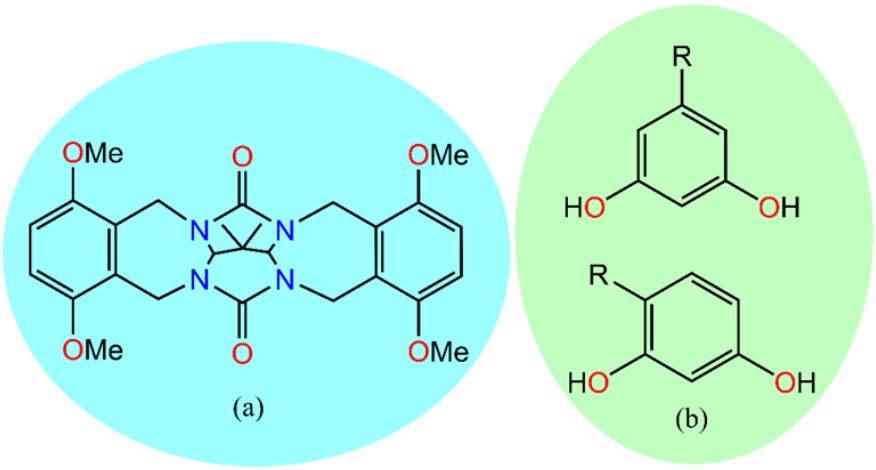

R= H, Me, OMe, NH_2,F, Cl, NO_2,NMe_2,CF_3, CN, CHO

This Chapter explored the electronic structure and noncovalent interactions in a series of host-guest complexes. These complexes comprised a propanediurea-based molecular clip receptor and various guest molecules derived from resorcinol. These guest molecules were attached with different electron withdrawing or donating groups. There are no significant changes in the interaction energy value when the electron-donating groups are substituted. Introducing an electron-withdrawing group on the resorcinol molecule increases the interaction energy. Also, it increases the strength of the hydrogen bonding form between the guest's hydroxy groups and the host's carbonyl groups. Energy decomposition analysis of the complexes found that the role played by the electrostatic interaction term was more prominent when the guest molecule derived from resorcinol had an electron-withdrawing group attached to it. In simpler terms, the strength of the electrostatic forces between the host and guest molecules increased when the guest molecule had a group that tended to pull electrons away.

Chapter 6: Investigation of the Noncovalent Interactions of the Histidine Functionalized Perylene diimide (PDI) with amyloid-β (Aβ) Fibrils Protein

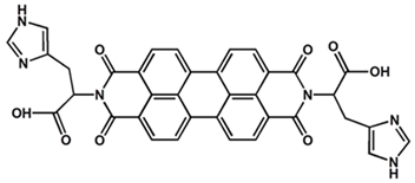

PDI-HIS

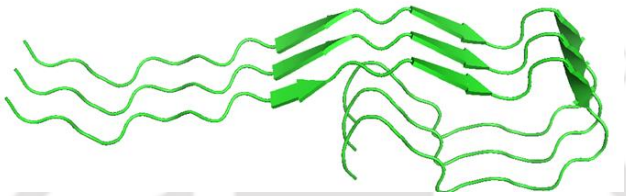

Amyloid-*β* (A*β*) fibril

In this Chapter, we have explored the noncovalent interactions and the structural disruption of the amyloid-*β* (A*β*) fibril protein when the histidine functionalized perylene diimide (PDI-HIS) binds with it. It is believed that the aggregation of amyloid-*β* (A*β*) peptides resulting in the formation of senile plaque, is the primary cause of Alzheimer's disease (AD). The inclusion of two histidine (HIS) moieties on the perylene diimide (PDI) makes it a biocompatible compound. Experimental studies proposed that the PDI-HIS molecule co-assembly with the amyloid-*β* (A*β*) fibril through noncovalent interactions. However, there is still a gap in the investigation of the interplay between the amyloid-*β* (A*β*) fibril and the PDI-HIS system. In addition, the PDI-HIS carboxylic acid groups will deprotonate and exist in the anionic form. Therefore, in the current study, we delved into the interaction involved between PDI-HIS and amyloid-*β* (A*β*) fibrils. We have conducted computational studies using exhaustive molecular docking to generate the docking poses and binding energies. Subsequently, the docked poses were utilized, and 400 ns molecular dynamics (MD) simulations were performed to provide the atomistic-detail insights into the molecule binding and interactions.

Chapter 7: In *Silico* Designing of Alanine, Phenylalanine, and Tyrosine Functionalized Perylene diimide (PDI) and Exploring their Nature of Interaction with amyloid-*β* (A*β*) Fibrils

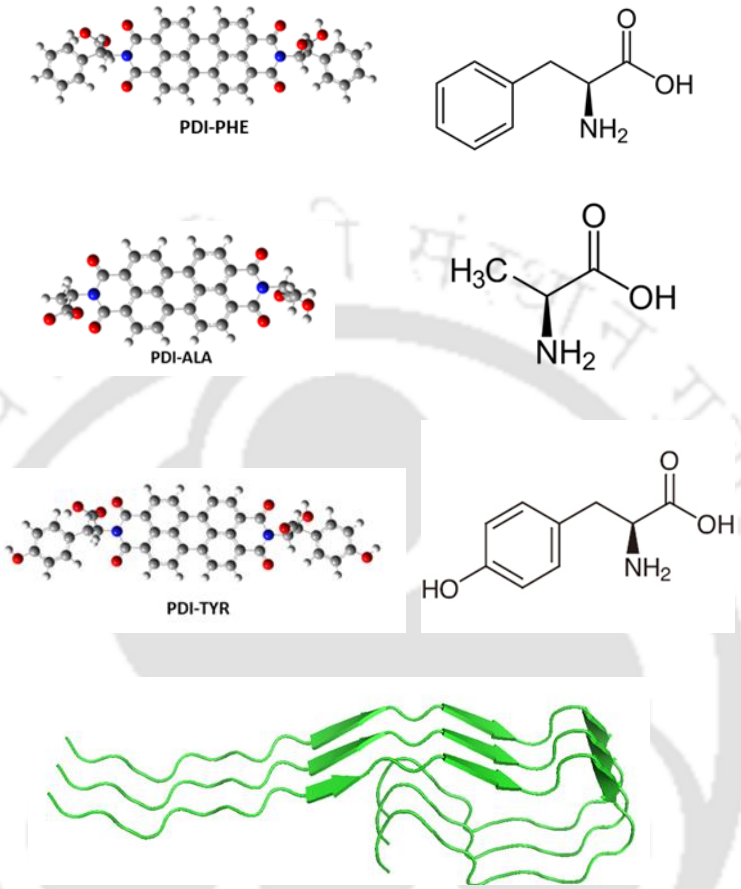

Amyloid-*β* (A*β*) fibril

In this Chapter, we proposed three compounds that functionalized the perylene diimide (PDI) with amino acids, namely Phenylalanine (PDI-PHE), Alanine (PDI-ALA), and Tyrosine (PDI-TYR). We study the structural changes and noncovalent interactions when these compounds bind with the amyloid-*β* (A*β*) fibril protein. At human physiological pH (pH=7.4), the carboxylic acid groups of the compound will be deprotonated and form an anion. Initially, the binding poses and energies of the compounds in complexes with amyloid-*β* (A*β*) fibril protein were generated using molecular docking. Further, we performed 400 ns molecular dynamics (MD) simulations for each of the docked poses of the complexes.

Chapter 8: Summary and Conclusions

In essence, the final Chapter of the thesis summarizes the work conducted in the present study and outlines potential avenues for further research. This Chapter encapsulates the main findings, conclusions, and contributions of the current research while indicating the potential directions for future investigations. It offers a wrap-up of what has been achieved and suggests what can be explored in the research domain moving forward. In the first work, we have shown the existence of different conformers through the torsional rotation of the ditopic receptor, which can bind a maximum of two guest resorcinol molecules. Moreover, different intramolecular noncovalent interactions and intermolecular hydrogen bonding between the receptor and guest exist. In our second study, we demonstrated the noncovalent π-π interactions and electron charges transport between a specific type of cage-shaped molecule with a positive charge (referred to as the "hexacationic cage host H") and polycyclic aromatic hydrocarbons (PAHs) with different sizes and structures (designated as G1-G7). We examined these interactions through various methods in quantum chemistry. In the third work, we explored the effect of the noncovalent interactions in the host-guest complexes formed between the propanediurea-based molecular clip receptor and different electron withdrawing and donating groups substituted resorcinol molecule. The last two working Chapters highlighted the noncovalent interactions of different amino acids: Histidine, Alanine, Phenylalanine, and Tyrosine functionalized perylene diimide (PDI) with amyloid-β (Aβ) fibrils.

LIST OF PUBLICATIONS/PREPARATIONS

Thesis work

1. **H. K. Singh** and M. Sarma, "Torsional Rotation in Ditopic Receptor Host and its Complex Formation with Resorcinol Guest: A Computational Study", *ChemPhysChem* **2023**, 24, e202200928 (1–12).
2. **H. K. Singh** and M. Sarma, "Exploring π-π Interactions and Electron Transport in Complexes Involving a Hexacationic Host and PAH Guest: A Promising Avenue for Molecular Devices", *Phys. Chem. Chem. Phys.* **2023**, 25, 26767–26778.
3. **H. K. Singh** and M. Sarma, "Insight into the Nature of Interaction between the Molecular Receptors based on Dimethylpropanediurea and Resorcinol derivatives", (**in preparation**).
4. **H. K. Singh** and M. Sarma, "Investigation of the Noncovalent Interactions of the Histidine Functionalized Perylene diimide (PDI) with Amyloid-β (Aβ) Fibrils Protein", (**in preparation**).
5. **H. K. Singh** and M. Sarma, "In *Silico* Designing of Alanine, Phenylalanine, and Tyrosine Functionalized Perylene diimide (PDI) and Exploring their Nature of Interaction with Amyloid-β (Aβ) Fibrils", (**in preparation**).

Outside of Thesis work

1. P. Kalita, B. Medhi, **H. K. Singh**, H. P. Bhattacharyya, N. Gupt, and M. Sarma, "Perturbing π-clouds with Substituents to Study the Effects on Reaction Dynamics of Gauche-1,3-butadiene to Bicyclobutane Electrocyclization", *ChemPhysChem* **2023**, 24, e202200727 (1–9).
2. S. Singh, G. R. Navale, S. Agrawal, **H. K. Singh**, L. Singla, D. Sarkar, M. Sarma, A. R. Choudhury, K. Ghosh "Design and Synthesis of Piano-Stool Ruthenium(II) Complexes and their Studies on the Inhibition of amyloid β (1-42) Peptide Aggregation", *Int. J. Biol. Macromol.* **2023**, 239, 124197 (1–17).
3. **H. K. Singh**, R. R. Changmai, N. Keot, H. P. Bhattacharyya, and M. Sarma "A Computational Insight on the Noncovalent Interactions of Aminothiazole-based Palladium(II) Complexes with DNA as a Potent Anticancer Agent ", *Polyhedron* **2023**, 239, 116448 (1–12).

4. R. Saini, G. R. Navale, S. Singh, **H. K. Singh**, R. Chauhan, S. Agrawal, D. Sarkar, M. Sarma, and K. Ghosh, "Inhibition of amyloid β1-42 Peptide Aggregation by Newly Designed Cyclometallated Palladium Complexes", *Int. J. Biol. Macromol*. **2023**, 248, 125847 (1–13).
5. S. Kumar, **H. K. Singh**, H. P. Bhattacharyya, and M. Sarma, "Low Energy Electron Interaction with Citric Acid: A Local Complex Potential based TimeDependent Wavepacket Study", *J. Chem. Sci.* **2023**, 135, 88 (1 – 10) (invited contribution in the Special Issue on Interplay of Structure and Dynamics in Reaction Pathways, Chemical Reactivity and Biological Systems)
6. T. L. Fischer, M. Bödecker, S. M. Schweer, J. Dupont, V. Lepère, A. ZehnackerRentien, M. A. Suhm, B. Schröder, T. Henkes, D. M. Andrada, R. M. Balabin, **H. K. Singh**, H. P. Bhattacharyya, M. Sarma, S. Käser, K. Töpfer, L. I. Vazquez-Salazar, E. D. Boittier, M. Meuwly, G. Mandelli, C. Lanzi, R. Conte, M. Ceotto, F. Dietrich, V. Cisternas, R. Gnanasekaran, M. Hippler, M. Jarraya, M. Hochlaf, N. Viswanathan, T. Nevolianis, G. Rath, W. A. Kopp, K. Leonhard, and R. A. Mata, "The First HyDRA Challenge for Computational Vibrational Spectroscopy", *Phys. Chem. Chem. Phys.* **2023**, 25, 22089–22102.
7. N. Keot, B. Lama, **H. K. Singh**, H. P. Bhattacharyya, and M. Sarma, "Unveiling the Noncovalent Interaction of Thiazol-2-ylidene and its Derivatives as N-heterocyclic Carbene with Different Proton Donor Molecules", *ChemPhysChem* **2023**, 24, e202300413 (1–11).

LIST OF CONFERENCES ATTENDED

1. **H. K. Singh** and M. Sarma, "Investigation of the Interaction of the Different Groups Modulated Galantamine Drug with Acetyl Cholinesterase by Molecular Docking and ONIOM Model", Theoretical Chemistry Symposium (TCS) 2019, February 13 – 16, 2019, Birla Institute of Technology and Science (BITS), Pilani, India (Poster).
2. **H. K. Singh** and M. Sarma, "DFT Studies on the Interaction between the Ditopic Receptor and Benzene Metabolites", Recent Advances in Chemistry (RAC) 2019, October 14 – 15, 2019, National Institute of Technology (NIT) Meghalaya, Shillong, India (Poster).
3. **H. K. Singh** and M. Sarma, "Analysing the Noncovalent Interactions between the Ditopic Receptor Host and Guest Benzene Metabolite Molecules through Density Functional Theory (DFT) Calculation", Spectroscopy and Dynamics of Molecules and Clusters (SDMC) 2020, February 20 – 23, 2020, Kumbhalgarh, Rajasthan, India (Poster).
4. **H. K. Singh** and M. Sarma, "Computational Investigation of the Noncovalent Interactions in Ditopic Receptor Host and its Complex Formation with a Benzene Metabolite Resorcinol Molecule", 57th Symposium on Theoretical Chemistry, September 20 – 24, 2021, Online, University of Würzburg, Germany (Poster).
5. **H. K. Singh** and M. Sarma, "Computational Investigation on the Nature of Host-Guest Interactions in PAHs-Hexacationic Cage Complexes", Theoretical Chemistry Symposium (TCS) 2021, December 11 – 14, 2021, Online, Indian Institute of Science Education and Research (IISER) Kolkata, Mohanpur, India (Poster).
6. **H. K. Singh** and M. Sarma, "A Molecular Dynamics Perspective on Interaction between Amino Acid functionalized Perylenediimide and Amyloid-β fibrils", Frontiers in Chemical Sciences-2022, December 02 – 04, 2022, Department of Chemistry, IIT Guwahati Research, India (Poster).

LIST OF ABBREVATIONS

Abbreviation	Description
CD	Cyclodextrin
CA	Calixarenes
CB	Cucurbit[n]urils
PAH	Polycyclic aromatic hydrocarbons
NEGF	Nonequilibrium Green's function
AD	Alzheimer's Disease
NFTs	Neurofibrillary tangles
APP	Amyloid precursor protein
MD	Molecular Dynamic
BO	Born-Oppenheimer
HF	Hartree-Fock
MP	Møller-Plesset perturbation theory
CC	Coupled cluster
DFT	Density Functional Theory
LDA	Local density approximation
GGA	Generalized gradient approximation
EDA	Energy decomposition analysis
SAPT	Symmetry-adapted perturbation theory
NEDA	Natural energy decomposition analysis
NBO	Natural bond orbitals
ETS-NOCV	Extended transition state-natural orbital for chemical valence
LED	Local energy decomposition
BSSE	Basis set superposition error
CP	Counterpoise
MEP	Molecular electrostatic potential
QTAIM	Quantum Theory of Atoms in Molecules
NCI	Noncovalent interaction
RDG	Reduced density gradient

bbh	1,6-bis(2,6-bis(benzothiazol-2-yl) pyridine-4-yloxy) hexane
CBS	Complete basis set
ESP	Electrostatic potential
I–V	Current-Voltage
gCP	Geometrical counterpoise correction
DOS	Density of states
PAW	Projected augmented wave
PDI	Perylenediimide
Aβ	Amyloid beta
GAFF	General Amber force field
PME	Particle Mesh Ewald

LIST OF FIGURES

Figures **Page No**

LIST OF TABLES

Tables **Page No**

Chapter 1

Introduction

1.1. Noncovalent Interactions

Noncovalent interactions, also known as noncovalent bonds, refer to molecular interactions that occur between one entity and another or within the same entity. Figure 1.1 illustrates the noncovalent interaction between the two entities XY and DZ. In which, Y and D represent the electron acceptor and donor atoms, respectively. When the two entities are arranged in a favourable geometrical configuration, leading to the delocalization of electrons mainly from the non-bonding orbital of D onto the antibonding orbital of XY. This non-bonded interaction between the two entities is termed as noncovalent interaction. If the non-bonded interaction has occurred within the same molecular entity, it is called as intramolecular noncovalent interaction.

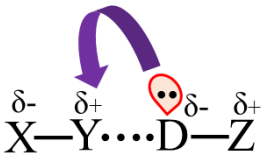

Figure 1.1. Pictorial representation of noncovalent interaction between two molecular entities XY and DZ.

Noncovalent interaction plays an essential role in various areas such as molecular recognition,[1] molecular assemblies,[2,3] protein-ligand interaction,[4,5] material sciences,[6,7] biomolecular systems,[8,9] and drug designing,[10] etc. The various types of noncovalent interactions include hydrogen bonding (H-bond),[11-14] van der Waals (vdW) interaction,[15-18] π-π stacking,[19,20] hydrophobic interaction,[21-23] cation-π,[24-26] anion-π,[27-29] etc. Some of the types of noncovalent interactions are displayed in Figure 1.2. Hydrogen bonding is one of the well-known noncovalent interactions. It occurs when a hydrogen atom bonded to a strongly electronegative atom (such as oxygen, nitrogen, or fluorine) is attracted to another electronegative atom in a different molecule or within the molecule.

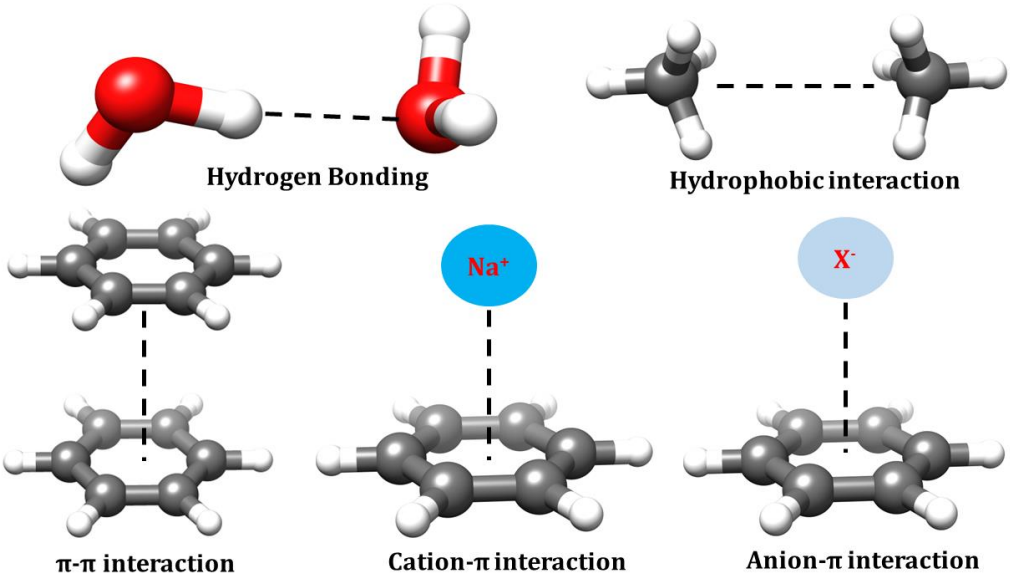

Figure 1.2. Schematic illustration of various noncovalent interactions.

Recent scientific studies open the broader scope of H-bond formation to less electronegative atoms such as sulphur (S),[30,31] carbon (C),[32,33] phosphorous (P),[34] and metals.[35] van der Waals (vdW) interaction[18,36] originate from the temporary dipoles, dipole-dipole, and induced-dipole interactions. π-π stacking interactions are mainly exhibited between aromatic ring molecules. An example of π-π stacking is the interaction of π-electron clouds between the two benzene rings.[19,20,37] Cation-π interaction involved the interaction of cation species with the π-electron cloud of an aromatic ring.[24-26] For example, the interaction of sodium ion with benzene ring.[38] Anion-π interactions are a type of noncovalent interaction that exists between the anion species and the π-electron cloud of the aromatic ring.[27-29] Example of the anion-π interaction is the interaction of fluoride anion with the hexafluoro-substituted benzene systems.[39] Hydrophobic interactions are another form of noncovalent interaction that does not directly involve the intermolecular attractive forces between two systems and is different from other types of noncovalent interactions. These interactions occur between nonpolar systems in the liquid phase (say water) in such a way that the tendency to form water-water hydrogen bonding drives the nonpolar species to arrange themselves to have minimum surface contact.[21-23]

1.2. Noncovalent Interactions in Supramolecular Host-Guest Chemistry

The primary development of supramolecular chemistry can be traced back to 1987 when Lehn, Cram, and Pederson won the Nobel Prize for their groundbreaking contribution of host-guest interactions.[40] After this, the popularity of supramolecular chemistry has increased among

chemists, biologists, and material scientists, in which they employed different noncovalent interactions, such as hydrogen bonding, π-π stacking, electrostatic, van der Waals interaction, hydrophobic interaction, to explain the interaction exhibited in the systems.[41-46] Over the last few decades, tremendous research efforts have been focused to study the host-guest complexes based on macrocyclic host molecules. Numerous macrocyclic host systems, including cyclodextrins (CDs),[47,48,49] calixarenes (CAs),[50-53] crown ethers,[54,55] cyclophanes,[56] cucurbit[n]urils (CBs),[57-60] and pillar[n]arenes were reported.[61,62] These systems geometrically possess cavities to accommodate various guest molecules. In addition, the cavities facilitate guest inclusion through noncovalent interactions. One of the key advantages of such macrocyclic hosts is their ability to bind the specific guest selectively. The size, shape, and functional groups of the host can be tailored to match the properties of the intended guest. Among different macrocyclic host molecules, the involvement of CAs, CDs, and CBs in drug delivery is experiencing a growing popularity.[63-65] Cyclodextrins (CDs) macrocyclic ring molecules, which are composed of α-1,4 glycosidic bond-linked oligosaccharides, have been extensively used in enzyme technology,[66] catalytic reactions,[67] and pharmaceutics.[68] Among the CDs family, the most commonly used are α, β, and γ forms, distinguished by 6, 7, and 8 glucose units.[69] The external and internal regions of the CDs have a hydrophilic and hydrophobic nature. They can potentially encapsulate a variety of guests, such as neutral molecules, cationic and anionic guests, proteins, and polymer chains.[70-74]

Calixarenes (CAs) host consists of phenolic units and is linked by methylene bridges at the meta-position. Geometrically, this host has a corn-like shape with a hollow cavity and two distinct rims on the primary and secondary sides. The cavity dimensions of the CAs vary depending on the number of phenolic units present.[50,51] The lower and upper rims of CAs are hydrophilic and hydrophobic due to the presence of phenolic oxygen and methyl groups, respectively. Various guests, including small organic molecules, cations, anions, sugars, and proteins, can fit inside the cavity of the CAs.[52] These host-guest interactions are mainly governed by noncovalent interactions such as hydrogen bonding, hydrophobic, and ion-dipole interactions.

Cucurbit[n]urils (CBs), a class of macrocyclic compounds, are significant in supramolecular chemistry. One of the well-known members of the CBs family is cucurbit [7] uril (CB [7]), which consists of seven glycoluril rings stacked on top of each other to form a tubular structure with hydrophobic cavities in the interior and hydrophilic carbonylated rims.[46] The width dimension of the CBs can be modulated with respect to the number of glycoluril units. Inside

the cavity of CBs is a nonpolar and hydrophobic nature, capable of binding the neutral guest molecules through noncovalent interactions.[46]

Designing host receptors for binding specific guest molecules needs to incorporate the particular groups in the host. Based on the characteristic of the guest molecule, the host can be tuned, like tuning host metal-organic frameworks (MOFs) to detect toxic pesticide guest molecules.[75] Chetia et al.[76] reported a host 2,6-bis(2-benzimidazolyl) pyridine to detect the toxic benzene metabolites compounds like phenol, resorcinol, catechol, hydroquinone, and *para*-benzoquinone. This host specifically binds the hydroquinone guest through hydrogen bonding.

With the remarkable progress in host-guest chemistry, there is a plethora of literature for designing, synthesizing, and computational studies of molecular hosts that can encapsulate only a single guest species. However, the development and advancement of the ditopic receptors host, capable of binding two guest molecules, are still limited. Reetz and coworkers demonstrate that the ditopic receptor comprises crown ether and are covalently linked with the Lewis-acidic boron center.[77] This receptor simultaneously formed complexes with the potassium and fluoride ions. The potassium ion is bound inside the crown ether cavity, while the fluoride ion is on the boron center. Reinhoudt and coworkers have reported the ditopic receptor host comprises a Lewis-acidic uranyl center and is covalently linked to two benzo [15] crown-5 units.[78] This receptor has the potential to recognize potassium and dihydrogen phosphate ions.

1.3. Noncovalent Interactions in Electron Transport

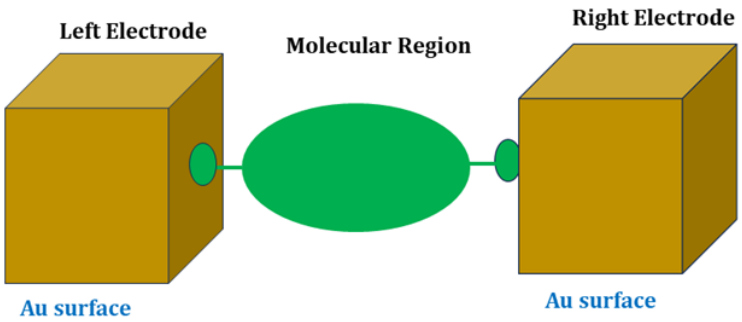

Figure 1.3. Illustration of a molecular system connected to the Au-electrodes for electron transport measurement.

The involvement of noncovalent interactions is also seen in the electron charge transport processes in biological and chemical systems. In biological systems, the electron charge transport occurs through π-stacked DNA base pairs and amino acid residues.[79,80] Regarding molecular systems, various groups have reported the process of electron charge transport through π-π stacking interactions. A simple model for the measurement of conductance of a molecular system connected to the gold (Au) electrode is shown in Figure 1.3. The conductance measurement of a single molecular system consisting of multiple π-π stacked benzene rings in a *para*-cyclophane scaffold provided evidence of electron charge transport across the two π-systems.[81] Moreover, the electron charge transport process was also found in the supramolecular host-guest system. Zhang et al. reported the electrical conductance of host-guest complexes generated between the host cucurbit [8] uril (CB [8]), which has a hydrophobic cavity environment, and guest that has three distinct viologens (bipyridinium) derivatives molecular wires.[82] A notable alteration in the conductance value was observed when the viologen was accommodate inside the cavity of CB [8]. This finding highlighted the influence of the host environment on the conductance of the guest molecule. Wen et al. reported the conductance of a host-guest system featuring noncovalent bonding interaction between the crown ether host and electron-deficient cationic guest.[83] Li et al. observed a notably elevated level of molecular conductance in the complex comprising host dibenzo-24-crown-8 and guest pyridinium-based molecular junction.[84] In this direction, Stang and coworkers reported the conductance of the host-guest complex form between the organoplatinum (II) metallocycle hosts and fullerene (C_{60}) guest. Using the scanning tunneling microscopy break junction technique and measured the conductance of the host-guest complex. They observed that the conductance of the metallocycle substantially increased when incorporating the C_{60} guest.[85] Stoddart and coworkers investigated the electrical conductivity of the 1:1 host-guest complex generated between the viologen-based cyclophane host $ExBox_2^{4+}$ and C_{60} guest molecule. This inclusion complex undergoes self-assembly to one another through nonbonding interaction and produces one-dimensional needle-like single crystals. The electrical conductivity of this crystal is found to be on the order of 10^{-7} S cm^{-1}.[86]

Tuning the electrical conductivity of the host-guest system by inserting different guests was also reported. In this regard, the Kiguchi group synthesized the columnar self-assembled cage host, which can accommodate the planar π-system guest molecule.[87] They found that the conductance value of the complexes decreases as the number of the π-systems guests increases. However, the decrease in conductance per unit of electron transport distance is less significant

than the reduction observed in conventional covalent molecular junctions with π-conjugation. In addition, the same group also studied the electron transport properties of the complexes, which consist of gold ion clusters embedded inside the cavity of the palladium-coordinated self-assembled cage.[88] This group investigated the electron transport properties of the complexes, which consist of a pair of naphthalenediimide and triphenylene that bound within the cavity of the palladium-coordinated self-assembled cage.[88] Inserting the same pairs, i.e., naphthalenediimide or triphenylene, enhances electronic conductivity, whereas introducing diverse pairs results in additional rectification properties.

Theoretical studies of electron transport in the molecular system of π-π stacking interaction were also reported. Yoshizawa and coworkers[89] studied the electron transport properties of molecular systems with nitrogen-doped polycyclic aromatic hydrocarbons (PAH), cyclophanes, and undoped PAH. Using nonequilibrium Green's function (NEGF) method in combination with the density functional theory (DFT), they investigated the electrical current rectifying properties of the considered molecular systems. They observed that the electron-rich nitrogen atom and electron-poor boron atom create the road for electrical conductance channels. This presence substantially increases the electrical conductance. Yoshizawa and Tsuji[90] also reported the electron transport properties of molecular systems consisting of a sequence of multilayered cyclophanes, where hydroquinone acts as the donor unit and quinone acts as the acceptor unit. The multilayered cyclophanes are double-layered, triple-layered, and quadruple-layered. The conductance value was found to be decreased exponentially as the length of the molecule increased. Frisenda et al.[91] studied the role of quantum-interference effects on the electron transport properties of the π-stacked dimer molecular systems. The studied molecule is an oligo-phenylene-ethynylene (OPE3) π-conjugated molecule with either one (S–OPE3) or two (S–OPE3–S) thiol anchoring groups. By employing *ab initio* calculations and single-molecule conductance assessments, they revealed the presence of a quasiperiodic destructive quantum interference pattern in the molecular systems. This study also highlighted the possibility of controlling the molecular conductance by tuning the structure-property relationship of π-stacked dimers.

1.4. Noncovalent Interactions in Protein-Ligand Interactions

Noncovalent interactions are indispensable in biomacromolecules, particularly in protein-ligand interactions. These interactions control the biomolecules' structural stability, protein folding mechanisms, and enzymatic substrate binding in this context.[4,5,8-10,92] It also plays a specific part in drug design and protein-drug binding.

Alzheimer's Disease (AD) is one of the neurodegenerative disorders, and the number of people affected by this disease is increasing day by day and is considered one of the major concerns.[93-95] The causes of the disorder have been partially elucidated and continue to be a subject of ongoing research. Many research groups proposed the factors involved in the initiation and progression of this disease. The destruction of nerve cells and loss of memory and other cognitive functions in the brain are the symptoms commonly occurring in the elderly population.[96,97] Some of the factors related to AD are an accumulation of insoluble senile plaques, which are composed of amyloid beta (Aβ) fibrils,[98-100] and neurofibrillary tangles (NFTs), which consist of hyperphosphorylated tau (pTau) protein.[101-103] Aβ fibrils are obtained by the aggregations of the generated monomer Aβ resulting from the enzymatic cleavages of amyloid precursor protein (APP). These fibrils destroy the function of brain neural cells, resulting in synaptic dysfunction.[94,104]

In 1992, Hardy and Higgins proposed the amyloid cascade hypothesis.[105] It has played an important role in elucidating the origins and causes of Alzheimer's disease (AD) and steering research in this field for the last two decades.[106] This hypothesis proposed that the aggregation of Aβ monomers or oligomers resulting to the formation of senile plaques and neurofibrillary tangles (NFTs). These plaques kill the brain cells, resulting in the gradual deterioration of memory and cognitive decline, ultimately leading to the demise of affected individuals. Aβ peptides are generated products from the transmembrane amyloid precursor protein (APP) after the cleavage by enzymes α, β, and γ-secretases, as illustrated in Figure 1.4.[107] When the α-secretases proceed, the cleavage of APP yields two products: an N-terminal ectodomain known as sAPPα and an 83-amino acid C-terminal membrane fragment (C83).

Further, the obtained 83-amino acid C-terminal membrane fragment is sequentially cleaved by γ-secretases and produces a non-pathogenic P3 peptide and APP intracellular domain (AICD). This pathway of the cleavage process is known as non-amyloidogenic pathway. On the other hand, when the β-secretase cuts the APP, it generates an N-terminal ectodomain (sAPPβ) and 99-amino acid C-terminal membrane fragment (C99). Sequentially, the γ-secretases cleavage the C-terminal membrane fragment (C99) and yield pathogenic Aβ peptide and AICD. This cleavage process pathway is called the amyloidogenic pathway[108,109] (Figure 1.4) due to the lack of inaccuracy in the cleavage by γ-secretases, resulting in the formation of different lengths of Aβ peptide. The most commonly obtained Aβ peptides are Aβ1-40 and Aβ1-42.[110]

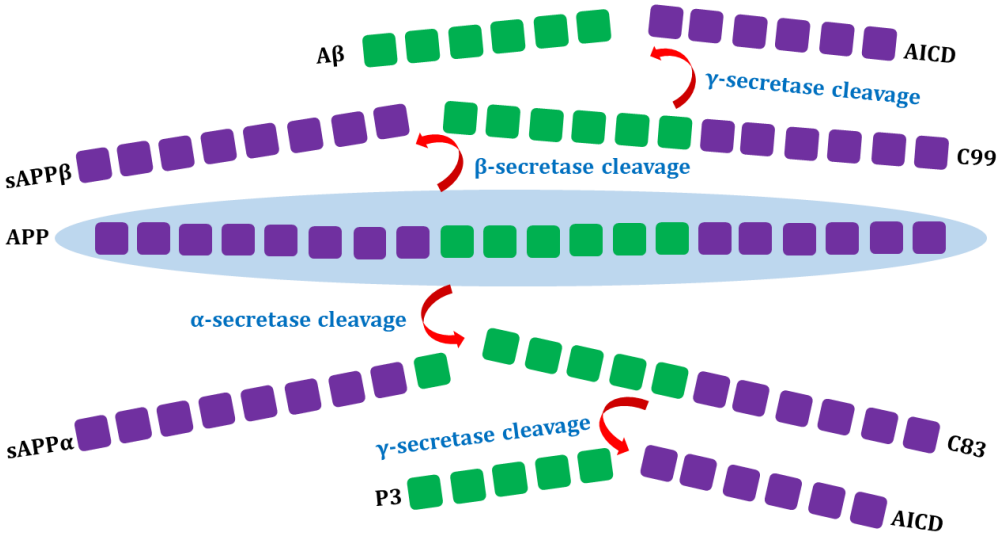

Figure 1.4. Schematic diagram of non-amyloidogenic and amyloidogenic pathways of APP cleavage. Aβ part of protein and other regions are shown in green and purple colours, respectively.

In 1984, the amino acid sequence contained in the Aβ was discovered.[111] The Aβ1-40 consists of eleven polar, seventeen hydrophobic, and twelve charged residues. On the other hand, in the Aβ1-42 peptide, two extra hydrophobic residues are attached at the C-terminal.[112] The differences in the amino acid residues for both peptides are displayed in Figure 1.5.

Aβ1-40

{Asp1}{Ala2}{Glu3}{Phe4}{Arg5}{His6}{Asp7}{Ser8}{Gly9}{Tyr10}{Glu11}{Val12}{His13}{His14}{Gln15}{Lys16}{Leu17}{Val18}{Phe19}{Phe20}{Ala21}{Glu22}{ASP_{23}}{Val24}{Gly25}{Ser26}{Asn27}{Lys28}{Gly29}{Ala30}{Ile31}{Ile32}{Gly33}{Leu34}{Met35}{Val36}{Gly37}{Gly38}{Val39}{Val40}

Aβ1-42

{Asp1}{Ala2}{Glu3}{Phe4}{Arg5}{His6}{Asp7}{Ser8}{Gly9}{Tyr10}{Glu11}{Val12}{His13}{His14}{Gln15}{Lys16}{Leu17}{Val18}{Phe19}{Phe20}{Ala21}{Glu22}{ASP_{23}}{Val24}{Gly25}{Ser26}{Asn27}{Lys28}{Gly29}{Ala30}{Ile31}{Ile32}{Gly33}{Leu34}{Met35}{Val36}{Gly37}{Gly38}{Val39}{Val40}{Ile41}{Ala42}

Figure 1.5. Illustration of amino acid residues present in Aβ1-40 and Aβ1-42.

The Aβ monomer is an intrinsically disordered peptide (IDP) in aqueous environments. Rather than adopting a single dominant folded conformation, Aβ peptide occupies a multitude of different conformations. The structures of Aβ monomers are mainly obtained from the Nuclear Magnetic Resonance (NMR) and molecular dynamics (MD) simulations. The monomers Aβ1-40 and Aβ1-42 predominantly existed in the α-helical conformation under a membrane environment. The amino acid residue region from Asp1 to His14 of the Aβ1-40 monomer remains unstructured, and the segment spanning from Gly25 to Val36 features an α-helical conformation.[113] The turn centered around the amino acid residues segment Gly25 to Asn27, as shown in Figure 1.6b. The monomer Aβ1-42 consists of two α-helix regions. Helix I consists of amino acid residues Ser8 to Val24, while helix II contains Lys28 to Val38, and the turning region occurs around Gly25 to Lys28 (Figure 1.6b).[114,115] In the complete water environment, the amino acid residue region His13 to Asp23 of Aβ1-40 monomer exhibited 3-helix, and the C and N-terminal remains unstructured (Figure 1.6a).[116] Many groups also reported the molecular dynamics (MD) simulation studies of Aβ monomers in aqueous and membrane environments. Fels and coworkers conducted the molecular dynamics (MD) simulations of full-length Aβ monomers within an aqueous environment.[117] Their findings revealed the presence of a turn region spanning from Ala21 to Gly33, and the amino acid residues between Asp1 and Tyr10 exhibited significant flexibility. Using monomers' peptides Aβ1-40 and Aβ1-42, Miyashita et al. performed the MD simulations based on the replica exchange in the membrane environment.[118] They observed that the C-terminal portion of both peptides prefers a membrane environment, while the N-terminal region prefers an aqueous environment and adopts a coiled structure. The molecular dynamic simulation was conducted by Valerio et al. on the Aβ1-40, and they found that misfolded structure.[119] Skelton and coworkers conducted MD simulations involving Aβ1-40 and Aβ1-42 monomers within the explicit water environment.[120] Their findings unveiled a significant increase in the presence of water molecules surrounding Lys28 while simultaneously observing a decrease in water molecules around Val24. These alterations in water molecule distribution were identified as pivotal factors contributing to the formation of turns in the protein structures.

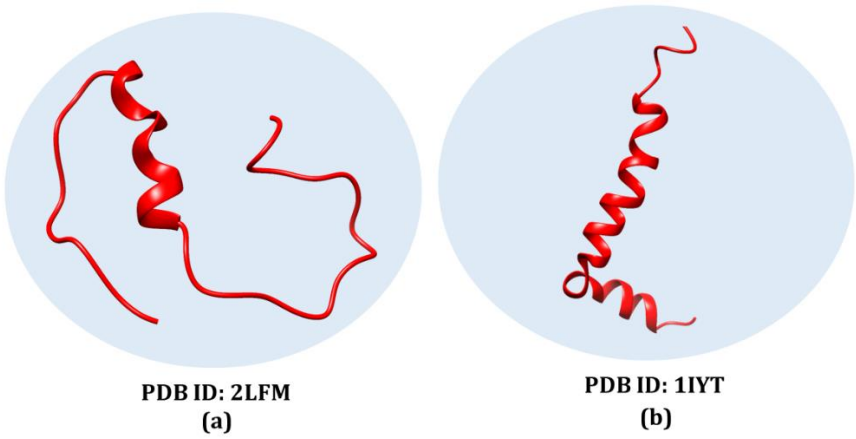

Figure 1.6. Representation of monomer structures of (a) Aβ40 (PDB ID: 2LFM) and (b) Aβ42 (PDB ID: 1IYT), respectively.

Aβ is typically a monomeric structure in the bloodstream and cerebrospinal fluid (CSF). The misfolding monomers are formed in the initial step from the monomeric Aβ. They subsequently led to the dimerization and the formation of oligomers and aggregations.[121-123] Based on the Aβ polymerization model, the generation of the Aβ fibrils proceeds through three steps: (a) nucleation, (b) elongation, and (c) saturation, as illustrated in Figure 1.7.[124-127] In nucleation, monomers undergo conformational alterations and join together to form an oligomeric core that comprises β-sheet structures. This step proceeds slowly due to the thermodynamic instability associated with the self-association of monomers. After the formation of the nucleus, the thermodynamically favourable elongation begins, leading to the generation of protofibrils, which convert into mature fibrils during the saturation phase. The process of amyloid fibril formation adheres to sigmoidal kinetics, where nucleation is succeeded by a phase of swift elongation (growth), ultimately leading to a state of saturation.

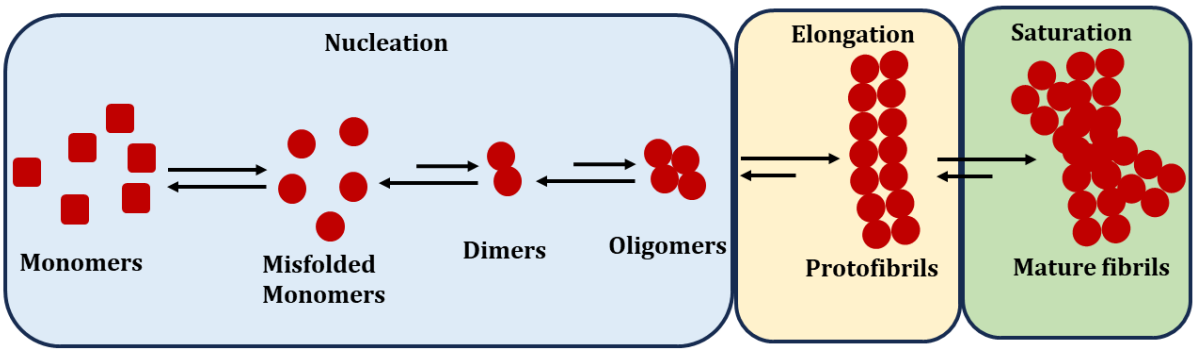

Figure 1.7. Different consecutive steps for the formation of Aβ fibrils.

There is a need for robust diagnostic tools for early AD detection, and effective treatments that can efficiently halt the formation of amyloid fibrils. However, targeting amyloid fibrillation is regarded as one of the most promising avenues in the quest to combat AD. Through this β-amyloid hypothesis, different species were used, such as metal ion chelators, small molecules, peptides, and nanoparticles, to modulate the Aβ fibril.[128-131] Various naturally occurring phytochemicals compounds were also reported that can inhibit the aggregation of Aβ.[132-134] Currently, there are a few drugs available to treat this disease and approved by the Food and Drug Administration (FDA), namely donepezil, tacrine, galantamine, rivastigmine, and N-methyl-D-aspartate (NMDA)-receptor antagonist memantine.[135] However, these drugs give temporary relief to the patient. Different strategies are used to lower the production of Aβ amyloid beta protein. The widely used strategies are (i) γ-secretase and β-secretase inhibitors development,[136,137], (ii) reducing the APP expression, and (iii) development of molecules to stop the (Aβ) amyloid beta protein aggregation[138]. However, developing inhibitors to inhibit γ-secretase and β-secretase is not ideal because both enzymes are essential for normal physiological function. Therefore, the widely use approach is designing a molecule to stop the aggregation of (Aβ) amyloid beta protein. Some molecules and antibodies that went into clinical phases II and III were Tramiprosate (Alzhemed®),[139,140] Solanezumab,[141–144] and Bapineuzumab (humanized 3D6).[145–147] These molecules and antibodies have failed at clinical stages II and III. These prompted researchers to seek innovative approaches for the development of drugs for Alzheimer's disease (AD).

Perylene diimide (PDI)-based materials have gained significant attention in recent years and are widely employed in the applications of optical and electrochemical properties.[148,149] This molecule has a strong tendency to form self-aggregations through π-π interaction and leads to poor solubility in many organic solvents.[150–152] The use of PDI-based materials in biochemistry is very limited. Transforming such PDI molecules into biocompatible materials makes it possible for researchers to delve deeper into the field of biochemical research. Muthuraj et al. introduced a biocompatible compound, histidine-functionalized perylene diimide (PDI-HIS), which is biocompatible.[153] This material has the potential to modulate the aggregated Aβ peptides. Different types of noncovalent interactions mainly govern the driving force for peptide-organic molecule interactions. So, understanding the noncovalent interactions between the amino acid functionalized PDI and Aβ proteins will generate the knowledge that could be applied to designing new, more potential drug molecules.

1.5. Motivation

Noncovalent Interactions have emerged as indispensable architects for shaping the structures and functions of numerous supramolecular host-guest and biological systems. Beyond the context of biological and molecular systems, these interactions are also seen in the realm of material sciences and molecular drug design. In this investigation, supramolecular host-guest and biological protein-ligand systems were considered in which Aβ peptides were the protein of interest. A thorough examination explored the various noncovalent interactions such as van der Waals forces, hydrogen bonding, hydrophobic interactions, and π-π stacking. In the context of host-guest systems, there is a scarcity of experimental and computational studies that focus on supramolecular host systems, which can exist in different conformations. Such possible conformations are also possible in the ditopic receptor host 1,6-bis(2,6-bis(benzothiazol-2-yl) pyridine-4-yloxy) hexane (bbh) which is lacking in the experimental studies reported by Goutam et al.[154] This missing opportunity allowed diverse quantum chemical investigations to explore the noncovalent interactions. The diversity in the involvement of noncovalent interactions is well recognised and one of the critical aspects is the electron charge transport through noncovalent interactions such as π-π stacking. So, supramolecular host–guest systems, which have π-π stacking interactions, are gaining much attention for constructing molecular electronic devices. Zhang et al.[155] reported that the cage-like hexatonic host (H^{6+}) could form complexes with π-electron-rich polycyclic aromatic hydrocarbon (PAH) guests. However, the possibility of electron charge transport through this π-π stacking interaction between the host and guest is yet to be explored.

Further, in the direction of host-guest interactions, understanding the effect of electron-withdrawing and donating groups on the host-guest systems consists of mainly hydrogen bonding and π-π stacking interactions. Jansen et al.[156] reported a molecular receptor based on the 2,4,6,8-tetraazabicyclo [3.3.1] nonane-3,7-dione (propanediurea) and geometrically exhibited U-shaped and capable of forming complexes with resorcinol molecule. Such complex systems open an avenue to explore the effect of the electron-withdrawing, and donating groups substituted guest molecules on the interaction energy interaction and nature of interactions. The involvement of noncovalent interactions is not limited to host-guest systems. Therefore, transitioning from the host-guest systems, these interactions play a crucial role in the protein-ligand system. Aβ peptide aggregations, the formation of Aβ fibrils, and the destruction of the brain neural cells are the main culprits of Alzheimer's disease (AD). Designing an inhibitor that can bind with Aβ fibrils protein through various noncovalent interactions and effectively

destabilize the fibrils is one of the primary strategies for curing AD. Varieties of inhibitors have been designed and reported, but none of them have succeeded so far. So, finding new molecules is of utmost importance.

Utilizing systems such as perylenediimide (PDI) derivatives and exploring the nature of interactions with Aβ fibrils is also one of the possibilities for the inhibitor designing of AD. The introduction of amino acid histidine (HIS) in the PDI system made it a biocompatible material (PDI-HIS).[153] The perylene core present in the PDI systems has the potential to form the noncovalent π-π stacking interaction. Experimental finding reported that PDI-HIS binds to the Aβ fibrils and eventually disaggregates the fibrils.[153] However, the disaggregation process and the interactions involved when the PDI-HIS binds on Aβ fibrils remain elusive. Further, the experimental studies of PDI-HIS trigger to explore the other amino acids such as alanine, phenylalanine, and tyrosine functionalized PDI. This thesis embarks on a journey through noncovalent interactions in supramolecular host-guest and protein-ligand systems.

1.6. Overview of Thesis

In this thesis, we explored various intramolecular and intermolecular noncovalent interactions in the supramolecular host-guest complexes and protein-ligand interactions using different quantum computational and molecular dynamics (MD) simulation methods. In Chapter 2, theoretical and computational methodologies used in the calculations are briefly discussed. Chapter 3 demonstrated the noncovalent interactions involved in the different conformers of the ditopic (two binding sites) receptor host 1,6-bis(2,6-bis(benzothiazol-2-yl) pyridine-4-yloxy) hexane and their complexes with resorcinol as a guest. Noncovalent interaction such as π-π plays an essential role in the construction of the building blocks of organic semiconductors. Taking these concepts into consideration, in Chapter 4, we explored the π-π interactions and electron transport in the host-guest complexes formed between three dimensions' hexa-cationic host which consists of two triscationic π-electron-deficient trispyridiniumtriazine (TPZ^{3+}) units and is bridged face-to-face by three ethylene-triazole-ethylene and guest polycyclic aromatic hydrocarbons (PAH). In Chapter 5, we explored the nature of the noncovalent interaction of propanediurea based molecular clip receptors with different electron withdrawing and donating groups substituted resorcinol molecules. In Chapter 6, we investigated the noncovalent interactions between the amino acids functionalized perylene diimide (PDI) compounds and amyloid-β (Aβ) fibrils. These fibrils are well recognized as the primary causative agents in the development of Alzheimer's disease (AD). In Chapter 7, we proposed three compounds functionalizing the perylene diimide (PDI) with amino acids: phenylalanine, alanine, and

tyrosine. A systematic study was carried out to explore the structural changes and noncovalent interactions when these compounds bind with the amyloid-β (Aβ) fibril protein. The last Chapter presents the summary of this thesis work.

1.7. References

[1] P. S. Murthy, *J. Chem. Educ*., 2006, **83**, 7, 1010.

[2] T. F. A. De Greef, M. M. J. Smulders, M. Wolffs, A. P. H. J. Schenning, R. P. Sijbesma and E. W. Meijer, *Chem. Rev.*, 2009, **109**, 5687.

[3] S. Samanta, P. Raval, G. N. M. Reddy and D. Chaudhuri, *ACS Cent. Sci.*, 2021, **7**, 1391.

[4] K. Ding, S. Yin, Z. Li, S. Jiang, Y. Yang, W. Zhou, Y. Zhang and B. Huang, *J. Chem. Inf. Model.*, 2022, **62**, 7, 1734.

[5] P. Zhou, J. Huang and F. Tian, *Curr. Med. Chem.*, 2012, **19**, 226.

[6] R. A. DiStasio Jr, V. V. Gobre and A. Tkatchenko, *J. Phys.: Condens. Matter*, 2014, **26**, 213202.

[7] V. Georgakilas, M. Otyepka, A. B. Bourlinos, V. Chandra, N. Kim, K. C. Kemp, P. Hobza, R. Zboril and K. S. Kim, *Chem. Rev.*, 2012, **112**, 6156.

[8] K. E. Riley and P. Hobza, *Acc. Chem. Res.*, 2013, **46**, 4, 927.

[9] K. E. Riley and P. Hobza, *Comp. Mol. Sci.*, 2011, **1**, 3.

[10] B. R. Beno, K. S. Yeung, M. D. Bartberger, L. D. Pennington and N. A. Meanwell, *J. Med. Chem.*, 2015, **58**, 11, 4383.

[11] P. L. Huyskens, *J. Am. Chem. Soc.*, 1977, **99**, 2578.

[12] L.J. Prins, D. N. Reinhoudt and P. Timmerman, *Angew. Chem., Int. Ed.*, 2001, **40**, 2382.

[13] M. Elstner, P. Hobza, T. Frauenheim, S. Suhai and E. Kaxiras, *J. Chem. Phys.*, 2001, **114**, 5149.

[14] V. R. Cooper, T. Thonhauser and D. C. Langreth, *J. Chem. Phys.*, 2008, **128**, 204102.

[15] D. Langbein, *Theory of van der Waals Attraction;* Springer Tracts in Modern Physics; Springer: Berlin Heidelberg, 1974; Vol. 72.

[16] J. Klimeš and A. Michaelides, *J. Chem. Phys.*, 2012, **137**, 120901.

[17] A. M. Reilly and A. Tkatchenko, *Chem. Sci.*, 2015, **6**, 3289.

[18] J. Hermann, R. A. DiStasio and A. Tkatchenko, *Chem. Rev.*, 2017, **117**, 4714.

[19] B. J. J. Timmer and T. J. Mooibroek, *J. Chem. Educ.*, 2021, **98**, 540.

[20] P. Mignon, S. Loverix, J. Steyaert and P. Geerlings, *Nucleic Acids Res.*, 2005, **33**, 1779.

[21] W. Blokzijl and J. B. F. N. Engberts, *Angew. Chem. Int. Ed. Engl.*, 1993, **32**, 1545

[22] L. R. Pratt and A. Pohorille, *Chem. Rev.*, 2002, **102**, 2671.

[23] S. Otto and J. B. F. N. Engberts, *Org. Biomol. Chem.*, 2003, **1,** 2809.

[24] D. Vijay, H. Zipse and G. N. Sastry, *J. Phys. Chem. B,* 2008, **112**, 8863.

[25] Q. Li, H. Zhuo, X. Yang, J. Cheng, W. Li and R. E. Loffredo, *ChemPhysChem*, 2014, **15**, 500.

[26] J. A. Carrazana-García, J. Rodríguez-Otero and E. Cabaleiro-Lago, *J. Phys. Chem. B,* 2012, **116**, 5860.

[27] O. Perraud, V. Robert, H. Gornitzka, A. Martinez and J. Dutasta, *Angew. Chem., Int. Ed.*, 2012, **51**, 504.

[28] D. Quiñonero, P.M. Deya, M.P. Carranza, A.M. Rodríguez, F.A. Jalon and B.R. Manzano, *Dalton Trans.*, 2010, **39**, 794.

[29] B. P. Hay and V.S. Bryantsev, *Chem. Commun.*, 2008, 2417.

[30] M. K. Krepps, S. Parkin and D. A. Atwood, *Crystal Growth & Design*, 2001, **1**, 291.

[31] H. S. Biswal and S. Wategaonkar, *J. Phys. Chem. A*, 2009, **113**, 12763.

[32] Y. Gu, T. Kar and S. Scheiner, *J. Am. Chem. Soc.*, 1999, 121, **40**, 9411.

[33] G. R. Desiraju, *Acc. Chem. Res.*, 1996, **29**, 441.

[34] A. S. Hansen, L. Du and H. G. Kjaergaard, *J. Phys. Chem. Lett.*, 2014, **5**, 4225.

[35] L. Brammer, *Dalton Trans.*, 2003, 3145.

[36] S. Grimme, *Wiley Interdiscip. Rev. Mol. Sci.*, 2011, **1**, 211.

[37] C. Chipot, R. Jaffe, B. Maigret, D. A. Pearlman and P. A. Kollman, *J. Am. Chem. Soc.* 1996, **118**, 11217.

[38] S. Mecozzi, A. P. West and D. A. Dougherty, *J. Am. Chem. Soc.*, 1996, **118**, 2307.

[39] D. QuiÊonero, C. Garau, C. Rotger, A. Frontera, P. Ballester, A. Costa and P. M. Dey, *Angew. Chem. Int. Ed.*, 2002, **41**, 3389.

[40] J. M. Lehn, *Angew. Chem. Int. Ed.* 1988, **27**, 89.

[41] R. P. Sijbesma, F. H. Beijer, L. Brunsveld, B. J. B. Folmer, J. H. K. K. Hirschberg, R. F. M. Lange, J. K. L. Lowe and E. W. Meijer, *Science*, 1997, **278**, 1601.

[42] T. Park, S.C. Zimmerman and S. Nakashima, J. *Am. Chem. Soc.*, 2005, **127**, 6520.

[43] J. H. Ryu, D. J. Hong and M. Lee, *Chem. Commun.* 2008, **9**, 1043.

[44] J. D. Hartgerink, E. Beniash and S. I. Stupp, *Science*, 2001, **294**, 1684.

[45] W. Zhang, W. Jin, T. Fukushima, A. Saeki, S. Seki and T. Aida, *Science*, 2011, **334**, 340.

[46] X. Ma and Y. Zhao, *Chem. Rev.*, 2015, **115**, 7794.

[47] V. C. R. Villiers, *Acad. Sci.*, 1891, **112**, 536.

[48] S. Li and W. C. Purdy, *Chem. Rev.*, 1992, **92**, 1457.

[49] V. T. D'Souza and K. B. Lipkowitz, *Chem. Rev.*, 1998, **98**, 1741.

[50] S. Mullins, *In Calixarenes*; Gutsche, C. D., Ed., Royal Society of Chemistry, Cambridge, 1989.

[51] J. Vicens, J.M. Harrowfield and L. Baklouti, *Calixarenes in the Nanoworld*; Springer, Dordrecht, 2007.

[52] S. B. Nimse and T. Kim, *Chem. Soc. Rev.*, 2013, **42**, 366.

[53] J. B. Simões, D. L. da Silva, S. A. Fernandes and A. de Fátima *Eur. J. Org. Chem.*, 2022, **38**, e202200532.

[54] G. W. Gokel, W. M. Leevy and M. E. Weber, *Chem. Rev.*, 2004, **104**, 2723.

[55] Y.-F. Zhang, F. F. Di, P.-F. Li and R.-G. Xiong, *Chem. Eur. J.*, 2022, **28**, e202102990.

[56] P. G. Ghasemabadi, T. Yaoa and G. J. Bodwell, *Chem. Soc. Rev.*, 2015, **44**, 6494.

[57] R. Behrend, E. Meyer and F. Rusche, *Justus Liebigs Ann. Chem.*, 1905, **339**, 1.

[58] W.A. Freeman, W.L. Mock and N.Y. Shih, *J. Am. Chem. Soc.*, 1981, **103**, 7367.

[59] J. Kim, L. S. Jung, S. Y. Kim, E. Lee, J.-K. Kang, S. Sakamoto, K. Yamaguchi and K. Kim, *J. Am. Chem. Soc.*, 2000, **122**, 540.

[60] A. Day, A. P. Arnold, R. J. Blanch and B. J. Snushall, *Organomet. Chem.*, 2001, **66**, 8094.

[61] Y. Yao, M. Xue, J. Chen, M. Zhang and F. Huang, *J. Am. Chem. Soc.*, 2012, **134**, 15712.

[62] X. Hou, C. Ke, C. Cheng, N. Song, A. K. Blackburn, A. A. Sarjeant, Y. Y. Botros, Y.-W. Yang and J. F. Stoddart, *Chem. Commun.*, 2014, **50**, 6196.

[63] V. Stella and R. Rajewski, *Pharm. Res.*, 1997, **14**, 556.

[64] G. Hettiarachchi, D. Nguyen, J. Wu, D. Lucas, D. Ma, L. Isaacs and V. Briken, *PloS One*, 2010, **5**, e10514.

[65] N. J. Wheate and C. Limantoro, *Supramolecular Chemistry*, 2016, **28**, 849–856.

[66] R. Villalonga, R. Cao and A. Fragoso, *Chem. Rev.*, 2007, **107**, 3088.

[67] R. Breslow and S. D. Dong, *Chem. Rev.*, 1998, **98**, 1997.

[68] M. E. Davis and M.E. Brewster, *Nat. Rev. Drug Discov.*, 2004, **3**, 1023.

[69] K. L. Liu, Z. Zhanga and J. Li, *Soft Matter*, 2011, **7**, 11290.

[70] M. V. Rekharsky and Y. Inoue, *Chem. Rev.*, 1998, **98**, 1875.

[71] M. V. Rekharsky and Y. Inoue, *J. Am. Chem. Soc.*, 2002, **124**, 813.

[72] T. Irie and K. Uekama, *Adv. Drug Delivery Rev.*, 1999, **36**, 101.

[73] E. Marttin, J. C. Verhoef and F. W. H. M. J. Merkus, *Drug Targeting*, 1998, **6**, 17.

[74] G. Wenz, B.H. Han and A. Müller, *Chem. Rev.*, 2006, **106**, 782.

[75] B. Lalchawimawia, A. Sil, T. Banerjee, N. Singh, A. Bhatnagar, R. Mukhopadhyay and A. Mandal, *Coord. Chem. Rev.*, 2023, **490**, 215214.

[76] B. Chetia and P. K. Iyer, *Tetrahedron Lett.*, 2006, **47**, 8115.

[77] M. T. Reetz, C.M. Niemeyer and K. Harms, *Angew. Chem. Int. Ed. Engl.*, 1991, **30**, 1472.

[78] D. M. Rudkevich, Z. Brzozka, M. Palys, H. C. Visser, W. Verboom and D. N. Reinhoudt, *Angew. Chem. Int. Ed. Engl.*, 1994, **33**, 467.

[79] B. Giese, *Annu. Rev. Biochem.*, 2002, **71**, 51.

[80] H. B. Gray and J. R. Winkler, *Chem. Phys. Lett.*, 2009, **483**, 1.

[81] S. T. Schneebeli, M. Kamenetska, Z. Cheng, R. Skouta, R. A. Friesner, L. Venkataraman and R. Breslow, *J. Am. Chem. Soc.*, 2011, **133**, 2136.

[82] W. Zhang, S. Gan, A. Vezzoli, R. J. Davidson, D. C. Milan, K. V. Luzyanin, S. J. Higgins, R. J. Nichols, A. Beeby, P. J. Low, B. Li and L. Niu, *ACS Nano*. 2016, **10**, 5212.

[83] H. Wen, W. Li, J. Chen, G. He, L. Li, M. A. Olson, A. C. H. Sue, J. F. Stoddart and X. Guo, *Sci. Adv.*, 2016, **2**, 1.

[84] S. Li, J. Li, H. Yu, S. Pudar and B. Li, *J. Electroanal. Chem.*, 2020, **875**, 114070.

[85] J.-H. Tang, Y. Li, Q. Wu, Z. Wang, S. Hou, K. Tang, Y. Sun, H. Wang, H. Wang, C. Lu, X. Wang, X. Li, D. Wang, J. Yao, C. J. Lambert, N. Tao, Y.-W. Zhong and P. J. Stang, *Nat. Commun.*, 2019, **10**, 4599.

[86] J. C. Barnes, E. J. Dale, A. Prokofjevs, A. Narayanan, I. C. GibbsHall, M. Jurícek, C. L. Stern, A. A. Sarjeant, Y. Y. Botros, S.I. Stupp and J. F. Stoddart, *J. Am. Chem. Soc.*, 2015, **137**, 2392.

[87] M. Kiguchi, T. Takahashi, Y. Takahashi, Y. Yamauchi, T. Murase, M. Fujita, T. Tada and S. Watanabe, *Angew. Chem. Int. Ed.*, 2011, **50**, 5708.

[88] M. Kiguchi, J. Inatomi, Y. Takahashi, R. Tanaka, T. Osuga, T. Murase, M. Fujita, T. Tada, and S. Watanabe, *Angew. Chem. Int. Ed.*, 2013, **52**, 6202.

[89] A. Staykov, X. Li, Y. Tsuji and K. Yoshizawa, *J. Phys. Chem. C*, 2012, **116**, 1845.

[90] Y. Tsuji and K. Yoshizawa *J. Phys. Chem. C*, 2012, 116, **50**, 26625.

[91] R. Frisenda1, V. A. E. C. Janssen, F. C. Grozema, H. S. J. van der Zant and N. Renaud, *Nat. Chem.*, 2016, **8**, 1099.

[92] W. Neuhauser, D. Haltrich, K. D. Kulbe, and B. Nidetzky, *Biochemistry*, 1998, **37**, 1116.

[93] C. A. Ross and M. A. Poirier, *Nat. Rev. Mol. Cell Biol.*, 2005, **6**, 891.

[94] D. J. Selkoe and J. Hardy, *EMBO Mol. Med.*, 2016, **8**, 595.

[95] C. Reitz, C. Brayne and R. Mayeux, *Nat. Rev. Neurol.*, 2011, **7**, 137.

[96] V. J. De-Paula, M. Radanovic, B. S. Diniz and O. V. Forlenza, *Sub-Cell. Biochem.*, 2012, **65**, 329.

[97] R. E. Tanzi and L. Bertram, *Cell*, 2005, **120**, 545.

[98] M. P. Murphy and H. LeVine, *J. Alzheimer's Dis.*, 2010, **19**, 311.

[99] S. Lesne, T. K. Ming, L. Kotilinek, R. Kayed, C. G. Glabe, A. Yang, M. Gallagher and K. H. Ashe, *Nature*, 2006, **440**, 352.

[100] K. Ono, *Neurochem. Int.*, 2018, **119**, 57.

[101] E. Drummond, G. Pires, C. MacMurray, M. Askenazi, S. Nayak, M. Bourdon, J. Safar, B. Ueberheide and T. Wisniewski *Brain*, 2020, **143**, 2803.

[102] L. Buee, T. Bussiere, V. Buee-Scherrer, A. Delacourte and P. R. Hof, *Brain Res Brain Res Rev.*, 2000, **33**, 95.

[103] T. F. Gendron and L. Petrucelli, *Mol. Neurodegener.* 2009, **4**, 13.

[104] A. R. Nelson, M.D. Sweeney, A.P. Sagare and B. V. Zlokovic, *Biochim. Biophys. Acta, Mol. Basis Dis.* 2016, **1862**, 887.

[105] J. A. Hardy and G. A. Higgins, *Science*, 1992, **2556**, 184.

[106] E. Karran, M. Mercken and B. De Strooper, *Nat. Rev. Drug Discov.*, 2011, **10**, 698.

[107] R. J. O'Brien and P. C. Wong, *Annu. Rev. Neurosci.*, 2011, **34**, 185.

[108] D. Del Prete, F. Checler and M. Chami, *Mol. Neurodegener.* 2014, **9**, 21.

[109] P. E. Spies, M.M. Verbeek, T. van Groen and J. Claassen, *Front. Biosci.*, 2012, **17**, 2024.

[110] P. Bergström, L. Agholme, F. H. Nazir, T. M. Satir, J. Toombs, H. Wellington, J. Strandberg, T. O. Bontell, H. Kvartsberg, M. Holmström, C. Boreström, S. Simonsson, T. Kunath, A. Lindahl, K. Blennow, E. Hanse, E. Portelius, S. Wray and H. Zetterberg, *Sci. Rep.*, 2016, **6**, 1.

[111] G. Glenner and C. Wong, *Alzheimer Dis. Assoc. Disord.* 1988, **2**, 134.

[112] Y. Yoshiike, D.-H. Chui, T. Akagi, N. Tanaka and A. Takashima, *J. Biol. Chem.*, 2003, **278**, 23648.

[113] M. Coles, W. Bicknell, A. A. Watson, D. P. Fairlie and D. J. Craik, *Biochemistry*, 1998, **37**, 11064.

[114] O. Crescenzi, S. Tomaselli, R. Guerrini, S. Salvadori, A. M. DUrsi, P. A. Temussi and D. Picone, *FEBS J.*, 2002, **269**, 5642.

[115] K. Janek, S. Rothemund, K. Gast, M. Beyermann, J. Zipper, H. Fabian, M. Bienert and E. Krause, *Biochemistry*, 2001, **40**, 5457.

[116] S. Vivekanandan, J. R. Brender, S. Y. Lee and A. Ramamoorthy, *Biochem. Biophys. Res. Commun.*, 2011, **411**, 312.

[117] E. Luttmann and G. Fels, *Chem. Phys.*, 2006, **323**, 138.

[118] N. Miyashita, J. E. Straub and D. Thirumalai, *J. Am. Chem. Soc.* 2009, **131**, 49, 17843.

[119] M. Valerio, A. Colosimo, F. Conti, A. Giuliani, A. Grottesi, C. Manetti and J. P. Zbilut, *Proteins*, 2005, **58**, 110.

[120] N. Agrawal and A. A. Skelton, *Mol. Pharm.*, 2017, **15**, 289.

[121] Y. Yoshiike, R. Minai, Y. Matsuo, Y. R. Chen, T. Kimura and A. Takashima, *PLOS ONE*, 2008, **3**, e3235.

[122] S. B. Prusiner, *Science.* 2012, **336**, 1511.

[123] A. A. Kulikova, A. A. Makarov and S. A. Kozin, *Mol. Biol.* 2015, **49**, 217.

[124] C. L. Ni, H. P. Shi, H. M. Yu, Y. C. Chang and Y.R. Chen, *FASEB J.* 2011, **25**, 1390.

[125] J. D. Harper and P. T. Lansbury, *Annu. Rev. Biochem.*, 1997, **66**, 385.

[126] H. Naiki and F. Gejyo, *Methods Enzymol.* 1999, **309**, 305.

[127] S. Kumar and J. Walter, *Aging*, 2011, **3**, 803.

[128] Q. Nie, X.-G. Du and M.-Y. Geng, *Acta Pharmacol. Sin.*, 2011, **32**, 545.

[129] F. Tahmasebinia and S. Emadi, *Biometals*, 2017, **30**, 285.

[130] J. R Horsley, B. Jovcevski, K. L Wegener, J. Yu, T. L. Pukala and A. D. Abell, *Biochem J.* 2020, **477**, 2039.

[131] X. Shao, C. Yan, C. Wang, C. Wang, Y. Cao, Y. Zhou, P. Guan, X. Hu, W. Zhu and S. Ding, *Nanoscale Adv.*, 2023, **5**, 46.

[132] K. Ono, K. Hasegawa, H. Naiki and M. Yamada, *J. Neurosci. Res.*, 2004, **75**, 742.

[133] K. Jimenez-Aliaga, P. Bermejo-Bescos, J. Benedı and S. Martın-Aragon, *Life Sci.*, 2011, **89**, 939.

[134] A. Pugazhendhi, R. Beema Shafreen, K. Pandima Devi and N. Suganthy, *J. Mol. Liq.*, 2018, **257**, 69.

[135] E. D. Roberson and L. Mucke, *Science*, 2006, **314**, 781.

[136] A. F. Kreft, R. Martone and A. Porte, *J. Med. Chem.*, 2009, **52**, 6169.

[137] D. Oehlrich, D. J.-C. Berthelot and H. J. M. Gijsen, *J. Med. Chem.*, 2011, **54**, 669.

[138] C. A. Hawkes, V. Ng and J. McLaurin, *Drug Dev. Res.*, 2009, **70**, 111.

[139] F. Gervais, J. Paquette, C. Morissette, P. Krzywkowski, M. Yu, M. Azzi, D. Lacombe, X. Kong, A. Aman, J. Laurin, W. A. Szarek and P. Tremblay, *Neurobiol. Aging*, 2007, **28**, 537.

[140] R. R. Watson, *Foods and Dietary Supplements in the Prevention and Treatment of Disease in Older Adults*, Academic Press, San Diego, 2015.

[141] G. A. Crespi, S. J. Hermans, M. W. Parker and L. A. Miles, *Sci. Rep.*, 2015, **5**, 9649.

[142] E. R. Siemers, S. Friedrich, R. A. Dean, C. R. Gonzales, M. R. Farlow, S. M. Paul and R. B. DeMattos, *Clin. Neuropharmacol.*, 2010, **33**, 67.

[143] M. Farlow, S. E. Arnold, C. H. Van Dyck, P. S. Aisen, B. J. Snider, A. P. Porsteinsson, S. Friedrich, R. A. Dean, C. Gonzales and G. Sethuraman, *Alzheimer's & Dementia*, 2012, **8**, 261.

[144] C. A. Sacks, J. Avorn and A.S. Kesselheim, *N. Engl. J. Med.*, 2017, **376**, 1706.

[145] H. Feinberg, J. W. Saldanha, L. Diep, A. Goel, A. Widom, G. M. Veldman, W. I. Weis, D. Schenk and G. S. Basi, *Alzheimer's Res. Ther.*, 2014, **6**, 31.

[146] L. A., G. A. Crespi, L. Doughty and M.W. Parker, *Sci. Rep.* 2013, **3**, 1302.

[147] R. Vandenberghe, J. O. Rinne, M. Boada, S. Katayama, P. Scheltens, B. Vellas, M. Tuchman, A. Gass, J. B. Fiebach and D. Hill, *Alzheimer's Res. Ther.*, 2016, **8**, 18.

[148] F. Würthner, V. Stepanenko, Z. Chen, C. R. Saha-Möller, N. Kocher and D. Stalke, *J. Org. Chem.*, 2004, **69**, 7933.

[149] M. J. Ahrens, M. J. Tauber and M. R. Wasielewski, *J. Org. Chem.*, 2006, **71**, 2107.

[150] L. C. Kasi Viswanath, L. D. Shirtcliff, S. Krishnan, N. V. Handa and K. Darrell Berlin, *Tetrahedron Lett.* 2014, **55**, 4199.

[151] Z. Mahmood, K. Xu, B. Küçüköz, X. Cui, J. Zhao, Z. Wang, A. Karatay, H. G. Yaglioglu, M. Hayvali and A. Elmali, *J. Org. Chem.*, 2015, **80**, 3036.

[152] D. Meng, H. Fu, C. Xiao, X. Meng, T. Winands, W. Ma, W. Wei, B. Fan, L. Huo, N. L. Doltsinis, Y. Li, Y. Sun and Z. Wang, *J. Am. Chem. Soc.* 2016, **138**, 10184.

[153] B. Muthuraj, S. R. Chowdhury and P. K. Iyer, *ACS Appl. Mater. Interfaces*, 2015, **7**, 21226.

[154] P. J. Goutam and P. K. Iyer, *Sens. Actuators B*, 2015, **211**, 263.

[155] C. Zhang, H. Wang, J. Zhong, Y. Lei, R. Du, Y. Zhang, L. Shen, T. Jiao, Y. Zhu and H. Zhu, et al., *Sci. Adv.*, 2019, **5**, eaax6707.

[156] R. J. Jansen, R. de Gelder, A. E. Rowan, H. W. Scheeren and R. J. M. Nolte, *J. Org. Chem.*, 2001,**66**, 2643.

Chapter 2

Theoretical and Computational Methodologies

2.1. Electronic Structure Theory

For a molecular system consisting of n electrons and M nuclei, the fundamental quantum mechanics that describe the system's non-relativistic is given by a time-independent Schrödinger equation and expressed as:

$$\hat{H}\psi_i(r_1,r_2 \dots \dots r_n,R_1,R_2 \dots \dots R_M) = E_i\psi_i(x_1,x_2 \dots \dots x_n,R_1,R_2 \dots \dots R_M) \quad (2.1)$$

where $\hat{H}$ is the Hamiltonian operator of the electrons and nuclei of the systems. $\hat{H}$ comprises the sum of kinetic energy and potential energy. ψ_i represents the wavefunction of the i-th state of the system, which describes the quantum state and E_i denotes the corresponding eigenvalue or energy states. The wavefunction ψ_i depends on the positions of electrons (r) and nuclei (R). In terms of atomic units, $\hat{\mathrm{H}}$ may be expressed as[1]:

$$\hat{H} = -\sum_{i=1}^{n}\frac{1}{2}\nabla_i^2 - \sum_{A=1}^{M}\frac{1}{2M_A}\nabla_A^2 - \sum_{i=1}^{n}\sum_{A=1}^{M}\frac{Z_A}{r_{iA}} + \sum_{i=1}^{n}\sum_{j>1}^{n}\frac{1}{r_{ij}} + \sum_{A=1}^{n}\sum_{B>A}^{M}\frac{Z_AZ_B}{R_{AB}} \quad (2.2)$$

In Eq. 2.2, ∇_i^2 and ∇_A^2 are the Laplacian operators which involve the differentiation with respect to coordinates of the i-th electron and the A^{th} nucleus. M_A is the nucleus mass of A, while Z_A and Z_B represent atomic numbers of nuclei A and B, respectively. The distance between i-th and j-th electron is represented by r_{ij} while distance between the two nuclei A and B is denoted by R_{AB}. In addition, the distance between i-th electron and A^{th} nucleus is represented by r_{iA}.

In Eq. 2.2, the first and second terms correspond to the operators associated with kinetic energy of the electrons and nucleus, respectively. The third term accounts for the coulomb attraction between the electrons and nuclei; the fourth and fifth terms deal with the repulsion between the electrons and between the nuclei, respectively. Further, $\hat{\mathrm{H}}$ can be rewritten as

$$\hat{H} = \hat{T}_e(\boldsymbol{r}) + \hat{T}_N(\boldsymbol{R}) + \hat{V}_{eN}(\boldsymbol{r},\boldsymbol{R}) + \hat{V}_{ee}(\boldsymbol{r},\boldsymbol{r}) + \hat{V}_{NN}(\boldsymbol{R}) \quad (2.3)$$

Where $\hat{T}_e(\boldsymbol{r})$ and $\hat{T}_N(\boldsymbol{R})$ represent the kinetic energy of electrons and nuclei, respectively. $\hat{V}_{eN}(\boldsymbol{r},\boldsymbol{R})$ denotes the coulombic attraction between the electrons and nuclei, $\hat{V}_{ee}(\boldsymbol{r},\boldsymbol{r})$

represents the electron-electron repulsion, and last term $\hat{V}_{NN}(\boldsymbol{R})$ accounts the nuclei repulsion interaction.

2.2. Born-Oppenheimer Approximation

The Born-Oppenheimer (BO) approximation[1,2] is the central part of solving the quantum chemical calculation of the system. Qualitatively, this approximation relies on the observation that nuclei are exhibited heavier mass than electrons. In this scenario, the movement of electrons in the field of fixed nuclei. Consequently, the second-term kinetic energy of the nuclei of Eq. 2.3 can be disregarded, and the repulsion between the nuclei can be considered constant. Furthermore, any constant added to the operator will only add to the operator eigenvalues and do not affect on the operator eigenfunctions. The remaining first [$\hat{T}_e(\boldsymbol{r})$], third [$\hat{V}_{eN}(\boldsymbol{r},\boldsymbol{R})$], and fourth [$\hat{V}_{ee}(\boldsymbol{r},\boldsymbol{r})$] terms of Eq. 2.3 are collectively called the electronic Hamiltonian. So, the electronic Hamiltonian part can be expressed as

$$\hat{H}_{el}=\hat{T}_{el}(\boldsymbol{r})+\hat{V}_{eN}(\boldsymbol{r},\boldsymbol{R})+\hat{V}_{ee}(\boldsymbol{r},\boldsymbol{r}) \tag{2.4}$$

and the electronic wavefunction is expressed as

$$\psi_{el}=\psi_{el}(\boldsymbol{r};\boldsymbol{R}) \tag{2.5}$$

In Eq. 2.5, the electronic wavefunction, ψ_{el}, accounts for the motion of electrons, and it depends on the coordinates of the electrons and parametrically on the nuclear coordinates. The Schrödinger equation involving the electronic wave function is represented as

$$\hat{H}_{el}\psi_{el}=E_{el}\psi_{el}(\boldsymbol{r};\boldsymbol{R}) \tag{2.6}$$

Where, E_{el} is the electronic eigenvalue of the corresponding eigen function ψ_{el}. The total energy, E_{tot}, for the system with the fixed nuclei includes the nucleus-nucleus repulsion energy term and is expressed as

$$E_{tot}=E_{el}+\hat{V}_{NN}(\boldsymbol{R}) \tag{2.7}$$

2.3. Hartree-Fock Method

The Hartree-Fock (HF) method is the fundamental method of quantum physics and chemistry, which approximates the electronic structure of atoms and molecules. The method owes its named after Douglas Hartree[3] and Vladimir Fock,[4] who independently developed this approach.

In this method, a mean-field theory treats electrons in a many-electron system by considering their average electrostatic interactions and neglecting the electron-electron correlation effects.

The electronic wave functions, ψ_{el}, of the molecular system consisting of *n* electrons can be represented as a product of wave functions (ϕ_i) of each electron known as Hartree product and expressed as

$$\psi_{el}(r_1,r_2 \dots\dots r_n) = \phi_1(r_1)\phi_2(r_2)\,\phi_3(r_3) \dots\dots \phi_n(r_n) \tag{2.8}$$

The Hartree product (Eq. 2.8) does not account for the antisymmetry principle and violates the Pauli exclusion principle.[5] To solve this problem, ψ_{el}, represented in the form of Slater determinant as

$$\psi_{el}(r_1,r_2 \dots\dots r_n)=\frac{1}{\sqrt{n!}}\begin{vmatrix} \phi_1(x_1) & \phi_2(x_1) & \phi_3(x_1) & .. & \phi_n(x_n) \\ \phi_1(x_2) & \phi_2(x_2) & \phi_3(x_2) & .. & \phi_n(x_n) \\ . & . & . & .. & . \\ . & . & . & .. & . \\ \phi_1(x_n) & \phi_2(x_n) & \phi_3(x_n) & .. & \phi_n(x_n) \end{vmatrix} \tag{2.9}$$

The quantity $\frac{1}{\sqrt{n!}}$ is the normalization factor. In the Slater determinant expression of Eq. 2.9, the rows are labelled by *n* electrons, while the columns are labelled by spin orbitals.

The main motive is to find a set of orbitals $\{\phi_n\}$ that minimize the electronic energy. This led to the Hartree-Fock equation:

$$f_i\,\phi_i(r) = \varepsilon_i\,\phi_i(r) \tag{2.10}$$

Where f_i is the Fock operator and ε_i is the orbital energy.

$$\text{And } f_i = -\frac{1}{2}\nabla_i^2 + V_{ext}(r_i) + \sum_{j=1}^{N}[<\phi_j|\hat{J}|\phi_i> - <\phi_j|\hat{K}|\phi_i>]$$

Where $\hat{J}$ and $\hat{K}$ represent the coulomb and exchange operators, respectively.

The solution to these equations provides the set of orbitals that minimize the electronic energy within the Hartree-Fock approximation. This iterative procedure persists until self-consistency is reached.

2.4. Post-Hartree-Fock Methods

The Hartree-Fock (HF) method provides a good starting point for many calculations, but it fails to adequately consider the electron correlation effects. To address this problem, several groups introduced the post-HF methods to accurately add the electron correlation effects. Some of the well-known post-HF methods are the Møller-Plesset perturbation (MP) theory,[6] coupled clusters (CC),[7-10] and multireference methods.[11] In this context, the Møller-Plesset perturbation theory (MP) and the extension of the coupled cluster method, such as the domain-based local pair natural orbital coupled cluster theory with single, double, and perturbative triple excitations [DLPNO-CCSD(T)] method,[12-15] which we employed in our work are discussed.

2.5. Møller-Plesset Perturbation Theory

The Møller-Plesset perturbation theory (MP) is one of the post-HF methods to correct the electron correlation effects through perturbing the Hamiltonian. In this method, the full Hamiltonian, $\hat{H}$, consists of two parts; the unperturbed part Hamiltonian operator, $\hat{H}_0$, and the perturbation part operator, $\hat{H}'$.

$$\hat{H} = \hat{H}_0 + \hat{H}' \tag{2.11}$$

The eigen value problem can be written as,

$$\hat{H}\psi_i = \left(\hat{H}_0 + \widehat{H'}\right)\psi_i = E_i\psi_i \tag{2.12}$$

This sum can be further written over Fock operators

$$\hat{H}_0 = \sum_i^N F_i\,(h_i + V_i^{HF}) \tag{2.13}$$

and the perturbed part can be written as

$$\hat{H}' = \sum_{i<j}\frac{1}{r_{ij}} - \sum_i V_i^{HF} \tag{2.14}$$

Where V_i^{HF} is Hartree-Fock potential, which consists of Coulomb *J* and exchange *K* operators.

Through this method, the HF energy is expressed as

$$E(HF) = E_0^{(0)} + E_0^{(1)} \tag{2.15}$$

which is the sum of zeroth and first order energies.

The correlation energy (E_{corr}) can be expressed as

$$E_{corr} = \sum_{n=2}^{\infty} E_0^{(n)} \tag{2.16}$$

For the second-order MP i.e., MP2 method, the correlation energy is written as

$$E_0^{(2)} = -\frac{1}{4}\sum_{ab}^{occ}\sum_{ij}^{vir}\frac{|<ij||ab>|^2}{\varepsilon_i+\varepsilon_i-\varepsilon_a-\varepsilon_b} \tag{2.17}$$

In Eq. 2.17, a, b, and i, j represent the occupied and virtual orbitals while ε_a, ε_b , ε_i, and ε_j are the corresponding orbital energies, respectively.

2.6. Domain-Based Local Pair Natural Orbital Coupled Cluster Theory with Single, Double, and Perturbative Triple Excitations [DLPNO-CCSD(T)]

The chemical accuracy of the coupled cluster method is established as the primary approach for quantum chemists. Upon closer examination, the benchmark energy obtained utilizing the coupled cluster with single, double, and perturbative triple excitations [CCSD(T)] method is treated as the "gold standard".[16,17] However, CCSD(T) scales as N^7 where N defined by the system size. So, recovering the dynamic electron correlation for the large system is computationally expensive. To generate close results to CCSD(T), an alternative method, such as DLPNO approach, has been used in conjunction with CCSD(T).

In the DLPNO-CCSD(T) approach, using either Foster-Boys[18] or the Pipek-Mezey methods,[19] the occupied orbitals of HF are localized. The correlation energy (E_{corr}) is represented as a sum of electron pair correlation energies ε_{rs}, where r and s are occupied HF orbitals. The E_{corr} is expressed as

$$E_{corr} = 2\sum_{r,\tilde{a}_{rr}} F_{r,\tilde{a}_{rr}} t^{i}_{\tilde{a}_{rr}} + \sum_{r\geq s}\varepsilon_{rs} + E^{(T)} \tag{2.18}$$

and pair energy under PNO (Pair Natural Orbital) approximation,

$$\varepsilon_{rs} = \sum_{\tilde{a}_{rs}\,\tilde{b}_{rs}} (i\tilde{a}_{rs}|j\,\tilde{b}_{rs})\tilde{\tau}^{rs}_{\tilde{a}_{rs}\,\tilde{b}_{rs}} \tag{2.19}$$

In Eq. 2.18 and Eq. 2.19, $\tilde{a}_{rs}$ and $\tilde{b}_{rs}$ are PNOs for pair electron rs, while $(i\tilde{a}_{rs}|j\tilde{b}_{rs})$ represent the two electron integrals. $\tilde{\tau}^{rs}_{\tilde{a}_{rs}\,\tilde{b}_{rs}}$ denotes the contravariant amplitude. The last term $E^{(T)}$ of Eq. 2.18 accounts for the perturbative triple correction.

2.7. Density Functional Theory (DFT)

The basic idea behind the Density Functional Theory (DFT) is that the electronic energy of the system containing electrons is obtained from the probability distribution, the total electron

density $\rho(r)$. Kohn and Sham[20] introduced the DFT energy of a system as a functional of the electron density $\rho(r)$, and the expression is given as

$$E_{DFT}\,[\rho(r)] = T[\rho(r)] + V_{eN}[\rho(r)] + V_{ee}[\rho(r)] + E_{xc}[\rho(r)] \tag{2.20}$$

where $T[\rho(r)]$, $V_{eN}[\rho(r)]$, and $V_{ee}[\rho(r)]$ represent the kinetic energy of the non-interacting electrons, nuclei electron attraction energy, and electron-electron repulsion energy. The last term, $E_{xc}[\rho(r)]$, accounts for the exchange-correlation term. The second and third terms $V_{eN}[\rho(r)]$ and $V_{ee}[\rho(r)]$ are obtained from the classical expressions and are given in Eq. 2.21 and Eq. 2.21

$$V_{eN}[\rho(r)] = -\sum_A^N \int \frac{Z_A\,\rho(r)}{|R_A - r|}\,dr \tag{2.21}$$

$$V_{ee}[\rho(r)] = \frac{1}{2}\iint \frac{\rho(r_1)\,\rho(r_2)}{|r_1 - r_2|} dr_1 dr_2 \tag{2.22}$$

2.8. Exchange-Correlation Functionals

The $E_{xc}[\rho(r)]$ term in the DFT expression of Eq. 2.19 accounts for the electron correlations. This term is the most complex and challenging part of the DFT total energy functional. The $E_{xc}[\rho(r)]$ is fragmented into two distinct parts, a pure exchange $E_x[\rho(r)]$ and a correlation part $E_c[\rho(r)]$, as expressed in Eq. 2.23

$$E_{xc}\,[\rho(r)] = E_x[\rho(r)] + E_c[\rho(r)] = \int \rho(r)\varepsilon_x[\rho(r)]dr + \int \rho(r)\varepsilon_c[\rho(r)]dr \tag{2.23}$$

The specific form of this functional is remains elusive and must be approximated. Over the last few decades, a plethora of exchange-correlation functionals have been proposed, such as the local density approximation (LDA),[21-23] generalized gradient approximation (GGA),[24-26] meta-GGA,[27] and hybrid functionals.[28,29] Some of the functionals, along with their approximation, are displayed in Figure 2.1 in Jacob's ladder form.[30]

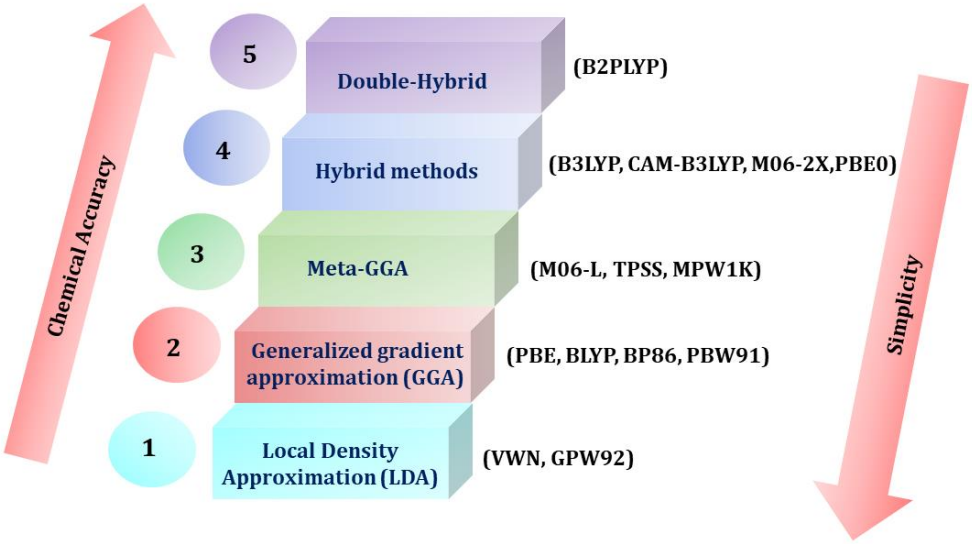

Figure 2.1. Jacob's ladder of quantum mechanical method in quantum chemistry shows different approximations of DFT functionals and their accuracy level.

2.9. Dispersion-Corrected DFT

The importance of DFT method is quite well-known for calculating the electronic structures of molecular systems. However, the standard functionals of DFT methods do not consider the long-range dispersion interaction correction, which is indispensable for systems containing noncovalent interactions such as hydrogen bonding, π-π interactions, etc. To cooperate such interactions, Grimme's dispersion (D) correction[31-33] method has been widely employed. In this approach, the dispersion correction term E_{disp} is added to the DFT energy obtained from the Kohn-Sham (KS) theory. The expression for the dispersion corrected DFT is written as

$$E_{DFT-D} = E_{KS} + E_{disp} \tag{2.24}$$

and

$$E_{disp} = -\sum_{AB}\sum_{n=6,8,10,\ldots} s_n \frac{C_n^{AB}}{R_{AB}^n} f_{damp}(R_{AB}) \tag{2.25}$$

In Eq. 2.25, the sum is over all the atom pairs, C_n^{AB} represents the dispersion coefficient for the atom pair AB, R_{AB} denotes the internuclear distance, s_n accounts for the scaling factor used for correction to the repulsive behaviour, and f_{damp} is the damping function.[34]

The expressions for the damping function f_{damp} are

$$f_{damp}(R_{AB}) = \frac{1}{1+6(R_{AB}/(s_{r,n}\,R_0^{AB})^{-\gamma}} \tag{2.26}$$

$$f_{damp}(R_{AB}) = \frac{1}{1+e^{-\gamma(R_{AB}/s_{r,n}\,R_0^{AB}-1)}} \quad (2.27)$$

Where R_0^{AB} is the cutoff radius for the atom pair AB, γ denotes the global constant related to the steepness of the functions for small interatomic distance, and $s_{r,n}$ is the scaling factor that depends on the density functionals (DFs).

The other DFT dispersion correction, which employed the damping function proposed by Becke and Johnson,[35] is expressed as,

$$E_{disp}^{D3BJ} = -\frac{1}{2}\sum_{AB} s_6 \frac{C_6^{AB}}{R_6^{AB}+[f_{damp,BJ}+(R_{AB}^0)]^6} + s_8 \frac{C_8^{AB}}{R_8^{AB}+[f_{damp,BJ}+(R_{AB}^0)]^8} \quad (2.28)$$

and

$$f_{damp,BJ} = a_1\sqrt{\frac{C_8^{AB}}{C_6^{AB}}}\,R_{AB}^0 + a_2 \quad (2.29)$$

In Eq. 2.29, a_1 and a_2 are adjustable parameters and can be obtained from the benchmark parameters.

2.10. Energy Decomposition Method

The most commonly used approach to estimate the strength of interaction between the two molecules or fragments is calculated by using the supermolecular method, as shown in Eq. 2.30

$$\Delta E = E(XY) - E(X) - E(Y) \quad (2.30)$$

Where $E(XY)$, $E(X)$, and $E(Y)$ are the energies of complex XY, fragment X, and fragment Y, respectively. ΔE gives the single value interaction energy between the two molecules but could not provide the different energy components involved in the interaction between two fragments. The energy decomposition method is one of the ways to partition the interaction energy into several meaningful and distinct components such as electrostatic, polarization, charge transfer, exchange, and correlation contributions. So far, various methods have been established to assign the energy components of the interaction between the two fragments.

In 1976, Kitaura and Morokuma[36] introduced the energy decomposition analysis (EDA) based on the Hartree-Fock (HF) method. This approach decomposes the energy between the molecular fragments into four components: electrostatic interaction, exchange, polarization, and charge transfer. The symmetry-adapted perturbation theory (SAPT)[37] and natural energy decomposition analysis (NEDA)[38] are also widely used to dissect the interaction energy. In

the NEDA scheme, the calculation is based on the natural bond orbitals (NBOs) to build the concept of Lewis structures and create localized molecular orbitals. However, SAPT is based on the perturbation in which the interaction between the fragments is treated as a perturbation to the non-interacting description. Recently, another category of energy decomposition scheme called the extended transition state-natural orbital for chemical valence (ETS-NOCV) was developed.[39] This scheme is developed by combining two parts: (a) extended transition state (ETS) scheme,[40,41] which accounts for the energy decomposition approach, and (b) natural orbitals for chemical valence (NOCV) method,[42-46] which deals with the changes in the charge density associated to the bond formation between the atoms or molecular fragments. Overall, this analysis will provide insight into the chemical bonds in terms of orbitals (NOCV) and elucidate the charge rearrangement and energy contributions. In addition, ETS-NOCV analysis also provides about the types of bonding interactions, such as σ, π, δ, etc., involved in various chemical bonds, including covalent bonds, intra and intermolecular interactions, and donor-acceptor interactions.

In the ETS scheme, the total binding energy (ΔE_{total}) between the two fragments (X and Y) is partitioned into four physical meaningful components, Eq. 2.31

$$\Delta E_{total} = \Delta E^{prep} + \Delta E^{elst} + \Delta E^{Pauli} + \Delta E^{orb} \quad (2.31)$$

Where, ΔE^{prep} referred to as preparation or distortion energy. The ΔE^{prep} deals with the energy required to bring the molecular fragments (X and Y) from their equilibrium geometry to the complex formation state (XY). The term ΔE^{elst} represents the classical electrostatic interaction involved between the fragments in the complex. The third term, ΔE^{Pauli}, denotes the Pauli repulsive interaction between electrons of the two fragments in their complex formation state. The last term, ΔE^{orb}, accounts for the orbital interaction energy between the occupied molecular orbitals of one fragment with the unoccupied molecular orbitals of another fragment and also considers the mixing of occupied orbitals and virtual orbitals within the same fragment.

2.11. Local Energy Decomposition Method

The other category of energy decomposition analysis (EDA) scheme called local energy decomposition (LED) was introduced.[47] In this approach, the energy decomposition is based on the local coupled cluster method, DLPNO-CCSD(T). The DLPNO-CCSD (T) interaction energy was dissected into repulsive electronic preparation, electrostatic, exchange, dispersion,

and nondispersive correlation. The dimerization energy (ΔE) of the two interacting molecular fragments A and B, can be written as:

$$\Delta E = \Delta E^{geo-prep} + \Delta E^{int} \tag{2.32}$$

Where $\Delta E^{geo-prep}$ denotes the geometrical preparation energy which deals with the energy required to distort the molecular fragments A and B from their isolated optimized equilibrium geometries to adduct formation geometry AB. The term ΔE^{int} accounts for the interaction energy of the molecular fragments A and B at the adduct geometry AB.

Using the post-HF method DLPNO-CCSD(T), the ΔE^{int} of Eq. 2.32 is divided into two parts, namely, HF (ΔE_{HF}^{int}) and correlation (ΔE_{C}^{int}) contributions, and can be represented as:

$$\Delta E^{int} = \Delta E_{HF}^{int} + \Delta E_{C}^{int} \tag{2.33}$$

In the LED scheme, the ΔE_{HF}^{int} term of Eq. 2.33 is decomposed into various components under the localization of the occupied orbitals of the DLPNO-CCSD(T) approach and represented as:

$$\Delta E_{HF}^{int} = \Delta E_{HF}^{el-prep} + E_{elst} + E_{exch} \tag{2.34}$$

Where $\Delta E_{HF}^{el-prep}$ represents the electronic preparation energy that is needed by molecular fragments to bring the electronic structure to the optimal state for interaction. Furthermore, E_{elst} and E_{exch} account for the electrostatic and exchange interactions, respectively, between molecular fragments A and B. The expression for the term E_{elst} is written as:

$$E_{elst} = P_{X\leftrightarrow Y}\left[\sum_{A_X>B_Y}\frac{Z_A^{(X)}\,Z_B^{(Y)}}{\left|R_A^{(X)}-R_B^{(Y)}\right|} - 2\sum_{i_X,A_Y}\langle i_X\left|\frac{Z_A^{(Y)}}{\left|r_i^{(X)}-R_A^{(Y)}\right|}\right|i_X\rangle + 4\sum_{i_X>j_Y}(i_X\,i_X|j_Yj_Y)\right] \tag{2.35}$$

$$E_{exch} = P_{X\leftrightarrow Y}\left[-2\sum_{i_X>j_Y}(i_X\,j_Y|i_Xj_Y)\right] \tag{2.36}$$

Where Z_A and Z_B are the nuclear charges of atoms A and B at the position R_A and R_B in fragments X and Y, respectively, and i and j denote the localized orbitals. The terms $(i_Xi_X|j_Yj_Y)$ and $(i_Xj_Y|i_Xj_Y)$ represent the two-electron integrals. In Eq. 2.35, the second term accounts for the attractive, and the first and last terms are repulsive.

The correlation energy part ΔE_{C}^{int} of Eq. 2.33 can be obtained by combining the three components: the energy (ΔE_{C-SP}^{int}) associated with the strong electron pairs correlation, which is considered at the coupled cluster level, the correction term called weak pair electron

correlation energy denoted as ΔE_{C-WP}^{int} and this term compensates for the truncation of the pair space and the truncation of the virtual PNO space, which is calculated at the MP2 level, and last contribution arising from the perturbative triples correction, which is represented as $\Delta E_{C-(T)}^{int}$.

$$\Delta E_{C}^{int} = \Delta E_{C-SP}^{int} + \Delta E_{C-WP}^{int} + \Delta E_{C-(T)}^{int} \quad (2.37)$$

Moreover, in the context of the DLPNO-CCSD(T) method, ΔE_{C-SP}^{int} can be decomposed based on the localization of occupied and virtual orbitals as:

$$\Delta E_{C-SP}^{int} = \Delta E_{C-SP}^{el-prep} + \Delta E_{C-SP}^{C-(T)} + \Delta E_{C-SP}^{disp} \quad (2.38)$$

where $\Delta E_{C-SP}^{el-prep}$, $\Delta E_{C-SP}^{C-(T)}$, and ΔE_{C-SP}^{disp} denote the electronic preparation energy, charge transfer, and London dispersion, respectively.

Combining all the contributions obtained from the HF energy and correlation energy, the ΔE for the adduct complex AB can be written as:

$$\Delta E = \Delta E^{geo-prep} + \Delta E_{HF}^{el-prep} + E_{elst} + E_{exch} + \Delta E_{C-SP}^{el-prep} + \Delta E_{C-SP}^{C-(T)} + \Delta E_{C-SP}^{disp} + \Delta E_{C-WP}^{int} + \Delta E_{C-(T)}^{int} \quad (2.39)$$

2.12. Basis Set Superposition Error (BSSE)

When the two atoms or fragments come into proximity, a condition arises that their respective basis sets borrow from each atom and overlap. Subsequently, increased the size of the basis sets functions and therefore stabilized the energy of the fragments. This effect increases as the interatomic distances decreases, and the phenomenon is called basis set superposition error (BSSE).[48,49]

One of the widely used prescription for eliminating the BSSE error is the Boys and Bernardi counterpoise (CP) correction approach.[50] In order to understand this approach, let us consider two fragments A and B. The interaction energy between the two fragments (A and B) can be calculated as:

$$\Delta E_{AB}^{int} = E_{AB}^{ab} - E_{A}^{a} - E_{B}^{b} \quad (2.40)$$

where, superscripts ab, a, and b represent the basis sets while subscripts AB, A, and B denote the molecular geometries. The E_{AB}^{ab} term accounts for the energy of the dimer AB calculated at the dimer basis set ab; E_{A}^{a} and E_{B}^{b} represent the energies of the isolated molecular fragments A

and B on their own basis sets a and b. The extra stabilization energy acquired by the fragment A due to the extra basis set extended from the fragment B (and vice versa) can be computed as:

$$E_A(BSSE) = E_A^{ab} - E_A^a \tag{2.41}$$

$$E_B(BSSE) = E_B^{ab} - E_B^b \tag{2.42}$$

Where in Eq. 2.41 and Eq. 2.42, the energy $[E_A^a]$ of the molecular fragment A in its own basis set is subtracted from the energy $[E_A^{ab}]$ of molecular fragment A in the dimer basis sets (and same for molecular fragment B). We have assumed that the geometries of molecular fragments A and B are in the dimeric forms. In calculating the energy of a molecular fragment A in dimer basis set, one considered all the basis functions of molecular fragment B's atomic centers and neglecting the electrons and nuclear charges of fragment B. These functions on atoms of fragment B are termed a ghost orbital. Likewise, the fragment B also estimated.

After subtracting Eq. 2.41 and Eq. 2.42 from the interaction energy (Eq. 2.40), the counter poise (CP) corrected interaction energy is given as:

$$\Delta E_{AB}^{int}(CP) = E_{AB}^{ab} - E_A^a - E_B^b - E_A^{ab} + E_A^a - E_B^{ab} + E_B^b \tag{2.43}$$

$$\Delta E_{AB}^{int}(CP) = E_{AB}^{ab} - E_A^{ab} - E_B^{ab} \tag{2.44}$$

2.13. Molecular Electrostatic Potential

The molecular electrostatic potential (MEP)[51,52] at a given point, $P(x, y, z)$, on the surface of the molecule, is defined as the force acting on the positive test charge (a proton) located at the point P under the electrical charge cloud generated from the molecules through electrons and nuclei. The molecular electrostatic potential $V(r)$ at a point r is given as[53]

$$V(r) = \sum_A \frac{Z_A}{|R_A - r|} - \int \frac{\rho(r')dr'}{|r' - r|} \tag{2.45}$$

where Z_A denotes the charge on nucleus A, located at R_A, $\rho(r)$ accounts for the electron density function at the point. The electrostatic potential $V(r)$ can be estimated computationally and investigated experimentally by diffraction methods.

2.14. Quantum Theory of Atoms in Molecules (QTAIM)

The Quantum Theory of Atoms in Molecules (QTAIM)[54,55] is a technique developed by Bader and coworkers to provide the topological analysis of the electron density ρ. The basic idea of this method is to use electron density ρ as a tool to identify and characterise the nature of

chemical bonding in molecular systems. When observing the electron density ρ of a given molecular system, its most prominent feature is that the maximum electron density is associated near the atomic nuclei and comparatively lower concentration in other regions. The electron density ρ is a function of three spatial coordinates, and one can analyse the associated gradient vector field. The gradient of the electron density ($\nabla\rho$) is obtained and presented as

$$\nabla\rho(r_c) = \hat{\imath}\frac{\delta\rho}{\delta x} + \hat{\jmath}\frac{\delta\rho}{\delta y} + \hat{k}\frac{\delta\rho}{\delta z} \tag{2.46}$$

Where $\hat{\imath}$, $\hat{\jmath}$, and $\hat{k}$ are unit vectors. In a molecular system, the electron density exhibits maximum, minimum, and saddle points in space. These points are known as critical points (CP),[56] and at these points $\nabla\rho(r)$ vanishes [$\nabla\rho(r_c) = 0$]. Four possible critical points are there: (a) nuclear critical points (NCP), (b) bond critical points (BCP), (c) ring critical points (RCP), and (e) cage critical points (CCP). The classification and characteristics of these points are identified by the number of non-zero eigenvalues obtained from the Hessian of ρ and their sum of the signs of the eigenvalues. The second derivative $\nabla^2\rho$, which is defined as Hessian of ρ and is expressed as–

$$\nabla^2\rho(r_c) = \begin{vmatrix} \frac{\partial^2\rho}{\partial x^2} & \frac{\partial^2\rho}{\partial x\partial y} & \frac{\partial^2\rho}{\partial x\partial z} \\ \frac{\partial^2\rho}{\partial y\partial x} & \frac{\partial^2\rho}{\partial y^2} & \frac{\partial^2\rho}{\partial y\partial z} \\ \frac{\partial^2\rho}{\partial z\partial x} & \frac{\partial^2\rho}{\partial z\partial y} & \frac{\partial^2\rho}{\partial z^2} \end{vmatrix} \tag{2.47}$$

After diagonalization, this matrix (Eq. 2.47), by setting the off-diagonal elements to zero with the help of unitary transformation and obtaining the Laplacian of ρ to get the eigenvalues λ_1, λ_2, and λ_3.

$$\nabla^2\rho(r_c) = \frac{\partial^2\rho}{\partial x^2} + \frac{\partial^2\rho}{\partial y^2} + \frac{\partial^2\rho}{\partial z^2} = \lambda_1 + \lambda_2 + \lambda_3 \tag{2.48}$$

The critical points (CPs) are classified according to rank and signature. The rank of the CP refers to the number of non-zero eigenvalues, and the signature is defined as the sum of the signs of eigenvalues. The critical point is labelled using the notation (rank, signature). All four possible types of critical points exhibited the identical number of non-zero eigenvalues of rank three, while the signature varies. The four possibilities of CPs arise based on the signature values and are discussed below in the following lines.

(a) **(3, -3) critical point:** All three eigenvalues are negative, meaning the electron density falls in all three perpendicular directions of space and electron density ρ is a local

maximum at the nucleus. Therefore, this critical point is called the nuclear critical point (NCP).

(b) **(3, -1) critical point:** Two eigenvalues are negative, which means the electron density ρ falls in two perpendicular directions in space and rises in the third direction. So, this critical point appears as the saddle point of electron density. This critical point is generally observed between the attractive atom pairs and is commonly termed a bond critical point (BCP).

(c) **(3, +1) critical point:** Only one negative eigenvalue characterises the first saddle point. The electron density ρ falls in one direction and rises in the other two directions of space. This critical point generally appears in the center of the ring system and is commonly known as the ring critical point (RCP).

(d) **(3, +3) critical point:** None of the eigenvalues are negative, and electron density ρ rises in all three directions of space. This critical point appears in the center of the cage system and is termed a cage critical point (CCP).

The number of critical points and types that can coexist in the isolated molecular system follow the topological relationship given by Poincare´–Hopf:[57]

$$\mathrm{n(NCP)} - \mathrm{n(BCP)} + \mathrm{n(RCP)} - \mathrm{n(CCP)} = 1 \qquad (2.49)$$

Where $\mathrm{n(NCP)}$, $\mathrm{n(BCP)}$, $\mathrm{n(RCP)}$, and $\mathrm{n(CCP)}$ represent the number of the nuclear critical point, bond critical point, ring critical point, and cage critical point, respectively. On the other hand, for crystal or periodic molecular systems, the relationship is given by Morse:

$$\mathrm{n(NCP)} - \mathrm{n(BCP)} + \mathrm{n(RCP)} - \mathrm{n(CCP)} = 0 \qquad (2.50)$$

In the topological analysis of electron density, $\rho(r)$, the Laplacian of electron density, $\nabla^2\rho(r_c)$, provides the description of atomic interactions. The $\nabla^2\rho(r_c) < 0$ indicates the concertation of charge towards the interaction line. The concentration of charge leads to contraction of $\rho(r_c)$ perpendicular to the interaction line and lowers the potential energy. As a result, the attractive force and bound shared interaction will be observed. The $\nabla^2\rho(r_c) > 0$ indicates the interaction is dominated by the contraction of $\rho(r_c)$ towards the nucleus.

Some meaningful relationships are found between the energetic topological parameters and the Laplacian of electron density $[\nabla^2\rho(r_c)]$ at the critical points. One of the important relationships is the local form of the virial theorem:

$$\frac{1}{4}\nabla^2\rho(r_c) = 2G(r_c) + V(r_c) \quad (2.51)$$

$$H(r_c) = G(r_c) + V(r_c) \quad (2.52)$$

Where $G(r_c)$, $V(r_c)$, and $H(r_c)$ represent the kinetic energy, potential energy, and the total energy densities, respectively. $G(r_c)$ and $V(r_c)$ are positive and negative quantities, respectively. The balance between the $G(r_c)$ and $V(r_c)$ reveals the nature of interaction. If $|V(r_c)| > 2G(r_c)$, then in this condition the interaction is covalent. If $|V(r_c)|$ is one time more than the $G(r_c)$, then $\nabla^2\rho(r_c)$ is positive and $H(r_c)$ is negative. In this condition, $\nabla^2\rho(r_c)$ and $H(r_c)$ have been employed to characterise the bonding interactions.

2.15. Noncovalent Interaction Index

The noncovalent interaction (NCI) method, commonly known as the reduced density gradient (RDG) method, is widely used to determine the weak interactions.[58] In this method, the identification of the strength of the interaction is based on the electron density ρ and its first derivative or gradient of ρ ($\nabla\rho$). To identify the types of interactions, the NCI plots of RDG and electron density, ρ, have been generated. The expression for the RDG is written as:

$$\text{RDG} = s = \frac{1}{2(3\pi^2)^{1/3}} \frac{|\nabla\rho|}{\rho^{4/3}} \quad (2.53)$$

RDG is a dimensionless quantity and used in DFT to describe the deviation from a homogeneous electron distribution. The strength and types of interaction in the molecular system can be predicted from the RDG versus $sign(\lambda_2)\rho$ plot. In $sign(\lambda_2)\rho$, where λ_2 is the second eigenvalue obtained from the Hessian matrix of electron density ρ.

2.16. Natural Bond Orbital (NBO)

The natural bond orbital (NBO) method was developed by F. Weinhold and coworkers.[59] This method is based on transforming a given wavefunction into a localized form corresponding to the one-center (lone pair) and two-center (bond) elements of the chemist's Lewis structure picture. All possible interactions between 'filled' (donor) Lewis-type NBOs and 'empty' (acceptor) non-Lewis NBOs are investigated in this analysis, estimating their energetic importance by second-order perturbation theory. Since these interactions lead to loss of occupancy from the localized NBOs of the idealized Lewis structure into the empty non-Lewis orbitals (and thus, to departures from the idealized Lewis structure description), they are referred to as 'delocalization' corrections to the zeroth-order natural Lewis structure. For each

NBO donor (i) and NBO acceptor (j), the stabilization for $(i \rightarrow j)$ orbital interaction energy E^2 is estimated using Eq. 2.54

$$E^2 = \Delta E = q_i \frac{{F_{ij}}^2}{\varepsilon_j - \varepsilon_i} \tag{2.54}$$

Where q_i is the donor orbital occupancy, F_{ij} is the off-diagonal NBO Fock matrix elements, and ε_i and ε_j are orbital energies.

2.17. Molecular Dynamics Simulations

Classical molecular dynamics (MD) simulations are a powerful computational technique used in the different fields of science, including chemistry, physics, materials science, and biology, to understand the behaviours of atoms or molecules over time. The MD simulation is based on classical mechanics, which uses Newton's second law equation of motion. Solving the equation of motion provides velocity, a trajectory containing positions and accelerations of atoms along the time. Newton's equation of motion is expressed as,

$$F_x = m_x a_x \tag{2.55}$$

Where F_x is the force applied on the particle x of mass m_x and a_x is the acceleration of the particle x.

$$\frac{d^2 r_x}{dt^2} = \frac{F_x}{m_x} \tag{2.56}$$

$$\frac{dr_x}{dt^2} = a_x \tag{2.57}$$

$$\frac{v_x}{dt} = \frac{F_x}{m_x} \tag{2.58}$$

Force is the derivative of potential with respect to position that can be calculated analytically. In order to obtain the velocities and positions in the next time step, we have to integrate the force. Few algorithms to integrate the equation of motion are Verlet[60], Leapfrog,[61] and Velocity Verlet.[62]

2.18. Force Fields in Classical Molecular Dynamics

In classical molecular dynamics simulation, a force field is defined as the mathematical model or expression describing the energy of a system, which depends on the coordinates of the particles. It consists of interatomic potential energy and associated parameters. The parameters are usually derived through either *ab initio* or semi-empirical quantum mechanical calculations

or from experimental observations, including neutron, X-ray, and electron diffraction, as well as nuclear magnetic resonance (NMR), infrared, Raman, and neutron spectroscopy data. The typical expression of a force field is written as:[63,64]

$$U = \sum_{bonds}\frac{1}{2}k_b\,(r - r_0)^2 + \sum_{angles}\frac{1}{2}k_a\,(\theta - \theta_0)^2 + \sum_{torsions}\frac{V_n}{2}[1 + \cos(n\phi - \delta)] + \sum_{improper} V_{imp} + \sum_{LJ} 4\varepsilon_{ij}\left(\frac{\sigma_{ij}^{12}}{r_{ij}^{12}} - \frac{\sigma_{ij}^{6}}{r_{ij}^{6}}\right) + \sum_{elec}\frac{q_i q_j}{r_{ij}} \quad (2.59)$$

The first four terms' summations include all over the bonds, angles, torsion angles, and improper torsions, while the last two terms described the nonbonded interactions of repulsive and van der Waals interactions (in this case by modelling with Lennard-Jones potential) and the Coulombic interactions. Different types of available force fields are OPLS-AA,[65] AMBER,[66] CHARMM,[67] GROMOS,[68] MARTINI,[69] etc.

2.19. Molecular Mechanics Poisson-Boltzmann or Generalized Born Surface Area (MM/PB(GB)SA) Method

The binding free energy of the protein-ligand complexes was obtained by using the most well-known method of molecular mechanics Poisson-Boltzmann surface area (MM/PBSA) and molecular mechanics generalized Born surface area (MM/GBSA).[70-73] In this method, the binding free energy of the ligand (L) to the protein (P) to form the complex (PL) can be estimated as,

$$\Delta G^{bind} = G^{PL} - G^{P} - G^{L} \quad (2.60)$$

In Eq. 2.59, each term on the right-hand side can be represented by

$$G^{X} = E^{MM} + G^{sol} - T\Delta S \quad (2.61)$$

Further ΔG^{bind} can be expressed as

$$\Delta G^{bind} = \Delta H - T\Delta S \quad (2.62)$$

Where ΔH denotes the enthalpy associated with binding and $-T\Delta S$ accounts for the conformational entropy when after the ligand is bind with protein. The estimation of entropy term is computationally expensive and the omitted of this term is highlighted in the earlier literature.[73,74]

The term ΔH can be decomposed as,

$$\Delta H = \Delta E^{MM} + \Delta G^{sol} \quad (2.63)$$

Where ΔE^{MM} represents the change in the molecular mechanics (MM) energy in the gas phase and the term ΔG^{sol} denotes the solvation free energy. Further, the molecular mechanics energy ΔE^{MM} can be expressed as,

$$\Delta E^{MM} = \Delta E^{bonded} + \Delta E^{non-bonded} \quad (2.64)$$

Where the ΔE^{bonded} term is known as internal energies includes bond, angle, and dihedral angle energies while $\Delta E^{non-bonded}$ term accounts for the electrostatic and van der Waals energies. Therefore, both s ΔE^{bonded} and $\Delta E^{non-bonded}$ term can be written as,

$$\Delta E^{bonded} = \Delta E^{bond} + \Delta E^{angle} + \Delta E^{dihedral} \quad (2.65)$$

$$\Delta E^{non-bonded} = \Delta E^{ele} + \Delta E^{vdW} \quad (2.66)$$

So, Eq. 2.64 can be rewritten as:

$$\Delta E^{MM} = \Delta E^{bond} + \Delta E^{angle} + \Delta E^{dihedral} + \Delta E^{ele} + \Delta E^{vdW} \quad (2.67)$$

The solvation free energy ΔG^{sol} term of Eq. 2.63 can be decomposed into

$$\Delta G^{sol} = \Delta G^{polar} + \Delta G^{non-polar} \quad (2.68)$$

Where ΔG^{polar} and $\Delta G^{non-polar}$ terms account for the polar and non-polar contribution. The polar contribution ΔG^{polar} is estimated by implementing the PB or GB approaches while the $\Delta G^{non-polar}$ non-polar contribution is calculated by using the solvent accessible surface area (SASA) method.[75]

2.20. References

[1] A. Szabo and N. S. Ostlund, *Modern Quantum Chemistry: Introduction to Advanced Electronic Structure Theory*, Dover Publications, Inc., Mineola, 1996.

[2] J.-M. Combes, P. Duclos and R. Seiler, *The Born-Oppenheimer Approximation. In: Rigorous Atomic and Molecular Physics*, New York, Plenum, 1981.

[3] D. R. Hartree, *Math. Proc. Camb. Philos. Soc.*, 1928, **24**, 89.

[4] V. Fock, *Z Phys.*, 1930, **61**, 126.

[5] W. Pauli, *Writings on Physics and Philosophy*, Spinger, Berlin, 1994.

[6] C. Møller and M. S. Plesset, *Phys. Rev.*, 1934, **46**, 618.

[7] I. Shavitt and R. J. Bartlett, *Many-body methods in chemistry and physics: MBPT and coupled-cluster theory*, Cambridge University Press, 2009.

[8] J. Čížek, *J. Chem. Phys.*, 1966, **45**, 4256.

[9] J. Čížek and J. Paldus, *Int. J. Quantum Chem.*, 1971, **5**, 359.

[10] R. J. Barlett and M. Musial, *Rev. Mod. Phys.*, 2007, **79**, 291.

[11] K. Hirao, *Recent Advances in Multireference Methods*, World Scientific, Singapore, 1999.

[12] F. Neese, A. Hansen and D. G. Liakos, *J. Chem. Phys.*, 2009, **131**, 064103.

[13] C. Riplinger and F. Neese, *J. Chem. Phys.*, 2013, **138**, 034106.

[14] C. Riplinger, B. Sandhoefer, A. Hansen and F. Neese, *J. Chem. Phys.*, 2013, **139**, 134101.

[15] C. Riplinger, P. Pinski, U. Becker, E. F. Valeev and F. Neese, *J. Chem. Phys.*, 2016, **144**, 024109.

[16] Q. Zhang, R. Bell and T. N. Truong, *J. Phys. Chem.*, 1995, **99**, 592.

[17] A. K. Rappe and E. R. Bernstein, *J. Phys. Chem. A*, 2000, **104**, 6117.

[18] S. F. Boys, *Rev. Mod. Phys.*, 1960, **32**, 296.

[19] J. Pipek and P. G. Mezey, *J. Chem. Phys.*, 1989, **90**, 4916.

[20] W. Kohn and L. J. Sham, *Phys. Rev.*, 1965, **140**, A1133.

[21] J. P. Perdew and A. Zunger, *Phys. Rev. B*, 1981, **23**, 5048.

[22] J. P. Perdew and Y. Wang, *Phys. Rev. B*, 1992, **45**, 13244.

[23] S.H. Vosko, L. Wilk and M. Nusair, *Canadian J. Phys.*, 1980, **58**, 1200.

[24] J. P. Perdew, K. Burke and Y. Wang, *Phys. Rev. B*, 1996, **54**, 16533.

[25] J. P. Perdew, K. Burke and M. Ernzerhof, *Phys. Rev. Lett.*, 1996, **77**, 3865.

[26] J. P. Perdew, K. Burke and M. Ernzerhof, *Phys. Rev. Lett.*, 1997, **78**, 1396.

[27] J. Tao, J. P. Perdew, V. N. Staroverov and G. E. Scuseria, *Phys. Rev. Lett.*, 2003, **91**, 146401.

[28] A. D. Becke, *J Chem. Phys.*, 1993, **98**, 5648.

[29] C. Lee, W. Yang and R. G. Parr, *Phys. Rev. B*, 1988, **37**, 785.

[30] J. P. Perdew and K. Schmidt, *AIP Conf. Proc.*, 2001, **577**, 1.

[31] S. Grimme, A, Hansen, J. G. Brandenburg and C. Bannwarth, *Chem. Rev.* 2016, **116**, 5105.

[32] S. Grimme, *J. Comput. Chem.*, 2004, **25**, 1463.

[33] S. Grimme, *J. Comput. Chem.*, 2006, **27**, 1787.

[34] J.-D. Chai and M. Head-Gordon, *Phys. Chem. Chem. Phys.*, 2008, **10**, 6615.

[35] S. Grimme, S. Ehrlich and L. Goerigk, *J Comput Chem.*, 2011, **32**, 1456.

[36] K. Morokuma and K Kitaura, *Chemical Applications of Atomic and Molecular Electrostatic Potentials*, Plenum, New York, 1981.

[37] K. Szalewicz, *Wiley Interdiscip. Rev. Comput. Mol. Sci.*, 2012, **2**, 254.

[38] E. D. Glendening, *J. Am. Chem. Soc.*, 1996, **118**, 10, 2473.

[39] M. P. Mitoraj, A. Michalak and T. Ziegler, *J. Chem. Theory Comput.*, 2009, **5**, 962.

[40] T. Ziegler and A. Rauk, *Theor. Chim. Acta.*, 1977, **46**, 1.

[41] T. Ziegler and A. Rauk, *Inorg. Chem.*, 1979, **18**, 1755.

[42] M. Mitoraj and A. Michalak, *J. Mol. Model.*, 2007, **13**, 347.

[43] M. Mitoraj and A. Michalak, *Organometallics*, 2007, **26**, 6576.

[44] M. Mitoraj and A. Michalak, *J. Mol. Model.*, 2008, **14**, 681.

[45] A. Michalak, M. Mitoraj and T. Ziegler, *J. Phys. Chem. A*, 2008, **112**, 1933.

[45] M. Mitoraj, H. Zhu, A. Michalak and T. Ziegler, *Int. J. Quantum Chem.*, 2008, **109**, 3379.

[46] M. Srebro and M. Mitoraj, *Organometallics*, 2009, **28**, 3650.

[47] W. B. Schneider, G. Bistoni, M. Sparta, M. Saitow, C. Riplinger, A. A. Auer and F. Neese, *J. Chem. Theory Comput.*, 2016, **12**, 4778.

[48] N.R. Kestner and J. E. Combariza, *Rev. Comput. Chem.*, 1999, **13**, 99.

[49] C.D. Sherill, *Counterpoise correction and basis set superposition error*, School of Chemistry and Biochemistry, Georgia Institute of Technology, 2010.

[50] S. F. Boys and F. Bernardi, *Mol. Phys.*, 1970, **19**, 553.

[51] C. A. Hunter, *Angew. Chem. Int. Ed.*, 2004, **43**, 5310.

[52] P. Politzer, J. S. Murray and T. Clark, *J. Mol. Model.*, 2015, **21**, 1.

[53] S. R. Gadre, C. H. Suresh and N. Mohan, *Molecules*, 2021, **26**, 3289.

[54] R. F. W. Bader, *Acc. Chem. Res.*, 1985, **18**, 9.

[55] R. F. W. Bader, *Chem. Rev.*, 1991, **91**, 893.

[56] R. F. W. Bader, *Atoms in Molecules, A Quantum Theory*, Oxford University Press, Oxford, 1990.

[57] A. M. Pendás, A. Costales and V. Luaña, *Phys. Rev. B*, 1997, **55**, 4275.

[58] E. R. Johnson, S. Keinan, P. Mori-Sánchez, J. Contreras-García, A. J. Cohen and W. Yang, *J. Am. Chem. Soc.*, 2010, **132**, 6498.

[59] J. P. Foster and F. Weinhold, *J. Am. Chem. Soc.*, 1980, **102**, 7211.

[60] L. Verlet, *Phys. Rev.*, 1967,**159**, 98.

[61] M. A. Cuendet and W. F. van Gunsteren, *J. Chem. Phys.*, 2007, **127**, 184102.

[62] D. Frenkel and B. Smit, *Understanding molecular simulations: from algorithms to applications*, Academic Press, San Diego, 1996

[63] M.A. González, *Collection SFN*, 2011, **12**, 169.

[64] O. Guvench and A. D. MacKerell, *Molecular Modeling of Proteins*, ed. K. Andreas, Humana Press, Totowa, NJ, 2008, vol. 443, p. 63.

[65] W. L. Jorgensen, D. S. Maxwell and J. Tirado-Rives, *J. Am. Chem. Soc.*, 1996, **118**, 11225.

[66] Y. Duan, C. Wu, S. Chowdhury, M. C. Lee, G. Xiong, W. Zhang, R. Yang, P. Cieplak, R. Luo, T. Lee, J. Caldwell, J. Wang and P. Kollman, *J. Comput. Chem.*, 2003, **24**, 1999.

[67] J. Huang and A. D MacKerell, *J. Comput. Chem.*, 2013, **25**, 2135.

[68] N. Schmid, A. P. Eichenberger, A. Choutko, S. Riniker, M. Winger, A. E. Mark and W. F. van Gunsteren, *Eur. Biophys. J.*, 2011, **40**, 843.

[69] S. J. Marrink, H. J. Risselada, S. Yefimov, D. P. Tieleman and A. H. de Vries, *J. Phys. Chem. B*, 2007, 111, **27**, 7812.

[70] J. Srinivasan, T. E. Cheatham, P. Cieplak, P. A. Kollman and D.A. Case, *J. Am. Chem. Soc.*, 1998, **120**, 9401.

[71] I. Massova and P. A. Kollman, *Perspect. Drug Discovery Des.*, 2000, **18**, 113.

[72] M. S. Valdés-Tresanco, M. E. Valdés-Tresanco, P. A. Valiente and E. Moreno, J. *Chem. Theory Comput.* 2021, **17**, 6281.

[73] E. Wang, H. Sun, J. Wang, Z. Wang, H. Liu, J. Z. H. Zhang and T. Hou, *Chem. Rev.*, 2019, **119**, 9478.

[74] R. Kumari, R. Kumar and A. Lynn, *J. Chem. Inf. Model.*, 2014, **54**, 1951.

[75] C. Tan, Y.-H. Tan and Ray Luo, *J. Phys. Chem. B*, 2007, **111**, 12263.

Chapter 3

Torsional Rotation in Ditopic Receptor Host and its Complex Formation with Resorcinol Guest: A Computational Study

The work of this Chapter is published in *ChemPhysChem* **2023**, *24*, e202200928 (1-12).

3.1. Introduction

Noncovalent interactions are the holy grail in nature and are central to biology, chemistry, material science, and many more.[1–19] Unlike covalent interactions, noncovalent interactions range from angstroms to nanometres.[10] In creating large and complex molecular clusters, contributions from noncovalent interactions are enormous.[1,10] It is well known that noncovalent interactions show reversibility, weak specificity, and moderate directionality properties.[11] Thus, these interactions are generally the leading forces behind molecular recognition,[16] molecular self-assemblies,[20] surface-molecule interactions and enzyme catalysis.[21] They are exploited in research areas like supramolecular chemistry, drug design, materials design, etc., to create new compounds, materials, and technologies.

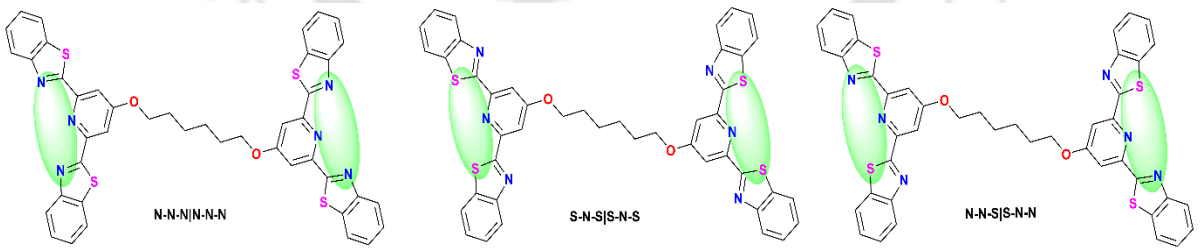

Figure 3.1. Molecular structures of different conformers, i. e., N-N-N|N-N-N, S-N-S|S-N-S and N-N-S|S-N-N of the host bbh. The shaded green color region indicates the binding sites.

In 1978, Lehn coined the term “supramolecular chemistry” which suggests the “chemistry beyond molecules”.[22] Supramolecular chemistry plays a prominent role in diverse fields, namely self-interactions of nanomaterials,[23] organocatalysts interaction,[24] biological processes such as substrate enzyme binding,[25] protein-ligand,[26] protein-protein

interactions[27] and many others. The exploration in this research area is gradually increasing. Since the mid-twentieth century, the supramolecular chemistry of synthetic macrocyclic receptors host has a great interest in different multidisciplinary areas of chemistry and biology.

The supramolecular host-guest complex formation and assemblies needed a specific interaction between the host and guest. Pedersen reported the first artificial host-guest complex, in which the alkali metal cations act as the guest species, and crown ether was considered a macrocyclic host.[28] It is also noted that crown ethers are considered the first-generation macrocyclic host in the area of supramolecular host-guest chemistry. Pedersen's discovery of the host-guest complex laid the foundation and platform for the design and construction of ample macrocyclic host molecules having various applications, especially in the domains of sensors, biomedical, and nanotechnology. In contrast to conventional molecular chemistry, which deals with the covalent bond, supramolecular host-guest chemistry mainly relies on noncovalent interactions. Further, such supramolecular system can be modulated to achieve different properties and useful applications through external aid such as pH, light, salt, electrical input, temperature, chemical agents, etc.[29-33]

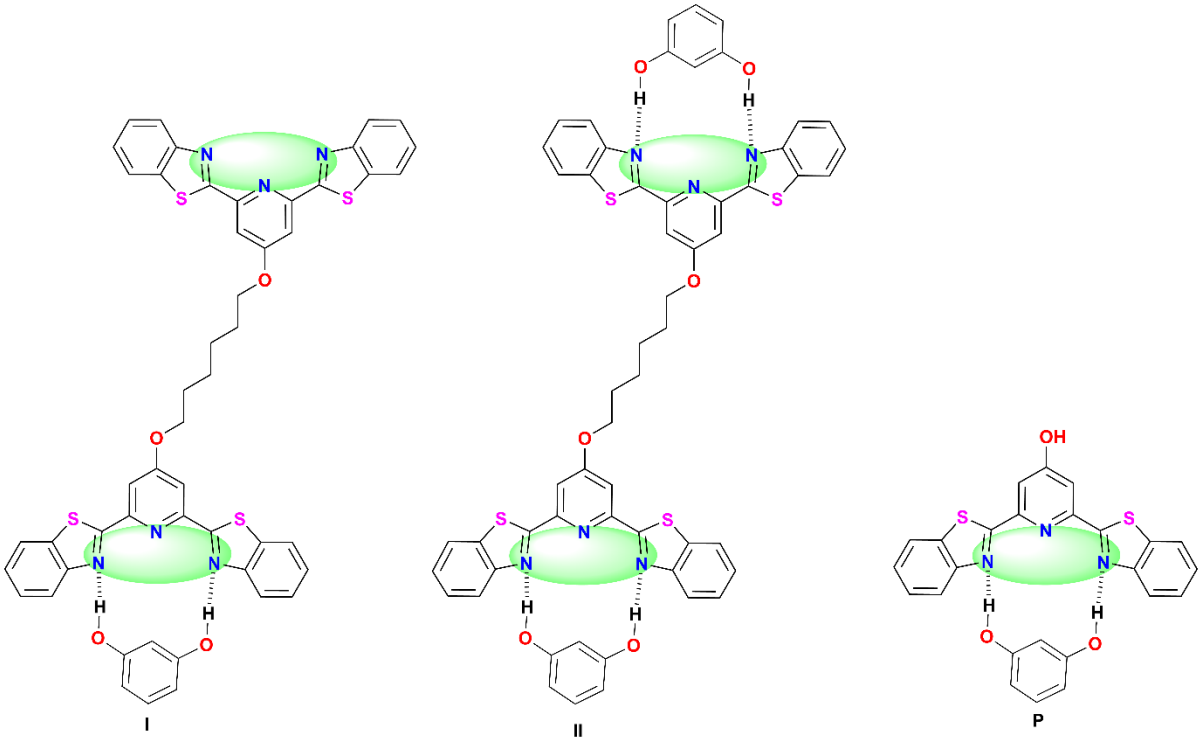

Figure 3.2. Molecular structures of complexes I, II, and P.

In host-guest chemistry, the selective binding of guest molecules requires the designing of a specific host system, which needs great effort and is the current focus of the research area. The

commonly used approach is introducing the heteroatom(s), such as nitrogen, sulphur, oxygen, etc., in the molecular structure of the host. Additionally, in host-guest complexes, the guest molecules are encapsulated into the cavity of the host either partially or entirely. Therefore, the compatibility of geometrical parameters such as the shape and size of the host cavity and the guest molecule is essential in the formation of the host-guest complex. In such a complex, the mutual orientation and interaction between the host and guest units are determined by the types of noncovalent interactions involved between the recognition sites of the host and functional groups present in the guest molecules.[34–37] Examples of these noncovalent interactions include hydrogen bonding,[38–46] halogen bonding,[47] π-π stacking,[48] cation-π,[49] anion-π,[50] van der Waals,[51] etc.

Over the last few decades, diverse classes of supramolecular hosts molecules were reported, which include cyclodextrins,[52,53] cucurbit[n]uril,[54] calixarenes,[55] porphyrins,[56] crown ethers,[57] pillarenes,[58] cyclophanes,[59] molecular tweezers,[60] and many more. These host molecules have a rigid binding cavity with varying dimensions and are able to accommodate the guest molecules.

Since the field of host-guest chemistry and its application is extremely vast, in this present article, we have restricted our studies towards the host-guest complex formation between the macrocyclic ditopic receptor host and resorcinol guest molecule. Here the ditopic receptor host can accommodate a maximum of two guest molecules. Resorcinol has many industrial applications and is used in synthesizing different products such as plastics, rubber, pharmaceuticals, and cosmetics.[61] However, the waste products from these industries are a major cause of contributing resorcinol to polluting the environment. Some of the health hazards due to the exposure of resorcinol molecule are: it suppresses the thyroid hormone in the human body,[62,63] induction of chromatid ruptures, exchanges in Chinese hamster ovary cells,[64] carcinogenesis in the upper digestive tract,[65] anomalies of hematology,[66] and even fatal cases of the human fetus.[67] Apart from the above applications and hazards, it also shows medicinal importance, such as antioxidant, antifungal, and anticancer.

Many research groups synthesized the supramolecular host systems which can bind the resorcinol guest molecule and also discussed the involvement of noncovalent interactions. Sijbesma et al.[68] synthesized a series of molecular receptors having U-shaped geometry that could bind the molecules such as resorcinol, phenol, catechol, and 2,7-dihydroxynapthalene. Receptors based on propanediurea as building blocks have been reported by Jansen and co-

workers.[69] They found that some receptors bind the resorcinol molecule with a higher value of association constant. Wang et al.[70] synthesized heteroatoms bridged azacalix[4]pyridines macrocyclic molecule and studied the noncovalent interactions involved in the formation of a host-guest complex with resorcinol molecule. In this direction, the underlying noncovalent interactions between the hosts calix [4] pyridine, azacalix[4]pyridines, and the guest resorcinol were studied under the light of density functional theory (DFT) calculations.[71]

Chetia et al.[72] synthesized a molecule 2,6-bis(2-benzimidazolyl) pyridine that selectively binds the para-benzoquinone through hydrogen bonding among phenol, resorcinol, catechol, and hydroquinone. Ditopic receptor host 1,6-bis(2,6-bis(benzothiazol-2-yl) pyridine-4-yloxy) hexane (bbh) which has capable of forming 1: 1 and 1: 2 host-guest complexes with resorcinol guest molecule, was also reported by Goutam et al.[73] This ditopic receptor selectively recognized the resorcinol guest in the presence of the other molecules like catechol, phenol, and hydroquinone. As confirmed by the NMR studies, their investigation observed that the resorcinol molecule binds to the bbh through the formation of hydrogen bonding.[73] M.Boca et al.[74] reported the ligand 2,6-bis(benzthiazol-2-yl) pyridine, which has similarities to the region of the binding site of the host bbh. They observed that the ligand existed in two isomeric forms and underwent the facile dihedral angle rotation along the C-C bond connecting the benzothiazole and pyridine rings. However, the dihedral angle rotation process of the host bbh was not mentioned in the literature. Therefore, our hypothesis is the host bbh is also likely to have the dihedral angle rotation as similarly observed in the ligand 2,6-bis(benzthiazol-2-yl) pyridine and different conformers exist, as shown in Figure 3.1. From the above discussion, it is yet to understand and investigate the stability of the conformers of host bbh. It is interesting to study the nature of noncovalent interactions in the host-guest complexes formed between the host bbh and guest resorcinol molecule.

In this Chapter, we investigate the intramolecular noncovalent interactions in different conformers of the host, bbh, using different quantum mechanical approaches. This work also accounts the analyses of torsional angle rotation and conformational preference of the host bbh to bind resorcinol molecule. In addition, to gain more insight into the interaction energies and nature of noncovalent interactions between the host and guest in complexes I (1:1) and II (1:2), as presented in Figure 3.2, different theoretical calculations were considered. The Computational Details used in these investigations are discussed in the following sections. Results and Discussion are provided thereafter. A Summary of the salient results concludes this Chapter.

3.2. Computational Details

Geometry optimization and vibrational frequency calculation of conformers (N-N- N|N-N-N, S-N-S|S-N-S, and N-N-S|S-N-N) of the host bbh were performed by combining Grimme's dispersion (D3) correction[75] model with the DFT functional B3LYP,[76] utilizing the 6-311++G(d,p) basis set. To obtain the torsional angle rotation barrier, we used the optimized geometry of the conformers generated at the B3LYP-D3/6-311++G(d,p) level of theory. We calculated the energies at 10° intervals (from 0° to 180°) by rotating the inter ring C-C bond connecting the adjoining pyridine and benzothiazole rings of the conformers. Energies of all these data points at different dihedral angles were obtained by fixing one dihedral angle and optimizing the remaining degrees of freedom at the B3LYP-D3/6-311++G(d,p) level of theory, following a similar protocol of Jackson et al.[77] However, the overstabilization and delocalization error in DFT leads to inaccurate results of torsional barrier energies were also reported elsewhere.[78,79] To deal with this problem, many groups used the wavefunction-based method, such as the Møller-Plesset perturbation theory (MP2), which provided reliable results of the torsional energy barrier.[80,81] In our work, we performed the calculations with a computationally less expensive method, the resolution of the identity MP2 (RI-MP2) method, which gives nearly identical results to that of the full MP2 method. The fixed dihedral angle optimized geometries of the conformers obtained at the B3LYP-D3/6-311++G(d,p) method were used as an input structure to perform the single-point energy calculations at the RI-MP2/cc-pVTZ level of theory. Further, we consider the one binding moiety S-N-S of the parent conformer S-N-S|S-N-S and perform the torsional potential energy surface (PES) scan. The calculations were also performed in solvent phases acetonitrile and chloroform, using the polarizable continuum (PCM) model.[82] To see the torsional energy barrier when both the dihedral angles were rotated simultaneously, the relaxed potential energy surface scan of S-N-S|S-N-S was performed by considering two dihedral angles. All the calculations related to the B3LYPD3/6-311++G(d,p) level of theory were performed in the Gaussian 16 package[83] and for the RI-MP2/cc-pVTZ level of theory, we utilized the ORCA 4.2.0 program package.[84,85]

To understand the electrostatic interactions of the atoms present in the conformers, the partial atomic charges using a reliable charge analysis method, ChelpG,[86] based on the electrostatic potential fitting was employed. The analysis was performed at the B3LYP-D3/6-311++G(d,p) theoretical accuracy.

To analyse the interaction energy, ΔE, of the host-guest complexes, geometry optimization, and vibrational frequency calculations of the host bbh (N-N-N|N-N-N), the guest molecule

resorcinol, and their complexes I (bbh: resorcinol) and II (resorcinol: bbh: resorcinol) were carried out using the dispersion (D3) corrected DFT functionals B3LYP, PBE0, and TPSSTPSS with 6-311++G(d,p) and def2-TZVP basis sets.[87–89] The interaction energy, ΔE, was predicted by applying the supermolecular approach, subtracting the energies of the constituent fragments from the total energy of the complex as given in Eq. 3.1 and Eq. 3.2,

$$\Delta E_{HG}(1:1) = E_{HG} - (E_H + E_G) \tag{3.1}$$

$$\Delta E_{GHG}(1:1) = E_{GHG} - (E_H + 2E_G) \tag{3.2}$$

Where E_{HG} and E_{GHG} are the optimized electronic energies of host-guest complexes 1:1 and 1:2, respectively, E_H and E_G are the optimized energies of the host and guest, respectively. Basis set superposition error (BSSE)[90] corrections were computed using the counterpoise correction (CP) methods of Boys and Bernardi,[91] as implemented in Gaussian 16 package.

The use of hybrid meta-generalized gradient approximation (hybrid meta-GGA) functional M06-2X to describe the hydrogen bonding and other weak interactions is also known.[92,93] Thus, in our calculations, we adopted the M06-2X level of theory in conjunction with the 6-311++G(d,p) and def2-TZVP basis sets. In addition, Grimme's composite functional PBEh-3c was implemented in our calculations, which includes geometrical counterpoise (gCP) and dispersion (D3) corrections.[94] Further, we estimated the interaction energy of complexes I and II by incorporating the dispersion correction model with the Becke-Johnson damping function D3(BJ)[89] to the B3LYP, PBE0, and TPSSTPSS functionals. For the calculations with the PBEh-3c functional, we utilized the ORCA 4.2.0 program package, and for the remaining functionals, the calculations were performed in the Gaussian 16 package.

For benchmarking the interaction energy, ΔE, we designed a prototype complex P, as shown in Figure 3.2, by considering only the binding moiety region of the host bbh and guest resorcinol molecule. Before estimating the benchmark interaction energy, ΔE, we obtained the interaction energy of complex P at the same level of theory and basis sets used in complexes I and II. The optimized equilibrium geometry of complex P generated at the B3LYP-D3/6-311++G(d,p) level of theory was used to calculate the interaction energy, ΔE, at the domain-based local pair natural orbital coupled cluster theory with single, double, and perturbative triple excitations [DLPNO-CCSD(T)],[95] with employing the TightPNO and TightSCF convergence criteria settings environment in the ORCA package. Two points extrapolation complete basis set (CBS) limit was performed with the consideration of counterpoise correction

employing the def2-TZVPP and def2-QZVPP basis sets. Further, to see the nature of interactions between the host and guest in complex, the extended transition state-natural orbital chemical valence (ETS-NOCV)[96] analysis was performed using the BP86-D3(BJ)/TZ2P method as implemented in the ADF2021 software package.[97] Molecular electrostatic potential surfaces (MEPS) analysis was performed to obtain information about the charge distribution on the van der Waals surface of the molecules and explain the interactions between the host and guest.[98-101] Further, to see the underlying strength of the interaction between the host and the guest, natural bond orbital (NBO) analysis was performed.[102] In addition, to investigate the nature of interactions in host-guest complexes, in detail, atoms in molecules (AIM),[103] reduced density gradient (RDG), and noncovalent interaction (NCI)[104] analyses were performed in Multiwfn[105] program package. The visual molecular dynamics (VMD)[106] program was used to visualize and plot the NCIs maps.

3.3. Results and Discussion

3.3.1. Conformational Analysis of Host bbh

The electronic energy of conformers of the host bbh calculated at the B3LYP-D3 level of theory with 6-311++G(d,p) basis set follow the order S-N-S|S-N-S (0.00 kcal mol^{-1}) < N-N-S|S-N-N (11.58 kcal mol^{-1}) < N-N-N|N-N-N (26.17 kcal mol^{-1}). The energy trends show that bbh preferably exists in the S-N-S|S-N-S conformer. The molecular geometry of optimized conformer S-N-S|S-N-S exhibited a planar structure with torsional angles θ_1, θ_2, θ_3, and θ_4 having the value of 0° as shown in Figure A1 of Appendix-A. In the case of N-N-N|N-N-N conformer, (Figure A2 of Appendix-A), the torsional angles ϕ_1 and ϕ_2 are 28.52° and 30.44°, respectively. In contrast, the remaining torsional angles ϕ_3 and ϕ_4 values are 30.44° and 28.52°, respectively. Further, the torsional angles γ_2 and γ_3 of conformer N-N-S|S-N-N values are close to 0°, while the remaining torsional angles γ_1 and γ_4 have equal value of 22.66° (Figure A3 of Appendix-A). The conformer having torsional angle value 0° and their corresponding adjoining pyridine and benzothiazole rings show a planar structure. However, we have observed that the twisted geometry structures for the torsional angle have non-zero values.

To shed in-depth insight into the stability of the conformers, the torsional rotation barrier and possible interactions among them were calculated by generating the torsional potential energy surfaces (PESs). We considered the parent conformer S-N-S|S-N-S and their extracted fragment unit S-N-S (Figure A4 of Appendix-A) to perform the PES scan.

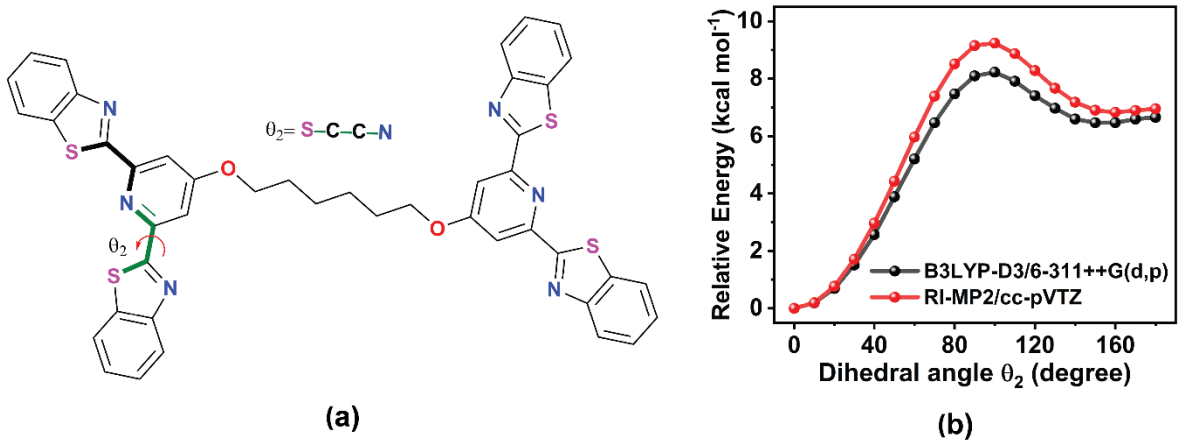

Figure 3.3. (a) Molecular structure of the S-N-S|S-N-S conformer showing the dihedral angle θ_2 form by connecting the C-C bond between the pyridine and benzothiazole rings. (b) Potential energy surface (PES) of dihedral angle θ_2 rotation from 0° to 180° with a step size of 10°.

The PES scan was performed by rotating across the inter-ring C-C bond from 0° to 180° with an increment of 10° step size, as described in the Computational Details. The obtained PES scan of the S-N-S|S-N-S conformer is portrayed in Figure 3.3, and their energy values along with the corresponding angles, are provided in Table A1 of Appendix-A. For the remaining conformers, torsional PESs are provided in Table A2 of Appendix-A and Table A3 of Appendix-A. Figure 3.3 shows that for the conformer S-N-S|S-N-S, θ_2=0° conformation is more energetically stable than the rotated 180° conformation. The maximum energy barrier height of 8.22 kcal mol^{-1} and 9.23 kcal mol^{-1} were obtained for B3LYP-D3/6-311++G(d,p) and RI-MP2/cc-pVTZ//B3LYP-D3/6-311++G(d,p) level of theory, respectively. Similarly, the equal value of torsional energy barrier height in the case of S-N-S was observed. In addition, the torsional rotational barrier height is equal in both the cases of parent and fragmented conformer. The torsional barrier height of the S-N-S conformer is reduced in the solvent environment of acetonitrile and chloroform. The calculated barrier height at the B3LYP-D3/6-311++G(d,p) level of theory is 6.34 kcal mol^{-1} (acetonitrile) and 6.90 kcal mol^{-1} (chloroform). The PES scan (Figure A5 and Figure A6 of Appendix-A) and energy values, along with their corresponding angles of fragmented S-N-S conformer, are provided in Table A4 and Table A5 of Appendix-A. Further, the torsional PES of the S-N-S|S-N-S conformer and the noncovalent interaction (NCI) analysis were incorporated. The RDG isosurface maps at torsional angles 0°, 90°, and 180° of the conformers are presented in Figure 3.4. At θ_2=0° torsional angle conformation, hetero atom S···N interaction and weak hydrogen bonding (C-H···N) interaction are seen between the C-H group of the middle pyridine ring and the nitrogen atom of the

benzothiazole ring. In contrast, at angle θ_2=180°conformation, we observed that the N···N repulsive interaction and weak (C-H···S) interaction. The torsional PESs revealed that the weak hydrogen bonding (C-H···N) and heteroatom S···N interactions are the driving forces to stabilize the S-N-S|S-N-S conformer. However, the alternative N···N repulsive interaction and the hydrogen bonding (C-H···S) lead the conformer to a higher energy level. So, the presence of four intramolecular S···N and four hydrogen bonding (C-H···N) interactions make the S-N-S|S-N-S conformer relatively more stable than others. Similarly, the torsional energy barrier is nearly equal and close to 10 kcal mol^{-1} for both N-N-N|N-N-N and N-N-S|S-N-N conformers. Further, to see the effect on the torsional rotation barrier when the two dihedral angles were rotated simultaneously, we performed a relaxed PES scan of two dihedral angles θ_1 and θ_2 (Figure 3.5) from 0° to 360° in step size of 10° for the S-N-S|S-N-S conformer calculated at the B3LYPD3/6-311++G(d,p) level of theory. The 3D PES, along with the contour plot, is shown in Figure 3.5. The PES result infer that the energy required to cross the barrier is 17.0 kcal mol^{-1}.

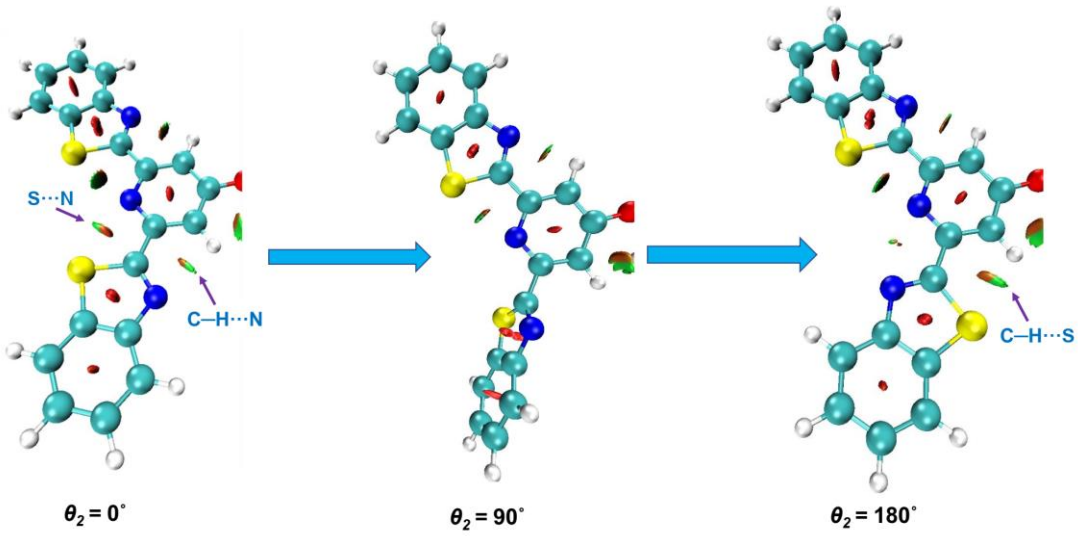

Figure 3.4. RDG isosurface maps at torsional angles 0°, 90°, and 180°for the S-N-S|S-N-S conformer calculated at the B3LYP-D3/6-311++G(d,p) theoretical accuracy.

To understand the nature of interactions and stability of the conformers, we performed the CHelpG charge analysis. We considered the optimized conformers calculated at the B3LYPD3/6-311++G(d,p) level of theory. The atomic charges are presented in Figure A7 of Appendix-A. The nitrogen atoms in each conformer bear a negative charge in the range of 0.52 to 0.58. Similarly, the sulphur atoms of benzothiazole possess negative charge ranging from 0.08 to 0.14. This fact rules out any possibility of electrostatic interactions between the sulphur

and nitrogen atoms in the S-N-S|S-N-S and N-N-S|S-N-N conformers, although van der Waals interaction may play a role. The S···N interaction distance calculated at the B3LYP-D3/6-311++G(d,p) is 2.95 Å which is considerably less than the sum of the van der Waals radii for S (1.80 Å) and N (1.55 Å), at 3.35 Å. From the NCI analyses of S-N-S|S-N-S and N-N-S|S -N-N, (Figure A8 of Appendix-A) S···N interaction paths highlighted the existence of van der Waals interaction. However, the projecting hydrogen atom (C-H groups) of the pyridine rings carry positive charges ranging from 0.1 to 0.14 and can form the electrostatic interactions of nitrogen-hydrogen and sulphur hydrogen as shown in Figure A7 of Appendix-A. Observing the atomic charges of nitrogen and sulphur atoms, the nitrogen atom possesses more negative charge value than the sulphur atom. It hence favours the C-H···N hydrogen bonding interaction over the C-H···S interaction.

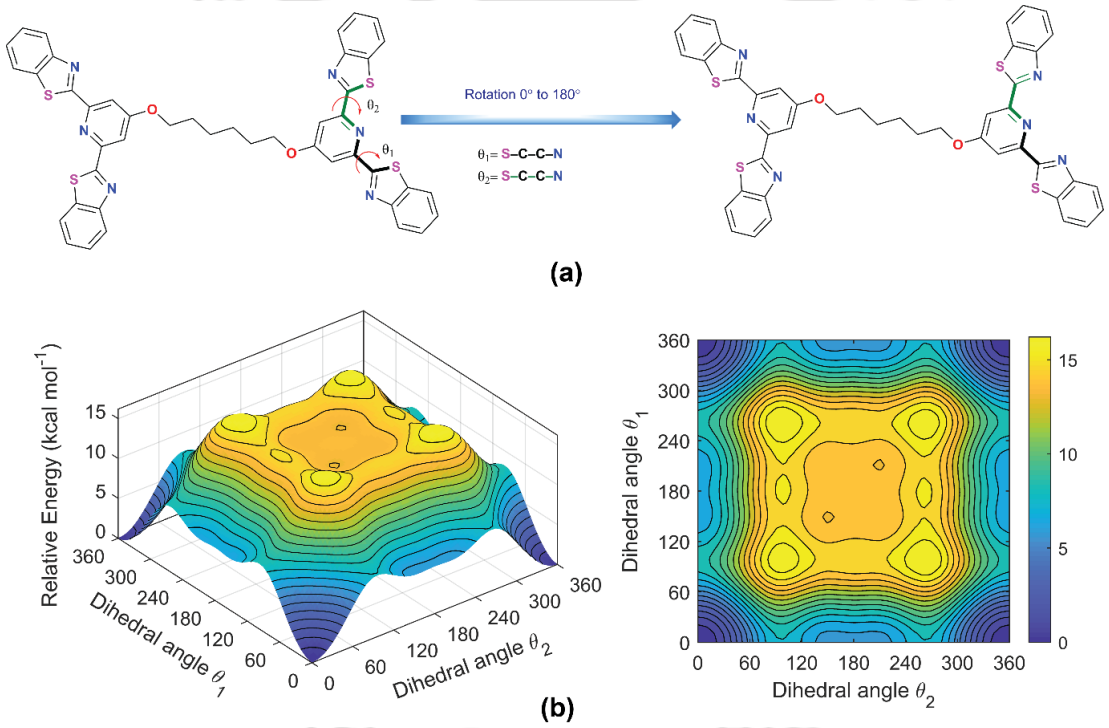

Figure 3.5. a) Molecular structures of the S-N-S|S-N-S conformer showing dihedral angles θ_1 and θ_2. (b) Contour plots of 3D relax potential energy surfaces (PES) scan of dihedral angles θ_1 and θ_2 generated at the B3LYP-D3/6-311++G(d,p) level of theory.

Our theoretical investigation for the rotation of the torsional angle in the host bbh has correlated with the experimental studies of M. Boca et al.[74] ligand 2,6-bis (benzthiazol-2-yl) pyridine. The compound 2,6-bis(benzthiazol-2-yl) pyridine has a similar molecular structure to the binding sites of the host, bbh. The X-ray structure studies of the ligand 2,6- bis(benzthiazol-2-yl) reported that the free ligand exists in the S-N-S form, while in the complex, it exists in the

N-N-N form.[74] This result shows the torsional rotation of the inter ring C-C bond between the benzothiazole and pyridine rings. Therefore, we also agreed that torsional angle rotation existed in the host bbh and exhibited effective binding sites to accommodate guest resorcinol molecule.

3.3.2. Interaction Energy

Interaction energy, ΔE, of the 1:2 host-guest complexes formed by the different conformers N-N-N|N-N-N, S-N-S|S-N-S, and N-N-S|S-N-N of the host bbh with resorcinol guest molecule were evaluated at the B3LYP-D3/6-311++G(d,p) level of theory. The highest ΔE value corresponds to the complex's host conformer N-N-N|N-N-N. The optimized geometries of all the complexes and their corresponding interaction energy, ΔE, values are presented in the Figure A9 of Appendix-A. Further, we computed the interaction energy, ΔE, of the host-guest complexes by considering only the N-N-N|N-N-N conformer as the host. The ΔE of complexes I (1:1) and II (1:2) were calculated with the DFT functionals PBE0-D3 and TPSSTPSS-D3 with 6-311++G(d,p) and def2-TZVP as basis sets. We also evaluated the ΔE with the M06-2X and PBEh-3c functionals. Additionally, for complexes I and II, we extended the calculations using the dispersion correction model with the Becke-Johnson damping function D3(BJ) in conjunction with B3LYP, PBE0, and TPSSTPSS functionals. To incorporate the BSSE effect, the counterpoise corrections methods implemented in the Gaussian 16 package. The BSSE corrected interaction energies for the complexes are tabulated in Table 3.1, while the uncorrected interaction energies values are provided in Table A6 of Appendix-A. From Table 3.2, we observed that the ΔE values of complex I range from -18.06 to -21.65 kcal mol^{-1} and for complex II from -36.05 to -43.23 kcal mol^{-1}, respectively, in all the functionals. The ΔE of complex II is approximately twice that of complex I. Further, we considered the prototype 1:1 host-guest complex P (Figure 3.2), the fragmented part of complexes I and II. The calculated ΔE of the complex P at the different levels of theory are provided in Table 3.2. Comparing the optimized interatomic bond distances calculated at the B3LYP-D3/6-311++G(d,p) level of theory, between the host and guest, in complexes I, II, and P, we observed that the distances are almost equivalent and are presented in Figure A10 of Appendix-A. We also observed that the ΔE value of 1:1 host-guest complexes of I and P are negligible differences (Table 3.1) and for the 1:2 complex II, it is almost equal to twice that of complex I. These results also revealed that the nature of the interactions between the host and guest within complexes I, II, and P is the same.

Table 3.1. Interaction energy (ΔE) of complexes I, II, and P with counterpoise corrections. All values are in kcal mol^{-1}.

Method	ΔE (I)	ΔE (II)	ΔE (P)
B3LYP-D3/6-311++G(d,p)	-21.65	-43.23	-21.45
PBE0-D3/6-311++G(d,p)	-21.27	-42.46	-21.08
TPSSTPSS-D3/6-311++G(d,p)	-20.64	-41.21	-20.41
M06-2X/6-311++G(d,p)	-19.42	-38.57	-19.03
B3LYP-D3/def2-TZVP	-20.92	-41.77	-20.89
PBE0-D3/def2-TZVP	-20.27	-40.47	-20.12
TPSSTPSS-D3/def2-TZVP	-19.65	-39.28	-19.49
M06-2X/def2-TZVP	-18.06	-36.05	-17.93
PBEh-3c/def2-mSVP	-20.74	-41.41	-20.61
B3LYP-D3BJ/6-311++G(d,p)	-21.51	-42.95	-21.30
PBE0-D3BJ/6-311++G(d,p)	-21.07	-42.12	-20.83
TPSSTPSS-D3BJ/6-311++G(d,p)	-20.30	-40.49	-20.04
DLPNO-CCSD(T)/CBS (def2-TZVPP/def2-QZVPP)			-21.49

To benchmark the, ΔE, we considered the complex P rather than complexes I and II, which have large numbers of atoms. We chose the optimized structures of complex P obtained from the B3LYP-D3/6-311++G(d,p) method and calculated the ΔE at the DLPNOCCSD(T)/(def2-TZVPP/def2-QZVPP) level of theory, considering the complete basis set (CBS) limit and counterpoise correction method. Comparing the interaction energy values of complex P (Table 3.1) evaluated from the DLPNO-CCSD(T) method and DFT functionals are found to be equal.

3.3.3. Extended Transition State-Natural Orbital Chemical Valence (ETS-NOCV) Analysis

To see the nature of interactions in detail between the host bbh and guest in complexes I, II, and P, we employed the ETS-NOCV scheme. In this method, the interaction energy (ΔE_{int}) between the two fragments is decomposed into electrostatic (ΔE_{elst}) interaction, Pauli repulsion (ΔE_{Pauli}), orbital (ΔE_{orb}) interaction and dispersion (ΔE_{disp}) interaction energies. The total interaction energy is given in Eq. 3.3. The result of ETS-NOCV analysis calculated at the BP86-D3(BJ)/TZ2P (utilizing optimized geometries calculated at the B3LYP-D3/6-311++G(d,p) method) level of theory for complexes I, II, and P are presented in Table 3.2. For the ETS-NOCV calculation of complex II, we have approximated as Type 1 [fragA (resorcinol): fragB (bbh: resorcinol)] and Type 2 [fragA (resorcinol:bbh): fragB (resorcinol)].

$$\Delta E_{int} = \Delta E_{elst} + \Delta E_{Pauli} + \Delta E_{orb} + \Delta E_{disp} \quad (3.3)$$

Table 3.2. ETS-NOCV results in the decomposition of total interaction energy (ΔE_{int}) into electrostatic (ΔE_{elst}) interaction, Pauli repulsion (ΔE_{Pauli}), orbital (ΔE_{orb}) interaction, and dispersion (ΔE_{disp}) interaction. The energy values are in kcal mol^{-1}.

Complex	ΔE_{elst}	ΔE_{Pauli}	ΔE_{orb}	ΔE_{disp}	ΔE_{int}
I	-29.18	32.27	-15.77	-10.98	-23.71
II (Type 1)	-29.08	32.21	-15.72	-10.98	-23.56
II (Type 2)	-29.08	32.21	-15.72	-10.98	-23.56
P	-28.96	32.03	-15.81	-10.97	-23.70

From Table 3.2, we observed that electrostatic interaction (ΔE_{elst}) energy is one of the most significant terms contributing to the interaction energy for stabilizing the complex. Further, it is followed by orbital (ΔE_{orb}) interaction and dispersion (ΔE_{disp}) term. Representation of the first three deformation densities contour plots, $\Delta\rho_1$, $\Delta\rho_2$, and $\Delta\rho_3$ and their corresponding energy contributions $\Delta E_1(orb)$, $\Delta E_2(orb)$, and $\Delta E_3(orb)$ of complex P are depicted in Figure 3.6. And complexes I and II are presented in Figure A11 of Appendix-A.

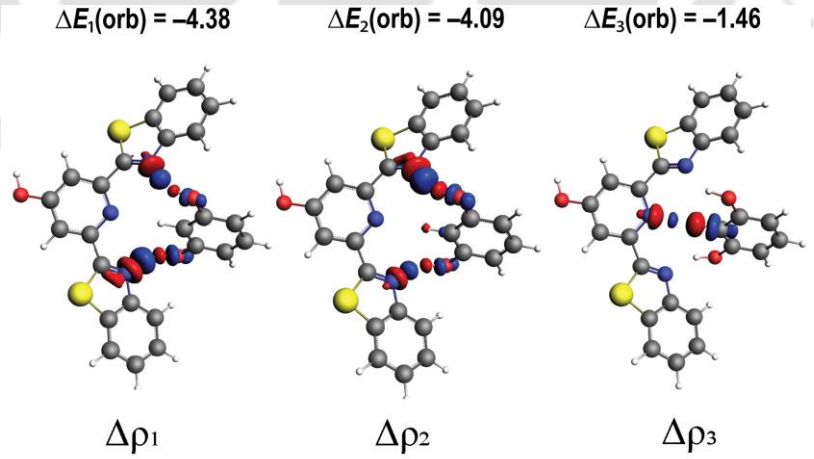

Figure 3.6. Contour plots of the deformation densities describing the O-H···N ($\Delta\rho_1$), O-H···N ($\Delta\rho_2$), and C-H···N ($\Delta\rho_3$) hydrogen bonding interactions of complex P (contour value=0.001). Also showed their corresponding energy contributions [$\Delta E_1(orb)$, $\Delta E_2(orb)$, $\Delta E_3(orb)$] in kcal mol^{-1}.

In Figure 3.6, the deformation electron density ($\Delta\rho$) plots are presented to understand the symmetry and the direction of the charge flow. The three leading deformation densities components $\Delta\rho_1$, $\Delta\rho_2$, and $\Delta\rho_3$ and their corresponding associated energy contribution $\Delta E_1(orb)$, $\Delta E_2(orb)$, and $\Delta E_3(orb)$ of complex P, are also depicted in Figure 3.6. The deformation densities, $\Delta\rho$s, are portrayed in such a way that the red region marked the depletion ($\Delta\rho < 0$, outflow) of electron density on bond formation while the blue region represents the accumulation ($\Delta\rho > 0$, inflow) of electron density. In a simple way, the direction of the charge flow is red to blue. The deformation density ($\Delta\rho$) plots of complexes I and II are presented in Figure A11 of Appendix-A. Further, the deformation densities, $\Delta\rho_1$, $\Delta\rho_2$, and $\Delta\rho_3$, are the main components contributing to the host-guest bonding interaction in complex P. Similarly, we observed the same in complexes I and II, which are presented in Figure A11 of Appendix-A. In Figure 3.6, we can see that two O-H···N hydrogen bonding interactions in the complex P and their deformation densities $\Delta\rho_1$ and $\Delta\rho_2$ have almost equal amount of corresponding energy contribution $\Delta E_1(orb)$ = – 4.38 kcal mol^{-1} and $\Delta E_2(orb)$ = – 4.09 kcal mol^{-1}, respectively. Further, the hydrogen bonding C-H···N ($\Delta\rho_3$) interaction contributes to the stabilizing energy with $\Delta E_3(orb)$ = –1.46 kcal mol^{-1}.

3.3.4. Electrostatic Potential (ESP) Analysis

To envisage further insight, the interactions between the host bbh and the resorcinol molecule in complexes. The charge distribution on the van der Waals surface of the molecules has been calculated using the electrostatic potential (ESP) method. Through this method, the properties like reaction sites on the molecular surface, electrostatic interactions among the molecules between the electron-rich and electron-deficient sites, etc., can be predicted. The 3D ESP maps of the host bbh, the guest resorcinol molecule, and their complexes I and II are shown in Figure 3.7. Observing the ESP values of bbh and resorcinol, we found that the bbh molecule has two maximum electrostatic potentials ($V_{S1,max}$ and $V_{S2,max}$) of equal values 28.12 kcal mol^{-1} that lies around the H atoms (Figure 3.7). However, the two minimum electrostatic potentials ($V_{S1,min}$ and $V_{S2,min}$) of equal values -55.56 kcal mol^{-1}, located near the N atoms binding sites of bbh. On the other hand, for the resorcinol guest molecule, the two maximum ESP values ($V_{S1,max}$ and $V_{S2,max}$) of equal values 53.62 kcal mol^{-1} were found near the hydrogen atom of the O-H groups. In contrast, the minimum ESPs values ($V_{S1,min}$ and $V_{S2,min}$) with an equal value of -25.55 kcal mol^{-1} are located around the O atoms. Hunter and co-workers [98] pointed out that the more negative ESPs value on the molecular surface acts as a better hydrogen

acceptor. A higher positive ESP value has better hydrogen donor abilities. Therefore, the nitrogen atom located at the region of the host molecule, which has the most negative ESP value, will interact with the O-H group region of the resorcinol molecule with the maximum ESP values.

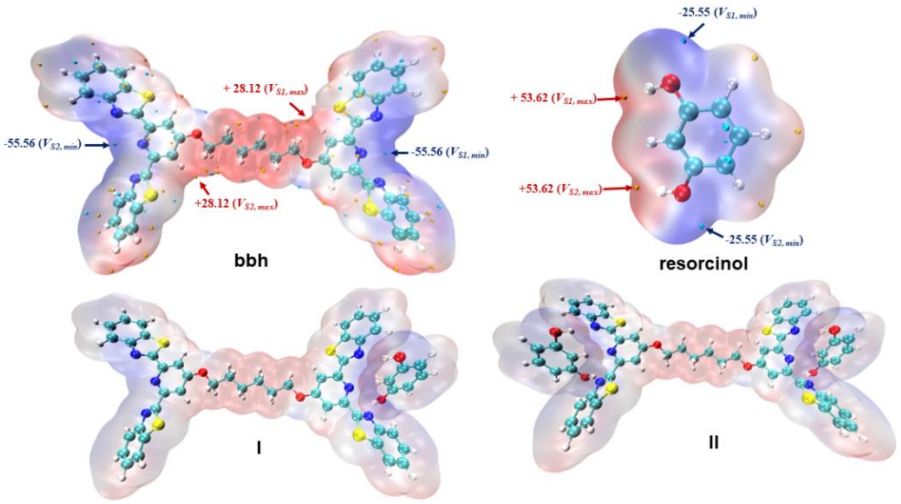

Figure 3.7. Molecular electrostatic potential values on the van der Waals surface of host bbh, resorcinol, and complexes I and II calculated at the B3LYP-D3/6-311++G(d,p) level of theory. Minima and maxima potentials are represented by cyan and orange, respectively. Blue and red regions on the molecular surface indicate the negative and positive electrostatic potentials regions, respectively. $V_{S1,max}$ and $V_{S2,max}$ represent the two maximum electrostatic potentials, while $V_{S1,min}$ and $V_{S2,min}$ represent the two minimum electrostatic potentials (units in kcal mol^{-1}).

3.3.5. Quantum Theory of Atoms in Molecules (QTAIM) Analysis

To understand the nature of intermolecular interactions present in the host-guest complexes, the quantum theory of atoms in molecules (QTAIM) analysis proposed by Bader[103] was employed. This theory is widely used to characterize the weak interactions between the interacting atoms. This method analyses the wavefunction to find the bond critical point (bcp), which gives the characteristic topological parameters between the interacting atoms. Electron density $\rho(r)$, Laplacian of electron density $\nabla^2\rho(r)$, energy density $H(r)$, Lagrangian kinetic energy $G(r)$, potential energy density, $V(r)$, etc., are the main topological parameters used to identify the nature of interactions between the interacting atoms. For the shared covalent bond interactions, the electron density $\rho(r)$ is large and $\nabla^2\rho(r) < 0$, whereas for the noncovalent

hydrogen bond and ionic bond for the closed-shell shared systems, the value of $\nabla^2\rho(r)$> 0 is positive, and $\rho(r)$ is relatively low. [103,107,108] In Cremer and Kraka's calculations,[109] they obtained a positive value of $\nabla^2\rho(r)$ for the covalent bond, which leads to an imperfect conclusion for classifying the types of interactions. They proposed to include the parameters $G(r)$ and $V(r)$ to interpret the nature of noncovalent and covalent interactions. The relation among $G(r)$, $V(r)$, $\nabla^2\rho(r)$, and to obtain $H(r)$ are given in Eqns. 3.4 and 3.5.

$$\frac{1}{4}\nabla^2\rho(r) = 2G(r) + V(r) \tag{3.4}$$

$$H(r) = G(r) + V(r) \tag{3.5}$$

Espinosa et al.[110] proposed and classified the interactions according to the $|V(r)|/G(r)$ ratio value. When $|V(r)|/G(r)$<1, then there are closed-shell interactions, $|V(r)|/G(r)$ > 2, represents the shared shell type of interactions, and if the $|V(r)|/G(r)$ values are observed between 1 and 2, then the interactions are partially covalent and electrostatic. Closed-shell interactions include noncovalent, ionic, and van der Waals, and shared-shell interactions define covalent bond interactions.

The atom interaction path and electron density $\rho(r)$ value at bcps of complexes I and II are presented in Figure 3.8. At the same time, the remaining topological parameter values are also provided in Table A7, Figure A12 and Table A8, Figure A13 of Appendix-A. From Figure 3.8, we observed that complexes I and II have similar nature of hydrogen bonding interactions such as O-H···N, C H···N, and C-H···O between the host bbh and the guest resorcinol. Complexes I and II exhibit two and four O-H···N types of hydrogen bonding interactions. The electron density $\rho(r)$ and their corresponding $\nabla^2\rho(r)$ values at the bcps of this interaction for both complexes I and II have almost equal values of 0.02 au and 0.07 au, respectively. Apart from this interaction, there are also two each of C-H···N and C-H···O types of interactions present in complex I (Figure 3.8). Similarly, complex II has four each of the C-H···N and C-H···O types of hydrogen bonding interactions. All these interactions satisfied the hydrogen bonding criterion $\rho(r)$ in the range of 0.002-0.035 au, and their corresponding $\nabla^2\rho(r)$ in the range of 0.014-0.139 au, proposed by Koch and Popelier.[111] Among all the interactions, the O H···N interaction has a larger $\rho(r)$ value which results in strong interactions. Further, the interactions O-H···N, C-H···N, and C-H···O for both complexes I and II are classified based on the ratio of $|V(r)|/G(r)$. In all these interactions, the ratio $|V(r)|/G(r)$ is found to be less than one (0.78-0.93), indicating the existence of closed shell interactions.

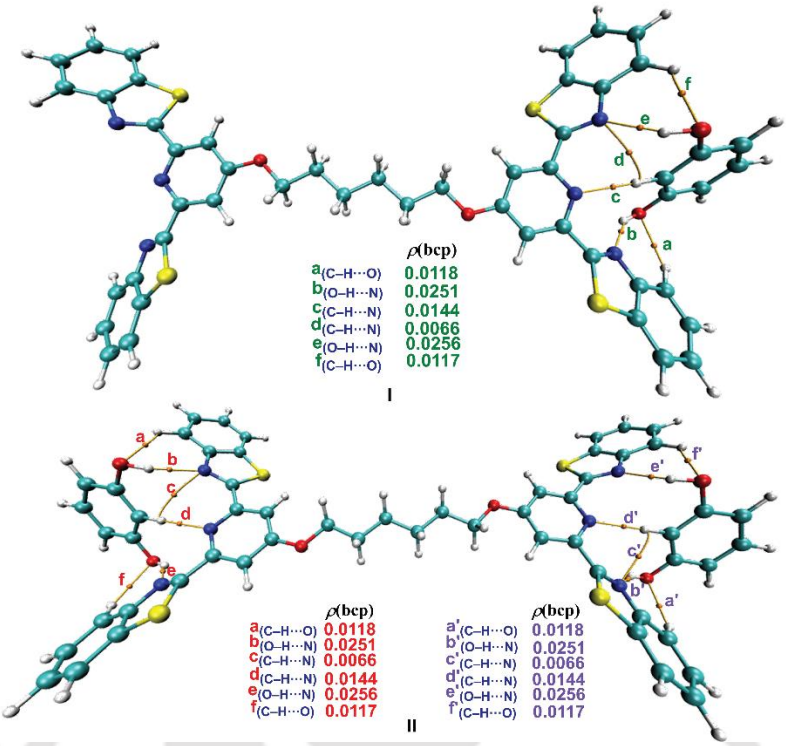

Figure 3.8. QTAIM topological analysis of complexes I and II showing atom interactions paths and electron density $\rho(r)$ [au] at bond critical point (bcp).

3.3.6. Natural Bond Orbital (NBO) Analysis

To probe the strength of interactions between the host and resorcinol guest molecule in complexes I and II, the NBO analysis was performed. This analysis measures the orbital interactions between the donor and acceptor orbitals and provides the second-order perturbation energies. The NBO results calculated at the B3LYP-D3/def2-TZVP level of theory for both complexes are provided in Table A9 of Appendix-A. In both complexes, the O-H···N hydrogen bonding interactions involved were between the donor nitrogen lone pair orbital of the host bbh and the corresponding antibonding orbital of the O H bond of the guest resorcinol molecule. Similarly, the hydrogen bonding C-H···N involved the interaction of nitrogen lone pairs orbital and antibonding orbital of the C-H bond.

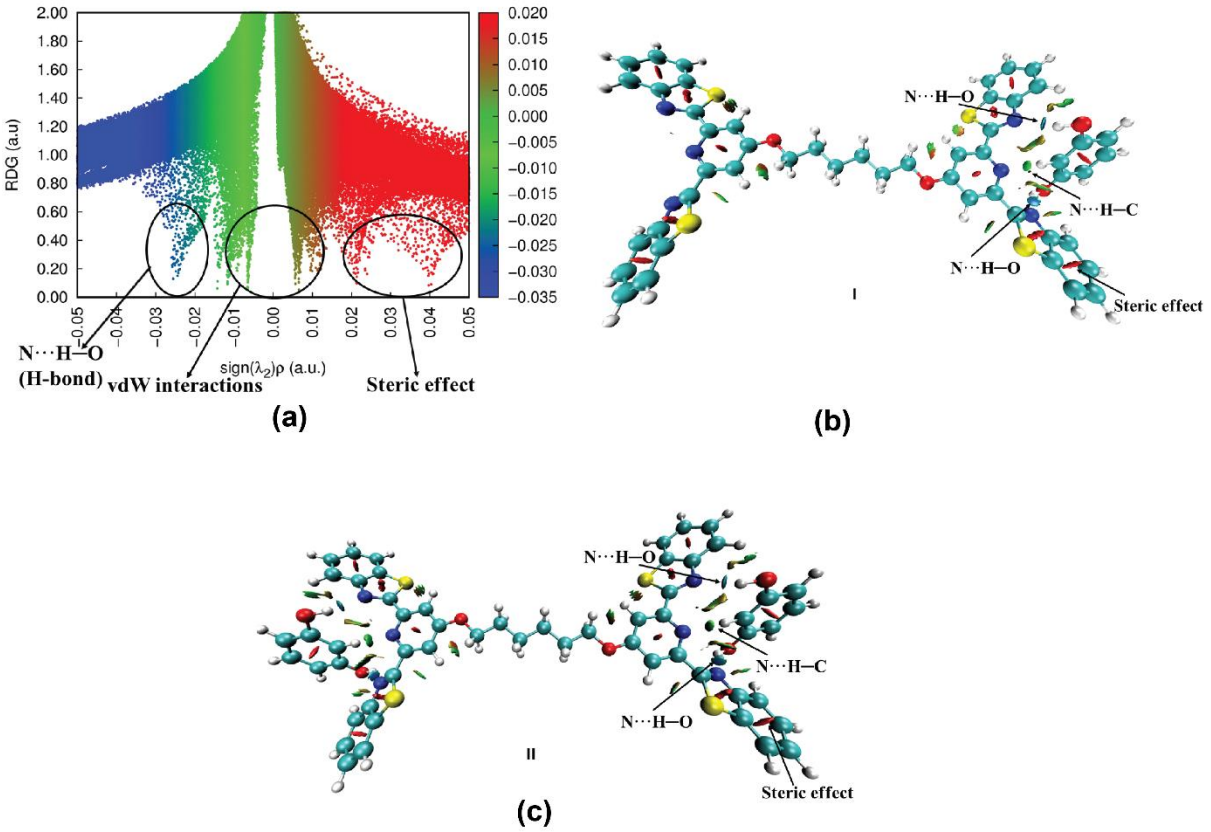

Figure 3.9. (a) RDG scatter plot for complex II. (b) and (c) represent RDG isosurface maps for complexes I and II.

3.3.7. Reduced Density Gradient (RDG) Analysis

The reduced density gradient (RDG) analysis proposed by Yang and co-workers[104] has been adopted to acquire information about the noncovalent interactions between the host and guest in both complexes I and II. The hydrogen bonding and other weak interactions can be predicted from the isosurface plot RDG versus $sign(\lambda_2)\rho(r)$. The expression for the RDG is defined as in Eq. 3.6.

$$\mathrm{RDG} = s = \frac{1}{2(3\pi^2)^{1/3}} \frac{|\nabla\rho|}{\rho^{4/3}} \tag{3.6}$$

In Eq. 3.6, $sign(\lambda_2)\rho$ denotes the product of the λ_2 and electron density $\rho(r)$, with λ_2 being the second eigenvalue of the Hessian matrix of electron density. Electron density $\rho(r)$ and $sign(\lambda_2)$ signify the interaction strength and the type of interactions involved, respectively. Since the RDG scattered plots of both complexes calculated at the B3LYP-D3/6-311++G(d,p) theoretical accuracy have similar intensities, we have presented here only for complex II. The isosurface maps (isovalue = 0.5) of complexes I and II are presented in Figure 3.9. It is evident from the RDG plot in Figure 3.9 that the presence of different colors region reflected the

existence of hydrogen bonding and other weak interactions in complexes I and II. Strong hydrogen bonding O-H···N interactions between the host-guest in both complexes I and II are supported by the existence of blue circular as shown in Figure 3.5. Meanwhile, the presence of the other weak hydrogen bonding interactions C H···N and C H···O is suggested from the appearance of the yellow-green colors in the isosurface maps. Further, the filled red color region presented in the middle of the aromatic rings represented the repulsive interactions (steric effect). Complexes I and II show similar nature of interactions when the bbh binds the resorcinol guest molecule.

3.4. Conclusions

In this Chapter, we have explored the conformational preferences of the host bbh. The S-N-S|S-N-S conformer is relatively more stable than the others. Torsional potential energy surfaces (PESs) scan and NCI analysis identified that the intramolecular hydrogen bonding interactions, C-H···N and C-H···S play a prominent role in stabilizing the conformer. However, these hydrogen-bonding interactions become non-existent through the rotation of the torsional angle that contains the C-C interring bond between the pyridine and benzothiazole rings of the conformers. The torsional barrier height of 8.22 kcal mol^{-1} and 9.23 kcal mol^{-1} were obtained for the B3LYP-D3/6-311++G(d,p) and the RI-MP2/ccpVTZ//B3LYP-D3/6-311++G(d,p) level of theory, respectively for the S-N-S|S-N-S conformer. In addition, for the N-N-N|N-N-N and N-N-S|S-N-N conformers, the barrier height is approximately around 10.0 kcal mol^{-1}.

Our computations considered different DFT functionals to obtain the interaction energies and the underlying nature of the noncovalent interactions between the N-N-N|N-N-N conformer of the host bbh and the guest resorcinol. The interaction energy, ΔE, of 1:1 host-guest formation in complexes I and P was equal. The DLPNO-CCSD(T) method was used to benchmark the interaction energy, ΔE, by considering the prototype complex P. Extended transition state-natural orbital chemical valence (ETS-NOCV) analysis revealed that the electrostatic interaction between the host bbh and the guest resorcinol is the main contribution to stabilized the interaction energy. The major component of electrostatic interactions in the interaction energy reflected the presence of intermolecular hydrogen bonding interactions O-H···N, C H···N, and C-H···O, in the host-guest complex. Further, the molecular electrostatic potential (MESP) surface analysis showed an interaction between the maximum electrostatic potential region of the resorcinol molecule that lies near the hydrogen atoms of the O-H groups. In contrast, the minimum potential region was observed in the nitrogen atoms of the host bbh.

The existence of intermolecular hydrogen bond interactions in all the complexes was confirmed from the analyses of NBO, AIM, RDG, and NCI studies. In summary, these computational studies provide important implications for designing new supramolecular host systems.

3.5. References

[1] J.-M. Lehn, *Science*, 1993, **260**, 1762.

[2] J.-M. Lehn, *Supramolecular Chemistry: Concepts and Perspectives*, Wiley-VCH, Weinheim, 1995.

[3] J. L. Atwood, J. W. Steed, *Supramol. Chem.*, John Wiley & Sons, 2009.

[4] H.-J. Schneider and A. Yatsimirsky, *Principles and Methods in Supramolecular Chemistry*, Wiley, Chichester, 2000.

[5] K. Ariga and T. Kunitake, *Supramolecular Chemistry-Fundamentals and Applications*, Springer, Berlin, 2006.

[6] J. W. Steed, D. R. Turner and K. J. Wallace, *Core Concepts in Supramolecular Chemistry and Nanochemistry*, Wiley, Chichester, 2007.

[7] P. Gale, J. Atwood and J. Steed, *Encyclopedia of Supramolecular Chemistry*, Marcel Dekker, New York, 2004.

[8] T. Schrader and A. D. Hamilton, *Functional Synthetic Receptors*, Wiley-VCH, Weinheim, 2006.

[9] H. Dodziuk, *Introduction to Supramolecular Chemistry*, Kluwer Academic Pub., Dordrecht 2002.

[10] K. E. Riley and P. Hobza, *Wiley Interdiscip. Rev.: Comput. Mol. Sci.*, 2011, **1**, 3.

[11] J. N. Israelachvili, *Intermolecular and Surface Forces*, Academic, San Diego, CA 2011.

[12] H.-J. Schneider, *Supramolecular systems in biomedical fields*, Royal Society of Chemistry, Cambridge, 2013.

[13] R. Breslow, *Highlights in bioorganic chemistry: methods and applications*, John Wiley & Sons 2006.

[14] H.-J. Schneider, *Applications of Supramolecular Chemistry*, Taylor & Francis, Boca Raton, 2012.

[15] J. W. Steed and P. A. Gale, *Supramolecular Chemistry: From molecules to Nanomaterials*, Wiley, Chichester, 2012.

[16] E. Persch, O. Dumele and F. Diederich, *Angew. Chem. Int. Ed.*, 2015, **54**, 3290.

[17] F. Biedermann and H. J. Schneider, *Chem. Rev.*, 2016, **116**, 5216.

[18] D. Xia, P. Wang, X. Ji, N. M. Khashab, J. L. Sessler and F. Huang, *Chem. Rev.*, 2020, **120**, 6070.

[19] J. Chen, Q. Peng, X. Peng, H. Zhang and H. Zeng, *Chem. Rev.*, 2022, **122**, 14594.

[20] H. Fenniri, P. Mathivanan, K. L. Vidale, D. M. Sherman, K. Hallenga, K. V. Wood and J. G. Stowell, *J. Am. Chem. Soc.*, 2001, **123**, 3854.

[21] D. H. Williams, E. Stephens, D. P. O'Brien and M. Zhou, *Angew. Chem. Int. Ed.* 2004, **43**, 6596.

[22] J.-M. Lehn, *Chem. Soc. Rev.*, 2007, **36**, 151.

[23] X. Tong, G. A. DiLabio, O. J. Clarkin and R. A. Wolkow, *Nano Lett.*, 2004, **4**, 357.

[24] S. E. Wheeler, T. J. Seguin, Y. Guan and A. C. Doney, *Acc. Chem. Res.*, 2016, **49**, 1061.

[25] R. R. Knowles and E. N. Jacobsen, *Proc. Natl. Acad. Sci. USA*, 2010, **107**, 20678.

[26] P. Zhou, J. Huang and F. Tian, *Curr. Med. Chem.*, 2012, **19**, 226.

[27] O. Keskin, N. Tuncbag and A. Gursoy, *Chem. Rev.*, 2016, **116**, 4884.

[28] C. J. Pedersen, *J. Am. Chem. Soc.*, 1967, **89**, 7017.

[34] W. Liu and J. F. Stoddart, *Chem.*, 2021, **7**, 919.

[35] G. Yu, K. Jie and F. Huang, *Chem. Rev.*, 2015, **115**, 7240.

[36] R. N. Dsouza, U. Pischel and W. M. Nau, *Chem. Rev.*, 2011, **111**, 7941.

[37] M. Sayed and H. Pal, *J. Mater. Chem. C*, 2016, **4**, 2685.

[38] A. Das, P. K. Mandal, F. J. Lovas, C. Medcraft, N. R. Walker and E. Arunan, *Angew. Chem. Int. Ed.*, 2018, **57**, 15199.

[39] J. A. Swain, G. Iadevaia and C. A. Hunter, *J. Am. Chem. Soc.*, 2018, **140**, 11526.

[40] D. Mani and E. Arunan, *ChemPhysChem*, 2013, **14**, 754.

[41] M. Khera and N. Goel, *ChemPhysChem*, 2022, **23**, e202100776.

[42] S. Ghosh and S. Wategaonkar, *J. Phys. Chem. A*, 2019, **123**, 385.

[43] S. Ghosh, P. Chopra and S. Wategaonkar, *Phys. Chem. Chem. Phys.*, 2020, **22**, 17482.

[44] P. Politzer, J. S. Murray and T. Clark, *J. Mol. Model.*, 2015, **21**, 1.

[45] T. Clark, J. S. Murray and P. Politzer, *Phys. Chem. Chem. Phys.*, 2018, **20**, 30076.

[46] J. S. Murray and P. Politzer, *J. Ind. Inst. Sci.* 2020, **100**, 21.

[47] P. Politzer and J. S. Murray, *ChemPhysChem*, 2020, **21**, 579.

[48] T. Chen, M. Li and J. Liu, *Cryst. Growth Des.*, 2018, **18**, 2765.

[49] J. C. Ma and D. A. Dougherty, *Chem. Rev.*, 1997, **97**, 1303.

[50] D. X. Wang and M. X. Wang, *J. Am. Chem. Soc.*, 2013, **135**, 892.

[51] J. Hermann, R. A. DiStasio Jr and A. Tkatchenko, *Chem. Rev.*, 2017, **117**, 4714.

[52] F. L. Aachmann, D. Otzen, K. L. Larsen and R. Wimmer, *Protein Eng. Des. Sel.*, 2003, **16**, 905.

[53] M. Sayed and H. Pal, *Phys. Chem. Chem. Phys.*, 2021, **23**, 26085.

[54] S.-R. Wang, Y. Y. Song, L. Wei, C. X. Liu, B.-S. Fu, J.-Q. Wang, X.-R. Yang, Y.-N. Liu, S.-M. Liu, T. Tian and X. Zhou, *J. Am. Chem. Soc.*, 2017, **139**, 16903.

[55] J. Rebek Jr, *Chem. Commun.*, 2000, 637.

[56] M. J. Webb, S. Deroo, C. V. Robinson and N. Bampos, *Chem. Commun.*, 2012, **48**, 9358.

[57] T. G. Levitskaia, J. C. Bryan, R. A. Sachleben, J. D. Lamb and B. A. Moyer, *J. Am. Chem. Soc.*, 2000, **122**, 554.

[58] Y. Wang, G. Ping and C. Li, *Chem. Commun.*, 2016, **52**, 9858.

[59] E. J. Dale, N. A. Vermeulen, M. Juricek, J. C. Barnes, R. M. Young, M. R. Wasielewski and J. F. Stoddart, *Acc. Chem. Res.*, 2016, **49**, 262.

[60] F.-G. Klarner and B. Kahlert, *Acc. Chem. Res.*, 2003, **36**, 919.

[61] P. W. Milligan and M. M. Haggblom, *Environ. Toxicol. Chem.*, 1998, **17**, 1456.

[62] R. L. Divi and D. R. Doerge, *Biochemistry*, 1994, **33**, 9668.

[63] B. S. Lynch, E. S. Delzell and D. H. Bechtel, *Regul. Toxicol. Pharmacol.*, 2002, **36**, 198.

[64] H. F. Stich, M. P. Rosin, C. H. Wu and W. D. Powrie, *Cancer Lett.*, 1981, **14**, 251.

[65] S. Yamaguchi, M. Hirose, S. Fukushima, R. Hasegawa and N. Ito, *Cancer Res.*, 1989, **49**, 6015.

[66] R. West and D. Stafford, *Leuk. Res.*, 1997, **21**, 675.

[67] B. Duran, S. Gursoy, M. Cetin, N. Demirkoprulu, Y. Demirel and B. Gurelik, *Clin. Toxicol.*, 2004, **42**, 663.

[68] R. Sijbesma, A. Kentgens, E. Lutz, J. Van der Maas and R. Nolte, *J. Am. Chem. Soc.*, 1993, **115**, 8999.

[69] R. J. Jansen, A. E. Rowan, H. W. Scheeren, R. J. Nolte and R. de Gelder, *Chem. Commun.*, 1998, 121.

[70] M. X. Wang, *Chem. Commun.*, 2008, 4541.

[71] D. N. Lande, S. A. Bhadane and S. P. Gejji, *J. Phys. Chem. A*, 2017, **121**, 1814.

[72] B. Chetia and P. K. Iyer, *Tetrahedron Lett.*, 2007, **48**, 47.

[73] P. J. Goutam and P. K. Iyer, *Sens. Actuators B*, 2015, **211**, 263.

[74] M. Boča, R. Boča, G. Kickelbick, W. Linert, I. Svoboda and H. Fuess, *Inorg. Chim. Acta*, 2002, **338**, 36.

[75] S. Grimme, J. Antony, S. Ehrlich and H. Krieg, *J. Chem. Phys.*, 2010, **132**, 154104.

[76] A. D. Beck, *J. Chem. Phys.*, 1993, **98**, 5648.

[77] N. E. Jackson, B. M. Savoie, K. L. Kohlstedt, M. Olvera de la Cruz, G. C. Schatz, L. X. Chen and M. A. Ratner, *J. Am. Chem. Soc.*, 2013, **135**, 10475.

[78] A. J. Cohen, P. Mori-Sanchez and W. Yang, *Science*, 2008, **321**, 792.

[79] A. J. Cohen, P. Mori-Sanchez and W. Yang, *Chem. Rev.*, 2012, **112**, 289.

[80] S. Kwasniewski, L. Claes, J. P. Francois, and M. Deleuze, *J. Chem. Phys.*, 2003, **118**, 7823.

[81] G. Raos, A. Famulari and V. Marcon, *Chem. Phys. Lett.*, 2003, **379**, 364.

[82] B. Mennucci, *Wiley Interdiscip. Rev.: Comput. Mol. Sci.*, 2012, **2**, 386.

[83] M. J. Frisch, G. W. Trucks, H. B. Schlegel, G. E. Scuseria, M. A. Robb, J. R. Cheeseman, G. Scalmani, V. Barone, G. A. Petersson, H. Nakatsuji, X. Li, M. Caricato, A. V. Marenich, J. Bloino, B. G. Janesko, R. Gomperts, B. Mennucci, H. P. Hratchian, J. V. Ortiz, A. F. Izmaylov, J. L. Sonnenberg, D. Williams-Young, F. Ding, F. Lipparini, F. Egidi, J. Goings, B. Peng, A. Petrone, T. Henderson, D. Ranasinghe, V. G. Zakrzewski, J. Gao, N. Rega, G. Zheng, W. Liang, M. Hada, M. Ehara, K. Toyota, R. Fukuda, J. Hasegawa, M. Ishida, T. Nakajima, Y. Honda, O. Kitao, H. Nakai, T. Vreven, K. Throssell, J. A. Montgomery, Jr., J. E. Peralta, F. Ogliaro, M. J. Bearpark, J. J. Heyd, E. N. Brothers, K. N. Kudin, V. N. Staroverov, T. A. Keith, R. Kobayashi, J. Normand, K. Raghavachari, A. P. Rendell, J. C. Burant, S. S. Iyengar, J. Tomasi, M. Cossi, J. M. Millam, M. Klene, C Adamo, R. Cammi, J. W. Ochterski, R. L. Martin, K. Morokuma, O. Farkas, J. B. Foresman and D. J. Fox, Gaussian, 16 Revision C.01, Gaussian Inc. Wallingford CT, 2016.

[84] F. Neese, *Wiley Interdiscip. Rev.: Comput. Mol. Sci.*, 2012, **2**, 73.

[85] F. Neese, *Wiley Interdiscip. Rev.: Comput. Mol. Sci.*, 2018, **8**, e1327.

[86] C. M. Breneman and K. B. Wiberg, *J. Comput. Chem.*, 1990, **11**, 361.

[87] S. Grimme, A. Hansen, J. G. Brandenburg and C. Bannwarth, *Chem. Rev.*, 2016, **116**, 5105.

[88] J. Tao, J. P. Perdew, V. N. Staroverov and G. E. Scuseria, *Phys. Rev. Lett.*, 2003, **91**, 146401.

[89] S. Grimme, S. Ehrlich and L. Goerigk, *J. Comput. Chem.*, 2011, **32**, 1456.

[90] J. Rezac and P. Hobza, *Chem. Rev.*, 2016, **116**, 5038.

[91] S. F. Boys and F. Bernardi, *Mol. Phys.*, 1970, **19**, 553.

[92] Y. Zhao and D. G. Truhlar, *Theor. Chem. Acc.*, 2008, **120**, 215.

[93] E. G. Hohenstein, S. T. Chill and C. D. Sherrill, *J. Chem. Theory Comput.*, 2008, **4**, 1996.

[94] S. Grimme, J. G. Brandenburg, C. Bannwarth and A. Hansen, *J. Chem. Phys.*, 2015, **143**, 054107.

[95] C. Riplinger and F. Neese, *J. Chem. Phys.*, 2013, **138**, 034106.

[96] M. P. Mitoraj, A. Michalak and T. Ziegler, *J. Chem. Theory Comput.*, 2009, **5**, 962.

[97] G. te Velde, F. M. Bickelhaupt, E. J. Baerends, C. Fonseca Guerra, S. J. A. van Gisbergen, J. G. Snijders and T. Ziegler, *J. Comput. Chem.*, 2001, **22**, 931.

[98] C. A. Hunter, *Angew. Chem. Int. Ed.*, 2004, **43**, 5310.

[99] C. B. Aakeroy, T. K. Wijethunga and J. Desper, *New J. Chem.*, 2015, **39**, 822.

[100] E. Espinosa, C. Lecomte, N. Ghermani, J. Devemy, M. Rohmer, M. Benard and E. Molins, *J. Am. Chem. Soc.*, 1996, **118**, 2501.

[101] J. S. Murray and P. Politzer, *Wiley Interdiscip. Rev.: Comput. Mol. Sci.*, 2017, **7**, e1326.

[102] J. P. Foster and F. Weinhold, *J. Am. Chem. Soc.*, 1980, **102**, 7211.

[103] R. F. W. Bader, *Chem. Rev.*, 1991, **91**, 893.

[104] E. R. Johnson, S. Keinan, P. Mori-Sanchez, J. Contreras-Garcia, A. J. Cohen and W. Yang, *J. Am. Chem. Soc.*, 2010, **132**, 6498.

[105] T. Lu and F. Chen, *J. Comput. Chem.*, 2012, **33**, 580.

Chapter 4

Exploring π−π Interactions and Electron Transport in Complexes Involving a Hexacationic Host and PAH Guest: A Promising Avenue for Molecular Devices

The work of this Chapter is published in *Phys. Chem. Chem. Phys.* 2023, **25**, 26767.

4.1. Introduction

π-π stacking, a typical form of noncovalent interaction between the aromatic groups, has been involved in various applications, including supramolecular chemistry,[1] chemical sensing,[2] material science[3,4] and molecular biology.[5] One important area of interest is electrical conductivity through π-π stacking interaction in synthetic molecular systems, which will be essential for constructing the building blocks of molecular electronic devices. In biological systems, electron charge transport occurs in π-π stacked DNA base pairs and aromatic amino acid residues.[6,7] Moreover, this electron transport process plays a key role in metabolism,[8] photosynthesis,[9] and repair of DNA damage.[10] On the other hand, the conductance measurement of synthetic molecular layers consisting of a paracyclophane scaffold[11,12] with spontaneous π-π stacking has highlighted the evidence of electron transport across two π-systems.[13,14] In extension to this, the electron charge transport in the supramolecular host–guest complex, which consists of π-stacked interactions, was also studied and the molecular electronic properties of the complex were tuned by accommodating different interesting guest molecules.[15,16] The scientific advent of molecular receptors or hosts based on the derivatives of cyclophane has tremendously increased and governed enormous interest in the scientific community owing to their wide range of applications, including catalysis,[17] molecular devices,[18] etc. These receptors have exhibited the ability to accommodate electron-rich polycyclic aromatic hydrocarbon (PAH) molecules.[19] They can be classified into first, second, and third dimensions. The first and second-dimension molecular receptors are generated from the $Ex^nBox_m^{4+}$, as shown in Figure 4.1a, and the third-dimension molecular receptors are

presented in Figure 4.1b, where n and m are variables that represent the different molecular units to modulate the length and width of the receptors.[20] Some of the possible molecular units of n and m have been reported in the literature. Stoddart and coworkers[19,21] experimentally characterized the complex formation between the receptors ($ExBox^{4+}$ and Ex^2Box^{4+}) and PAH molecules. Inside the cavity of the second dimension $ExBox_2^{4+}$, the sizeable spherical fullerene, C_{60}, embedded and a 1:1 inclusion complex ($C_{60}\subset ExBox_2^{4+}$) was obtained.[18] This complex undergoes self-assembly through solvophobic processes and yields one dimensional crystal arrays with a length span of millimetre size and shows electrical conductivity of 5.83×10^{-7} S cm^{-1}. In the absence of C_{60}, the average electrical conductivity of the $ExBox_2^{4+}$ crystal is $1.20 \pm 0.17 \times 10^{-9}$ S cm^{-1}.[18]

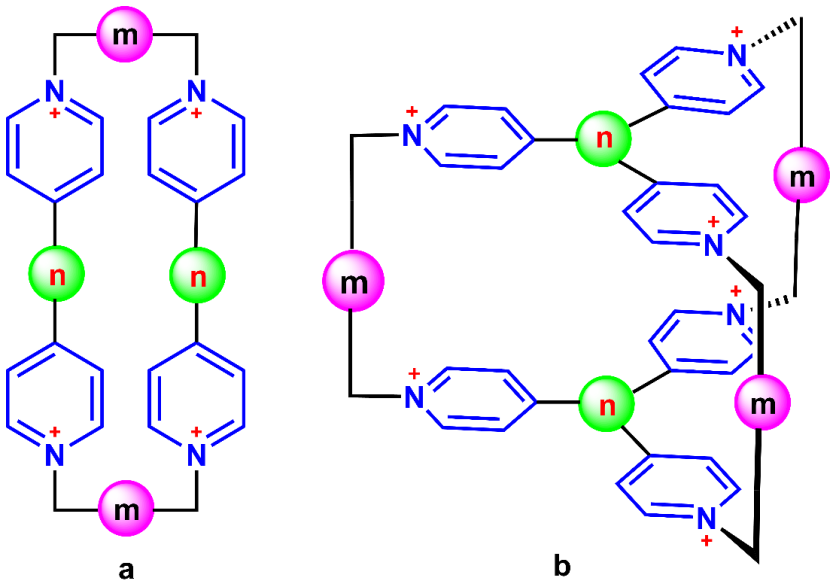

Figure 4.1. Molecular structures representing (a) one and two-dimensional, and (b) three-dimensional cyclophane derivative receptors. The m and n variables represent the molecular units to modulate the length and width of the receptor, respectively.

The arrangement of stacked aromatic molecules shows significant potential as a fundamental building block for developing molecular electronic devices. One of the promising approaches is integrating host–guest systems that are connected through noncovalent π-π interactions. Kiguchi et al. also highlighted the electron transport in the caged molecule, enclosed with a π-stacked aromatic molecule.[15,22] Tang et al. reported the host–guest complex (metallocycle-C_{60}) form between the organoplatinum (II) metallocycle host and fullerene (C_{60}) guest.[23] In addition, the host–guest system can further refine its electronic properties through the alteration of the guest molecule. In this approach, our focus is examining host–guest complexes that arise between the 3D cage like hexacationic host and different polycyclic aromatic hydrocarbon

(PAH) guests. The three-dimensional cage-like molecular receptors $Excage^{6+}$ and $AzaExcage^{6+}$were also reported in the literature.[24,25] Both receptors were electron-deficient and showed strong donor–acceptor interaction with PAH molecules. Recently, Zhang et al. reported the three-dimensional hexacationic cage receptor (H^{6+}) (Figure 4.2), which consists of two triscationic π-electron-deficient trispyridinium triazine (TPZ^{3+}) units and is connected in a face-to-face manner by bridging three ethylene-triazole-ethylene molecules.[26] In addition, the receptor (H^{6+}) formed 1: 1 inclusion complexes with PAH molecules (Figure 4.2), such as naphthalene, anthracene, triphenylene, phenanthrene, pyrene, corannulene, and perylene.

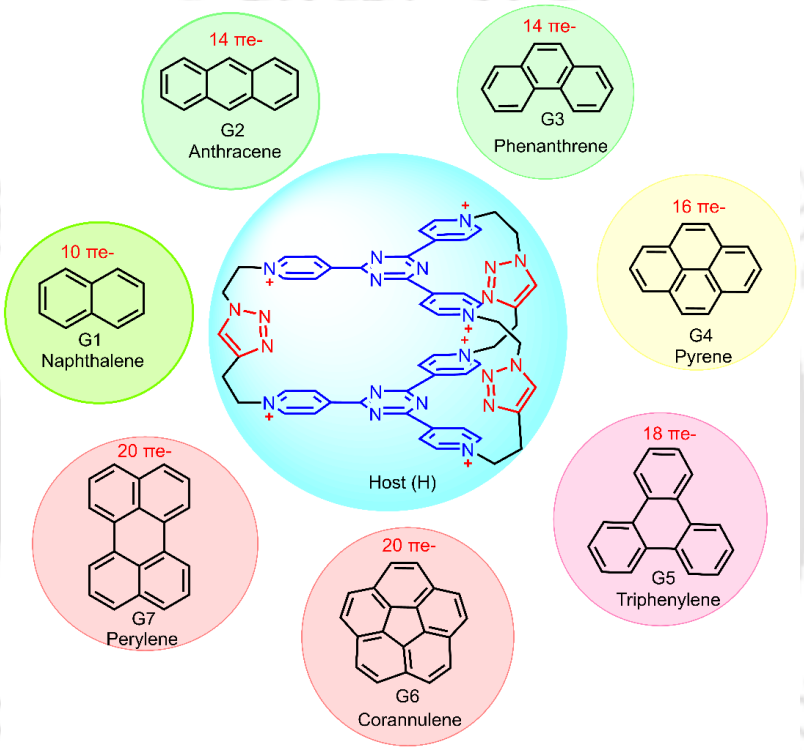

Figure 4.2. Molecular structures of the host (H) and guest (G) molecules: naphthalene (G1), anthracene (G2), phenanthrene (G3), pyrene (G4), triphenylene (G5), corannulene (G6), and perylene (G7).

Utilizing different methods of density functional theory (DFT), many groups have studied the properties such as electronic energy, geometries, modes of vibrations, the excitation energy of receptors $ExBox^{4+}$ and Ex^nBox^{4+}, and their 1:1 complex formation with electron-rich guests.[21,27–29] Nagurniak et al. reported the nature of interactions using noncovalent interaction (NCI) and energy decomposition analysis (EDA) approaches for the host–guest complexes formed between the $ExBox^{4+}$ and PAH molecules.[30] However, the theoretical findings devoted to studying the physical nature of interactions in the host-guest complex formed

between the three-dimensional cage-like receptor and π-electron-rich guest molecules are still limited to the best of our knowledge.

Herein, in this chapter we investigate the nature of interaction in the series of host–guest complexes generated between the hexacationic host (H^{6+}) and guests: naphthalene (G1), anthracene (G2), triphenylene (G3), phenanthrene (G4), pyrene (G5), corannulene (G6), and perylene (G7) (Figure 4.2) within the framework of quantum chemical approaches. At the same time, we have explored the conductance and electron transport properties in our considered host and host–guest complexes. Understanding the electron charge transport in connection with π-π interaction in such a supramolecular host–guest complex at the molecular level gives a new insight by providing essential information about the interaction strength, type of interaction, and junction conductance.

4.2. Computational Details

The molecular geometries of host–guest complexes G1⊂H to G5⊂H and G7⊂H were constructed according to the X-ray crystal structures reported by Zhang et al.[26] To perform the calculations uniformly, we considered the corannulene (G6) molecule encapsulated inside the host cavity (H). Geometry optimization of the host (H), guests (G1–G7), and host–guest complexes (G1⊂H to G7⊂H) applying appropriate charges (+6) was performed using the Grimme's composite functional PBEh-3c with the def2-mSVP basis set.[31] The functional PBEh-3c includes dispersion correction with Becke–Johnson damping (D3BJ) and also considers three-body dispersion interaction via the Axilrod–Teller–Muto (ATM) method and geometrical counterpoise corrections (gCP).[32–34] It has been extensively used for investigating noncovalent interactions such as π–π and hydrogen bonding in supramolecular host–guest systems (test sets S22[35] and S66[36]) consisting of small to large numbers of atoms.[37] It demonstrated sufficiency in elucidating the noncovalent interactions and yielded molecular structures with a close agreement with the reference structure.[31,37] Moreover, this functional shows excellent performance in predicting noncovalent interaction energies of the systems. As a result, we employed this functional for the preliminary investigation of our host-guest systems. The interaction energy, ΔE, of the complex was estimated by employing the supermolecular approach, as shown in Eq. 4.1,

$$\Delta E = E_{HG} - E_H - E_G \tag{4.1}$$

Where E_{HG}, E_H, and E_G are the energies of the host–guest, host, and guest, respectively. Subsequently, we have extended our investigation using the hybrid functional PBE0,[38] with

Grimme's dispersion correction (D3) along with the Becke–Johnson (BJ) damping function.[33,34] The basis set def2-TZVP developed by Ahlrichs and coworkers was implemented in our calculation.[39] The basis set superposition error (BSSE) was estimated by implementing the counterpoise correction (CP)[40] method. Earlier studies also reported the use of the PBE0-D3(BJ) method to explore the noncovalent interaction in host–guest systems.[41,42] Simultaneously, we noted consistency in prior literature where the computed HOMO–LUMO energy gap value, obtained through the PBE0 functional, exhibited favourable alignment with experimental findings.[43] So, we have incorporated this functional in our work and opted for the basis set def2-TZVP to balance the dependable interaction energy and computational cost of our host–guest complexes, which comprise a substantial number of atoms. We also noticed from the preceding literature that this basis set elucidates the noncovalent interactions.[41,44,45] Furthermore, the interaction energy, ΔE, was estimated using the domain based local pair natural orbital coupled cluster with single, double, and perturbative triple excitations [DLPNO-CCSD(T)][46–49] method in conjunction with the def2-TZVP basis set under the environment of TightSCF and NormalPNO setting. We performed the single-point energy calculation using the optimized geometries obtained from the PBE0-D3BJ/def2-TZVP level of theory.

Ab initio molecular dynamics (AIMD) simulations were performed to access the conformational stability of the host–guest complexes in the gas phase at the B97-3c[50] level of theory with the def2-mTZVP basis set. For all the complexes, the duration of the simulations run was set as 1000 fs with a time step of 0.5 fs under the Berendsen thermostat temperature of 298.15 K.

The PBEh-3c/def2-mSVP, DLPNO-CCSD(T)/def2-TZVP, and B97-3c/def2-mTZVP calculations (AIMD simulations) were performed using the ORCA 4.2.0 software package.[51] In addition, the calculations for the PBE0/def2-TZVP and BSSE error were performed in the Gaussian 16 package.[52]

To estimate the physical nature of the interaction between the host and guest in complexes G1⊂H to G7⊂H, we performed the energy decomposition analysis by implementing the extended transition-state natural orbitals for chemical valence (ETS-NOCV) scheme.[53] In this calculation, the BP86[54,55] functional proposed by Becke–Perdew, with Grimme's dispersion correction and the Becke–Johnson damping function (D3BJ) was employed. The basis set TZ2P was applied, and the calculation was performed in the ADF2021 program package.[56] In

the ETS-NOCV scheme, the total interaction energy, $\Delta E^{int}_{ETS-NOCV}$, between the two interacting fragments is partitioned into physically meaningful terms, as shown in Eq. 4.2,

$$\Delta E^{int}_{ETS-NOCV} = \Delta E^{elst} + \Delta E^{Pauli} + \Delta E^{orb} + \Delta E^{disp} \quad (4.2)$$

Where ΔE^{elst} represents the classical electrostatic interaction between the host and guest fragments. The Pauli repulsive interaction term, ΔE^{Pauli}, provides the repulsive interaction between electrons of the same spin in occupied orbitals of the fragments. The ΔE^{orb} term corresponds to the orbital interaction between occupied and unoccupied orbitals of the interacting fragments and accounts for the orbital interaction in the same fragments. Moreover, the dispersion interaction (ΔE^{disp}) term is obtained through the dispersion correction used in the functional BP86-D3BJ. For G7⊂H complex, the orbital interaction component, ΔE^{orb}, is decomposed into contribution ΔE_i^{orb} and the corresponding charge transfer channel can be described through the deformation densities ($\Delta\rho_i$).

To visualize the noncovalent interactions between the host and guest in the complexes, we performed NCI[57] analysis via calculating the reduced density gradient (RDG), which used electron density [$\rho(r)$] and its first derivatives [$\nabla\rho(r)$]. The reduced density gradient (RDG)[57] is defined in Eq. 4.3,

$$\mathrm{RDG} = s = \frac{1}{2(3\pi^2)^{1/3}} \frac{|\nabla\rho|}{\rho^{4/3}} \quad (4.3)$$

Where $\nabla\rho(r)$ represents the electron density gradient. To visualize the interactions, present in the complexes, the scatter plot is generated by employing the RDG versus electron density $\rho(r)$ multiplied by the sign of λ_2, which can be denoted as a sign(λ_2)$\rho(r)$, where λ_2 is the eigenvalue of the Hessian matrix of the electron density function. The term sign(λ_2)$\rho(r)$ distinguishes the attractive [sign(λ_2)$\rho(r) < 0$] and repulsive interactions [sign(λ_2)$\rho(r) > 0$]. The NCI analysis was performed using the Multiwfn program.[58] The images of the molecular structures were obtained using the UCSF Chimera 1.16 and VMD 1.9.3 software packages.[59,60] For generating the 3D NCI isosurface and AIMD molecular structures of the complexes, we employed VMD 1.9.3 software, while the 2D RDG scatter graphs were generated using the Gnuplot[61] package.

The transport properties of the optimized host and host–guest complexes were estimated using the TRANSIESTA program with the combination of the post-processing tool TBtrans.[62] The TRANSIESTA code incorporates the nonequilibrium Green's function (NEGF) and density

functional theory (DFT) formalism.[63] Using the Landauer–Büttiker formula (Eq. 4.4) the current flow through the systems was calculated.[64,65]

$$I(V_b) = G_0 \int_{\mu_L}^{\mu_R} T(E, V_b)[f(E-\mu_L) - f(E-\mu_R)]dE \quad (4.4)$$

Where $G_0 = 2e^2/h$ denotes the quantum conductance (e and h are charges of electron and Planck constant, respectively), and $T(E, V_b)$ is the transmission coefficient of electrons striking at energy (E) while subject to a potential bias (V_b). The Fermi distribution function is represented by $f(E)$. The chemical potential difference across left and right electrodes is represented by μ_L and μ_R. The GGA-PBE exchange–correlation functional and the single-zeta with polarization (SZP) basis sets[66] with an energy shift of 0.02 Ry was used to characterize the central scattering region in the DFT framework. The temperature has been set at 300 K with a 150 Ry energy cutoff for the current calculations. Furthermore, along the transmission path, a 32 k-point grid was considered.[63]

Furthermore, to calculate the density of states (DOS) of host–guest complexes G1⊂H and G7⊂H, the optimization was performed using the Quantum ESPRESSO software package[67] within the framework of DFT. The core electron was treated using the projected augmented wave (PAW) pseudo-potential, and the exchange–correlation term was approximated by the generalized gradient approximation (GGA) with the Perdew–Burke–Ernzerhof (GGA-PBE) functional.[38,68] A cut-off energy of 50 Ry and $5 \times 5 \times 1$ *k*-point was employed.[69,70]

4.3. Results and Discussion

4.3.1. Host–Guest Interaction Energies and Geometric Features

When the inclusion complexes were formed inside the host cavity (H), the PAH molecules G1–G5 and G7 were oriented in a parallel face-to-face geometry to the host's TPZ^{3+} units. Due to the non-planar geometry, the corannulene (G6) exhibits a bowl-shaped geometry, and the middle pentagon ring portion of corannulene exists in parallel relation to the middle triazine ring of the host. For the empty host (H), the calculated distance between the two centers of the triazine rings was found to be 7.8 Å (PBE0-D3BJ/def2-TZVP), as shown in Figure 4.3. When the PAH molecules were embedded inside the host cavity, a noticeable decrease in the distance between the centroids of the triazine rings was observed. The distance between the two centroids of the triazine rings of the host (H) in complexes G1⊂H to G5⊂H and G7⊂H were found to have approximately equal values of 7.0 Å. The complex G6CH incorporating corannulene as the guest has exhibited the centroid distance 7.4 Å. All the centroid distances

of complexes G1⊂H to G7⊂H calculated at the PBE0-D3BJ/def2-TZVP level of theory are presented in the Figure B1 of Appendix-B.

The inter-distances between the guest and triazine ring of the host (H) in all the complexes were in the range of 3.2–3.6 Å and are provided in the Figure B2 of Appendix-B. The corannulene formation complex G6⊂H shows the shortest host–guest distance. Our calculated host–guest distances in complexes G1⊂H to G5⊂H and G7⊂H were in line with the experimental distance (3.3 Å) reported by Zhang et al.[26]

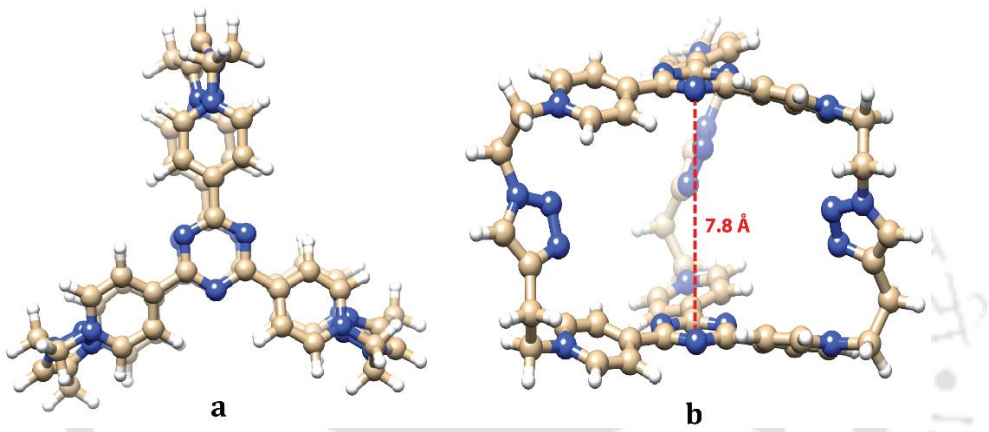

Figure 4.3. Optimized geometry of the host (H) calculated at the PBE0-D3BJ/def2-TZVP level of theory, (a) top view, and (b) side view of the host. The distance between two centroids of triazine rings is 7.8 Å.

To understand the strength of the host–guest interaction in complexes (G1⊂H to G7⊂H), the interaction energy, ΔE, was evaluated by employing two different DFT functionals, PBEh-3c and PBE0-D3BJ, with basis sets def2-mSVP and def2-TZVP, respectively. Using the optimized geometries obtained at the PBE0-D3BJ/def2-TZVP level of theory, we estimated ΔE at the DLPNO-CCSD(T)/def2-TZVP level of theory. The ΔE values of all the complexes are presented in Figure 4.4. Among the complexes, perylene inclusion complex G7⊂H shows the highest interaction energy value of 61.32 kcal mol^{-1}. On the other hand, the naphthalene inclusion complex G1⊂H has the least interaction energy value of 38.20 kcal mol^{-1}. Meanwhile, complexes G6⊂H and G7⊂H have the same π-electron guests corannulene and perylene, respectively, and were expected to have almost equal interaction energy values. However, it can be seen from Figure 4.4 that there is a large difference in the interaction energy value between the two complexes. The reason is likely due to the corannulene (G6) molecule-

oriented non-planar and bowl-shaped geometry inside the host cavity (H), which results in the improper π-π interaction with the TPZ^{3+} units of the host. On the other hand, perylene (G7) has a planar molecular structure and parallel relation to the TPZ^{3+} unit of the host (H) and can form efficient π-π interaction. Furthermore, we noticed a similar pattern of interaction energy values in the DLPNO-CCSD(T)/def2-TZVP level as obtained in the PBE0-D3BJ/def2-TZVP and PBEh-3c/def2-mSVP levels.

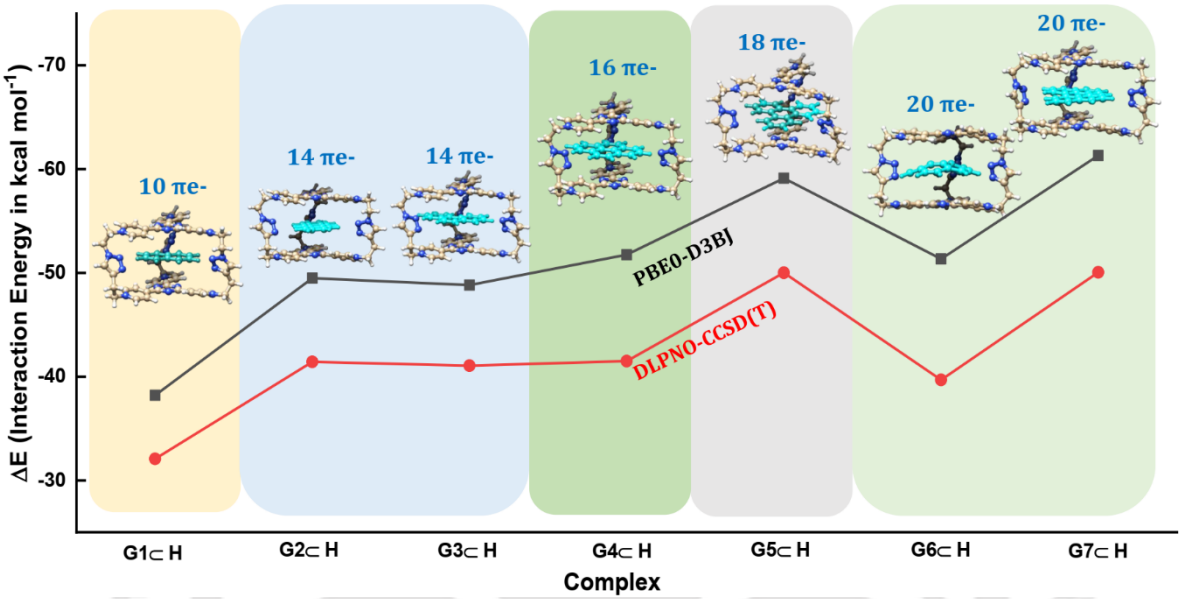

Figure 4.4. Interaction energy, ΔE , of host–guest complexes (G1⊂H to G7⊂H) calculated using the PBE0-D3BJ/def2-TZVP (black) and DLPNO-CCSD(T)/def2-TZVP//PBE0-D3BJ/def2-TZVP (red) levels of theory. Here the interaction energy considered at the PBE0-D3BJ/def2-TZVP level is BSSE corrected.

The distortion in the molecular geometry of the host (H) in complexes (G1⊂H to G7⊂H) was directly related to the strain energy, ΔE_{host}^{strain}, of the host. This energy was estimated by taking the energy difference between the optimized geometry of the host (H) and the geometry of the host acquired in the host–guest complex formation. Likewise, the strain energy of the guest, $\Delta E_{guest}^{strain}$, was also calculated. In extension, summing the strain energies of the host and guest generated the preparation energy, ΔE^{prep}, of the complex, presented in Table 4.1. Among all the host–guest complexes, G6⊂H shows the largest ΔE_{host}^{strain} value of 5.77 kcal mol^{-1} followed by the complex G7⊂H, which has a value of 5.61 kcal mol^{-1}. The remaining complexes displayed small strain energy, ΔE_{host}^{strain} values, ranging from 1.74 kcal mol^{-1} to

2.69 kcal mol^{-1}. In the case of guest structures, there were no significant changes in $\Delta E_{guest}^{strain}$ value.

Table 4.1. ΔE_{host}^{strain} and $\Delta E_{guest}^{strain}$ represent the host and guest strain energies, respectively, and ΔE^{prep} denotes the preparation energy in complexes (G1⊂H to G7⊂H) calculated at the PBE0-D3BJ/def2-TZVP level of theory. Here, $\Delta E^{prep} = \Delta E_{host}^{strain} + \Delta E_{guest}^{strain}$. The energy values are given in kcal mol^{-1}.

Complexes	ΔE_{host}^{strain}	$\Delta E_{guest}^{strain}$	ΔE^{prep}
1⊂H	1.86	0.09	1.95
2⊂H	2.56	0.16	2.72
3⊂H	2.22	0.19	2.41
4⊂H	2.69	0.23	2.92
5⊂H	1.74	0.23	1.97
6⊂H	5.77	0.68	6.45
7⊂H	5.61	0.19	5.8

4.3.2. Ab initio Molecular Dynamics Simulations

Ab initio molecular dynamics simulations, based on quantum mechanics, was performed to assay the stability of the complexes. In our computations, we employed DFT functional B97-3c with the def2-mTZVP basis set. The simulation was conducted for 1000 fs with a step size of 0.5 fs under the thermostat Berendsen temperature of 298.15 K for each complex. The potential and total energy vs. time variation for all the complexes were investigated. The energy variation plots for complex G7⊂H are presented in Figure 4.5, while the remaining complexes are provided in the Figure B3 to Figure B8 of Appendix-B. The molecular structure snapshots of the complex G7⊂H

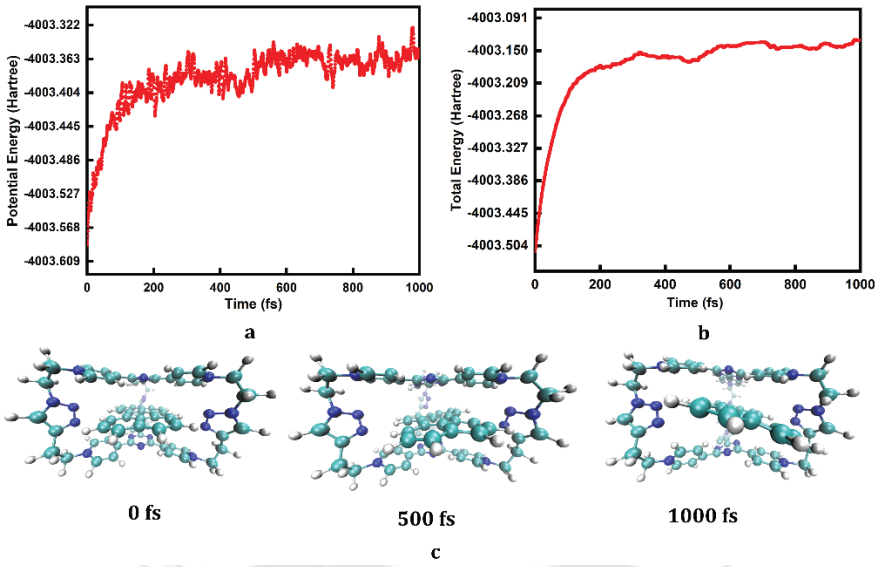

Figure 4.5. *Ab initio* molecular dynamics simulations of complex G7⊂H calculated at the B97-3c/def2-mTZVP level of theory. (a) potential energy versus time and (b) total energy versus time and (c) molecular snapshots of complex G7⊂H at 0, 500, and 1000 fs, respectively.

were collected at three different time steps, 0, 500, and 1000 fs, shown in Figure 4.5. From Figure 4.5c, within 500 fs, the guest perylene moves slightly away from the center of the host. At 1000 fs, some molecular region of the perylene is outside the host environment. In the case of the G1⊂H complex, the naphthalene guest remains inside the host cavity throughout the simulation period, and the molecular geometries at three different time steps are provided in the Figure B3 of Appendix-B. Within the 1000 fs, a certain portion of the anthracene molecule of the G2⊂H complex is slightly moving outside the host cage. The collected molecular structures of the G2⊂H complex at different times is shown in the Figure B4 of Appendix-B. On the other hand, the guests of complexes G3⊂H, G4⊂H, G5⊂H, and G6⊂H stayed within the cavity of the host.

4.3.3. Energy Decomposition Analysis

To map the overall energy contributions from the host–guest interactions in complexes G1⊂H to G7⊂H, we carried out ETS-NOCV analysis. Both host and guest fragments were considered in singlet electronic states. The interaction energy, $\Delta E^{int}_{ETS-NOCV}$, and their corresponding energy component values of the complexes are provided in Table 4.2. The $\Delta E^{int}_{ETS-NOCV}$ values become more negative when moving from G1⊂H to G7⊂H excluding G6⊂H. The highest and lowest, $\Delta E^{int}_{ETS-NOCV}$, values were found in complexes G7⊂H and G1⊂H, respectively. The $\Delta E^{int}_{ETS-NOCV}$ is partitioned into Pauli repulsion (ΔE^{Pauli}), electrostatic (ΔE^{elst}), orbital interaction (ΔE^{orb}), and dispersion interaction (ΔE^{disp}). From Table 4.2, it can be noted that

the stabilizing energies of the complexes were mainly contributed from the dispersion interaction term (ΔE^{disp}). It shared the majority of the contribution (55.7–61.6%), followed by electrostatic, ΔE^{elst} (25.5–29.4%), and orbital interaction term, ΔE^{orb} (12.7–16.4%). Interestingly, we observed that the dispersion term (ΔE^{disp}) increases from G1⊂H to G7⊂H. The complexes G1⊂H and G7⊂H have the least and highest contribution ΔE^{disp} of –38.60 kcal mol^{-1} and –68.87 kcal mol^{-1}, respectively. Although G6⊂H and G⊂CH have the same number of π-electron guests corannulene and perylene, respectively, the dispersion term (ΔE^{disp}) contributed in G7⊂H was larger than that of the G6⊂H. The reason may be due to the bowl-shaped geometry of corannulene, which could not properly interact with the TPZ^{3+} units of the host. Table 4.2 shows that complexes G7⊂H and G1⊂H have the largest and smallest orbital interaction energy (ΔE^{orb}) contribution. The ΔE^{orb} is comparatively less among the energy components. The ΔE^{orb} value ranges from –8.04 to –20.16 kcal mol^{-1}.

Table 4.2. ETS-NOCV analysis of host-guest complexes (G1⊂H to G7⊂H) calculated at the BP86-D3BJ/TZ2P level of theory. Energy values are in kcal mol^{-1}.

	1⊂H	2⊂H	3⊂H	4⊂H	5⊂H	6⊂H	7⊂H
$\Delta E^{int}_{ETS-NOCV}$	-40.66	-54.38	-52.58	-56.06	-62.86	-59.70	-71.76
ΔE^{Pauli}	21.99	32.67	30.17	45.14	35.32	55.70	50.90
ΔE^{elst}	-16.00 (25.5 %)	-23.19 (26.6 %)	-21.98 (26.5 %)	-28.7 (28.3%)	-26.55 (27.0 %)	-33.99 (29.4 %)	-33.63 (27.4 %)
ΔE^{orb}	-8.04 (12.8 %)	-14.04 (16.1 %)	-11.48 (13.8 %)	-14.44 (14.2 %)	-12.52 (12.7 %)	-17.07 (14.7 %)	-20.16 (16.4 %)
ΔE^{disp}	-38.60 (61.6%)	-49.81 (57.2%)	-49.30 (59.5%)	-58.05 (57.3%)	-59.11 (60.2%)	-64.34 (55.7%)	-68.87 (56.1%)

In Figure 4.6, the deformation electron density ($\Delta\rho$) plots of the complex G7⊂H are presented to understand the symmetry and the direction of the charge flow. We obtained the five leading deformation density components in which $\Delta\rho_1(\pi)$, $\Delta\rho_2(\pi)$, and $\Delta\rho_3(\pi)$ are π–type interactions, and their corresponding associated orbital interaction energy contributions are $\Delta E_1(orb)$ = –2.60 kcal mol^{-1}, $\Delta E_2(orb)$ = –1.49 kcal mol^{-1}, and $\Delta E_3(orb)$ = –1.40 kcal mol^{-1}, respectively. On the other hand, $\Delta\rho_4(\sigma)$ and $\Delta\rho_5(\sigma)$ are σ-type interactions, and their corresponding orbital interaction energy contributions are $\Delta E_4(orb)$ = –1.48 kcal mol^{-1} and

$\Delta E_5(orb)$ = −1.00 kcal mol^{-1}, respectively. The deformation densities ($\Delta\rho$) are portrayed in such a way that the red region marked the depletion ($\Delta\rho < 0$, outflow) of electron density while the blue region represents the accumulation ($\Delta\rho > 0$, inflow) of electron density.

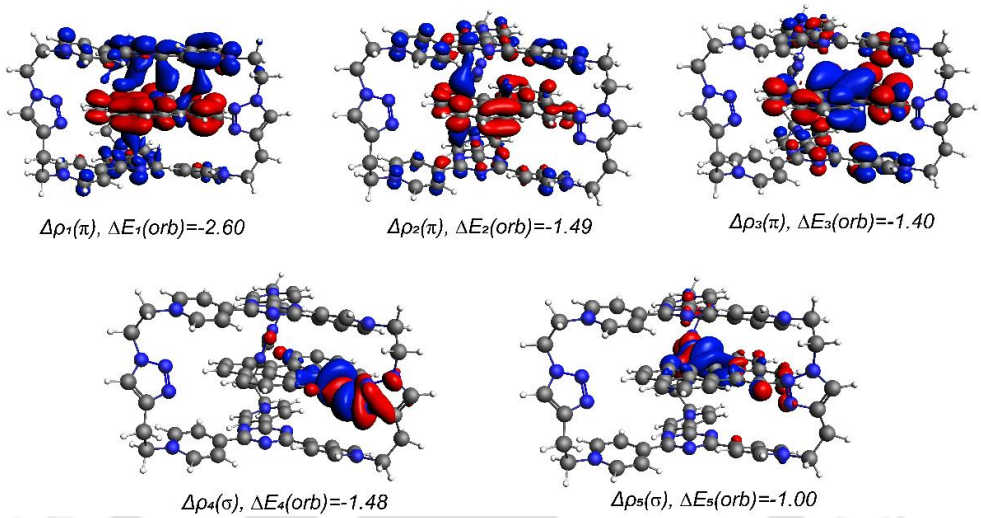

Figure 4.6. The contour of deformation density contributions $\Delta\rho_1(\pi)$, $\Delta\rho_2(\pi)$, $\Delta\rho_3(\pi)$, $\Delta\rho_4(\sigma)$, and $\Delta\rho_5(\sigma)$ between host and guest in complex G7⊂H. $\Delta E_1(orb)$ to $\Delta E_5(orb)$ (kcal mol^{-1}) represent the corresponding orbital interaction energy. The contour value used to visualize the deformation densities is 0.0001 au. Red and blue isosurface regions indicate the density of outflow and inflow, respectively.

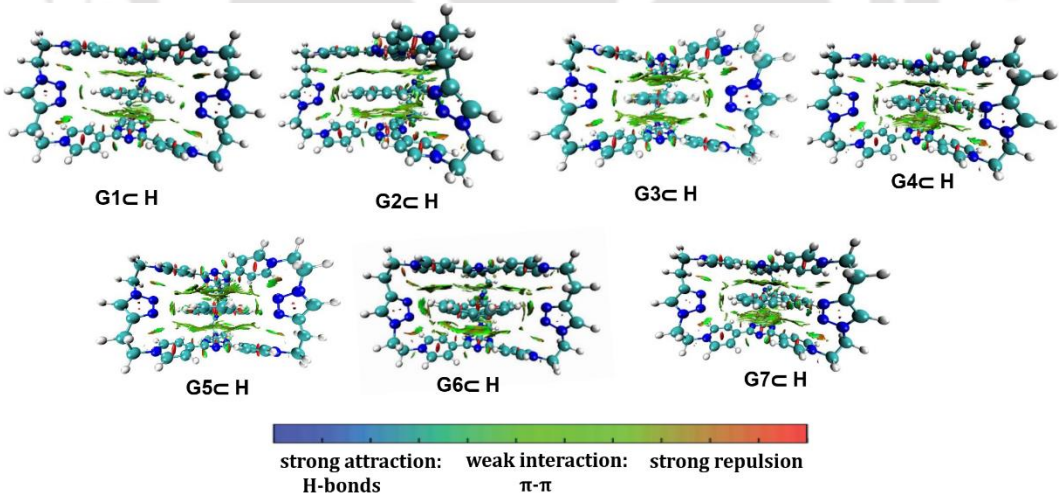

Figure 4.7. NCI isosurface showing the noncovalent interactions in host–guest complexes (G1⊂H to G7⊂H).

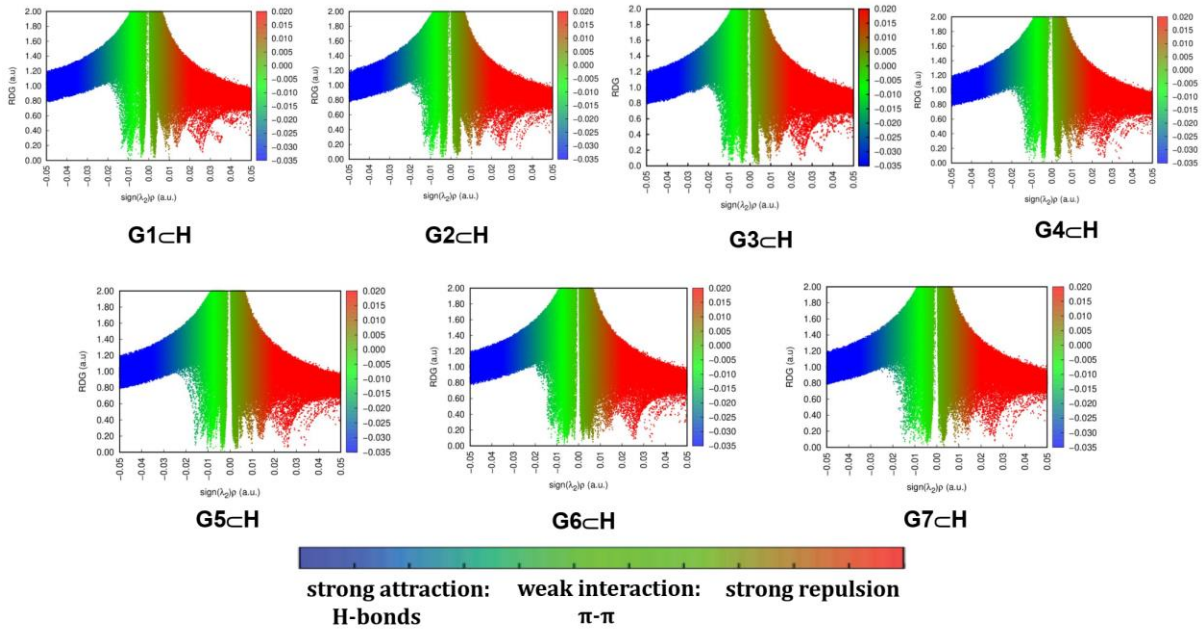

Figure 4.8. RDG scatter plots depicting the noncovalent interactions in host–guest complexes (G1⊂H to G7⊂H).

4.3.4. Noncovalent Interaction (NCI), HOMO–LUMO Gap and Density of States (DOS) Analysis

To probe the nature of noncovalent interactions between the host and guest in complexes G1⊂H to G7⊂H, we implemented the NCI-RDG[57] method based on electron density redistribution. Figures 4.7 and 4.8 depict 3D isosurface maps and 2D scatter plots of the complexes. As seen in Figure 4.7, the region green sheetlike extended surface between the guest and TPZ^{3+} units of the host revealed the existence of π-π van der Waals interaction. Furthermore, the π-π interaction region is correlated with the spike marked in the scatter plot of Figure 4.8, and the electron density at this spike region is low and close to zero.

The frontier molecular orbitals of the host (H) and complexes (G1⊂H to G7⊂H) were extracted utilizing the PBE0-D3BJ/def2-TZVP level of theory. Figure 4.9 illustrates the HOMO and LUMO and their energy gap ($\Delta E_{HOMO-LUMO}$) of the host and complexes. In the case of the empty host (H) system, the HOMO resides on the triazole rings, while the LUMO is localized on the TPZ^{3+} unit. The empty host's calculated $\Delta E_{HOMO-LUMO}$ of the host was found to be 3.32 eV. However, $\Delta E_{HOMO-LUMO}$ was reduced when the guest molecules (G1–G7) were embedded inside the host cavity and formed complexes. Furthermore, the HOMO was concentrated on the electron-rich guest, while the LUMO was located on the host in the complex. In the naphthalene inclusion complex (G1⊂H), the energy gap ($\Delta E_{HOMO-LUMO}$) was

found to be 2.88 eV which is greater than that of the perylene inclusion complex (G7⊂H) and has a value of 1.9 eV, since naphthalene has a lower number of p electrons than perylene, resulting in the lowering of the HOMO energy level in the G1⊂H complex. We also observed that the calculated LUMO energy level of the host increased by 0.11 eV when it formed a pyrene complex (G4⊂H). These changes in the energy level correlate with the cyclic voltammetry experimental result (0.095 eV) reported by Zhang et al.[26] Moreover, our calculated $\Delta E_{HOMO-LUMO}$ of complexes G1⊂H to G5⊂H and G7⊂H follows similar trends to the UV-vis charge transfer (CT) absorption band centered λ_{max} obtained in the literature.[26] The experimental studies showed that, among all the complexes, the G7⊂H complex exhibited a CT band centered at the longer wavelength region supporting our calculated smallest $\Delta E_{HOMO-LUMO}$ of the G7⊂H complex.

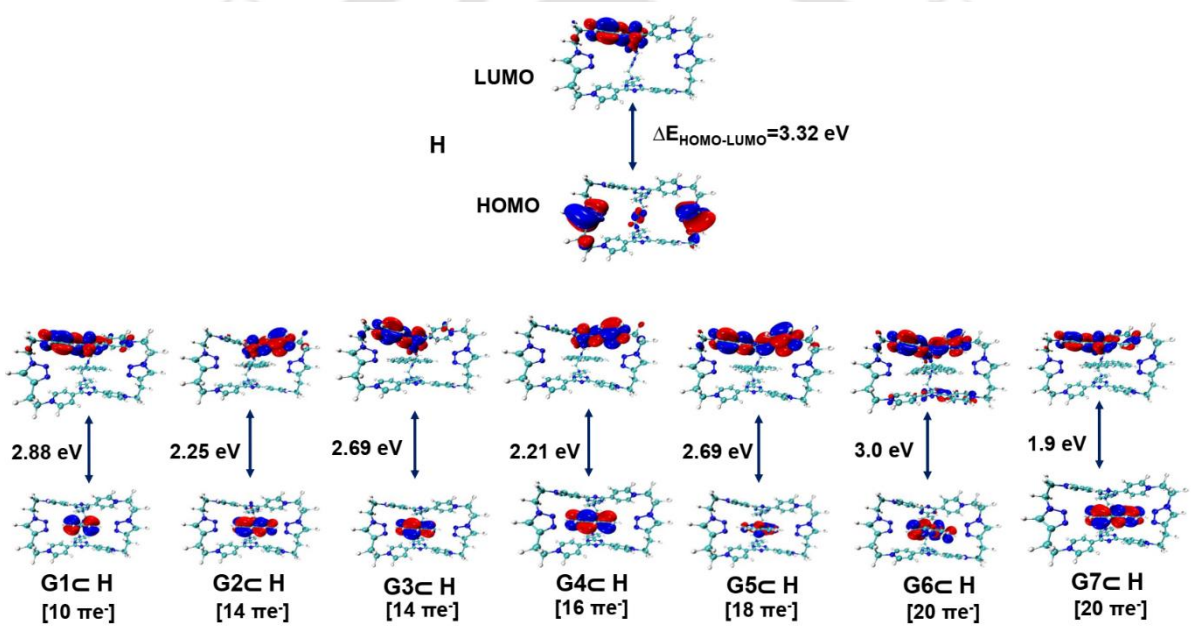

Figure 4.9. Frontier molecular orbitals along with the HOMO–LUMO energy gap ($\Delta E_{HOMO-LUMO}$) of the empty host (H) and host–guest complexes G1⊂H to G7⊂H obtained using the PBE0-D3BJ/def2-TZVP level of theory.

The process of orbital mixing plays a pivotal role in elucidating the nature of the interaction between the host and guest molecules. At the same time, this orbital hybridization will affect how the system's conductivity varies.[71] To better understand the orbital overlapping of the host–guest interaction, the density of states (DOS) was calculated for complexes G1⊂H and G7⊂H, which have a minimum and maximum number of π-electron guests, respectively. The DOS of the G1⊂H shows no observable hybridizing states near the Fermi level (E_F), as depicted in Figure 4.10a. The localization of orbital mixings of the host and guest (G1) predominantly occurs at energy levels below 2.0 eV in the valence bands (VBs) and above 1.0

eV in the conduction bands (CBs). This feature is characterized by a weaker interaction between the host (H) and guest G1 molecules, resulting in minimal impact on the electronic properties of the complex (G1⊂H). On the contrary, the notable orbital hybridizations between the host and the guest molecule (G7) exhibit localization mostly near the Fermi level, Figure 4.10b. This indicates that the host–guest interaction is more prominent and, hence, has a significant impact on the electrical characteristics of the complex.

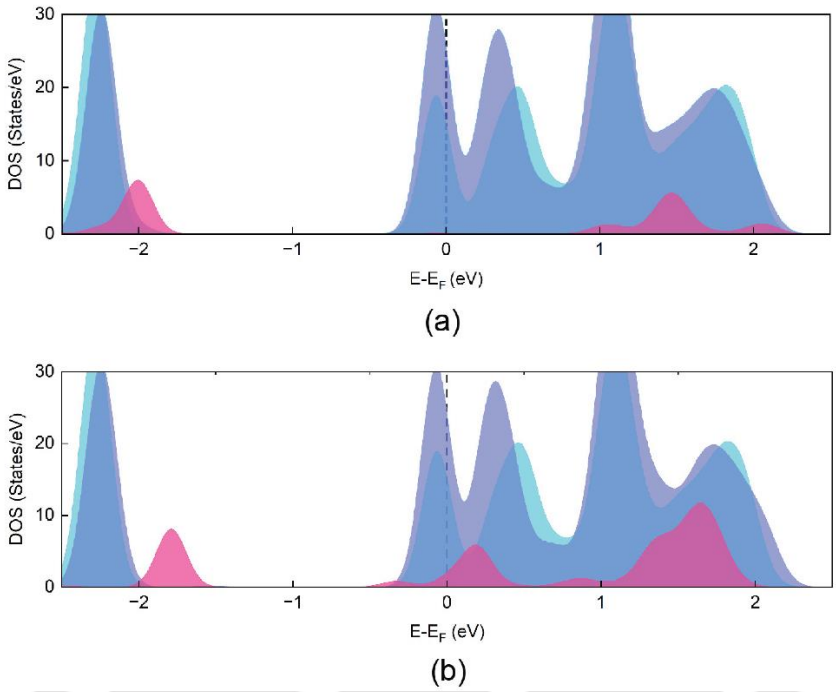

Figure 4.10. Density of states (DOS) plots of (a) G1⊂H (guest with the lowest number of π-electrons) and (b) G7⊂H (guest with the highest number of π-electrons) systems. Cyan, purple, and pink regions indicate the DOS of the host, the host after encapsulation of the guest and the guest, respectively.

4.3.5. Conductance Measurements of the Host–Guest Complexes

Gaining insight into the variations in conductance that occur when various polycyclic aromatic hydrocarbon (PAH) molecules are incorporated within the host cavity is crucial for further developing molecular devices and sensors. In this perspective, we performed a current–voltage (*I-V*) calculation having an identical contacting geometry to compare the transport properties of the host (H) and host–guest complexes (G1⊂H to G7⊂H). The transport device model was implemented in the analysis, and it is divided into three sections: the left electrode, the scattering zone, and the right electrode.[14] The central scattering area includes the host–guest complexes, and both electrodes comprised Au (111).[14]

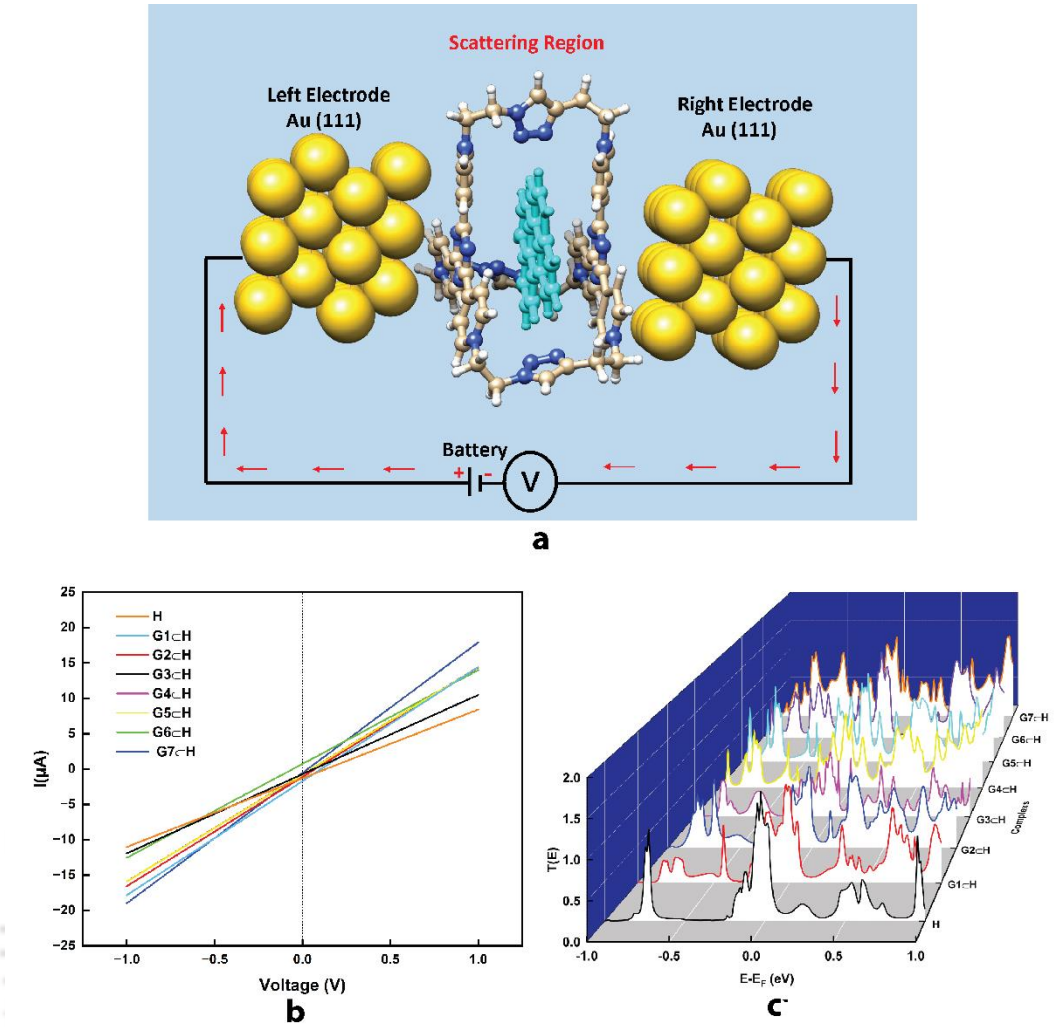

Figure 4.11. (a) A schematic diagram of the modelled host–guest system sandwiched between two Au (111) electrodes. (b) Linear fitting current–voltage (*I-V*) characteristics plots of the host (H) and host–guest complexes (G1⊂H to G7⊂H). (c) Zero-bias transmission spectra of the host (H) and host–guest complexes G1⊂H to G7⊂H.

Figure 4.11a depicts the model diagram of the host–guest system of our interest, which is sandwiched between two Au (111) electrodes. The left and right electrodes of Au-atoms are attached to the N-atoms of the centroid triazine rings at a distance ≥ 3.10 Å. The simulation configuration illustrates a weak-coupling region in which the complex and electrode orbitals are sufficiently separated to eliminate the interfacial states caused by direct interaction and hybridization of the complex and electrode orbitals.[72] The earlier study indicates that the conductance remains stable despite changes in contact configuration.[67] In our work, we considered only one interaction configuration.

In Figure 4.11b, we have illustrated the computed linear fitting current–voltage (*I-V*) characteristics plot of the host and host–guest junctions at a bias from 1.0 to +1.0 V [unfitted *I-V* plot is provided in Figure B9 of Appendix-B. The *I-V* plots clearly show the fluctuation in current with bias voltage for the host and all the host–guest complexes. The host's electrical current flow is noticeably lower than the host–guest structure, indicating the feasibility of readily detecting the presence of a guest molecule. Furthermore, we have calculated the conductance of the host and host–guest complexes from the *I-V* plot, as shown in the Table B2 of Appendix-B. Our investigation found that the G7⊂H complex shows the maximum conductance value of 1.84 $\times 10^{-5}$ S, which contains the maximum number of π-electrons (20) in the guest perylene (G7) molecule. In addition, the HOMO–LUMO energy gap of this complex is 1.90 eV which is comparatively smaller than other complexes. The anti-aromatic nature of perylene may also be one of the factors for getting maximum conductance value.[73] The previous study revealed that pure perylene showed better conductivity than pyrene, and we also obtained the same trend when the pyrene and perylene guest molecules were encapsulated inside the cavity of the host (H).[74] Moreover, on comparing the conductance between pure anthracene and naphthalene, naphthalene shows more conductivity, which is the same as host-wrapped anthracene and naphthalene.[75] Comparing the conductance of complexes G2⊂H with G3⊂H and G6⊂H with G7⊂H (that have the same number of guest molecule π-electrons), our calculations found that complexes having higher interaction energy and smaller HOMO–LUMO energy gap value show better conductivity values.

The quantum transmission spectrum can effectively elucidate the properties of quantum transmission. This spectrum reflects the coupling strength between the system and the electrode. Additionally, the transmission channel signifies the coupling strength between the molecular orbital and the energy band of the electrode.[76] To understand the correlation between the equilibrium conductance of the host–guest complexes with an increase in the number of π-electrons, we have plotted the zero-bias transmission spectra $T(E,V) = 0$ and provided them in Figure 4.11c. All systems exhibit a clear resonance peak near the Fermi level (E_F). Transmission spectra near the Fermi level (E_F) are of particular interest because they provide insight into the interaction between the energy of frontier molecular orbital and the electronic state of the electrode surface, which ultimately determines the electron transmission properties.[77] Figure 4.11c shows that the resonating peak has a maximum value of 1.36G_0 for the G7⊂H complex near the E_F, which corresponds to the maximum conductivity of the complex.

The preservation of the conductance order in all complexes is attributed to a substantial energy gap in each case. During electron transportation, the transfer of electrons predominantly occurs between the highest occupied molecular orbital (HOMO) and the lowest unoccupied molecular orbital (LUMO).[77] Moreover, we also observed that at zero bias, the conductance of the host is more than that of other host–guest complexes. However, the transmission probability at the Fermi level (E_F) is less pronounced with increasing the bias voltage (Figure B10 of Appendix-B) and hence reduces the overall conductance of the host. We found that the presence of a guest molecule significantly alters the conductance. The change in conductance depends on various parameters, including the type of guest molecule, the number of π-electrons, the HOMO–LUMO energy gap, and the interaction energy. Overall, this study showcases the approaches to explore the supramolecular host–guest systems consisting of noncovalent π–π interaction and intermolecular electron charge transport.

4.4. Conclusions

In this Chapter, we have examined the noncovalent interactions in the series of host–guest complexes (G1⊂H to G7⊂H) formed between the hexacationic host (H^{6+}) and polycyclic aromatic hydrocarbon (PAH) guests (G1–G7) by employing different quantum chemical methods. The ETS-NOCV analysis of the complexes revealed that the dispersion interaction part ΔE^{disp} has a major contribution to the total interaction energy, $\Delta E^{int}_{ETS-NOCV}$.This result indicates that mainly π–π interaction is involved between the host and guest in the complexes. We found that perylene and naphthalene inclusion complexes G7⊂H and G1⊂H show the largest and smallest dispersion interaction values, respectively. In addition, the NCI isosurface plots also confirmed the presence of π–π van der Waals interaction between the host and guest in the complexes. The HOMOs of the complex are localized on the electron-rich PAH guests, while the LUMOs exist on the pyridinium-conjugated triazine regions of the host. Among the complexes, the HOMO–LUMO energy gap of G7⊂H, consisting of a perylene (G7) guest, is the smallest. Interestingly, we observed that the HOMO–LUMO energy gap of complex G6⊂H is relatively larger than G7⊂H, although both the guests in the complexes have the same number of π-electrons. Furthermore, the molecular conductance of the empty host (H) and host–guest complexes (G1⊂H to G7⊂H) was estimated using the nonequilibrium greens function-density functional theory (NEGF-DFT). We have obtained that the conductance value increases when the guest molecules are encapsulated inside the host cavity. The complex G7⊂H, which has a 20 π-electron perylene guest, shows a maximum conductance value of 1.84×10^{-5} S. Nevertheless, our theoretical investigation suggests that the supramolecular host-

guest based systems offer promising opportunities to explore intermolecular charge transport between different aromatic groups.

4.5. References

[1] J.-H. Deng, J. Luo, Y.-L. Mao, S. Lai, Y.-N. Gong, D.-C. Zhong and T.-B. Lu, *Sci. Adv.*, 2020, **6**, eaax9976.

[2] M. R. Tuttle, S. T. Davis and S. Zhang, *ACS Energy Lett.*, 2021, **6**, 643.

[3] S. Biswas, S. Sen, J. Im, S. Biswas, P. Krstic, B. Ashcroft, C. Borges, Y. Zhao, S. Lindsay and P. Zhang, *ACS Nano*, 2016, **10**, 11304.

[4] C. Li, H. Wu, T. Zhang, Y. Liang, B. Zheng, J. Xia, J. Xu and Q. Miao, *Chem*, 2018, **4**, 1416.

[5] X. Wei, Y. Wang, X. Xiong, X. Guo, L. Zhang, X. Zhang and S. Zhou, *Adv. Funct. Mater.*, 2016, **26**, 8266.

[6] H. B. Gray and J. R. Winkler, *Chem. Phys. Lett.*, 2009, **483**, 1.

[7] H. Zheng, F. Jiang, R. He, Y. Yang, J. Shi and W. Hong, *Chin. J. Chem.*, 2019, **37**, 1083.

[8] L. J. Jeuken, A. K. Jones, S. K. Chapman, G. Cecchini and F. A. Armstrong, *J. Am. Chem. Soc.*, 2002, **124**, 5702.

[9] T. J. Meyer, M. H. V. Huynh and H. H. Thorp, *Angew. Chem. Int. Ed.*, 2007, **46**, 5284.

[10] E. Yavin, A. K. Boal, E. D. Stemp, E. M. Boon, A. L. Livingston, V. L. O'Shea, S. S. David and J. K. Barton, *Proc. Natl. Acad. Sci. USA.*, 2005, **102**, 3546.

[11] D. S. Seferos, S. A. Trammell, G. C. Bazan and J. G. Kushmerick, *Proc. Natl. Acad. Sci. USA.*, 2005, **102**, 8821.

[12] D. S. Seferos, A. S. Blum, J. G. Kushmerick and G. C. Bazan, *J. Am. Chem. Soc.*, 2006, **128**, 11260.

[13] S. Wu, M. T. González, R. Huber, S. Grunder, M. Mayor, C. Schönenberger and M. Calame, *Nat. Nanotechnol.*, 2008, **3**, 569.

[14] S. Martin, I. Grace, M. R. Bryce, C. Wang, R. Jitchati, A. S. Batsanov, S. J. Higgins, C. J. Lambert and R. J. Nichols, *J. Am. Chem. Soc.*, 2010, **132**, 9157.

[15] M. Kiguchi, T. Takahashi, Y. Takahashi, Y. Yamauchi, T. Murase, M. Fujita, T. Tada and S. Watanabe, *Angew. Chem.* Int. Ed., 2011, **123**, 5826.

[16] S. Fujii, T. Tada, Y. Komoto, T. Osuga, T. Murase, M. Fujita and M. Kiguchi, *J. Am. Chem. Soc.*, 2015, **137**, 5939.

[17] M. Juríček, N. L. Strutt, J. C. Barnes, A. M. Butterfield, E. J. Dale, K. K. Baldridge, J. F. Stoddart and J. S. Siegel, *Nat. Chem.*, 2014, **6**, 222.

[18] J. C. Barnes, E. J. Dale, A. Prokofjevs, A. Narayanan, I. C. Gibbs-Hall, M. Juríček, C. L. Stern, A. A. Sarjeant, Y. Y. Botros, S. I. Stupp and J. F. Stoddart, *J. Am. Chem. Soc.*, 2015, **137**, 2392.

[19] J. C. Barnes, M. Juricek, N. L. Strutt, M. Frasconi, S. Sampath, M. A. Giesener, P. L. McGrier, C. J. Bruns, C. L. Stern, A. A. Sarjeant and J. F. Stoddart, *J. Am. Chem. Soc.*, 2013, **135**, 183.

[20] E. J. Dale, N. A. Vermeulen, M. Juricek, J. C. Barnes, R. M. Young, M. R. Wasielewski and J. F. Stoddart, *Acc. Chem. Res.*, 2016, **49**, 262.

[21] M. Juríček, J. C. Barnes, E. J. Dale, W. Liu, N. L. Strutt, C. J. Bruns, N. A. Vermeulen, K. C. Ghooray, A. A. Sarjeant, C. L. Stern, Y. Y. Botros, W. A. Goddard and J. F. Stoddart, *J. Am. Chem. Soc.*, 2013, **135**, 12736.

[22] M. Kiguchi, J. Inatomi, Y. Takahashi, R. Tanaka, T. Osuga, T. Murase, M. Fujita, T. Tada and S. Watanabe, *Angew. Chem. Int. Ed.*, 2013, **24**, 6202.

[23] J.-H. Tang, Y. Li, Q. Wu, Z. Wang, S. Hou, K. Tang, Y. Sun, H. Wang, H. Wang and C. Lu, X. Wang, X. Li, D. Wang, J. Yao1, C. J. Lambert, N. Tao, Y.-W. Zhong and P. J. Stang, *Nat. Commun.*, 2019, **10**, 4599.

[24] E. J. Dale, N. A. Vermeulen, A. A. Thomas, J. C. Barnes, M. Juríček, A. K. Blackburn, N. L. Strutt, A. A. Sarjeant, C. L. Stern, S. E. Denmark and J. F. Stoddart, *J. Am. Chem. Soc.*, 2014, **136**, 10669.

[25] N. Hafezi, J. M. Holcroft, K. J. Hartlieb, E. J. Dale, N. A. Vermeulen, C. L. Stern, A. A. Sarjeant and J. F. Stoddart, *Angew. Chem. Int. Ed.*, 2015, **54**, 456.

[26] C. Zhang, H. Wang, J. Zhong, Y. Lei, R. Du, Y. Zhang, L. Shen, T. Jiao, Y. Zhu, H. Zhu, H. Li and H. Li, *Sci. Adv.*, 2019, **5**, eaax6707.

[27] S. M. Bachrach, *J. Phys. Chem. A*, 2013, **117**, 8484.

[28] S. M. Bachrach and A. E. Andrews, *J. Phys. Chem. A*, 2014, **118**, 6104.

[29] R. M. Young, S. M. Dyar, J. C. Barnes, M. Juríček, J. F. Stoddart, D. T. Co and M. R. Wasielewski, *J. Phys. Chem. A*, 2013, **117**, 12438.

[30] G. R. Nagurniak, G. F. Caramori, R. L. Parreira, P. A. Bergamo, G. Frenking and A. Munoz-Castro, *J. Phys. Chem. C*, 2016, **120**, 15480.

[31] S. Grimme, J. G. Brandenburg, C. Bannwarth and A. Hansen, *J. Chem. Phys.*, 2015, **143**, 054107.

[32] H. Kruse and S. Grimme, *J. Chem. Phys.*, 2012, **136**, 154101.

[33] S. Grimme, S. Ehrlich and L. Goerigk, *J. Comput. Chem.*, 2011, **32**, 1456.

[34] S. Grimme, J. Antony, S. Ehrlich and H. Krieg, *J. Chem. Phys.*, 2010, **132**, 154104.

[35] P. Jurečka, J. Šponer, J. Černý and P. Hobza, *Phys. Chem. Chem. Phys.*, 2006, **8**, 1985.

[36] J. Rezác, K. E. Riley and P. Hobza, *J. Chem. Theory Comput.*, 2011, **7**, 2427.

[37] R. Sure, J. G. Brandenburg and S. Grimme, *ChemistryOpen*, 2016, **5**, 94.

[38] J. P. Perdew, K. Burke and M. Ernzerhof, *Phys. Rev. Lett.*, 1996, **77**, 3865.

[39] F. Weigend and R. Ahlrichs, *Phys. Chem. Chem. Phys.*, 2005, **7**, 3297.

[40] S. F. Boys and F. Bernardi, *Mol. Phys.*, 1970, **19**, 553.

[41] L. M. Grimm, S. Spicher, B. Tkachenko, P. R. Schreiner, S. Grimme and F. Biedermann, *Chem. – Eur. J.*, 2022, **28**, e202200529.

[42] R. Hahn, F. Bohle, S. Kotte, T. J. Keller, S.-S. Jester, A. Hansen, S. Grimme and B. Esser, *Chem. Sci.*, 2018, **9**, 3477.

[43] M. H. Putra, S. Seidenath, S. Kupfer, S. Gräfe and A. Gros, *Chem. – Eur. J.*, 2021, **27**, 17104.

[44] R. Sure and S. Grimme, *J. Chem. Theory Comput.*, 2015, **11**, 3785.

[45] A. Bauza, D. Quinonero, P. M. Deya and A. Frontera, J. *Phys. Chem. A*, 2013, **117**, 2651.

[46] F. Neese, F. Wennmohs and A. Hansen, *J. Chem. Phys.*, 2009, **130**, 114108.

[47] F. Neese, A. Hansen and D. G. Liakos, *J. Chem. Phys.*, 2009, **131**, 064103.

[48] C. Riplinger, B. Sandhoefer, A. Hansen and F. Neese, *J. Chem. Phys.*, 2013, **139**, 134101.

[49] C. Riplinger and F. Neese, *J. Chem. Phys.*, 2013, **138**, 034106.

[50] J. G. Brandenburg, C. Bannwarth, A. Hansen and S. Grimme, *J. Chem. Phys.*, 2018, **148**, 064104.

[51] F. Neese, *Wiley Interdiscip. Rev.: Comput. Mol. Sci.*, 2012, **2**, 73.

[52] M. J. Frisch, G. W. Trucks, H. B. Schlegel, G. E. Scuseria, M. A. Robb, J. R. Cheeseman, G. Scalmani, V. Barone, G. A. Petersson, H. Nakatsuji, X. Li, M. Caricato, A. V. Marenich, J. Bloino, B. G. Janesko, R. Gomperts, B. Mennucci, H. P. Hratchian, J. V. Ortiz, A. F. Izmaylov, J. L. Sonnenberg, D. Williams-Young, F. Ding, F. Lipparini, F. Egidi, J. Goings, B. Peng, A. Petrone, T. Henderson, D. Ranasinghe, V. G. Zakrzewski, J. Gao, N. Rega, G. Zheng, W. Liang, M. Hada, M. Ehara, K. Toyota, R. Fukuda, J. Hasegawa, M. Ishida, T. Nakajima, Y. Honda, O. Kitao, H. Nakai, T. Vreven, K. Throssell, J. A. Montgomery, J. E. Peralta, F. Ogliaro, M. J. Bearpark, J. J. Heyd, E. N. Brothers, K. N. Kudin, V. N. Staroverov, T. A. Keith, R. Kobayashi, J. Normand, K. Raghavachari, A. P. Rendell, J. C. Burant, S. S. Iyengar, J. Tomasi, M. Cossi, J. M. Millam, M. Klene, C. Adamo, R. Cammi, J. W. Ochterski, R. L. Martin, K. Morokuma, O. Farkas, J. B. Foresman and D. J. Fox, Gaussian 16 Revision C.01, Gaussian Inc., Wallingford CT, 2016.

[53] M. P. Mitoraj, A. Michalak and T. Ziegler, *J. Chem. Theory Comput.*, 2009, **5**, 962.

[54] A. Becke, *Phys. Rev. A: At., Mol., Opt. Phys.*, 1988, **33**, 3098.

[55] J. P. Perdew, *Phys. Rev. B: Condens. Matter Mater. Phys.*, 1986, **33**, 8822.

[56] G. T. Velde, F. M. Bickelhaupt, E. J. Baerends, C. Fonseca Guerra, S. J. van Gisbergen, J. G. Snijders and T. Ziegler, *J. Comput. Chem.*, 2001, **22**, 931.

[57] E. R. Johnson, S. Keinan, P. Mori-Sánchez, J. Contreras- Garca, A. J. Cohen and W. Yang, *J. Am. Chem. Soc.*, 2010, **132**, 6498.

[59] E. F. Pettersen, T. D. Goddard, C. C. Huang, G. S. Couch, D. M. Greenblatt, E. C. Meng and T. E. Ferrin, *J. Comput. Chem.*, 2004, **25**, 1605.

[60] W. Humphrey, A. Dalke and K. Schulten, *J. Mol. Graph.*, 1996, **14**, 33.

[61] T. Williams, C. Kelley and many others, Gnuplot 4.6: an interactive plotting program, 2013, https://gnuplot.source forge.net/.

[62] N. Papior, N. Lorente, T. Frederiksen, A. Garca and M. Brandbyge, *Comput. Phys. Commun.*, 2017, **212**, 8.

[63] K. Stokbro, J. Taylor, M. Brandbyge and P. Ordejon, *Ann. N. Y. Acad. Sci.*, 2003, **1006**, 212.

[64] Y. Xue, S. Datta, S. Hong, R. Reifenberger, J. I. Henderson and C. P. Kubiak, *Phys. Rev. B: Condens. Matter Mater. Phys.*, 1999, **59**, R7852.

[65] P. Ou, P. Song, X. Liu and J. Song, *Adv. Theory Simul.*, 2019, **2**, 1800103.

[66] Y. Li, X. Yu, Y. Zhen, H. Dong and W. Hu, *Phys. Chem. Chem. Phys.*, 2019, **21**, 16293.

[67] P. Giannozzi, S. Baroni, N. Bonini, M. Calandra, R. Car, C. Cavazzoni, D. Ceresoli, G. L Chiarotti, M. Cococcioni, I. Dabo, A. D. Corso, S. de Gironcoli, S. Fabris, G. Fratesi, R. Gebauer, U. Gerstmann, C. Gougoussis, A. Kokalj, M. Lazzeri, L. Martin-Samos, N. Marzari, F. Mauri, R. Mazzarello, S. Paolini, A. Pasquarello, L. Paulatto, C. Sbraccia, S. Scandolo, G. Sclauzero, A. P. Seitsonen, A. Smogunov, P. Umari and R. M Wentzcovitch, *J. Phys.: Condens. Matter*, 2009, **21**, 395502.

[68] P. E. Blöchl, *Phys. Rev. B: Condens. Matter Mater. Phys.*, 1994, **50**, 17953.

[69] G. Kresse and D. Joubert, *Phys. Rev. B: Condens. Matter Mater. Phys.*, 1999, **59**, 1758.

[70] R. Evarestov and V. Smirnov, *Phys. Rev. B: Condens. Matter Mater. Phys.*, 2004, **70**, 233101.

[71] U. Nath and M. Sarma, *J. Phys. Chem. A*, 2023, **127**, 1112.

[72] J. Shen, H. He, T. Sengupta, D. Bista, A. C. Reber, R. Pandey and S. N. Khanna, *Nanoscale Adv.*, 2021, **3**, 6888.

[73] G.-P. Zhang, Z. Xie, Y. Song, M.-Z. Wei, G.-C. Hu and C.-K. Wang, *Org. Electron.*, 2017, **48**, 29.

[74] D. Northrop, O. Simpson and N. Mott, *Proc. R. Soc. London, Ser. A*, 1956, **234**, 124.

[75] C. Liu, S. Kaneko, Y. Komoto, S. Fujii and M. Kiguchi, *Appl. Phys. Lett.*, 2015, **106**, 103103.

[76] Z. Dai, X. Zheng, X. Shi and Z. Zeng, *Phys. Rev. B: Condens. Matter Mater. Phys.*, 2005, **72**, 205408.

[77] Y.-Q. Zhao, J.-Q. Lan, C.-E. Hu, Y. Mu and X.-R. Chen, *ACS Omega*, 2021, **6**, 15727.

Chapter 5

Insight into the Nature of Interaction between the Molecular Receptors based on Dimethylpropanediurea and Resorcinol Derivatives

5.1. Introduction

Noncovalent interactions are integral part of various areas, including biological sciences, construction of macromolecules, protein folding, material sciences, and supramolecular host-guest chemistry.[1-6] Various types of these interactions are hydrogen bonding, π-π stacking, cation-π, anion-π, etc.[7-14] The significance of these interactions is also explicitly seen in the context of supramolecular host-guest interactions. Designing specific supramolecular receptors and modulating them to accommodate particular guest molecules is considered one of the formidable challenges within host-guest chemistry. Many receptors were reported, such as crown ethers,[15] cyclodextrins,[16,17] foldamers,[18,19] calixarenes,[20,21] and cucurbiturils,[22,23] for binding varieties of guests. The molecular receptors based on glycouril were also reported and showcasing there potential to form host-guest complexation with dihydroxyaromatics molecules. Gosecki et al. both experimentally and theoretically demonstrated the two isomers of glycouril molecular receptors, which have the side walls of *N*-(4-methoxyphenyl) isonicotinamide. [24] One of the isomers can bind the resorcinol molecule through an inner mechanism, while the other isomer receptor has the potential to accommodate two resorcinol molecules. Furthermore, a series of macrocyclic receptors based on propanediurea as the fundamental building block were also reported.[25,26] Inside the cavity of such a receptor, the neutral dihydroxy benzene molecule can be accommodated via the formation of noncovalent hydrogen bonding and π-π interaction. Jansen et al. synthesized a series of molecular clip receptors utilizing 2,4,6,8-tetraazabicyclo[3.3.1]nonane-3,7-dione (propanediurea) as foundation.[27] These receptors feature a cavity generated from the side walls of two parallel aromatic rings on the top of a bis-urea framework. Notably, these receptors exhibited U-shaped

molecular geometry and possess the ability to bind the flat dihydroxy benzene and its derivatives molecules. Moreover, the complex formation occurs through π-π and hydrogen bonding interactions. Among the different synthesized receptors, the molecular receptor (A) displayed in Figure 5.1 showed an exceptionally high binding constant (K_a) value when it binds with dihydroxybenzene derivatives. This receptor's affinity for dihydroxy aromatic molecules makes them significant in designing the motifs for dihydroxy aromatic molecule removal systems. Therefore, such molecular receptors serve as containers for accommodating the dihydroxy aromatic molecules through hydrogen bonding and other weak interactions.

Resorcinol is significant in diverse areas such as medicinal applications, agrichemicals, clinical trials, and electronic devices.[28-32] However, the health hazards and environmental pollution associated with dihydroxy aromatic molecules, particularly resorcinol, are also widely known.[33] According to the World Health Organization (WHO), resorcinol is also one of the compounds responsible for erythrocyte changes, thyroid dysfunction, and central nervous system disturbances.[34]

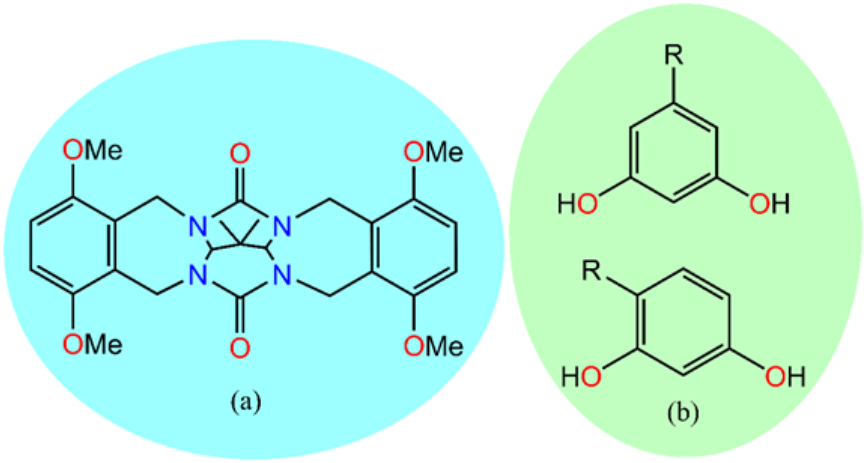

R= H, Me, OMe, NH_2,F, Cl, NO_2,NMe_2,CF_3, CN, CHO

Figure 5.1. Molecular structures of propanediurea-based host (A) and guest molecules (G1-G11).

Lande et al. employed density functional theory (DFT) and other quantum topological analyses to study the noncovalent interactions in inclusion complexes between resorcinol and calix [4] pyridine or azacalix[4] pyridine.[35] Their finding demonstrated that the substitution of heteroatom (-NH-) in place of -CH_2- unit at the bridging point of calix [4] pyridine changes the geometrical shape of the cavity from box-shaped to funnel one. Further, they observed that intermolecular hydrogen bonding, π-π, and other weak interactions are mainly present in the

complexes. Reek et al. reported experimental and molecular modelling using the semi-empirical method AM1 to obtain the interaction energies between the diphenylglycoluril molecular receptors and dihydroxy benzene molecules.[36] Hunter and Sanders studied the substituent effect in the π-π stacking interactions through the electrostatic model.[37-39] Cozzi and Siege also proposed the polar/π model to explain the π-π stacking interactions.[40-44]

Theoretical investigations have effectively demonstrated the comprehensive understanding and interpretation of noncovalent interactions, yielding results that complement experimental findings. However, the exploration aspects within the host-guest complexes utilizing propanediurea-based receptor host (A) and various dihydroxybenzene derivative guests (G1-G11) are relatively limited. Seizing this opportunity, we employed the density functional theory (DFT),[45] local energy decomposition (LED),[46] quantum theory of atoms in molecules (QTAIM),[47,48] and noncovalent interaction (NCI)[49] methods to explore the deeper insights into the underlying noncovalent interactions within the host-guest complexes. Moreover, the study considers electron-donating groups (−EDG) such as $-CH_3$, $-OCH_3$, $-NH_2$, $-NMe_2$ and electron-withdrawing groups (−EWG) such as −F, −Cl, $-NO_2$, $-CF_3$, −CN, −CHO substituted to the parent resorcinol molecule are presented in Figure 5.1. This finding illuminates how the -EDG and −EWG substituents affect the strength of the host-guest interactions and their impact on the intermolecular π-π and hydrogen bonding interactions. The Computational Details used in this study are discussed in the following sections. Results and Discussion are provided thereafter. A Summary of the salient results concludes this Chapter.

5.2. Computational Details

The geometry optimization and frequencies calculation of the host, guest, and host-guest complexes (A: G1 to A: G11) (Figure 5.1) were performed using the B3LYP[50] functional incorporating Grimme's dispersion correction with the Becke-Johnson damping scheme (D3BJ).[51,52] The def2-TZVP basis set was utilized in this investigation. The interaction energy, ΔE_{int}, of the host-guest complexes was estimated by implementing the supermolecular approach

$$\Delta E_{int} = E_{AG} - E_A - E_G \qquad (5.1)$$

Where E_{AG}, E_A, and E_G represent the optimized electronic energies of the complexes, host, and guest, respectively, and the calculations were executed using the Gaussian 16 software packages.[53]

To probe the nature of host-guest interactions within complexes, the local energy decomposition (LED)[46] analysis was performed by utilizing the domain-based local pair natural orbital coupled cluster method with single, double, and perturbative triple excitations [DLPNO-CCSD(T)] level of theory in conjunction with the correlation-consistent basis set cc-pVTZ.[54-56] Earlier studies also illustrated the use of correlation-consistent basis sets and performed the LED analysis to explain the dispersion interaction.[57] Under the LED approach,[46] the dissociation energy, ΔE, of the complex consisting of two molecular fragments, X and Y, can be expressed as,

$$\Delta E = \Delta E_{geo-prep} + \Delta E_{el-prep} + E_{elst}^{(X,Y)} + E_{exch}^{(X,Y)} + E_{disp} + E_{C-(T)}^{(X,Y)} \quad (5.2)$$

where $\Delta E_{geo-prep}$ denotes the geometric preparation energy, $\Delta E_{el-prep}$ accounts for the electronic preparation energy, $E_{elst}^{(X,Y)}$ represents the electrostatic interaction resulting from the distorted electron density distributions of the fragments, $E_{exch}^{(X,Y)}$ represents the exchange interaction energy, which describes the stabilizing component of the interactions, E_{disp} is the dispersion interaction energy, and $E_{C-(T)}^{(X,Y)}$ represents the charge transfer components. The calculation for the LED analysis was performed using the ORCA software. [58,59]

To understand the noncovalent interaction in complexes, we employed the quantum theory of atoms in molecules (QTAIM) [47,48] and noncovalent interaction (NCI) [49] analyses using the Multiwfn program package.[60]

5.3. Results and Discussion

5.3.1. Geometrical Features of the Host and Host-Guest Complexes

The molecular geometry optimization of the host (A) was performed at the B3LYP-D3BJ/def2-TZVP level of theory and the optimized structure is displayed in Figure 5.2. We found that the distance between the centers of the two benzene rings on the side walls of the host, configured in U-shaped arrangements, has been determined to be 5.1 Å. Comparing our calculated separation distance with the reported X-ray crystal structure distance of 6.4 Å,[27] we found that our calculated distance is shorter. However, upon encapsulation of guest inside the host cavity, the distance separation between the two benzene rings was increased and approximately found to be 6.0 Å in all the complexes. Meanwhile, we noticed the calculated distance between the guest and the benzene ring of the host in all the complexes is approximately 3.0 Å.

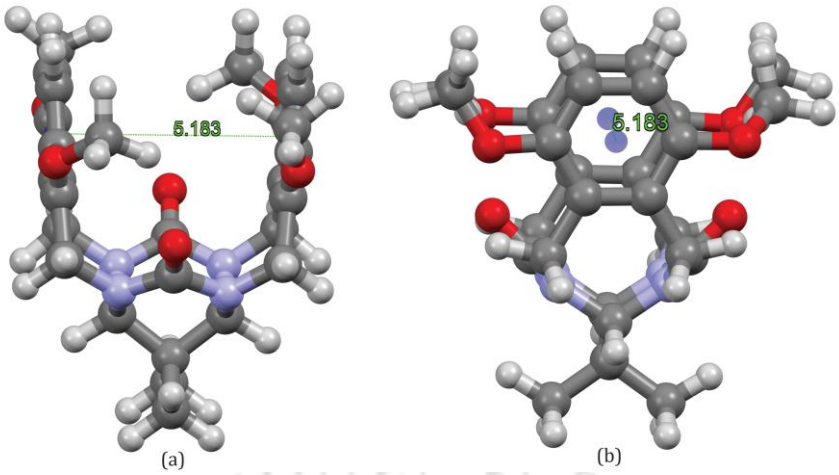

Figure 5.2. Optimized molecular geometry of the host (A) calculated at the B3LYP-D3BJ/def2-TZVP level of theory and (a) and (b) represent the front and side views. The distance between the center of two benzene rings of the empty host is 5.18 Å.

5.3.2. Interaction Energies of Host-Guest Complexes

The interaction energy, ΔE_{int}, was computed using the supermolecular approach (Eq. 5.1), as described in the computational details section, to estimate the strength of the interaction between the host and guest in complexes. In this method, ΔE_{int} is energy difference between the host-guest complex and the sum of host and guest. The ΔE_{int} value obtained using the B3LYP-D3BJ/def2-TZVP level of theory is presented in Table 5.1.

In Table 5.1, the Set I complex exhibits the interaction energy, ΔE_{int}, whose value ranges from –35.18 kcal mol^{-1} to –42.73 kcal mol^{-1}, excluding the parent complex A: G1. Within the host-guest complexes of Set I, the lowest interaction energy is observed in the parent complex A: G1. The electron-donating groups substituted resorcinol guest binding to the host, increasing the interaction energy, ΔE_{int}. These variation in the ΔE_{int} values can be noticed in complexes A: G2($-CH_3$), A: G3($-OCH_3$), A: G4($-NH_2$), and A: G5($-NMe_2$) of Set I. Similarly, the interaction energy, ΔE_{int}, value increases for the complexes A: G6(-F), A: G7($-Cl$), A: G8($-NO_2$), A: G9($-CF_3$), A: G10(-CN), and A: G11($-CHO$) when the electron-withdrawing group substituted guest embedded inside the cavity of host A.

Table 5.1. Interaction energy ΔE_{int} (kcal mol^{-1}) of the host-guest complexes calculated at the B3LYP-D3BJ/def2-TZVP level of theory.

Complex	−R	ΔE_{int} [R=4-position] Set I	ΔE_{int} [R=5-position] Set II
A: G1	−H	-35.05	-35.05
A: G2	$-CH_3$	-35.18	-34.90
A: G3	$-OCH_3$	-40.67	-34.97
A: G4	$-NH_2$	-37.68	-34.21
A: G5	$-NMe_2$	-39.86	-34.29
A: G6	−F	-40.98	-36.15
A: G7	−Cl	-39.16	-36.87
A: G8	$-NO_2$	-42.73	-39.17
A: G9	$-CF_3$	-38.59	-37.90
A: G10	−CN	-37.52	-38.53
A: G11	−CHO	-36.27	-37.58

In Set II of Table 5.1, the interaction energy, ΔE_{int}, values for the host-guest complexes range from –34.21 to –39.17 kcal mol^{-1}. Notably, within this set, we observed no significant variation in ΔE_{int} values among the complexes A: G2($-CH_3$), A: G3($-OCH_3$), A: G4($-NH_2$), and A: G5($-NMe_2$). Furthermore, no significant differences were observed in the ΔE_{int} values when compared with the parent complex A: G1. On the other hand, the ΔE_{int} values were found to be larger for the complexes A: G6(−F), A: G7(−Cl), A: G8($-NO_2$), A: G9($-CF_3$), A: G10(−CN), and A: G11(−CHO) when compared to the parent complex A: G1. These results suggest that the strength of interaction energy between the host and guest is diminished when the guest features substituted electron-donating groups enclosed within the host's cavity. Conversely, the strength of the interaction energy increases when the guest molecules are substituted with the electron-withdrawing groups. Further, these outcomes indicate that the

strength of the interaction energy between the host and guest is weaker when the electron-donating group is substituted at the 5-position of the resorcinol guest.

5.3.3. DLPNO-CCSD(T)-LED Analysis of Host-Guest complexes

The local energy decomposition (LED) analysis offers to decompose the energy of the DLPNO-CCSD(T) method into distinct and physically meaningful components. These components are geometric and electronic preparation, electrostatic interactions, interfragment exchange, dynamic charge polarization, and London dispersion contributions. Herein, we performed the LED analysis of all the host-guest complexes A: G1 to A: G11 and the results are tabulated in Table 5.2. The dispersion interaction energy E_{disp} in all the complexes of Set I was found in the range of –10.76 to –11.77 kcal mol^{-1} (Table 5.2). In Set I, we observed no substantial differences in the E_{disp} contributions. On the other hand, we noticed that the contribution of the electrostatic interaction energy E_{elst} term for the complexes in Set I is comparatively higher than in Set I. The complex A: G8($-NO_2$) shows the highest electrostatic interaction energy E_{elst} term, which is also similarly observed in Set II. The exchange energy E_{exch} contribution ranges from –27.79 to –30.36 kcal mol^{-1}.

The dispersion interaction energy, E_{disp}, between the host and guest in the complexes of Set II is in the range of –10.60 kcal mol^{-1} to –11.64 kcal mol^{-1}. Among the various complexes of Set II, we observed that complex A: G4 ($-NH_2$) shows the highest contribution of dispersion interaction energy of –11.64 kcal mol^{-1}. We have noticed that the variations in the dispersion energy term are relatively small across the different complexes.

Further, we observed that the electrostatic interaction energy E_{elst} is significantly significant in all the complexes. The complex A: G8($-NO_2$) shows the highest E_{elst} contribution, with a value of –138.14 kcal mol^{-1}, followed by complex A: G10($-CN$), which has an E_{elst} value of –136.30 kcal mol^{-1}. These results revealed that when the electron-withdrawing groups are substituted on the guest resorcinol of the parent complex A: G1, the contribution of E_{elst} increases, which can be seen in complexes A: G6($-F$) to A: G11($-CHO$) (Table 5.2). On the other hand, there are no significant differences in the exchange energy E_{exch} in all the complexes of Set II.

Comparing the complex A: G8($-NO_2$) of Set I with Set II, we observed that the electrostatic intermolecular interaction term between the host and guest in Set I is significantly larger than that of Set II. These results suggest that the electron-withdrawing group $-NO_2$ introduced at

the 4-position of the resorcinol guest is more considerable in the electrostatic interaction with the host compared to the 5-position.

Table 5.2. Dispersion energy (E_{disp}), electrostatic (E_{elst}), and exchange (E_{exch}) interactions (kcal mol^{-1}) contribution of the host-guest complexes obtained from the DLPNO-CCSD(T)-LED computation.

Complex	Set I [R = 4-position]			Set II [R = 5-position]		
	E_{disp}	E_{elst}	E_{exch}	E_{disp}	E_{elst}	E_{exch}
A: G1	-11.13	-126.30	-27.79	-11.13	-126.30	-27.79
A: G2($-CH_3$)	-10.91	-138.61	-28.73	-11.26	-126.24	-28.00
A: G3($-OCH_3$)	-10.94	-131.76	-29.14	-10.74	-127.21	-28.15
A: G4($-NH_2$)	-11.22	-129.71	-28.99	-11.64	-125.39	-28.00
A: G5($-NMe_2$)	-11.77	-130.61	-29.67	-11.58	-125.68	-28.29
A: G6($-F$)	-10.76	-133.35	-28.72	-11.46	-130.40	-28.13
A: G7($-Cl$)	-11.38	-138.32	-29.70	-11.53	-132.38	-28.47
A: G8($-NO_2$)	-11.69	-150.71	-30.94	-10.69	-138.14	-28.84
A: G9($-CF_3$)	-10.91	-138.61	-28.73	-11.20	-134.75	-28.66
A: G10($-CN$)	-11.59	-145.88	-30.36	-10.75	-136.30	-28.66
A: G11($-CHO$)	-11.09	-138.84	-29.42	-10.60	-133.12	-28.46

5.3.4. NCI Analysis of Host-Guest Complexes

The noncovalent (NCI) interaction analysis proposed by Yang and co-workers[49] was employed to identify the noncovalent interactions between the host and guest in complexes A: G1 to A: G11. The interaction is characterized based on the reduced density gradient (RDG), and the expression of RDG is written as,

$$\mathrm{RDG} = s = \frac{1}{2(3\pi^2)^{1/3}} \frac{|\nabla\rho|}{\rho^{4/3}} \qquad (5.3)$$

where $\nabla\rho$ represents the gradient of electron density ρ. The product sign$(\lambda_2)\rho$ represents the color code, i.e., the different bonding interactions (attractive or repulsive). The λ_2 is the second eigenvalue of the Laplacian ($\nabla^2\rho = \lambda_1 + \lambda_2 + \lambda_3$). The values $\lambda_2 < 0$, $\lambda_2 = 0$, and $\lambda_2 > 0$ denote favorable, van der Waals, and unfavorable interactions, respectively. The NCI-RDG isosurface plots of complex A: G8($-NO_2$), which has the highest host-guest interaction energy value in both Set I and Set II, is displayed in Figure 5.3, while the remaining complexes are presented in Figure C1 and Figure C2 of Appendix-C. Figure 5.3a and Figure 5.3b show that the existence of π-π interaction is represented by the green color region between the aromatic benzene ring of the host (A) and guest. Additionally, the presence of a blue circular region denotes the formation of hydrogen bonding (O─H···O) between the oxygen atom of the carbonyl groups of the host A and the hydroxy groups of the guest. The smaller red color region present inside the ring represents the steric repulsion. The RDG scatter plots of the complex A: G8($-NO_2$) are presented on the right side of Figure 5.3, and the remaining complexes are presented in Figure C3 and Figure C4 of Appendix-C. Blue and green color spikes regions of the RDG plots represent the hydrogen bonding and weak interactions such as van der Waals, respectively. The red spike region of the RDG plots indicates the steric repulsion.

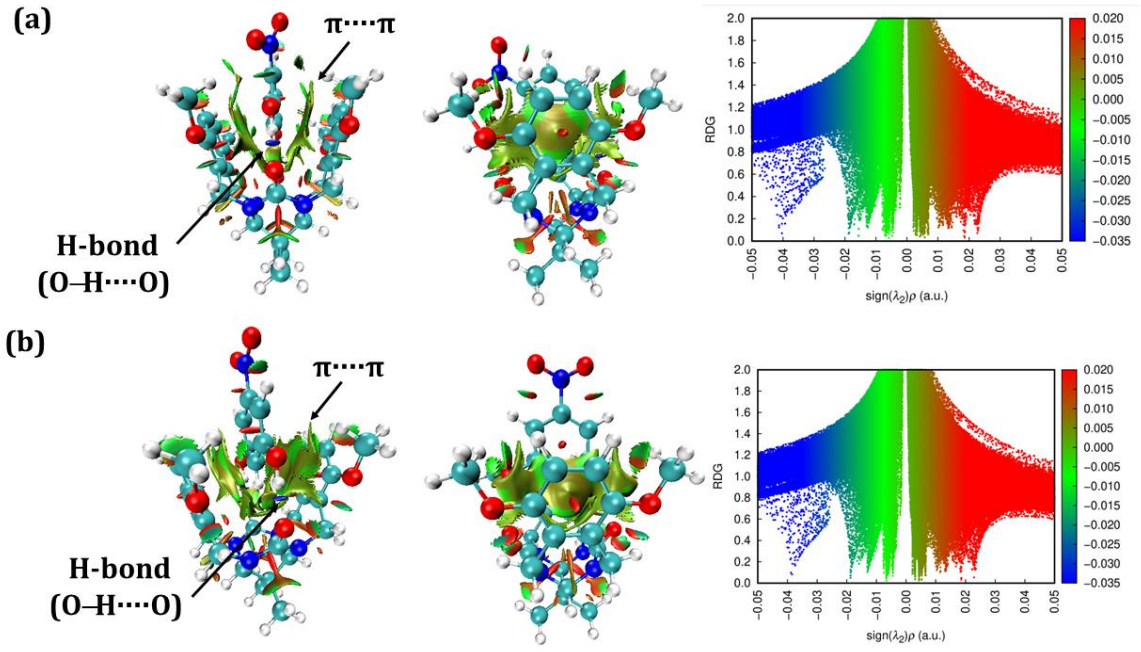

Figure 5.3. RDG isosurface (left) and scatter (right) maps of complex A: G8 ($-NO_2$) depicting the noncovalent interactions regions. (a) and (b) represent the complex A: G8 ($-NO_2$) of Sets I and II, respectively.

5.3.5. QTAIM Analysis of Host-Guest Complexes

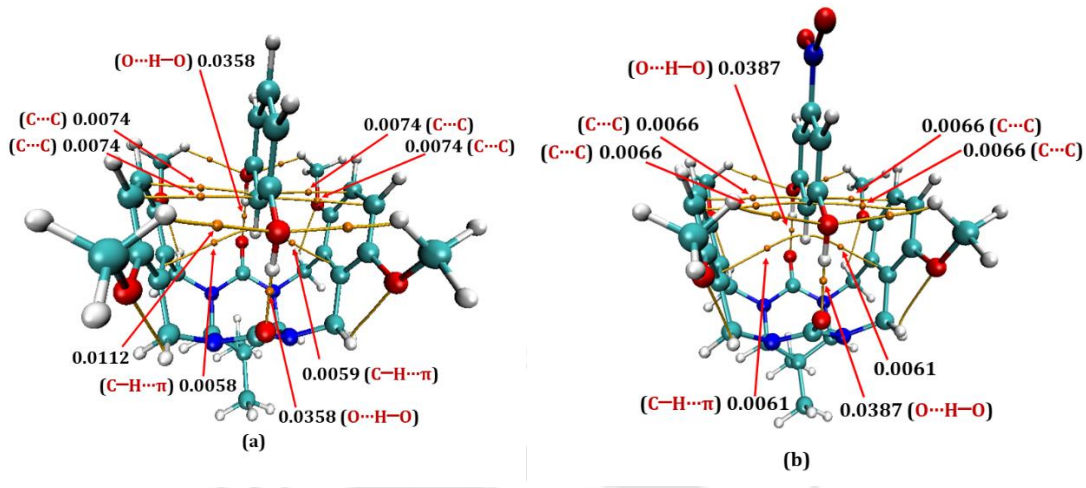

Figure 5.4. Electron density ρ [au] at the bond critical points (bcps) of the intermolecular interaction paths between the host and guest in complexes (a) A: G1 and (b) A: G8 of Set II.

In order to delve deeper into the atom-atom interaction between the host and guest for the complexes A: G1 to A: G11, the quantum theory of atoms in molecules (QTAIM) analysis was performed. Based on the electron density (ρ) and other topological parameters such as Lagrangian kinetic energy (G), potential energy density (V), and energy density (H) at the bond critical points (bcps), the nature of intermolecular interactions can be classified. From this analysis, we observed the stronger interaction is hydrogen bonding (O···H─O) form between the oxygen atom of the carbonyl group of the host and the hydroxyl groups of the guest molecule. Besides this hydrogen bonding, there is the existence of C···C interaction between the guest molecule and host, which represents the existence of π-π interaction. The electron density (ρ) values at the bcps on the intermolecular interaction path of complexes A: G1 and A: G8 of Set II are displayed in Figure 5.4. Complexes A: G1 and A: G8 of Set II have the same number of bcps. We have noticed that the electron density (ρ) values at bcps of the hydrogen bonding interaction (O···H─O) path of complex A: G8 is comparatively larger than the parent hydrogen bonding interaction of complex A: G1. This result indicates the hydrogen bonding O···H─O present in the complex A: G8 is stronger than the complex A: G1.

Consequently, incorporating an electron-withdrawing group onto the resorcinol guest molecule increased the strength of the hydrogen bonding interaction. However, there are no significant changes in the electron density values at the bcps of the C···C interaction path in both complexes. In addition, we also observed other weak intermolecular interactions, including C─H···π and C─H···O. Similarly, the increase in the electron density values at the bcps of the

hydrogen bonding O···H─O is observed when the resorcinol guest molecule is substituted with other electron-withdrawing groups such as −F, −Cl, $-CF_3$, −CHO, and −CN. However, the impact of the changes on the electron density values at the bcps is less significant when the electron donating groups ($-CH_3$, $-NMe_2$, $-NH_2$, $-OCH_3$) are substituted. Similar effect was also observed for the complexes of Set I.

5.3.6. HOMO-LUMO Analysis of Host-Guest Complexes

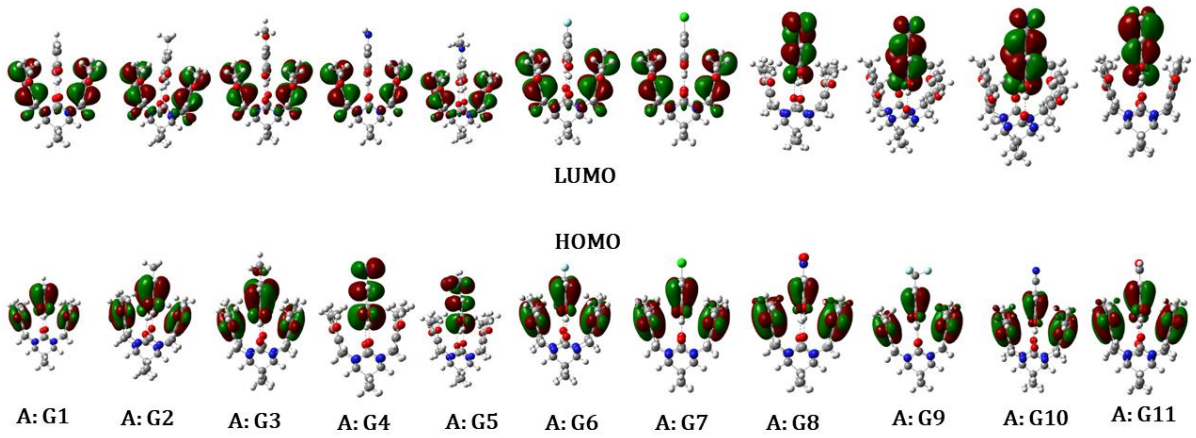

Figure 5.5. Frontier molecular orbitals of host-guest complexes A: G1 to A: G11 of Set II obtained at the B3LYP-D3BJ/def2-TZVP level of theory.

The frontier molecular orbitals, HOMOs (highest occupied molecular orbitals) and LUMOs (lowest unoccupied molecular orbitals), of the host-guest complexes of Set II were obtained at the B3LYP-D3BJ/def2-TZVP level of theory. The HOMOs and LUMOs of host-guest complexes of Set II are displayed in Figure 5.5, and the similar orbital localized were also observed in complexes of Set I. From Figure 5.5, we observed that the LUMOs of complexes A: G1 to A: G7 localized on the host molecule while the HOMO resides on both molecular surfaces of host and guest molecules except for complex A: G4, which is localized on the guest. On the other hand, the LUMOs of complexes A: G8 to A: G11 are distributed over the molecular surface of the guest, and also the location of the HOMOs remains on the host and guest.

5.4. Conclusions

In this Chapter, we have examined the noncovalent interactions, which primarily focus on hydrogen bonding and π-π interaction within the 1:1 complex formed by propanediurea-based molecular clip host and resorcinol guest, along with its derivatives molecules. We found that

electron-withdrawing groups such as $-NO_2$ and $-CN$ substituted guest molecules strongly bind to the host. The impact on the interaction energy changes is less when the electron donating groups ($-CH_3$, $-NMe_2$, $-NH_2$, $-OMe$) are substituted to the resorcinol molecule. The local energy decomposition (LED) analysis of the complexes shows that the electrostatic interaction energy between the host and guest is significant when the electron-withdrawing group moieties are present on the guest. However, the dispersion interaction energy contribution has no significant changes when the parent resorcinol guest molecule is modulated with the electron-withdrawing and donating groups. In future, we hope this work will stimulate the research community to design different cavity-size supramolecular receptors for binding varieties of guest molecules.

5.5. References

[1] W. Saenger, *Principles of Nucleic Acid Structure*; Springer-Verlag: New York, 1984

[2] L. P. G. Wakelin, *Med. Res. Rev.*, 1986, **6**, 275.

[3] S. K. Burley and G. A. Petsko, *Adv. Protein Chem.*, 1988, **39**, 125.

[4] M. J. Plevin, D. L. Bryce and J. Boisbouvier, *Nat. Chem.*, 2010, **2**, 466.

[5] S. Griessl, M. Lackinger, M. Edelwirth, M. Hietschold and W. M. Heckl, *Single Mol.*, 2002, **3**, 25.

[6] J. Teyssandier, S. De Feyter and K. S. Mali, *Chem. Commun.*, 2016, **52**, 11465.

[7] M. Jabłonski and M Palusiak, *Phys. Chem. Chem. Phys.*, 2009, **11**, 5711.

[8] M. Nishio, *Phys. Chem. Chem. Phys.*, 2011, **13**, 13873.

[9] S. Ghosh, P. Chopra and S. Wategaonkar, *Phys. Chem. Chem. Phys.*, 2020, **22**, 17482.

[10] R. Chelli, F. L. Gervasio, P. Procacci and V. Schettino, *J. Am. Chem. Soc.*, 2002, **124**, 6133.

[11] H. J. Schneider, *Angew. Chem. Int. Ed.*, 2009, **48**, 3924.

[12] S. Yamada and J. Fossey, *Org. Biomol. Chem.*, 2011, **9**, 7275.

[13] D. Kim, E. C. Lee, K. S. Kim and P. Tarakeshwar, *J. Phys. Chem. A*, 2007, **111**, 7980.

[14] P. Ballester, *Acc. Chem. Res.*, 2013, **46**, 874.

[15] J. W. Steed and J. L. Atwood, *Supramolecular Chemistry*, 3rd ed.; John Wiley & Sons: Hoboken, NJ, USA, 2022; pp. 1–20.

[16] B. W. Müller and U. Brauns, *J. Pharm. Sci.*, 1986, **75**, 571.

[17] A. R. S. Couto, A. Ryzhakov and T. Loftsson, *Materials*, 2018, **11**, 1971.

[18] T. Tyrikos-Ergas, G. Fittolani, P. H. Seerberger and M. Delianco, *Biomacromolecules*, 2020**, 21**, 18.

[19] S. H. Gellman, *Acc. Chem. Res.*, 1998, **31**, 173.

[20] C. D. Gutsche, *Calixarenes Revisited: Monographs in Supramolecular Chemistry*, Royal Society of Chemistry, Cambridge, 1998.

[21] P. Neri, J. L. Sessler and M. X. Wang, *Calixarenes and Beyond*; Springer International Publishing: Cham, Switzerland, 2016.

[22] R. Behrend, E. Meyer and F. Rusche, *Liebigs Ann. Chem.*, 1905, **339**, 1.

[23] K. I. Assaf and W. M. Nau, *Chem. Soc. Rev.*, 2015, **44**, 394.

[24] M. Gosecki, M. Urbaniak, B. Gostynski and M. Gosecka, *J. Phys. Chem. C*, 2020, **124**, 8401.

[25] R. P. Sijbesma, A. P. M. Kentgens and R. J. M. Nolte, *J. Org. Chem.*, 1991, **56**, 3199.

[26] R.P. Sijbesma, A. P. M. Kentgens and E. T. G. Lutz, *J. Am. Chem. Soc.*, 1993, **115**, 8999.

[27] R. J. Jansen, R. de Gelder, A. E. Rowan, H. W. Scheeren and R. J. M. Nolte, *J. Org. Chem.*, 2001,**66**, 2643.

[28] J. Boer and G. B. E. Jemec, *Clin. Exp. Dermatol.*, 2010, **35**, 36.

[29] P. Livant and W. Xu, *J. Org. Chem.*, 1998, **63**, 636.

[30] S. Khatib, O. Nerya, R. Musa, S. Tamir, T. Peter and J. Vaya, *J. Med. Chem.*, 2007, **50**, 2676.

[31] B. H. Patel and A. G. Barrett, *J. Org. Chem.*, 2012, **77**, 11296.

[32] A. Ballesteros-Gómez, Á. Aragón, N. Van den Eede, J. de Boer and A. Covaci, *Environ. Sci. Technol.*, 2016, **50**, 1934.

[33] S. Ferreira-Guedes and A. L. Lúcia Leitão, *Ecotoxicol. Environ. Saf.*, 2018, **150**, 240.

[34] S. K. Hahn, J. Kielhorn, J. Koppenhöfer, A. Wibbertmann and I. Mangelsdorf, *Resorcinol. Concise International Chemical Assessment Document 71*; World Health Organization, 2006.

[35] D. N. Lande, S. A. Bhadane and S. P. Gejji, *J. Phys. Chem. A*, 2017, **121**, 1814.

[36] J. N. H. Reek, A. H. Priem, H. Engelkamp, A. E. Rowan, J. A. A. W. Elemans and R. J. M. Nolte, *J. Am. Chem. Soc.*, 1997, **119**, 9956.

[37] C. A. Hunter, K. R. Lawson, J. Perkins and C. J. Urch, *J. Chem. Soc., Perkin trans.*, 2001, **2**, 651.

[38] S. E. Wheeler, *Acc. Chem. Res.*, 2013, **46**, 1029.

[39] C. A. Hunter and J. K. M. Sanders, *J. Am. Chem. Soc.*, 1990, **112**, 5525.

[40] F. Cozzi, M. Cinquini, R. Annunziata, T. Dwyer and J. S. Siegel, *J. Am. Chem. Soc.*, 1992, **114**, 5729.

[41] F. Cozzi, M. Cinquini, R. Annunziata and J. S. Siegel, *J. Am. Chem. Soc.*,1993, **115**, 5330.

[42] F. Cozzi, F. Ponzini, R. Annunziata, M. Cinquini and J. S. Siegel, *Angew. Chem. Int. Ed.*, 1995, **34**, 1019.

[43] F. Cozzi, R. Annunziata, M. Benaglia, M. Cinquini, L. Raimondi, K. K. Baldridge and J. S. Siegel, *Org. Biomol. Chem.*, 2003, **1**, 157.

[44] F. Cozzi, R. Annunziata, M. Benaglia, K. K. Baldridge, G. Aguirre, J. Estrada, Y. Sritana-Anant and J. S. Siegel, *Phys. Chem. Chem. Phys.*, 2008, **10**, 2686.

[45] W. Kohn, *Rev. Mod. Phys.*, 1999, **71**, 1253.

[46] W. B. Schneider, G. Bistoni, M. Sparta, M. Saitow, C. Riplinger, A. A. Auer and F. Neese, *J. Chem. Theory Comput.*, 2016, **12**, 4778.

[47] R. F. W. Bader, *Acc. Chem. Res.*, 1985, **18**, 9.

[48] R. F. W. Bader, *Atoms in Molecules: A Quantum Theory*. The International Series of Monographs of Chemistry, No. 22, Clarendon Press: Oxford, UK, 1990.

[49] E. R. Johnson, S. Keinan, P. Mori-Sanchez, J. Contreras-García, A. J. Cohen and W. J. Yang, *J. Am. Chem. Soc.*, 2010, **132**, 6498.

[50] A. D. Beck, *J. Chem. Phys.*, 1993, **98**, 5648.

[51] S. Grimme, J. Antony, S. Ehrlich and H Krieg, *J. Chem. Phys.*, 2010, **132**, 154104.

[52] S. Grimme, S. Ehrlich and L. Goerigk, *J. Comput. Chem.*, 2011, **32**, 1456.

[53] M. J. Frisch, G. W. Trucks, H. B. Schlegel, G. E. Scuseria, M. A. Robb, J. R. Cheeseman, G. Scalmani, V. Barone, G. A. Petersson, H. Nakatsuji, X. Li, M. Caricato, A. V. Marenich, J. Bloino, B. G. Janesko, R. Gomperts, B. Mennucci, H. P. Hratchian, J. V. Ortiz, A. F. Izmaylov, J. L. Sonnenberg, D. Williams-Young, F. Ding, F. Lipparini, F. Egidi, J. Goings, B. Peng, A. Petrone, T. Henderson, D. Ranasinghe, V. G. Zakrzewski, J. Gao, N. Rega, G. Zheng, W. Liang, M. Hada, M. Ehara, K. Toyota, R. Fukuda, J. Hasegawa, M. Ishida, T. Nakajima, Y. Honda, O. Kitao, H. Nakai, T. Vreven, K. Throssell, J. A. Montgomery, Jr., J. E. Peralta, F. Ogliaro, M. J. Bearpark, J. J. Heyd, E. N. Brothers, K. N. Kudin, V. N. Staroverov, T. A. Keith, R. Kobayashi, J. Normand, K. Raghavachari, A. P. Rendell, J. C. Burant, S. S. Iyengar, J. Tomasi, M. Cossi, J. M. Millam, M. Klene, C Adamo, R. Cammi, J. W. Ochterski, R. L. Martin, K. Morokuma, O. Farkas, J. B. Foresman and D. J. Fox, Gaussian, 16 Revision C.01, Gaussian Inc. Wallingford CT, 2016.

[54] T. H. Dunning, *J. Chem. Phys.*, 1989, **90**, 1007.

[55] D. E. Woon and T. H. Dunning, *J. Chem. Phys.*, 1993, **98**, 1358.

[56] A. K. Wilson, D. E. Woon, K. A. Peterson and T. H. Dunning, *J. Chem. Phys.*, 1999, **110**, 7667.

[57] A. Jaworski, N. Hedin and A. Jaworski, *Phys. Chem. Chem. Phys.*, 2021, **23**, 21554.

[58] F. Neese, *Wiley Interdiscip. Rev.: Comput. Mol. Sci.*, 2012, **2**, 73.

[59] F. Neese, *Wiley Interdiscip. Rev.: Comput. Mol. Sci.*, 2018, **8**, e1327.

[60] T. Lu and F. Chen, *J. Comput. Chem.*, 2012, **33**, 580.

Chapter 6

Investigation of the Noncovalent Interactions of the Histidine Functionalized Perylene diimide (PDI) with Amyloid-β (Aβ) Fibrils Protein

6.1. Introduction

One of the main pathological hallmarks of Alzheimer's disease (AD) is the accumulation of the amyloid-β proteins peptides (Aβ).[1-9] These Aβs are derived from the Aβ precursor protein (APP) through an enzymatic cleavage process and are released into the extracellular environment.[10] The neurotoxicity characteristics of the Aβ, as well as the aggregation properties of both the Aβ forms (Aβ40 and Aβ42), play a significant role in deteriorating the memory function of the AD's patient.[10-12] Regulating the production of Aβ and their toxicity, inhibition of the Aβ peptides aggregations using the compounds including small molecules,[13,14] natural products,[15,16] peptides,[17-19] and metal chelating agents[20-22] are the active research fields of AD. However, several drug molecules targeting the Aβ have encountered various obstacles.

Earlier studies reported that monomeric state of Aβ is nontoxic,[23,24] but, upon self-aggregation generated various forms such as oligomers, fibrils, and mature fibrils, which significantly escalate the toxicity.[25,26] Since identifying Aβ as an important target for AD, various molecules, including natural products such as alkaloids, terpenoids, polyphenols, etc., have been studied to develop drugs for AD.[15,16] *In vitro* studies found that curcumin compound and its derivatives inhibit and destabilize the Aβ fibril formation.[27] Flavonoid compounds such as quercetin and rutin exhibited the inhibition of Aβ fibril formation and disaggregated Aβ fibril.[28] *In vitro* studies demonstrated that the bioactive compound 7-methyl gallic acid extracted from the *Terminalia chebula* and *Terminalia arjuna* plants effectively inhibits and disaggregates the Aβ fibril.[29] Compounds such as melatonin and serotonin exhibited neuroprotective properties and can inhibit and destabilize the Aβ fibril.[30-32]

Perylenediimide (PDI) compounds are extensively explored in the domain of organic fluorescent materials due to their properties such as strong absorption in the visible region, high fluorescent quantum yields, optoelectronic properties, and potential to co-assembly with other supramolecular compounds.[33-36] Due to the significant π-π interactions between the perylene cores of the PDI and its derivates, they exhibit a high tendency to aggregate themselves.[37,38] Different PDI derivative compounds were reported by introducing the substituents on the side or end chain of the PDI. Such modified PDI derivatives have been widely used in various fields, including photocatalysis,[39] optical sensing,[40] light-emitting diodes,[41] organic electronics/semiconductors, etc.[42,43] Besides the above applications, PDI derivatives are also used in biochemical research. Barooah et al. reported the phenylalanine-derivatized perylenediimide (L-Phe-PDI) and studied the interaction with a model protein and insulin.[44] Bioimaging investigation for the interaction of L-Phe-PDI with Aβ-mutant *Drosophila* fly exhibited that L-Phe-PDI can cross over the blood-brain/blood-retina barrier with no toxicity. In addition, they also observed that this compound shows disintegration of the Aβ fibril aggregates.[44] Iyer and coworkers reported the histidine (HIS) functionalized perylenediimide (PDI-HIS) material which is biocompatible.[45] Moreover, the thioflavin T(ThT) assay, along with the spectroscopic and microscopic investigation, demonstrates that PDI-HIS molecule co-assembly with Aβ40 and amyloid aggregates in cerebrospinal fluid (CSF), leading to the formation of hybrid micro-rod structures.[45]

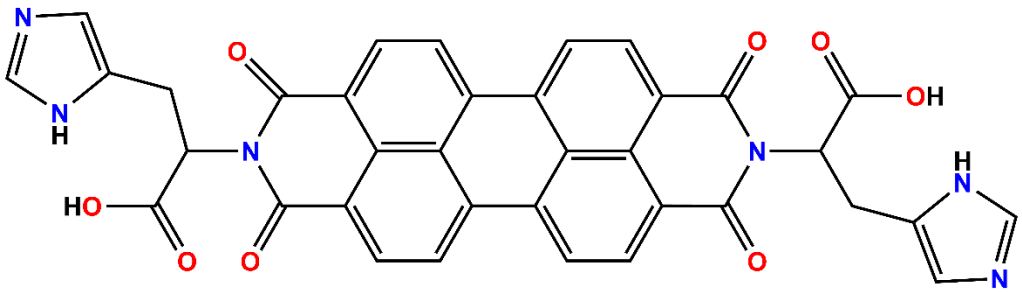

Figure 6.1. Molecular structure of histidine (HIS) functionalized perylenediimide (PDI-HIS).

Several computational molecular dynamics (MD) simulation studies have been documented about the atomic-scale mechanisms of molecules binding with Aβ fibrils. A combination of *in vitro* and MD simulation studies reported that the naturally occurring compounds Brazilin and hematoxylin extracted from the sappan wood show the effect of altering the Aβ monomer and mature fibrils.[46,47] Lemkul et al. highlighted the alteration of Aβ fibril by the bioflavonoid compound Morin.[48] This compound entered the hydrophobic core region of the Aβ fibril and alters the salt bridge between Asp23 and Lsy28. Tianhan Kai et al. demonstrated the natural

product compound Tabersonine can interact with the aromatic and hydrophobic residues of β-sheet grooves of the Aβ fibrils and inhibit the aggregations.[49] MD simulation studies demonstrated that the natural product compound dihydrochalcone extracted from pepper can potentially disrupt the Aβ fibrils.[50]

Moreover, the compound epigallocatechin-3-gallate was also reported as a β-sheet breaker and inhibits the aggregations.[51] Gupta et al. investigated the effect of the four phenolic compounds, namely caffeic acid, epigallocatechin, gallic acid, and ellagic acid, on the Aβ fibrils using molecular docking and molecular dynamics simulations.[52] In their investigation, the compound ellagic acid was the best binder to the Aβ fibril and destabilized the Aβ fibril. Agrawal et al. studied the molecular dynamics (MD) simulations for the interaction of 12-crown-4 molecule with Aβ1-40 fibrils.[53] They found that the 12-crown-4 entered into the hydrophobic region of the Aβ fibril and interacted with the hydrophobic residues of the fibrils. This process results in the breaking of intersheet hydrophobic interactions and the opening of the U-shaped topology of the Aβ fibrils.[53]

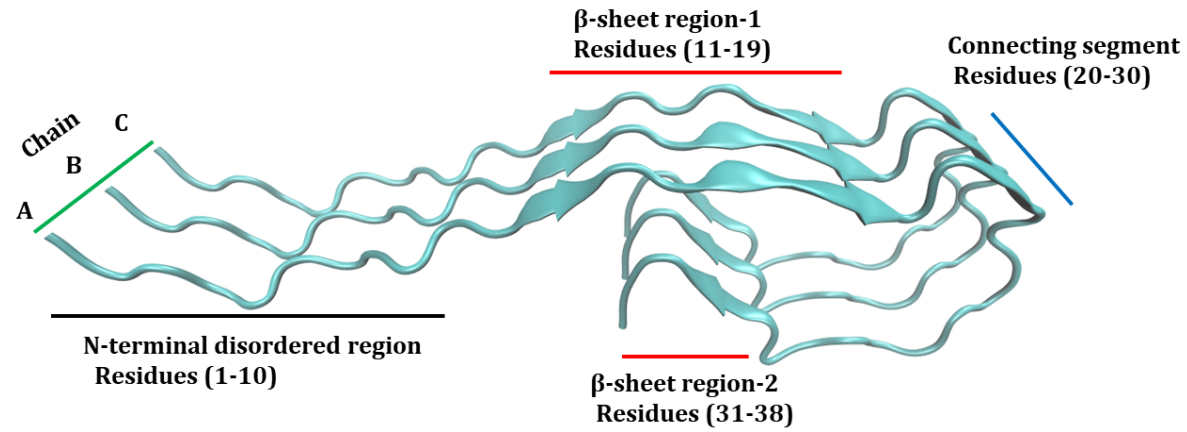

Figure 6.2. Illustration of single trimer Aβ1-40 (Aβ40) fibril structure consisting of β-sheet region-1, β-sheet region-2, N-terminal disordered region, and connecting segment. The below box shows the residues 1 to 40 present in the single chain of Aβ40 fibrils.

In this chapter, we have explored the modulating or disrupting effect of PDI-HIS on the Aβ fibril by implementing molecular docking and molecular dynamics (MD) simulations studies. Under physiological conditions the two nitrogen atoms present in the imidazole ring of the

histidine (HIS) have possibility to exhibited three protonation states δ (N-H) or ε (N-H) or combination of both.[54] At this moment, we consider δ and ε states of histidine present in PDI-HIS. The detail studied of δ form of PDI-HIS (Figure 6.1) are presented in this Chapter while the ε form are presented in the Appendix-D. Moreover, the noncovalent interactions between the PDI-HIS and Aβ fibril were also examined. We considered the single trimer Aβ40 fibril unit, as presented in Figure 6.2 for our study, which is obtained from the three trimeric units of the Aβ fibril (PDB: 2M4J).[55] This Aβ40 structure comprises an N-terminal disordered segment encompassing residues 1-10, two β-sheets regions containing residues 11-19 and residues 31-38, and a connecting segment. For the covinent

6.2. Computational Details

6.2.1. Electronic Structure Calculations

The molecular geometry optimization and vibrational frequency calculation of the histidine functionalized perylenediimide (PDI-HIS) was performed using the Minnesota Functional M06-2X with def2-TZVP basis set.[56,57] In this optimization, we considered the total charge of the PDI-HIS to be -2, which arises due to the deprotonation of the two carboxylic acid groups present in the PDI-HIS. The calculation was performed in the Gaussian 16 software package.[58]

6.2.2 Molecular Docking Analysis

Molecular docking calculations were performed using the Autodock Suite 4.2.1[59] between the optimized molecule PDI-HIS and amyloid-β protein (Aβ40) to generate the different protein-ligand docked poses. All the required input files, such as PDBQT for molecular docking, were obtained using the AutoDockTools. The three-dimensional molecular structure of Aβ40 fibril (PDB: 2M4J) was obtained from the protein data bank (PDB) and considered a receptor protein in our investigation. The Aβ40 fibril used in this study is the single trimer unit (Figure 6.2), extracted from the experimental reported three trimeric units and arranged in three-fold symmetry. The preparation for docking includes adding Gasteiger charges into the ligand and considering polar hydrogen atoms to both the protein and ligand since the specific binding site of Aβ40 fibril is not known. Therefore, we performed the blind docking, considering the entire protein surface. In this process of docking, the protein Aβ40 fibril was treated as a rigid entity, while the molecule PDI-HIS was regarded as a flexible system. The grid box size measuring 126 ×126× 68 $Å^3$ around the Aβ40 fibril protein was employed, with a grid default spacing of

0.375 Å. The Lamarckian genetic algorithm (GA) was implemented to search the conformation.[60]

Further, in our molecular docking calculations, the following parameters were considered: GA population size of 150, maximum energy evaluation of 2500000, maximum number generation of 27000, and rate of gene mutation and crossover are 0.02 and 0.08, respectively. The ten docked poses were generated, and visualization was done using the visual molecular dynamics (VMD) 1.9.3 software package.[61]

6.2.3. Molecular Dynamics Simulations Studies

The selected docked complexes of PDI-HIS-Aβ40 obtained from the molecular docking calculations were subjected to perform the MD simulations using the GROMACS software.[62] The restrained electrostatic potential (RESP) approach was implemented to obtain the atomic charges of the PDI-HIS, and calculation was performed at the M06-2X/def2-TZVP level of theory using the Gaussian and Multiwfn software packages.[63] Using the Sobtop package, [64] the general Amber force field (GAFF)[65] parameters for the PDI-HIS were generated. For the Aβ40 protein and ions, we employed the Amber99sb-ildnp.ff force field.[66] The protein-ligand complex was solvated in the cubic box size of $9.5 \times 9.5 \times 9.5$ nm^3 with the single-point charge (SPC) water model.[67] Proper numbers of eleven Na^+ ions were added to maintain the system's neutrality. Subsequently, the energy minimization was conducted using the steepest descent minimization algorithm with 5000 steps. The complexes were equilibrated for 100 ps under the canonical NVT ensemble, followed by 100 ps and isobaric-isothermic NPT ensemble.[68,69] The temperature and pressure used in the study are 310 K and 1 atm pressure, respectively. The hydrogen bond of the Aβ40 and PDI-HIS was constructed using the LINCS algorithm.[70] The long-range electrostatic interactions were determined using the Particle Mesh Ewald (PME) method with a cut-off value of 1.2 nm.[71]

Moreover, the van der Waals interaction was estimated with a cut-off value of 1.2 nm. Subsequently, the equilibrated system was subjected to a production MD for 400 ns for each docked pose. The MD trajectories were visualized using the VMD package.[61] Without PDI-HIS molecule, MD simulations were performed to check stability and the changes on the geometrical structure of the Aβ40 fibrils (nine Na^+ ions were added to maintain neutrality) and their U-shaped feature. The simulation was conducted for 400 ns.

6.2.4. Analysis of MD Trajectories

The generated MD trajectories were used for extracting several parameters through the tools available in the GROMACS software.[62] The structural stability of the Aβ40-PDI-HIS system was estimated by calculating the Cα-RMSD (Root Mean Square Deviation) using the g_rms tool. The g_hbond tool was employed to estimate the quantity of hydrogen bonds within the Aβ40 fibril, both with or without PDI-HIS. The solvent-accessible surface area (SASA) of the Aβ40 fibril with and without PDI-HIS systems was obtained through g_sasa module. In this analysis, the SASA value will be computed across the protein chain surface of the Aβ40, which provides information about the structural changes of the protein. Further, we assessed the secondary structural content of the Aβ40 fibril, and the analysis was conducted by utilizing the dictionary of the secondary structure of proteins (DSSP) tool.

6.2.5 Binding Free Energy Analysis by MM/PB(GB)SA

In order to estimate the interaction of Aβ40 with PDI-HIS, the binding free energy analysis was conducted by employing the most popular method known as Molecular Mechanics/Poisson-Boltzmann (Generalized-Born) Surface Area [MM/PB(GB)SA].[72-76] In MM/PB(GB)SA method, the binding free energy of the complex system can be obtained as

$$\Delta G_{binding} = \Delta E_{MM} + \Delta G_{polar} + \Delta G_{non-polar} - T\Delta S \quad (6.1)$$

In Eq. 6.1, ΔE_{MM} denotes the molecular mechanics energy contribution in a vacuum environment. The components ΔG_{polar} and $\Delta G_{non-polar}$ account for the polar and non-polar contribution to the solvation energy. The polar contribution ΔG_{polar} can be estimated by Poisson-Boltzmann (PB) or GB (Generalized-Born) methods. Meanwhile, $\Delta G_{non-polar}$ contribution to the binding energy is estimated through the solvent-accessible surface area (SASA). We have neglected "$T\Delta S$" term since estimating the entropy component is computationally expensive. The gmx_MMPBSA tool,[76] in cooperation with the GROMACS package, calculates binding free energy. In binding free energy calculations, we considered the last 20 ns trajectory employing a time interval of 100 ps to reduce the computational cost.

6.3. Results and Discussion

6.3.1. Molecular Docking of Aβ40 Fibril with PDI-HIS

The Computational Details section explains the molecular docking procedure of Aβ40 with PDI-HIS. The generated ten docked poses are displayed in Figure 6.2. The binding energies of

the ten docked poses obtained through molecular docking range from –7.97 kcal mol^{-1} to –5.62 kcal mol^{-1} (P1 to P10). The amino acid residues of Aβ40 fibrils participated in the interaction with PDI-HIS for the docked poses (P1 to P10) are presented in Table 6.1. Among the docked poses, P1 exhibited the highest binding energy value in magnitude, while P10 displayed the lowest. The more negative value signifies that PDI-HIS strongly binds to the Aβ40 fibrils. Docked poses P1, P2, and P3 exhibited similar binding regions of the PDI-HIS molecule (Figure 6.2). Some of the common residues of Aβ40 involved in the interactions for these three docked poses are namely Lys16 and Val18 of chain A; Lys16, Leu17, and Val18 of chain B; Lys16, Leu17, and Val18 of chain C. In the case of docked poses P4 and P6, the common residues that participated in the interactions with PDI-HIS are Val12, His13, and His14 of chain A; Val12, His13, and His14 of chain B; Val12, His13, and His14 of chain C. On the other hand, in docked pose P5 the involved residues are Lys16, Leu17, Val18, Phe19, Phe20, Ala21, Gly29, Ala30, Ile31, Ile32, and Leu34 of chain C. Moreover, in docked pose P7, PDI-HIS interacts with residues Val12, His14, and Lys16 of chain A and Lys16 of chain C. In docked pose P8, residues His14, Gln15, Lys16, Leu17, Phen19, and Leu34 of chain C are exhibited in the interaction with the PDI-HIS molecule. The docked pose P8 consists of residues Val12, His13, and His14 of chain A; Val12, His13, His14, and Lys16 of chain B; Lys16 of chain C. Finally, the residues Phe20, Lys28, Ile31, Ile32, Gly33, and Leu34 of chain C of Aβ40 exhibited interaction with PDI-HIS molecule in P10.

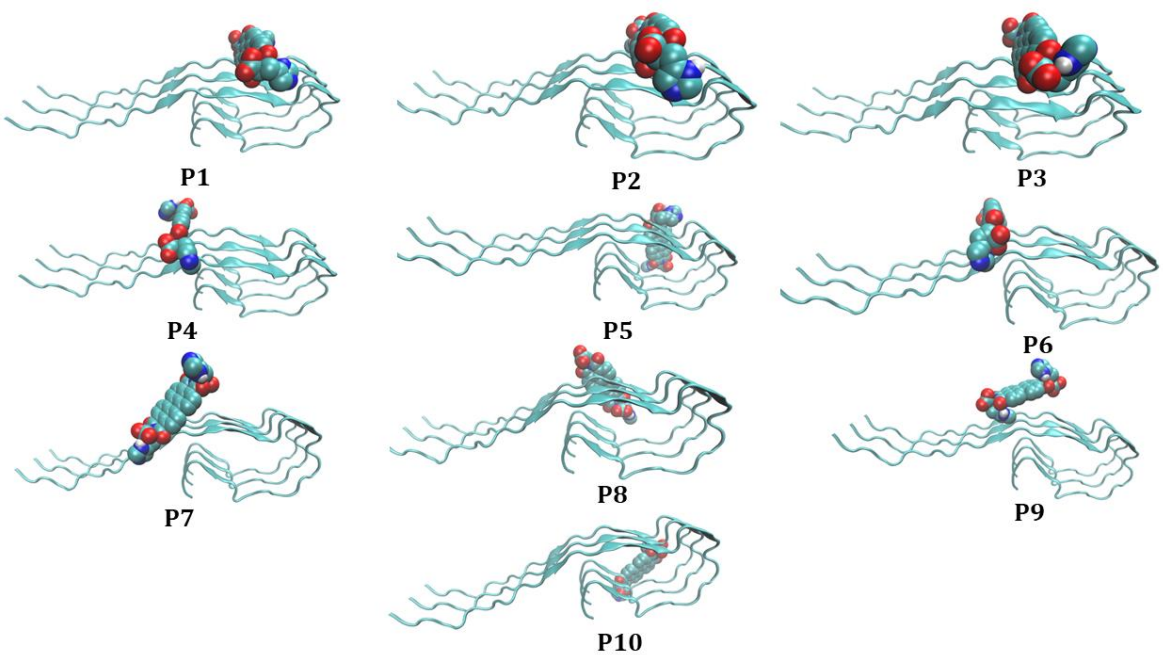

Figure 6.3. Docked poses P1 to P10 obtained from the molecular docking of PDI-HIS with Aβ40 fibril.

Table 6.1. Generated docked poses (P1 to P10) with their binding energy (ΔG) (in kcal mol^{-1}) and residues involved in the interactions.

Docked Pose	Binding Energy, ΔG	Residues involved
P1	−7.97	A (Lys16, Leu17, Val18); B (Lys16, Leu17, Val18) ; C (Lys16, Leu17, Val18)
P2	−7.69	A (Lys16, Leu17, Val18); B (Lys16, Leu17, Val18) ; C (Lys16, Leu17, Val18)
P3	−7.21	A (Lys16, Val18); B (Lys16, Leu17, Val18); C (Lys16, Leu17, Val18)
P4	−6.41	A (Val12, His13, His14); B (Val12, His13, His14); C (Val12, His13, His14)
P5	−6.27	C (Lys16, Leu17, Val18, Phe19, Phe20, Ala21, Gly29, Ala30, Ile31, Ile32, Leu34)
P6	−6.19	A (Val12, His13, His14); B (Val12, His13, His14); C (Val12, His13, His14)
P7	−6.14	A (Val12, His14, Lys16); B (Lys16)
P8	−5.62	C (His14, Gln15, Lys16, Leu17, Phen19, Leu34)
P9	−5.49	A (Val12, His13, His14); B (Val12, His13, His14, Lys16); C (Lys16)
P10	−5.37	C (Phe20, Lys28, Ile31, Ile32, Gly33, Leu34)

6.3.2. Molecular Dynamics Simulations Studies of PDI-HIS with Aβ40 Fibril

The Aβ40-PDI-HIS docked poses obtained from the molecular docking studies were considered for performing the MD simulations. The binding pattern of the PDI-HIS on the region of Aβ40 fibril in docked poses (P1, P2, P3, P4, and P6) were similar (Figure 6.3). At the same time, we also noticed that the docked poses P5, P8, and P10 have similar PDI-HIS binding

locations on the Aβ40 fibril. Moreover, in docked poses P7 and P9, we observed identical binding modes of PDI-HIS. Therefore, out of the ten generated docked poses, we have selected three pocked poses, namely P1, P5, and P7, for performing the MD simulations.

In order to understand the conformational changes and stability of Aβ40 fibril, we performed the MD simulations of 400 ns in the absence of PDI-HIS. Different snapshots of the Aβ40 structures collected at various times are presented in Figure 6.4. Subsequently, the MD simulations of the docked pose P1, P5, and P7 were performed. The comparison plots of Cα-RMSD of Aβ40 fibril with or without the PDI-HIS molecule are presented in Figure 6.5. In the absence of PDI-HIS, the Cα-RMSD value of the Aβ40 showed a rise to approximately 1.2 nm within the initial 1 ns simulation time. Afterward, the RMSD value decreased, fluctuated, and remained stable during the simulation. This observation aligns with the MD simulation studies of the Aβ40 reported by Agrawal et al.[53]. Therefore, these results revealed that the structure of the Aβ40 fibril is stable in the water solvent environment. The MD simulations result of the docked pose P1 showed that the Cα-RMSD of the Aβ40 in the PDI-HIS system is closely similar to the Cα-RMSD of the Aβ40 without PDI-HIS system (Figure 6.5a). At the initial time t = 0 ns, the PDI-HIS bound on β-sheet region-1 of Aβ40 fibril with the interaction of residues Lys16, Leu17, and Val18 of chains A, B, and C (Figure 6.6). After 100 ns, the PDI-HIS started moving towards the cavity region of Aβ40 fibril. However, we could not observe the PDI-HIS entered inside the cavity region of the Aβ40 under the considered simulation time of 400 ns. Likewise, for the P5 docked pose, the Cα-RMSD (Figure 6.5b) of Aβ40 fibril showed a slightly similar pattern as observed in the P1. During the simulation time of 400 ns, the PDI-HIS of P7 confined on the chain C near the cavity region of Aβ40 fibril (Figure 6.7). After 260 ns, the structural disruption of the Aβ40 fibril due to the presence of PDI-HIS was slightly increased. This observation correlates with the Cα-RMSD (Figure 6.5b) and Aβ40 fibril structural changes (Figure 6.7).

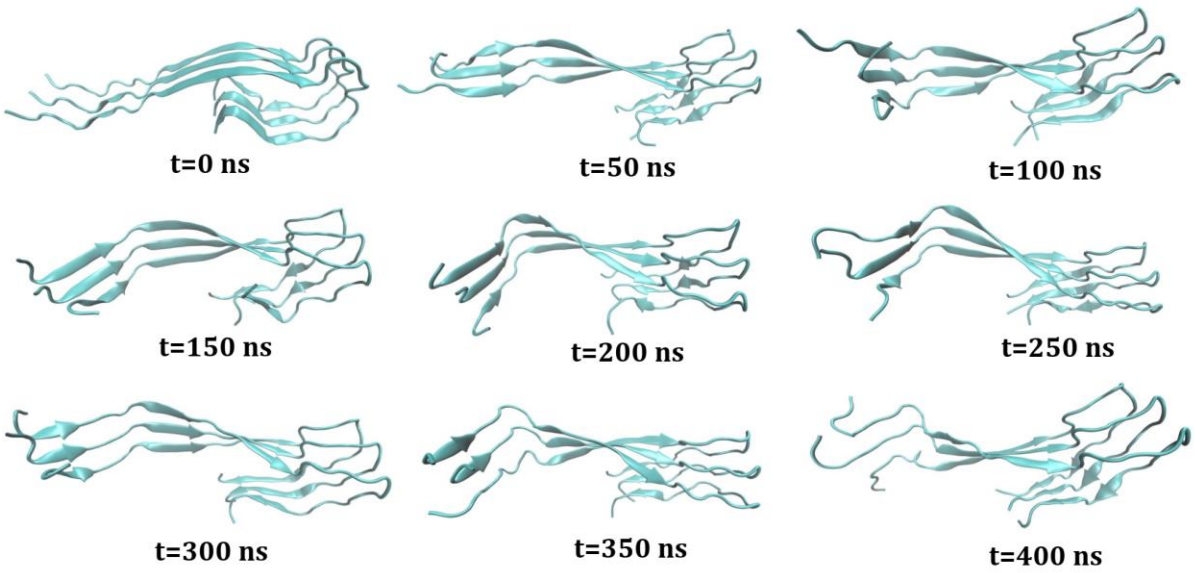

Figure 6.4. Some snapshots from the MD simulations representing the structures of the Aβ40 fibril protein in water collected at different times.

Moreover, in the case of P7, the Cα-RMSD value of Aβ40 increases and reaches the maximum value of approximately 1.4 nm at around 100 ns, as shown in Figure 6.5c. Afterward, the RMSD decreased and fluctuated before maintaining the equilibrium throughout the simulation. The structural disruption effect of PDI-HIS on the Aβ40 fibril is very significant in this case. This effect can be observed from the structural changes of the Aβ40 fibril presented in Figure 6.8. At t = 0 ns, the PDI-HIS bound on the β-sheet region-1 of the Aβ40 fibril with a maximum number of residues interaction of chain A. Over time, some residues, the parts of the N-terminal regions of chain A, started wrapping on the PDI-HIS (Figure 6.8) and slightly separated between chains A and B.

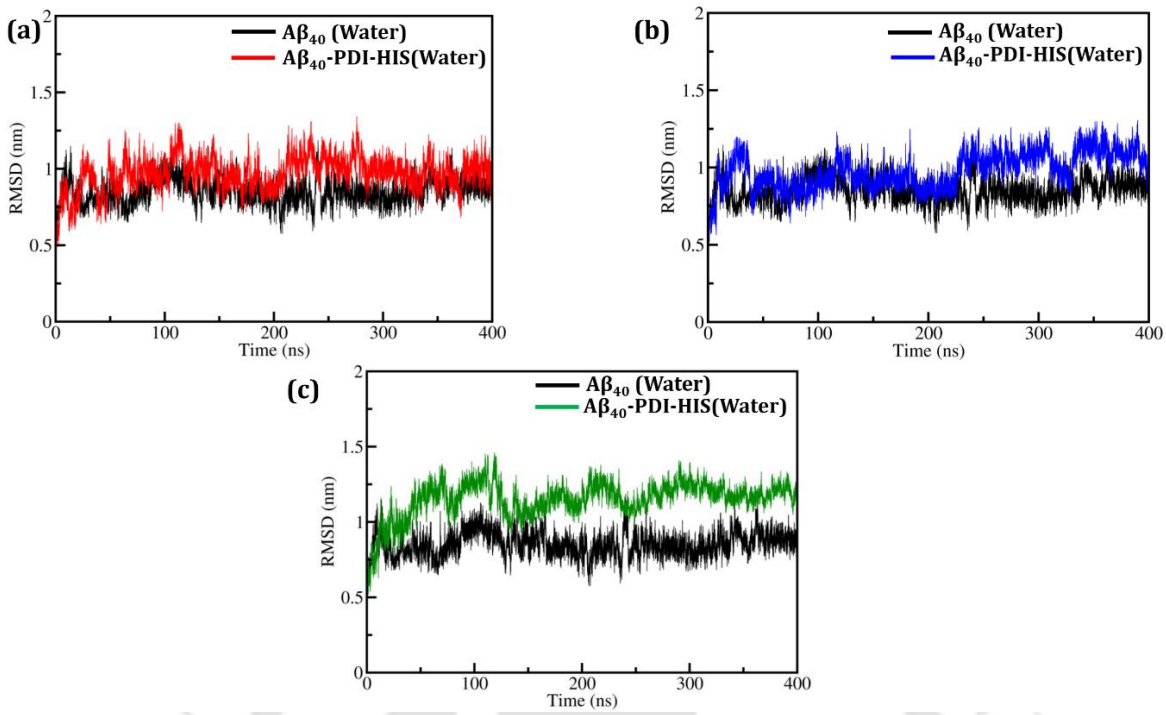

Figure 6.5. Cα-RMSD of Aβ1-40 fibril in the absence and presence of PDI-HIS; (a) Cα-RMSD of Aβ40 fibril in docked pose P1; (b) Cα-RMSD of the Aβ40 fibril in docked pose P5; and (c) Cα-RMSD of the Aβ40 fibril in docked pose P7.

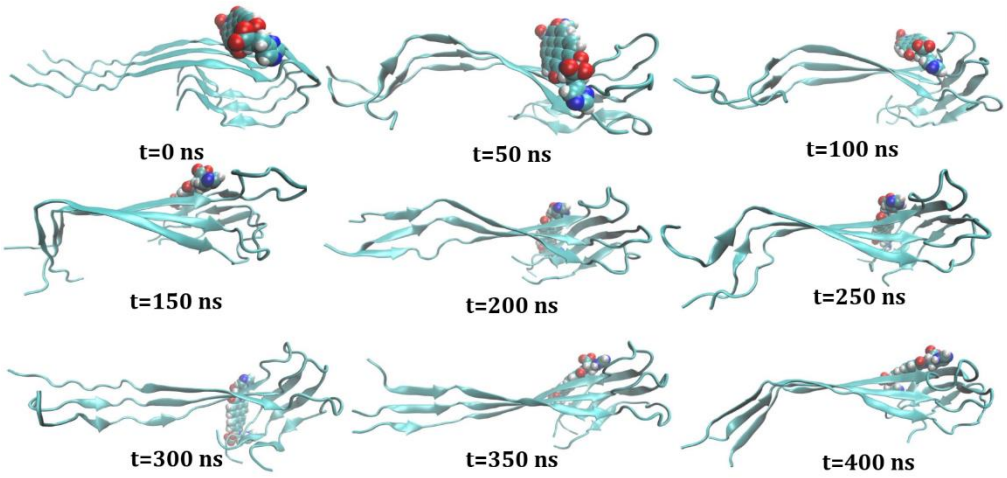

Figure 6.6. Some snapshots from the MD simulations representing the structures of the Aβ40-PDI-HIS of the P1 system collected at different times.

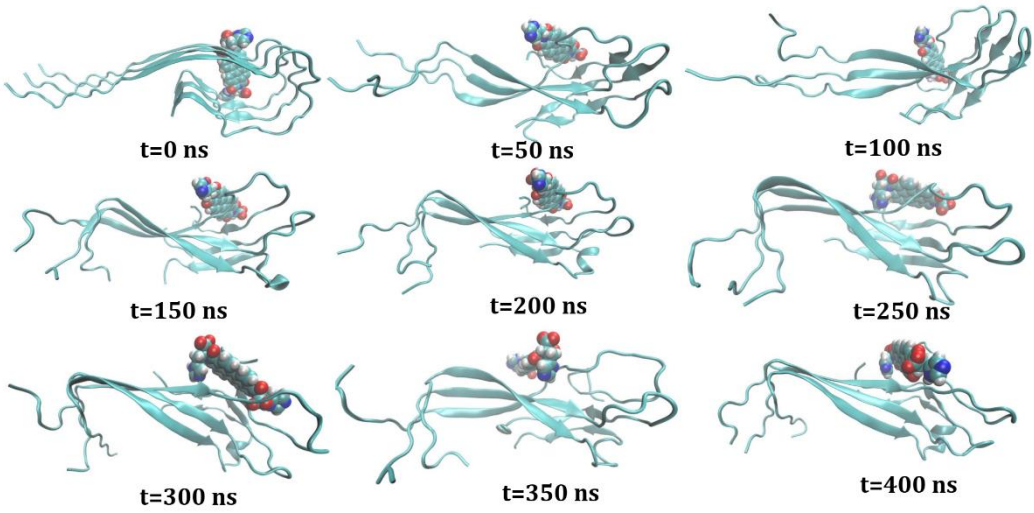

Figure 6.7. Some snapshots from the MD simulations representing the structures of the Aβ40-PDI-HIS of the P5 systems collected at different times.

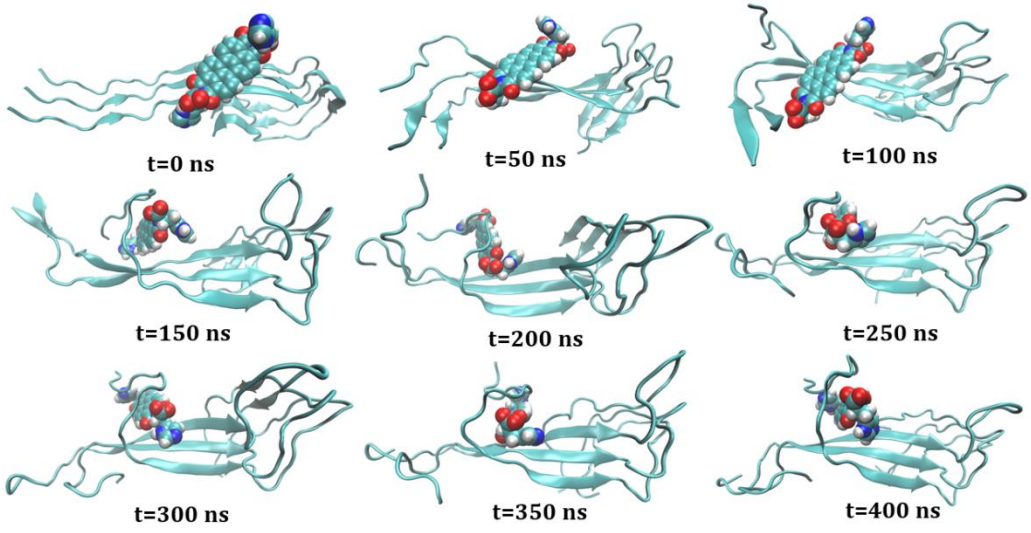

Figure 6.8. Some snapshots from the MD simulations representing the structures of the Aβ40-PDI-HIS of the P7 system collected at different times.

6.3.3. Hydrogen Bonding Interactions

The crucial role played by the noncovalent interactions, such as hydrogen bonding, for the stability of the protein is well known. Both theoretical[77] and experimental[78] studies highlighted the importance of the hydrogen bond network in enhancing the stability of the Aβ40 fibril protein. Moreover, in Aβ40 fibril, the interpeptide hydrogen bonds influenced the structural stability and aggregations. Therefore, evaluating the quantity of hydrogen bonds present in the systems of Aβ40 with and without the PDI-HIS molecule is necessary. The variation of overall intra and interpeptide hydrogen bonds present in Aβ40 with a simulation time for the docked poses P1, P5, and P7 are illustrated in Figure 6.9. Throughout the 400 ns

simulation period, we observed that the quantity of hydrogen bonds in the Aβ40 fibril of P1 and P5 was slightly diminished than that of the Aβ40 fibril system in water (Figure 6.9a and Figure 6.9b). This result suggests that the destabilizing effect of PDI-HIS on the Aβ40 is less significant in the case of P1 and P5.

Meanwhile, we found that the quantity of hydrogen bonds present in the Aβ40 of the P7 was significantly lower than the Aβ40 in the water system, which can be seen in Figure 6.9c. This result indicates that PDI-HIS destabilized the Aβ40. Furthermore, this reduction in the number of hydrogen bonds can be correlated with the Cα-RMSD (Figure 6.5c) and the structural changes of Aβ40 in the presence of PDI-HIS (Figure 6.8). At time t = 150 ns (Figure 6.8), the chain A region started separating away from chain B, resulting in increased interpeptide distances, and these consequences yield lesser chances of forming inter-hydrogen bonding between the chains.

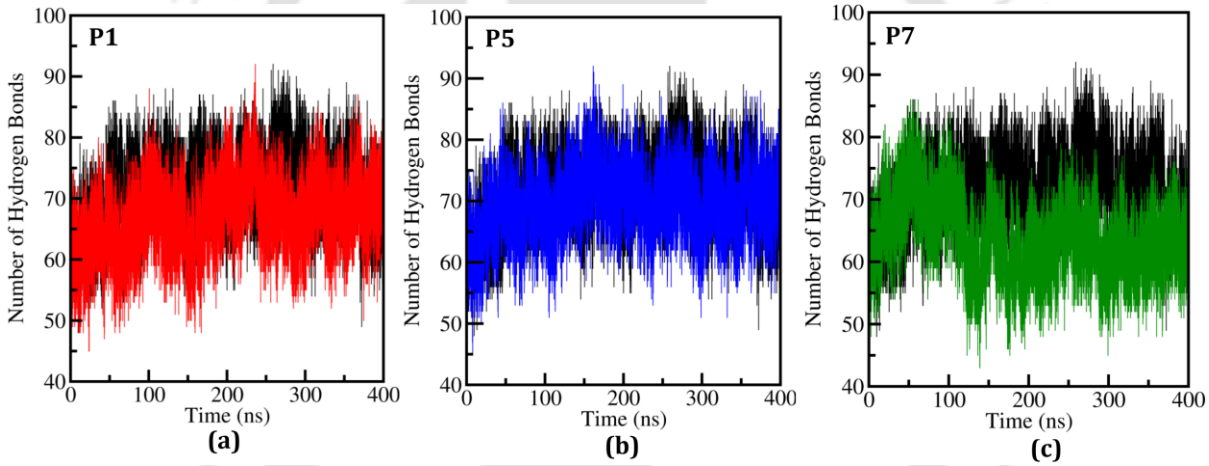

Figure 6.9. Number of hydrogen bonds of Aβ40 in water (black) and Aβ40-PDI-HIS of (a) docked pose P1 (red), (b) docked pose P5 (blue), and (c) docked pose P7 (green).

6.3.4. Solvent Accessible Surface Area (SASA) Analysis

SASA value of Aβ40 fibril protein was calculated in water, P1, P5, and P7. This value provides the water accessibility on the surface of protein. Moreover, it also suggested about the structural looseness of the protein. As the value increases, the structure of the Aβ becomes more flexible and relaxed. Figure 6.10 displays the variation of the SASA value of Aβ40 with time for the systems water and docked poses P1, P5, and P7. From Figure 6.10a and Figure 6.10b, the SASA value of Aβ40 in water is slightly lower than that of P1 and P5. This result shows that the exposure of protein chains of the Aβ40 in water solution is much less.

Furthermore, these results also indicate that the extent of structural disruption of Aβ40 fibril by PDI-HIS in P1 and P5 systems is less significant. On the other hand, we observed that the SASA value of Aβ40 fibril in P7 was comparatively larger than that of the values in the water system, as shown in Figure 6.10c. This major difference in the SASA value revealed that without PDI-HIS, the Aβ40 fibril exhibited stable conformation. But in the presence of PDI-HIS, the disruption of the chains for the Aβ40 increased and, consequently, more exposure to solvent environment. Notably, the elevated value observed in the SASA value in Figure 6.10c implies that PDI-HIS destabilized the Aβ40 fibril.

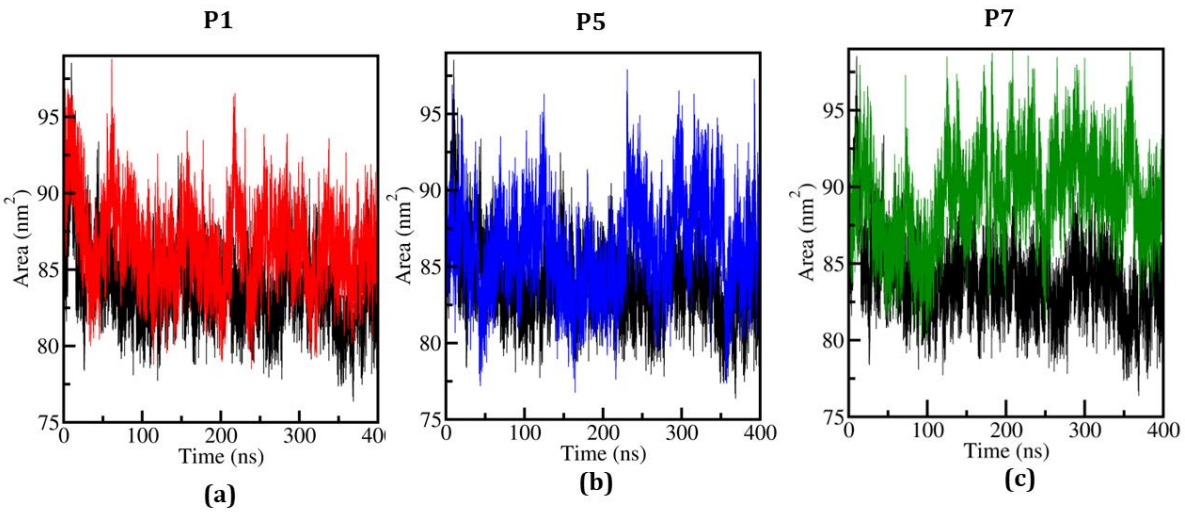

Figure 6.10. SASA value of Aβ40 in the absence of PDI-HIS (black); SASA value of Aβ40 in (a) P1 (red), (b) P5 (blue), and (c) P7 (green).

6.3.5. Secondary Structure Analysis

Earlier studies have highlighted that β-sheet is the primary structural constituent of the Aβ fibrils.[52,79] Additionally, it plays a significant role in the stability of the fibrils. Therefore, evaluation of β-sheet content is necessary to understand the effect of the ligand. In this direction, we have performed the secondary structure analysis for the systems Aβ40 in the absence of PDI-HI and Aβ40-PDI-HIS in P1, P5, and P7 docked poses by using the dictionary of the secondary structure of proteins (DSSP) tool. The plot for the profiles of the secondary structure of Aβ40 variation with time for the considered systems is presented in Figure 6.11. Figure 6.11 provides information about the contents of coil, β-sheet (B-sheet), β-bridge (B-sheet), bend, turn, and 3-Helix in Aβ40 fibril. From Figure 6.11, the red region represents the residues involved in the β-sheet content. The amount of β-sheet content of Aβ40 fibril in P7 (Figure 6.11d) is significantly lesser when compared to Aβ40 in water (Figure 6.11a). On the

other hand, the reduction in the β-sheet content is less significant in P1 (Figure 6.11b) and P5 (Figure 6.11c). In addition, the bend content of Aβ40 in P7 was increased with time, but this change is less in P1 and P5. Moreover, the variation of the other secondary structural parameters in P1, P5, and P7 are comparatively less pronounced.

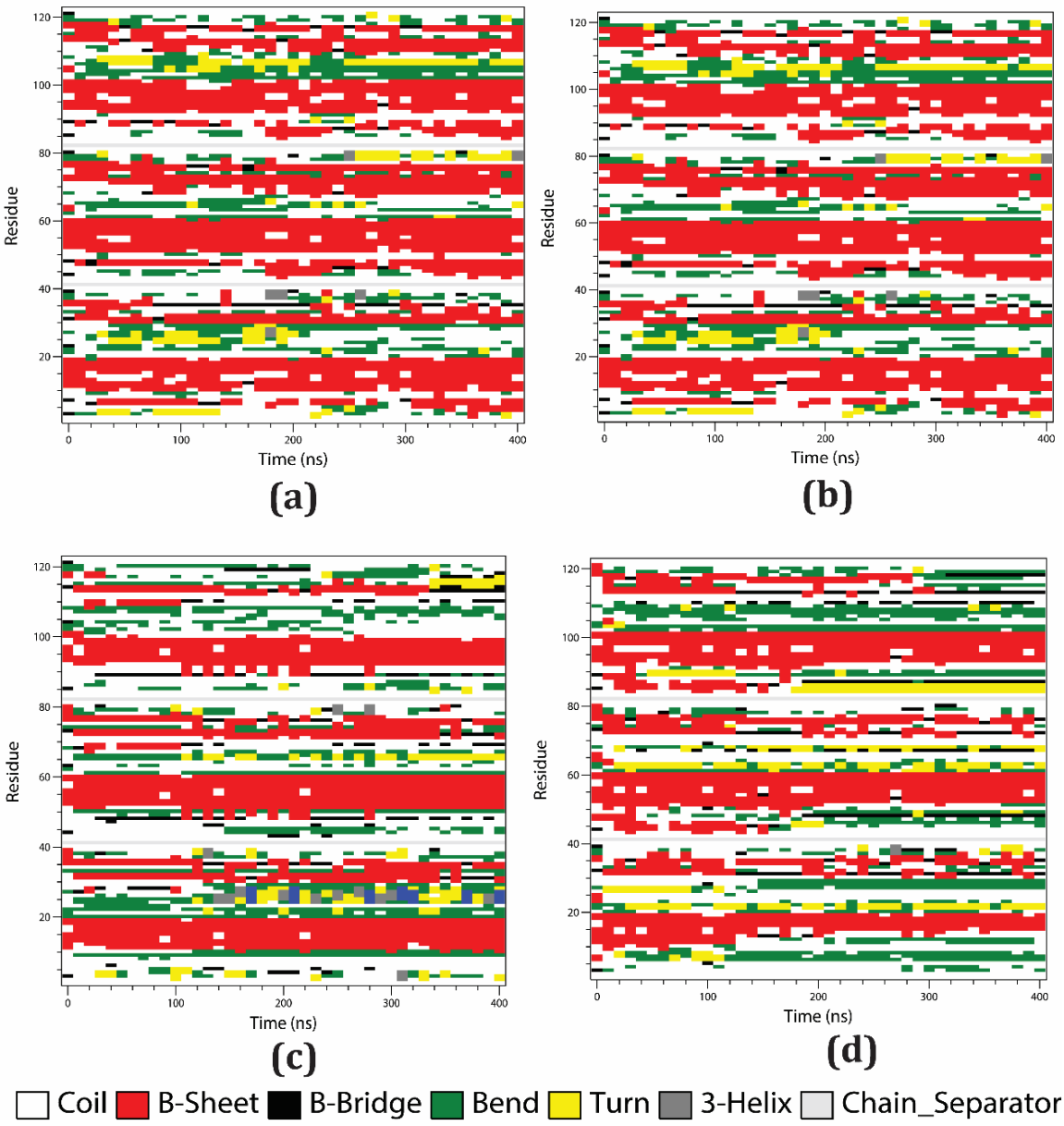

Figure 6.11. Representation of secondary structures of (a) Aβ40 in water, (b) Aβ40-PDI-HIS in P1, (c) Aβ40-PDI-HIS in P5, and (d) Aβ40-PDI-HIS in P7.

Furthermore, the reduction in the amount of β-sheet content of Aβ40 in P7 can also be correlated from Figure 6.12b. From Figure 6.12b, we observed that around 110 ns, the residues involved in the β-sheet configuration started decreasing. However, there were no significant

changes in the β-sheet content for the P1 system, which is illustrated in Figure D1 of Appendix-D.

A minute decreased in the coil content of Aβ40 was observed in the systems P1, P5, and P7 when compared with the water system, which can be seen in Figure D1 and Figure D2 of Appendix-D, and Figure 6.12a. Simultaneously, we have noticed a rise in the quantity of bend content of Aβ40 in P7 (Figure 6.12c). A slight increase in the bend content of Aβ40 in P1 and P5 (Figure D1 and Figure D2 of Appendix-D) was observed. So, the substantial loss in β-sheet content and generated secondary structure parameters indicate that the PDI-HIS disrupted the Aβ40.

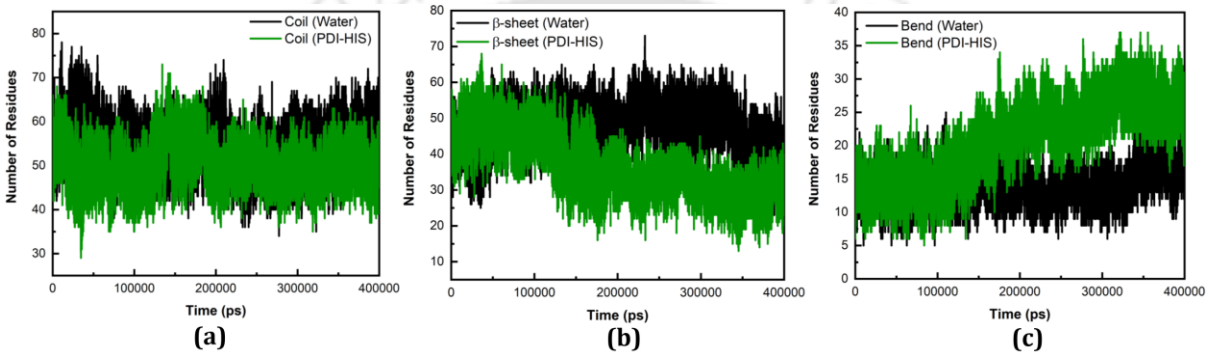

Figure 6.12. Representation of secondary structures of Aβ40-PDI-HIS of P7 for (a) coil content, (b) β-sheet content, and (c) bend content in Aβ40-water and Aβ40-PDI-HIS.

6.3.6. Binding Free Energy Analysis between Aβ40 and PDI-HIS

To gain more insight into the interactions between the Aβ40 and PDI-HIS in P1, P5, and P7 docked poses, the binding free energy ($\Delta G_{\text{binding}}$) was estimated by implementing the MM/PB(GB)SA method. The mathematical relations and approximation utilized in this method were discussed in the computational details section. The $\Delta G_{\text{binding}}$ values of P1, P5, and P7 were -24.67 ± 7.68, -17.74 ± 3.96, and -62.29 ± 2.39 kcal mol^{-1}, respectively. The $\Delta G_{\text{binding}}$ value of P7 is relatively higher than that of P1 and P5. Further, the van der Waals interaction energy (ΔE_{vdW}) component in all the systems was favourable for binding. However, the electrostatic interaction (ΔE_{elec}) contribution was unfavourable for binding. Both the polar (ΔG_{polar}) and non-polar ($\Delta G_{\text{non-polar}}$) contributions to the solvation energy (ΔG_{solv}) prefer favourable binding. Meanwhile, we observed that the contribution of polar (ΔG_{polar}) is more dominant than the non-polar ($\Delta G_{\text{non-polar}}$), as seen in Table 6.2.

Table 6.2. Binding free energy, $\Delta G_{\text{binding}}$, (in kcal mol^{-1}) of P1, P5, and P7 docked poses.

	P1	P5	P7
ΔE_{vdW}	-37.20 ± 1.23	-26.76 ± 1.73	-69.15 ± 0.44
ΔE_{elec}	162.00 ± 4.70	133.09 ± 1.98	167.59 ± 2.21
ΔE_{MM}	125.47 ± 4.86	106.33 ± 2.63	98.45 ± 2.25
ΔG_{polar}	-146.28 ± 5.95	-121.17 ± 2.97	-154.20 ± 0.80
$\Delta G_{\text{non-polar}}$	-3.86 ± 0.02	-2.90 ± 0.01	-6.54 ± 0.07
ΔG_{solv}	-150.14 ± 5.95	-124.07 ± 2.97	-160.74 ± 0.80
$\Delta G_{\text{binding}}$	-24.67 ± 7.68	-17.74 ± 3.96	-62.29 ± 2.39

6.3.7. Interaction Analysis between Aβ40 and PDI-HIS in P1, P5, and P7

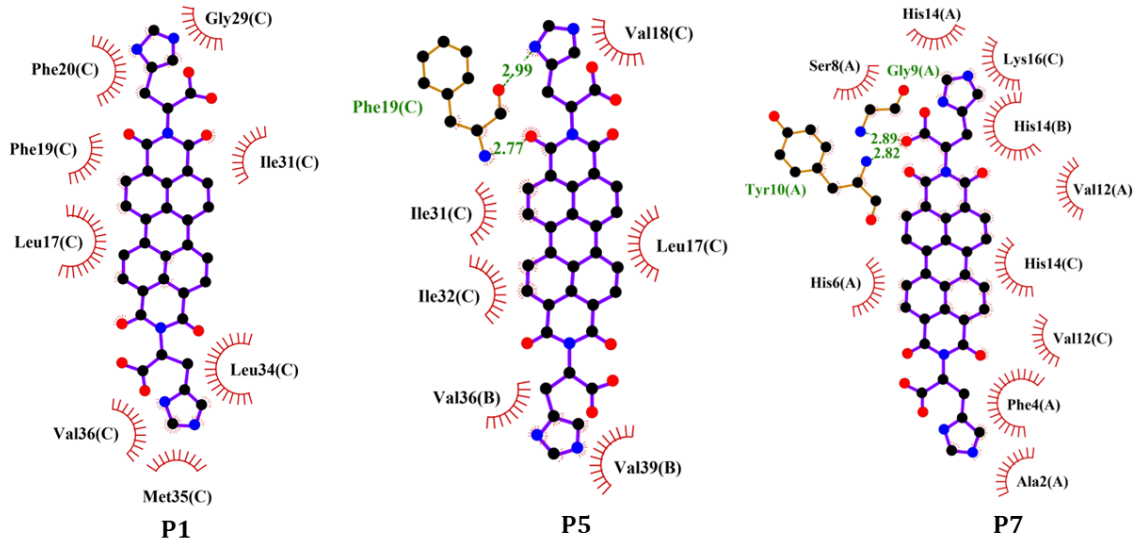

Figure 6.13. Showing the interaction form between the Aβ fibril and PDI-HIS at 400 ns for the systems P1, P5, and P7. The spike near the residues denotes the hydrophobic interactions, and the green line represents the existence of hydrogen bonding interaction (hydrogen bond distance in Å). A, B, and C represent the chains of Aβ fibril.

The interaction between the Aβ fibril and PDI-HIS was computed using the Ligplot plus.[80] In this analysis, we considered the structure of the Aβ40-PDI-HIS system at 400 ns for P1, P5,

and P7. Figure 6.13 displays the types of interactions and the residues involved. In P1, the hydrophobic interactions between the residues in chain C and PDI-HIS were exhibited. On the other hand, besides hydrophobic interaction, hydrogen bonding interactions were observed in P5 and P7. The residue Phe19 of chain C forms the hydrogen bonding interaction with the PDI-HIS in P5 (Figure 6.13). Likewise, the residues Tyr10 and Gly9 of chain A participated in the hydrogen bond formation (Figure 6.13) with PDI-HIS in P7.

6.4. Conclusions

In this chapter, we have investigated the modulating effect of histidine-functionalized perylenediimide (PDI-HIS) on the single trimer unit of Aβ40 fibril. Through molecular docking studies, we obtained the ten docked (P1 to P10) complexes formed between Aβ40 and PDI-HIS. Out of the ten docked poses, we selected three docked complexes, namely P1, P5, and P7, and performed the molecular dynamics (MD) simulations studies of time 400 ns. The MD simulations of P1 and P5 revealed that the PDI-HIS was confined towards the cavity of the Aβ40. On the other hand, in the P7 docked pose, the PDI-HIS bound toward β sheet region-1 of the Aβ40. During simulations, a slight interchain separation between chains A and B was observed in P7. This result is correlated with the parameters observed in RMSD, SASA, and hydrogen bond analysis. The β-sheet content of Aβ40 in P1 and P5 is slightly reduced when compared with the Aβ40 in the absence of PDI-HIS.

Meanwhile, a notable decreased in β-sheet content was observed in P7 docked pose. Comparatively, $\Delta G_{\text{binding}}$ value of P7 exhibited higher than that of P1 and P5. Further, the binding energies indicate that the PDI-HIS prefers to bind in the β sheet region-1 of the Aβ40 as observed in the P7 docked pose. Furthermore, the van der Waals interaction and solvation energy are the main dominant contributors to bind the PDI-HIS on Aβ40. The contribution is comparatively larger in P7 than in P1 and P5. Furthermore, hydrophobic and hydrogen bonding interactions were mainly involved between the PDI-HIS and Aβ40 fibril. This finding provides the roadmap for studying other PDI derivative compounds for treating Alzheimer's disease and is presented in Chapter 7.

6.5. References

[1] D. J. Selkoe, *Neuron*, 1991, **6**, 487.

[2] J. A. Hardy and G. A. Higgins, *Science*, 1992, **256**, 184.

[3] J. Hardy, *Proc. Natl. Acad. Sci. USA.*, 1997, **94**, 2095.

[4] S. H. Kim, R. Vlkolinsky, N. Cairns and G. Lubec, *Cell. Mol. Life Sci.*, 2000, **57**, 1810.

[5] F. M. LaFerla, K. N. Green and S. Oddo, *Nat. Rev. Neurosci.*, 2007, **8**, 499.

[6] M. P. Murphy and H. LeVine, *J. Alzheimer's Dis.*, 2010, **19**, 311.

[7] S. Lesné, T. K. Ming, L. Kotilinek, R. Kayed, C. G. Glabe, A. Yang, M. Gallagher and K. H. Ashe, *Nature*, 2006, **440**, 352.

[8] K. Ono, *Neurochem. Int.*, 2018, **119**, 57.

[9] A. Serrano-Pozo, M. P. Frosch, E. Masliah and B. T. Hyman, *Cold Spring Harb. Perspect. Med.*, 2011, **1**, a006189.

[10] M. Ahmed, J. Davis, D. Aucoin, T. Sato, S. Ahuja, S. Aimoto, J. I. Elliott, W. E. Van Nostrand and S. O. Smith, *Nat. Struct. Mol. Biol.*, 2010, **17**, 561.

[11] R. E. Tanzi and L. Bertram, Cell, 2005, **120**, 545.

[12] C. Haass and D. J. Selkoe, *Nat. Rev. Mol. Cell Biol.*, 2007, **8**, 101.

[13] W. Yao, H. Yang, J. Yang, W. W. Yao, H. H. Yang and J. F. Yang, *Front. Aging Neurosci.*, 2022, **14**, 1019412.

[14] Y. Tu, S. Ma, F. Liu, Y. Sun and X. Dong, *J. Phys. Chem. B*, 2016, **120**, 11360.

[15] A. Dey, R. Bhattacharya, A. Mukherjee and D. K. Pandey, *Biotechnol. Adv.*, 2017, **35**, 178.

[16] P. Williams, A. Sorribas and M.-J. R. Howes, *Nat. Prod. Rep.*, 2011, **28**, 48.

[17] L. A. Scrocchi, Y. Chen, S. Waschuk, F. Wang, S. Cheung, A. A. Darabie, J. McLaurin and P. E. Fraser, *J. Mol. Biol.*, 2002, **318**, 697.

[18] V. Villari, R. Tosto, G. Di Natale, A. Sinopoli, M. F. Tomasello, S. Lazzaro, N. Micali and G. Pappalardo, *ChemistrySelect*, 2017, **2**, 9122.

[19] M. A. Findeis, *Curr. Top. Med. Chem.*, 2002, **2**, 417.

[20] L. Lannfelt, K. Blennow, H. Zetterberg, S. Batsman, D. Ames, J. Hrrison, C. L. Masters, S. Targum, A. I. Bush, R. Murdoch, J. Wilson, C. W. Ritchie and P. E. S. Grp, *Lancet Neurol.*, 2008, **7**, 779.

[21] K. Chand, Rajeshwari, E. Candeias, S. M. Cardoso, S. Chaves and M. A. Santos, *Metallomics*, 2018, **10**, 1460.

[22] T. A. Sales, I. G. Prandi, A. A. de Castro, D. H. S. Leal, E. F. F. da Cunha, K. Kuca and T. C. Ramalho, *Int J Mol Sci.*, 2019, **20**, 1829.

[23] D. Puzzo and O. Arancio, *J. Alzheimers Disease*, 2013, **33**, S111.

[24] C. Haass and D. J. Selkoe, *Cell*, 1993, **75**, 1039.

[25] I. M. Ilie and A. Caflisch, *Chem. Rev.*, 2019, **119**, 6956.

[26] D. J. Selkoe and J. Hardy, *EMBO Molecular Med.*, 2016, **8**, 595.

[27] K. Ono, K. Hasegawa, H. Naiki and M. Yamada, *J. Neurosci. Res.*, 2004, **75**, 742.

[28] K. Jiménez-Aliaga, P. Bermejo-Bescós, J. Benedí and S. Martín-Aragón, *Life Sci.*, 2011, **89**, 939.

[29] A. Pugazhendhi, R. Beema Shafreen, K. Pandima Devi and N. Suganthy, *J. Mol. Liq.*, 2018, **257**, 69.

[30] R. Hornedo-Ortega, G. Da Costa, A. B. Cerezo, A. M. Troncoso, T. Richard and M. C. Garcia-Parrilla, *Mol. Nutr. Food Res.*, 2018, **62**, 1.

[31] G. Tin, T. Mohamed, A. Shakeri, A. T. Pham and P. P. N. Rao, *ACS Chem. Neurosci.*, 2019, **10**, 226.

[32] M. Pappolla, P. Bozner, C. Soto, H. Shao, N. K. Robakis, M. Zagorski, B. Frangione and J. Ghiso, *J. Biol. Chem.*, 1998, **273**, 7185.

[33] F. Würthner, V. Stepanenko, Z. Chen, C. R. Saha-Möller, N. Kocher and D. Stalke, *J. Org. Chem.*, 2004, **69**, 7933.

[34] M. J. Ahrens, M. J. Tauber and M. R. Wasielewski, *J. Org. Chem.*, 2006, **71**, 2107.

[35] S. Dey, A. Efimov and H. Lemmetyinen, *Eur. J. Org. Chem.*, 2012, **2012**, 2367.

[36] Y. Li, X. Zhang and D. Liu, *J. Photochem. Photobiol. C: Photochem. Rev.*, 2021, **48**, 100436,

[37] D. Meng, H. Fu, C. Xiao, X. Meng, T. Winands, W. Ma, W. Wei, B. Fan, L. Huo, N. L. Doltsinis, Y. Li, Y. Sun and Z. Wang, *J. Am. Chem. Soc.*, 2016, **138**, 10184.

[38] M. Milton, N. J. Schuster, D. W. Paley, R. Hernández Sánchez, F. Ng, M. L. Steigerwald and C. Nuckolls, *Chem. Sci.*, 2019, **10**, 1029.

[39] K. Kong, S. Zhang, Y. Chu, Y. Hu, F. Yu, H. Ye, H. Ding and J. Hua, *Chem. Commun.*, 2019, **55**, 8090.

[40] X. Zhang, S. Rehm, M.M. Safont-Sempere and F. Würthner, *Nat. Chem.*, 2009, **1**, 623.

[41] P. Posch, M. Thelakkat and H.W. Schmidt, *Synthetic Met.*, 1999, **102**, 1110.

[42] C. Huang, S. Barlow and S.R. Marder, *J. Org. Chem.*, 2011, **76**, 2386.

[43] L. Zang, Y. Che and J. S. Moore, *Accounts Chem.*, Res., 2008, **41**, 1596.

[44] N. Barooah, P. Karmakar, M. K. Sharanya, M. Mishra, A. C. Bhasikuttan and J. Mohanty, *J. Mater. Chem. B*, 2023, **11**, 9545.

[45] B. Muthuraj, S. R. Chowdhury and P. K. Iyer, *ACS Appl. Mater. Interfaces*, 2015, **7**, 21226.

[46] W. J. Du, J. J. Guo, M. T. Gao, S. Q. Hu, X. Y. Dong, Y. F. Han, F. F. Liu, S. Jiang and Y. Sun, *Sci. Rep.*, 2015, **5**, 1.

[47] Y. Tu, S. Ma, F. Liu, Y. Sun and X. Dong, *J. Phys. Chem. B*, 2016, **120**, 11360.

[48] J. A. Lemkul and D. R. Bevan, *Biochemistry*, 2010, **49**, 3935.

[49] T. Kai, L. Zhang, X. Wang, A. Jing, B. Zhao, X. Yu, J. Zheng and F. Zhou, *ACS Chem. Neurosci.*, 2015, **6**, 879.

[50] Y. Jin, Y. Sun, J. Lei and G. Wei, *Phys. Chem. Chem. Phys.*, 2018, **20**, 17208.

[51] Y. Wang, D. C. Latshaw and C. K. Hall, *J. Mol. Biol.*, 2017, **429**, 3893.

[52] S. Gupta and A. K. Dasmahapatra, *Phys. Chem. Chem. Phys.*, 2020, **22**, 19643.

[53] N. Agrawal and A. A. Skelton, *ACS Chem. Neurosci.*, 2016, **7**, 1433.

[54] S. Chatterjee, Y. Nam, A. Salim and J. Y. Lee, *Phys. Chem. Chem. Phys.*, 2022, **24**, 18691.

[55] J.-X. Lu, W. Qiang, W. -M. Yau, C. D. Schwieters, S. C. Meredith and R. Tycko, *Cell*, 2013, **154**, 1257.

[56] Y. Zhao and D. G. Truhlar, *Theor. Chem. Acc.*, 2008, **120**, 215.

[57] F. Weigend and R. Ahlrichs, *Phys. Chem. Chem. Phys.*, 2005, **7**, 3297.

[58] M. J. Frisch, G. W. Trucks, H. B. Schlegel, G. E. Scuseria, M. A. Robb, J. R. Cheeseman, G. Scalmani, V. Barone, G. A. Petersson, H. Nakatsuji, X. Li, M. Caricato, A. V. Marenich, J. Bloino, B. G. Janesko, R. Gomperts, B. Mennucci, H. P. Hratchian, J. V. Ortiz, A. F. Izmaylov, J. L. Sonnenberg, D. Williams-Young, F. Ding, F. Lipparini, F. Egidi, J. Goings, B. Peng, A. Petrone, T. Henderson, D. Ranasinghe, V. G. Zakrzewski, J. Gao, N. Rega, G. Zheng, W. Liang, M. Hada, M. Ehara, K. Toyota, R. Fukuda, J. Hasegawa, M. Ishida, T. Nakajima, Y. Honda, O. Kitao, H. Nakai, T. Vreven, K. Throssell, J. A. Montgomery, J. E. Peralta, F. Ogliaro, M. J. Bearpark, J. J. Heyd, E. N. Brothers, K. N. Kudin, V. N. Staroverov, T. A. Keith, R. Kobayashi, J. Normand, K. Raghavachari, A. P. Rendell, J. C. Burant, S. S. Iyengar, J. Tomasi, M. Cossi, J. M. Millam, M. Klene, C. Adamo, R. Cammi, J. W. Ochterski, R. L. Martin, K. Morokuma, O. Farkas, J. B. Foresman and D. J. Fox, Gaussian 16 Revision C.01, Gaussian Inc., Wallingford CT, 2016.

[59] R. Huey, G. M. Morris, A. J. Olson and D. S. Goodsell, *J. Comput. Chem.*, 2007, **28**, 1145.

[60] F. J. Solis and R.-J.-B. Wets, *Math. Oper. Res.*, 1981, **6**, 19.

[61] W. Humphrey, A. Dalke and K. Schulten, *J. Mol. Graph.*, 1996, **14**, 33.

[62] D. Van Der Spoel, E. Lindahl, B. Hess, G. Groenhof, A. E. Mark and H. J. C. Berendsen, *J. Comput. Chem.*, 2005, **26**, 1701.

[63] T. Lu and F. Chen, *J. Comput. Chem.*, 2012, **33**, 580.

[64] T. Lu, *Sobtop: A Tool of Generating Forcefield Parameters and GROMACS Topology*. Available online: http://sobereva.com/soft/Sobtop.

[65] J. Wang, R. M. Wolf, J. W. Caldwell, P. A. Kollman and D. A Case, *J. Comput. Chem.*, 2004, **25**,1157.

[66] K. Lindorff-Larsen, S. Piana, K. Palmo, P. Maragakis, J. L. Klepeis and R. O. Dror, *Proteins: Struct., Funct., Genet.*, 2010, **78**, 1950.

[67] H. J. C. Berendsen, J. R. Grigera and T. P. Straatsma, *J. Phys. Chem.*, 1987, **91**, 6269.

[68] G. Bussi, D. Donadio and M. Parrinello, *J. Chem. Phys.*, 2007, **126**, 014101.

[69] S. Nosé and M. L. Klein, *Mol. Phys.*, 1983, **50**, 1055.

[70] B. Hess, H. Bekker, H. J. Berendsen and J. G. Fraaije, *J. Comput. Chem.*, 1997, **18**, 1463.

[71] T. Darden, D. York and L. Pedersen, *J. Chem. Phys.*, 1993, **98**, 10089.

[72] J. Srinivasan, T. E. Cheatham, P. Cieplak, P. A. Kollman and D.A. Case, *J. Am. Chem. Soc.*, 1998, **120**, 9401.

[73] I. Massova and P. A. Kollman, *Perspect. Drug Discovery Des.*, 2000, **18**, 113.

[74] M. S. Valdés-Tresanco, M. E. Valdés-Tresanco, P. A. Valiente and E. Moreno, *J. Chem. Theory Comput.* 2021, **17**, 6281.

[75] E. Wang, H. Sun, J. Wang, Z. Wang, H. Liu, J. Z. H. Zhang and T. Hou, *Chem. Rev.*, 2019, **119**, 9478.

[76] M. S. Valdés-Tresanco, M. E. Valdés-Tresanco, P. A. Valiente and E. Moreno, J. *Chem. Theory Comput.*, 2021, **17**, 6281.

[77] J. Zheng, H. Jang, B. Ma, C.-J. Tsai and R. Nussinov, *Biophys. J.*, 2007, **93**, 3046.

[78] M. Sunde, L. C. Serpell, M. Bartlam, P. E. Fraser, M. B. Pepys and C. C. Blake, *J. Mol. Biol.*, 1997, **273**, 729.

[79] W. Zhao, L. Jiang, W. Wang, J. Sang, Q. Sun, Q. Dong, L. Li, F. Lu and F. Liu, *J. Mater. Chem. B*, 2021, **9**, 6902.

[80] R. A. Laskowski and M.B. Swindells, *J. Chem. Inf. Model.*, 2011, **51**, 2778.

Chapter 7

In Silico Designing of Alanine, Phenylalanine, and Tyrosine Functionalized Perylene diimide (PDI) and Exploring their Nature of Interaction with Amyloid-β (Aβ) Fibrils

7.1. Introduction

Alzheimer's disease (AD) is one of the neurodegenerative disorders diseases and globally affected approximately 46.8 million people in 2015 and is estimated to reach 131.5 million by 2050.[1,2] Individuals who are diagnosed with AD show the symptoms of memory loss, problems with visualization, and language deterioration. The pathological hallmark of this disease is the existence of extracellular senile plaques and intracellular neurofibrillary tangles inside the brain, which are obtained from the amyloid-β peptide and tau protein.[3] Several drug molecules were identified for addressing AD, but all of them failed to cure with the efficacy limited to treating symptoms.[4]

The two most important forms of amyloid β (Aβ)-peptides are Aβ1-40 and Aβ1-42.[5,6] These forms of Aβ are obtained from the amyloid β precursor protein (APP) via the process of enzymatic cleavage.[7] So far, many factors and hypotheses have been proposed regarding the occurrence of AD. Out of these, the amyloid hypothesis earned a significant interest, which talked about the aggregations of amyloid β-peptides that cause AD.[8] Earlier studies reported that the monomeric form of Aβ is soluble and non-toxic.[9,10] However, aggregated amyloid β-peptide species exhibited cytotoxicity, including oligomers, protofibrils, and mature fibrils.[5,11] Therefore, the occurrence of AD is related to the aggregation of Aβ. As a result, it is essential to focus on the development of compounds that inhibit the aggregations.

Several species were synthesized targeting to inhibit the aggregation of Aβ peptides. These species include small molecules extracted from plant sources,[12-14] peptides,[15-17] nanoparticles,[18-20] and metal-chelating compounds.[21-23] The polyphenol natural compounds,

such as resveratrol[24] and epigallocatechin-3-gallate,[25] obtained from the plant sources exhibited the inhibition of Aβ aggregations. The molecular dynamics (MD) simulations studies revealed that both compounds bind to the Aβ through noncovalent interactions and inhibit the aggregations. The binding of the resveratrol compound with Aβ peptide occurred through π-π interactions.

On the other hand, epigallocatechin-3-gallate binds to Aβ peptide via hydrophobic, π-π, and hydrogen bonding interactions.[25] The exploration of carbon nanotube material to stop the Aβ peptide aggregations was also reported. Recent studies suggested that single-walled carbon nanotubes (SWCNTs) showed the inhibition of Aβ aggregations.[26-28] Moreover, the hydroxyl content of SWCNT also appeared to inhibit the Aβ fibrillogenesis.[29] Zhao et al. reported the carboxylated single-walled carbon nanotubes (SWCNT-COOH) and observed that it inhibited the Aβ aggregations.[30] Further, they found that SWCNT-COOH depolymerises the mature fibrils of Aβ. Moreover, the MD simulations studies showed that SWCNT-COOH binds to the different regions of trimer Aβ40.[30] This binding involved noncovalent interactions such as π-π, hydrogen bonding, and electrostatic salt bridge interactions. Due to these interactions, a substantial structural disruption in the Aβ40 and lowered the quantity of β-sheet content.

The perylenediimide (PDI) compounds and their derivatives are treated as one of the best for constructing the n-type semiconductor.[31] Several studies also reported using PDI and its derivatives as dyes,[32] sensors,[33] and organic electronic materials.[35,36] It is also used as a photosensitizer to degrade phenolic compounds.[37] Moreover, the PDI molecule and its derivatives can self-assemble through noncovalent π-π stacking interactions.[38, 39] Such self-assembly systems were used in diverse applications. Many groups reported the biocompatible materials derived from the PDI by substituting the amino acids. Chen et al. reported four PDI derivatives functionalized with amino acids: L-phenylalanine, L-alanine, L-glutamic, and L-tyrosine.[40] These systems showed the selective binding with anion ions like fluoride and hydroxide. The L-phenylalanine functionalized PDI exhibited the disintegration of Aβ aggregations.[41] Iyer and coworkers studied the effect on the Aβ40 when it interacts with the histidine-functionalized perylenediimide (PDI-HIS).[42] They observed that PDI-HIS co-assembled with Aβ40 and turned into micro-size structures. Ultimately, these results lead to the disintegration of the fibrils. At the same time, MD simulation studies detailed in Chapter 6 revealed that PDI-HIS effectively disrupted the Aβ40 structures.

In this chapter, we performed MD simulations to explore the structural disruption impact of L-alanine perylenediimide (PDI-ALA), L-phenylalanine perylenediimide (PDI-PHE), and L-tyrosine perylenediimide (PDI-TYR) on Aβ40 fibril. We have also investigated the noncovalent interactions between the considered amino acids functionalized PDI and Aβ40 fibril.

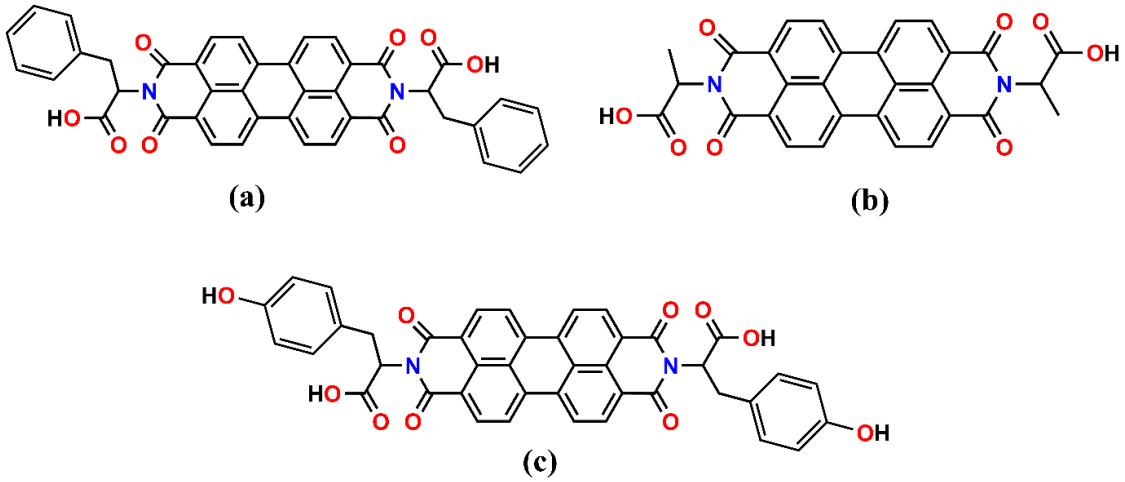

Figure 7.1. Molecular structures of phenylalanine (PHE), alanine (ALA), and tyrosine (TYR) functionalized perylenediimide (PDI) (a) PDI-PHE, (b) PDI-ALA, and (c) PDI-TYR.

7.2. Computational Details

7.2.1 Optimization of the Molecular Structures

The M06-2X functional[43] and the def2-TZVP basis set,[44] was employed for conducting the geometry optimization of PDI-PHE, PDI-ALA, and PDI-TYR (Figure 7.1). At the same level of theory frequency analysis was performed. The calculations were executed in the Gaussian 16 software package.[45] To attribute the deprotonation of the two carboxylic groups in the system, we assigned a -2 charge during the optimization.

7.2.2 Molecular Docking Studies

The optimized PDI-PHE, PDI-ALA, and PDI-TYR structures were utilized for molecular docking calculations. The calculations were performed using the Autodock Suite 4.2.1.[46] The single trimer unit amyloid β protein (Aβ40) is considered a receptor, and PDI-PHE, PDI-ALA, and PDI-TYR systems were treated as ligands. Using AutoDockTools, the necessary input files, such as PDBQT [Protein Data Bank, Partial Charge (Q), & Atom Type (T)], for the molecular docking calculations were generated. The three-dimensional protein structure of the single trimer unit Aβ40 was obtained from the protein data bank (PDB) (PDB ID: 2M4J).[47]

The single trimer unit Aβ40 fibril structure considered in this study is shown in Figure 6.2 of Chapter 6.

Further, we considered the addition of Gasteiger charges into the ligand and keeping polar hydrogen atoms. Since the specific binding site of the Aβ40 fibril is not known, we executed the blind docking by considering the grid box size of 126 ×126× 68 $Å^3$ to cover the maximum area of the protein. In addition, we considered Aβ40 fibril protein was treated as a rigid entity while PDI-PHE, PDI-ALA, and PDI-TYR systems were treated flexibly. Likewise, in Chapter 6, we used the Lamarckian genetic algorithm (GA)[48] for conformation search. The parameters such as GA population size of 150, maximum energy evaluation of 2500000, maximum number generation of 27000, rate of gene mutation, and crossover are 0.02 and 0.08, respectively. Ten docked poses were generated, which formed between the Aβ40 and each ligands PDI-PHE, PDI-ALA, and PDI-TYR.

7.2.3 Molecular Dynamics Simulations Studies

The resulting protein-ligand docked complexes obtained from the molecular docking calculations were utilized to perform the MD simulations. To fit the atomic charges of the ligand, we have calculated the charges by employing the restrained electrostatic potential (RESP) approach at the M06-2X/def2-TZVP level of theory.[43,44] The force field Amber99sb-ildn.ff[49] was used for the Aβ40 protein and the general Amber force field (GAFF)[50] was utilized for the ligand systems (PDI-PHE, PDI-ALA, and PDI-TYR). The GAFF force field parameters are generated by using the Sobtop package.[51] The protein-ligand complexes were solvated in a cubic box size of 9.5 × 9.5 × 9.5 nm^3 with the single-point charge (SPC) water model.[52] To preserve neutrality, eleven Na^+ ions were added to each protein-ligand system. Subsequently, the energy minimization was conducted by implementing the steepest descent minimization algorithm and encompassing 5000 steps. Under the canonical NVT ensemble, the complexes were equilibrated for 100 ps and followed by the NPT ensemble.[53,54] The LINCS algorithm was implemented for the hydrogen bond of Aβ40 and ligand systems.[55] Long-range electrostatic interactions were computed using the Particle Mesh Ewald (PME)[56] method, employing a cutoff value of 1.2 nm, and the van der Waals interaction was determined with the cutoff value of 1.2 nm. The obtained equilibrated protein-ligand systems were used to carry out the production MD for 400 ns. We considered the temperature and pressure conditions of 310 K and 1 atm, respectively. On the other hand, we considered the MD simulations of the Aβ40 fibril in the absence of ligands in water, as in Chapter 6. The calculations were executed

using the GROMACS package.[57] The protein, ligand, and protein-ligand complexes were visualized using the UCSF Chimera 1.16[58] and visual molecular dynamics (VMD) 1.9.3 packages.[59]

The binding free energy ($\Delta G_{\text{binding}}$) of the protein-ligand complexes was estimated by using the Molecular Mechanics/Poisson-Boltzmann (Generalized-Born) Surface Area [MM/PB(GB)SA][60-63] method and Eq. 6.1 provided in Chapter 6 was used. In this investigation, we used the gmx_MMPBSA[62] tool with obtained MD simulation results. Likewise, in Chapter 6, we considered the last 20 ns trajectories employing the time interval of 100 ps for estimating $\Delta G_{\text{binding}}$.

7.3. Results and Discussion

7.3.1. Molecular Docking of Aβ40 Fibril with PDI-ALA

Molecular docking calculations were performed between the Aβ40 protein and ligands PDI-ALA, PDI-PHE, and PDI-TYR. The protocol employed in the molecular docking calculations is discussed in the Computational Details section. The protein-ligand docked poses are presented in Figures 7.2, 7.3, and 7.4 for PDI-ALA, PD-PHE, and PDI-TYR, respectively. The corresponding binding energy (ΔG) (in kcal mol^{-1}) of the docked poses, along with the residues involved in the interactions, are displayed in Tables 7.1, 7.2, and 7.3 for PDI-ALA, PDI-PHE, and PDI-TYR, respectively.

Table 7.1 shows that the value of the ten docked poses for the PDI-ALA system ranges from –8.24 kcal mol^{-1} (A1) to –6.67 kcal mol^{-1} (A10). Docked pose A1 showed the highest value of ΔG, while A10 exhibited the lowest. In this docked pose, PDI-ALA interacts with chain C residue's Gln15, Lys16, Leu17, Phe19, Phe20, Lys28, Ile31, Leu34, and Val36 of Aβ40. These interactions can be seen in pose A1 of Figure 7.2 and Table 7.1. Moreover, the docked pose A10 has the lowest value of ΔG, where the number of residues involved in the interactions with PDI-ALA is comparatively lesser than A1. Meanwhile, we observed an electrostatic interaction between the residue Lys28 of chain C and the carboxylic group of PDI-ALA in A1. However, such kind of interaction is missing in docked pose A10.

In docked pose A2, PDI-ALA binds on the β-sheet region-1 of Aβ40 (Figure 7.2) and it interacts with residues Lys16, Leu17, and Val18 of chains A, B, and C. Docked poses A3, A4, A5, A6, and A7 showed the similar binding sites (Figure 7.2) as observed in A1 and also observed almost equal value of as shown in Table 7.1. Further, in docked conformations A8

and A9, PDI-ALA exhibited identical residue participation during the interactions and are displayed in Table 7.1.

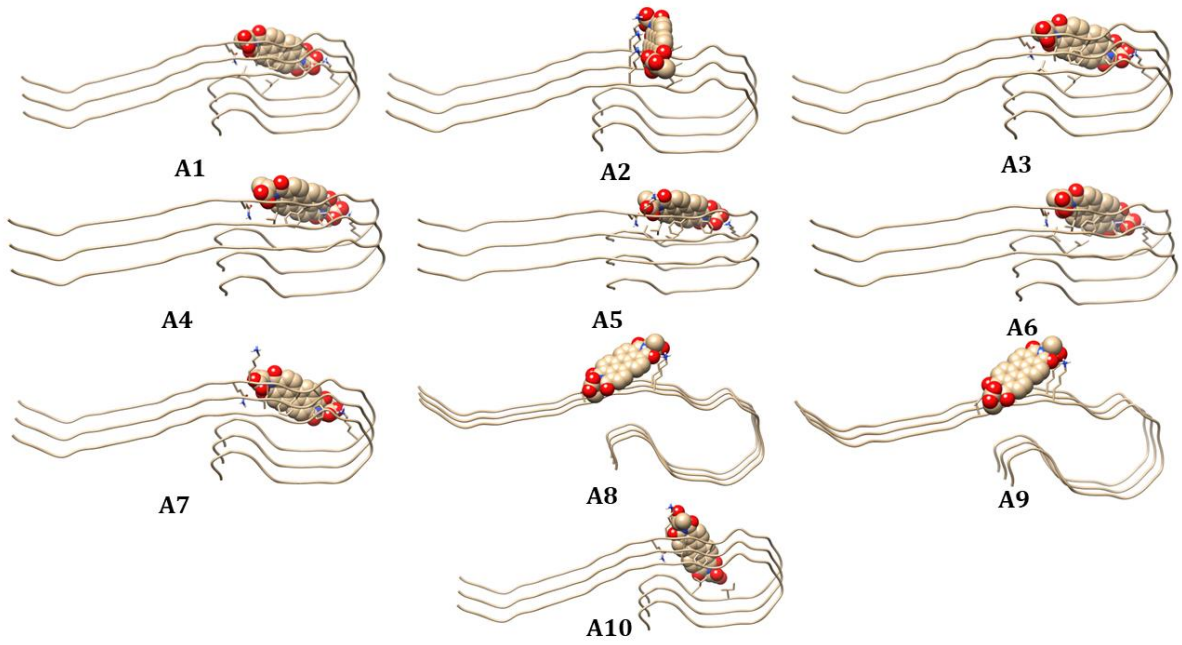

Figure 7.2. Docked poses A1 to A10 obtained from the molecular docking of Aβ40 fibril with PDI-ALA.

Table 7.1. Generated docked poses (A1 to A10) with their binding energy (ΔG) (in kcal mol^{-1}) and residues involved in the interactions.

Docked Pose	Binding Energy, ΔG	Residues involved
A1	−8.24	C (Gln15, Lys16, Leu17, Phe19, Phe20, Lys28, Ile31, Leu34, Val36)
A2	−8.14	A (Lys16, Leu17, Val18); B (Lys16, Leu17, Val18) ; C (Lys16, Leu17, Val18)
A3	−7.97	C (Gln15, Lys16, Leu17, Phe19, Phe20, Lys28, Ile31, Val36)
A4	−7.96	C (Gln15, Lys16, Leu17, Phe19, Phe20, Lys28, Val36)

A5	−7.95	C (Gln15, Lys16, Leu17, Phe19, Phe20, Lys28, Ile31, Leu34, Val36)
A6	−7.95	C (Gln15, Lys16, Leu17, Phe19, Phe20, Lys28, Ile31, Leu34, Val36)
A7	−7.81	C (Gln15, Lys16, Leu17, Phe19, Phe20, Lys28, Leu34, Val36)
A8	−7.07	A (Val12, His14, Lys16); B (Lys16)
A9	−7.06	A (Val12, His14, Lys16); B (Lys16)
A10	−6.67	C (Gln15, Lys16, Leu17, Phe19, Ile31, Leu34, Val36)

7.3.2. Molecular Docking of Aβ40 Fibril with PDI-PHE

For the molecular docking of Aβ40 with PDI-PHE, the binding energy ΔG of the generated ten docked poses ranges from −6.86 kcal mol^{-1} (P1) to −5.19 kcal mol^{-1} (P10), respectively. All the ten docked poses and their corresponding residues in the interactions are presented in Figure 7.3 and Table 7.2. From the docking results, we found that docked pose P1 exhibited the highest value of ΔG in magnitude, in which the PDI-PHE binds on β-sheet region-1 of Aβ40 (Figure 7.3). The residues interacting with PDI-PHE in pose P1 are Lys16, Leu17, and Val18, each from chains A, B, and C of Aβ40. In the docked pose P2, the PDI-PHE is bound on the chain C region of Aβ40, and the residues that participated in the interactions are Lys16, Leu17, Val18, Phe19, Ile31, Ile32, Gly33, and Leu34. On the other hand, PDI-PHE binds on the maximum region of chain A region and the small region of chain B of Aβ40 in docked pose P3. The residues involved in the interactions include Val12, His13, His14, Lys16 of chain A, and Lys16 of chain B. The docked pose P4 showed a similar interaction to that observed in P1. In docked pose P5, the ligand PDI-PHE binds on the chain C side of Aβ40, and the residues involved in the interactions are presented in Table 7.2. At the same time, docked poses P6, P7, and P8 exhibited the same type of interactions with residues Lys16 of chain A, Val12, His13, His14, Lys16 of chain B and Val12, His13, and His14 of chain C. In addition, ΔG values of these three docked poses are almost equal (Table 7.2). In the P9 docked pose, the ligand PDI-PHE showed interactions with Val12, His13, His14 of chain A, His14, Lys16 of chain B, and

Lys16 of chain C. Lastly, the docked pose P10 exhibited interactions with Val12, His13, His14, Lys16 of chain A and Val12, His13, His14, Lys16 of chain B.

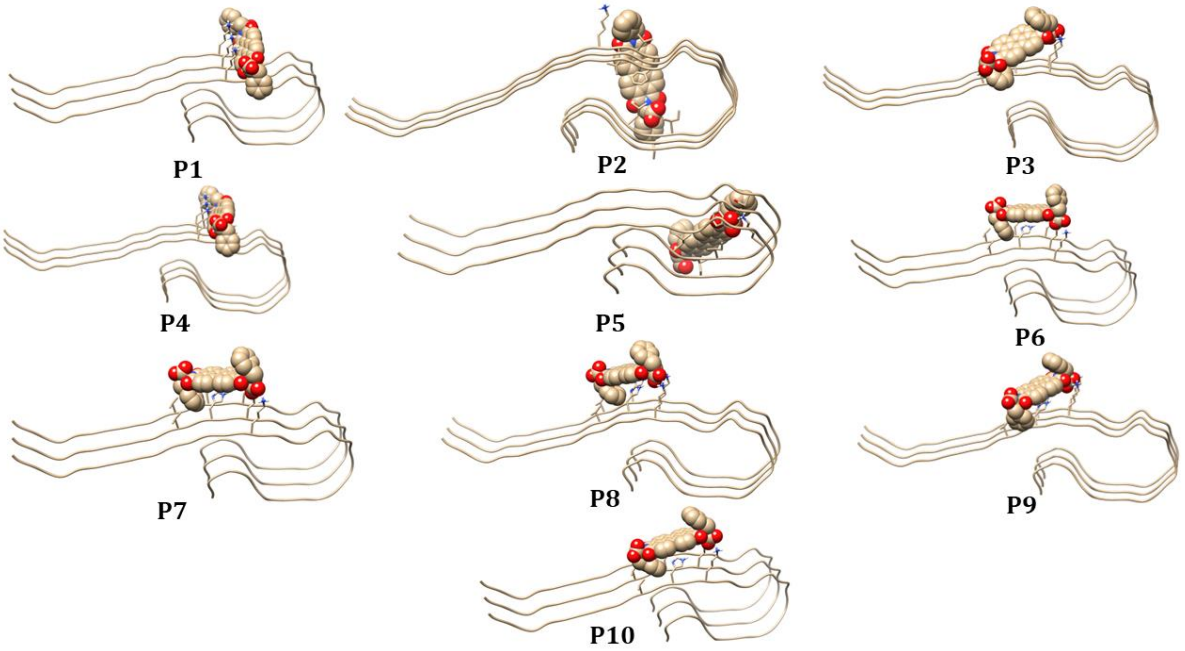

Figure 7.3. Docked poses P1 to P10 obtained from the molecular docking of Aβ40 fibril with PDI-PHE.

Table 7.2. Generated docked poses (P1 to P10) with their binding energy (ΔG) (in kcal mol^{-1}) and residues involved in the interactions.

Docked Pose	Binding Energy, ΔG	Residues involved
P1	−6.86	A (Lys16, Leu17, Val18); B (Lys16, Leu17, Val18) ; C (Lys16, Leu17, Val18)
P2	−6.78	C (Lys16, Leu17, Val18, Phe19, Ile31, Ile32, Gly33, Leu34)
P3	−6.59	A (Val12, His13, His14, Lys16); B (Lys16)
P4	−6.32	A (Lys16, Leu17, Val18); B (Lys16, Leu17, Val18) ; C (Lys16, Leu17, Val18)
P5	−5.85	C (Phe20, Asp23, Val24, Gly25, Lys28, Ile31, Ile32, Gly33, Leu34)

P6	−5.74	A (Lys16); B (Val12, His13, His14, Lys16) ; C (Val12, His13, His14)
P7	−5.72	A (Lys16); B (Val12, His13, His14, Lys16) ; C (Val12, His13, His14)
P8	−5.57	A (Lys16); B (Val12, His13, His14, Lys16) ; C (Val12, His13, His14)
P9	−5.42	A (Val12, His13, His14) ; B(His14, Lys16); C (Lys16)
P10	−5.19	A (Val12, His13, His14, Lys16); B (Val12, His13, His14, Lys16)

7.3.3. Molecular Docking of Aβ40 Fibril with PDI-TYR

In the molecular docking calculations of Aβ40 with PDI-TYR, the computed binding energies (ΔG) for the ten docked poses range from –8.59 kcal mol^{-1} (T1) to –4.87 kcal mol^{-1} (T10), respectively. Figure 7.4 illustrates the docked poses, while Table 7.3 provides the ΔG value of each pose and detailed information about the interactions between Aβ40 and PDI-TYR. In docked pose T1, the ligand PDI-TYR bind on the chain C region of Aβ40 and residues Gln15, Lys16, Leu17, Phe19, Phe20, Lys28, Gly29, Ala30, Ile31, Leu34, and Val36 are participated in the interactions. Other docked poses T3, T4, and T7, are also bound on the chain C region, and the corresponding residues involved in the interactions are presented in Table 7.3. Moreover, the docked poses T2, T5, and T10 exhibited a similar type of ligand binding location, and some residues of chains A, B, and C are involved in the interactions. In the docked pose T6, the PDI-TYR interacts with residues Val12, His13, His14, and Lys16 of chain A and Lys16 of chain B. Further, in docked pose T8, the residues involved are Tyr10, Val12, His14 of chain A, Tyr10, Val12, His14, Lys16 of chain B, and Lys16 of chain C. In T9, PDI-TYR establishes interactions with residues Val12, His13, His14, and Lys16 of chain B and Val12, His13, His14, and Lys16 of chain C.

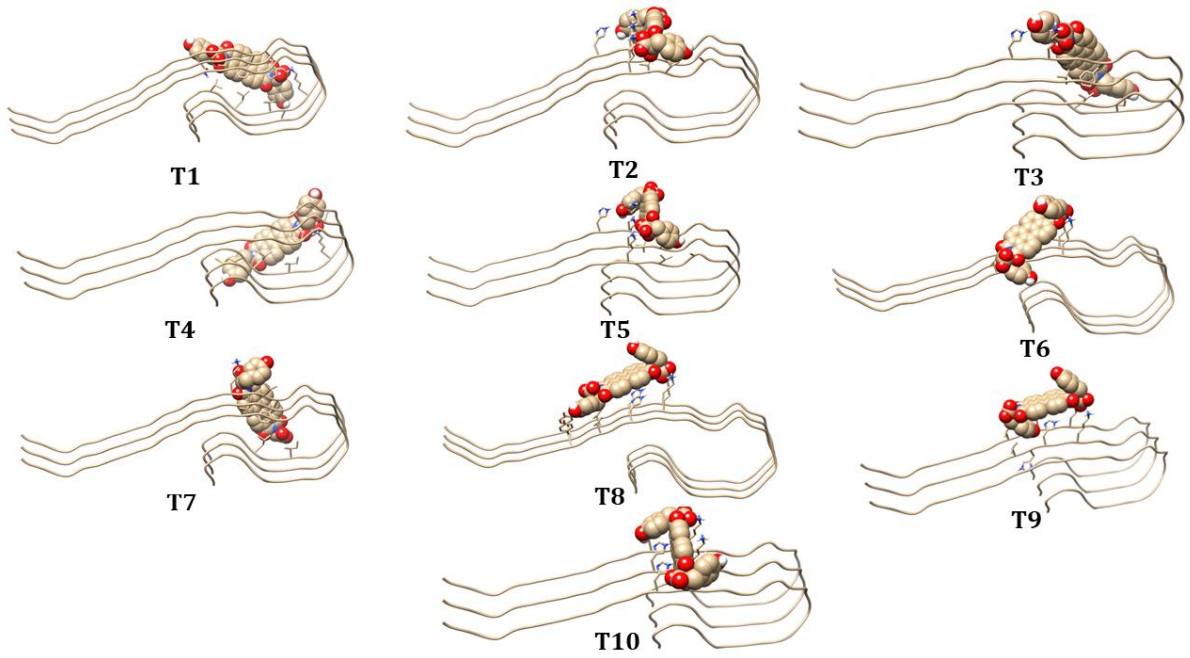

Figure 7.4. Docked poses T1 to T10 obtained from the molecular docking of Aβ40 fibril with PDI-TYR.

Table 7.3. Generated docked poses (T1 to T10) with their binding energy (ΔG) (in kcal mol^{-1}) and residues involved in the interactions.

Docked Pose	Binding Energy, ΔG	Residues involved
T1	−8.59	C (Gln15, Lys16, Leu17, Phe19, Phe20, Lys28, Gly29, Ala30, Ile31, Leu34, Val36)
T2	−7.92	A (Lys16, Leu17, Val18, Ala21); B (Lys16, Leu17, Val18) C (Gln15, Lys16, Leu17, Val18)
T3	−7.66	C (His14, Gln15, Lys16, Leu17, Phe19, Phe20, Gly29, Ala30, Ile31, Leu34)
T4	−7.59	C (Phe20, Ala21, Asp23 Gly25, Lys28, Ile31, Ile32, Gly33, Leu34, Met35, Val40)
T5	−6.40	A (Lys16, Val18); B (Lys16, Val18) C (Gln15, Lys16, Leu17, Val18)
T6	−6.25	A (Val12, His13, His14, Lys16); B (Lys16)

T7	−5.86	C (Gln15, Lys16, Leu17, Val18, Phe19, Phe20, Ile31, Leu34, Val36)
T8	−5.16	A (Tyr10, Val12, His14); B (Tyr10, Val12, His14, Lys16); C (Lys16)
T9	−4.93	B (Val12, His13, His14, Lys16); C (Val12, His13, His14, Lys16)
T10	−4.87	A (His14, Lys16); B (His14, Lys16) C (His14, Lys16)

7.3.4. Molecular Dynamics Simulations Studies of PDI-ALA, PDI-PHE, and PDI-TYR with Aβ40 Fibril

7.3.4.1. Molecular Dynamics Simulations Studies of PDI-ALA with Aβ40 Fibril

The docked poses (Aβ40-PDI-ALA) resulting from the molecular docking calculations were subsequently used for the molecular dynamics (MD) simulations studies. From Figure 7.2, we have noticed that docked poses A1, A3, A4, A5, A6, A7, and A10 have almost similar binding locations of PDI-ALA on Aβ40 with slight differences in the number of residues involved in the interactions. Moreover, PDI-ALA has closed related binding modes in A8 and A9 docked poses. On the other hand, in docked pose A2, the binding region of PDI-ALA on Aβ40 is different from others (Figure 7.2). So, among the ten docked poses (A1 to A10), we considered A1, A2, and A8 for MD simulations. The protocol employed in the calculation of MD simulation is discussed in the Computational Details section. Figure 7.5 illustrates the comparative Cα-RMSD (root mean square deviation) plots for Aβ40 fibril, both in the presence (A1, A2, and A8) and absence of PDI-ALA. The Cα-RMSD values for the systems Aβ40 in water and Aβ40 in docked poses A1, A2, and A8 are represented in black and red in Figure 7.5. In the absence of PDI-ALA, Cα-RMSD values of Aβ40 are averaged to 0.8 nm and slightly increased to 1 nm after 130 ns in the case of docked pose A1. However, there are no significant differences in the Cα-RMSD values of Aβ40 of A2 and A8 compared to the Aβ40 in the water system, which can be seen in Figure 7.5b and Figure 7.5c. In addition, the visual representation of different configurations of the Aβ40-PDI-ALA system for A1, A2, and A8 collected at different times are displayed in Figure 7.6, Figure 7.7, and Figure 7.8, respectively. From Figure 7.6, in the A1 system at time t = 0 ns, the PDI-ALA interacts with a few residues from

the β-sheet region and connecting region of chain C of Aβ40. Afterward, the disruption of the chains in the connecting region of the Aβ40 was found, and this can be seen from the structure of the Aβ40 at time t = 150 ns to t = 400 ns (Figure 7.6). However, the disruptive effect of PDI-ALA on the Aβ40 structure is almost negligible in the cases of A2 and A8 docked poses, which can be noticed from the Cα-RMSD values in Figures 7.5b and 7.5c.

Further, in the A2 docked pose, we observed that the PDI-ALA was confined to the β-sheet region of the Aβ40 during the initial simulation time. After some time, the PDI-ALA moves towards the connecting regions of the protein. These movements can be noticed from the structure of the Aβ40-PDI-ALA displayed in Figure 7.7 at time t = 0 ns to t = 400 ns. In the case of the A8 docked pose (Figure 7.8), during the considered simulation time, the PDI-ALA is confined to the β-sheet region of the Aβ40 protein. This result led to an almost negligible disruption effect on the Aβ40 protein structure.

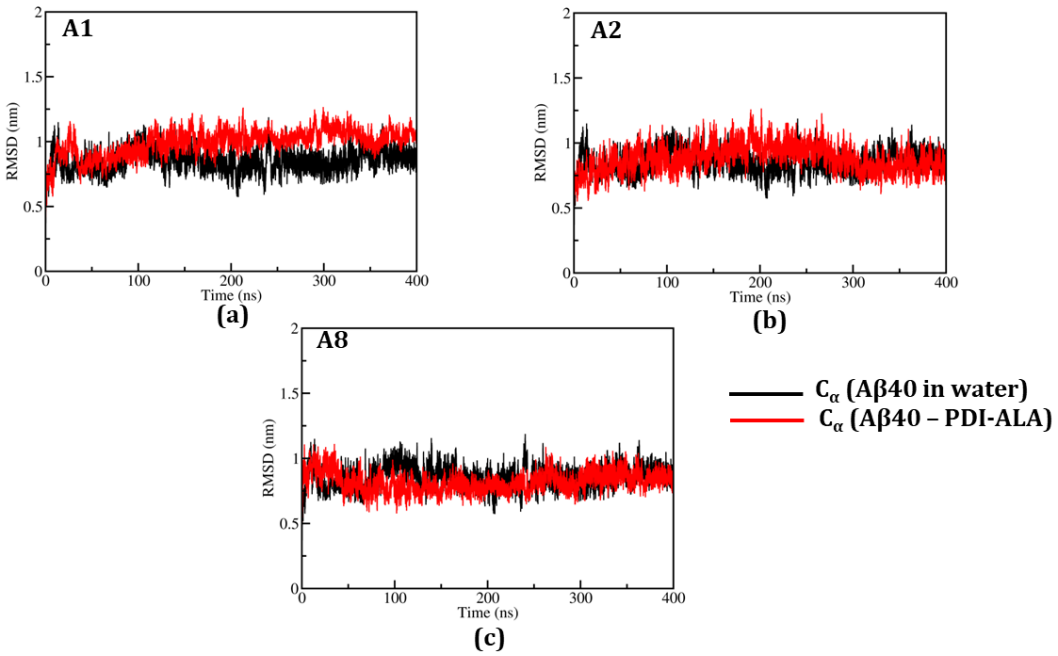

Figure 7.5. Cα-RMSD of Aβ40 fibril in the absence and presence of PDI-ALA; (a) Cα-RMSD of Aβ40 in docked pose A1; (b) Cα-RMSD of Aβ40 in docked pose A2; and (c) Cα-RMSD of Aβ40 in docked pose A8.

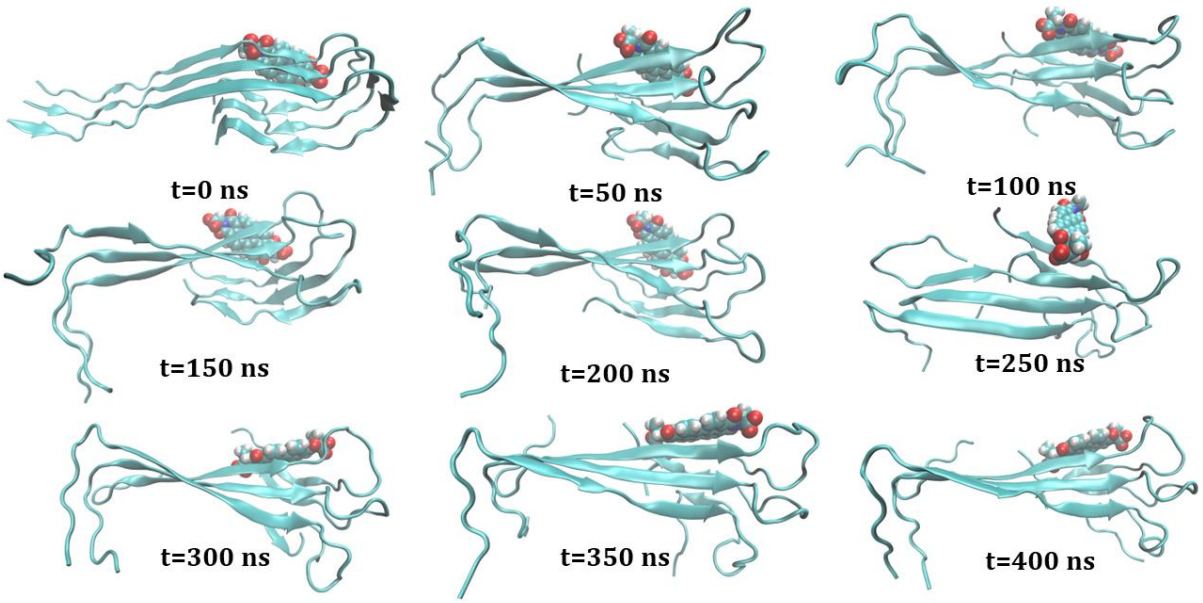

Figure 7.6. Some snapshots from the MD simulations representing the structures of the Aβ40-PDI-ALA of the A1 system collected at different times.

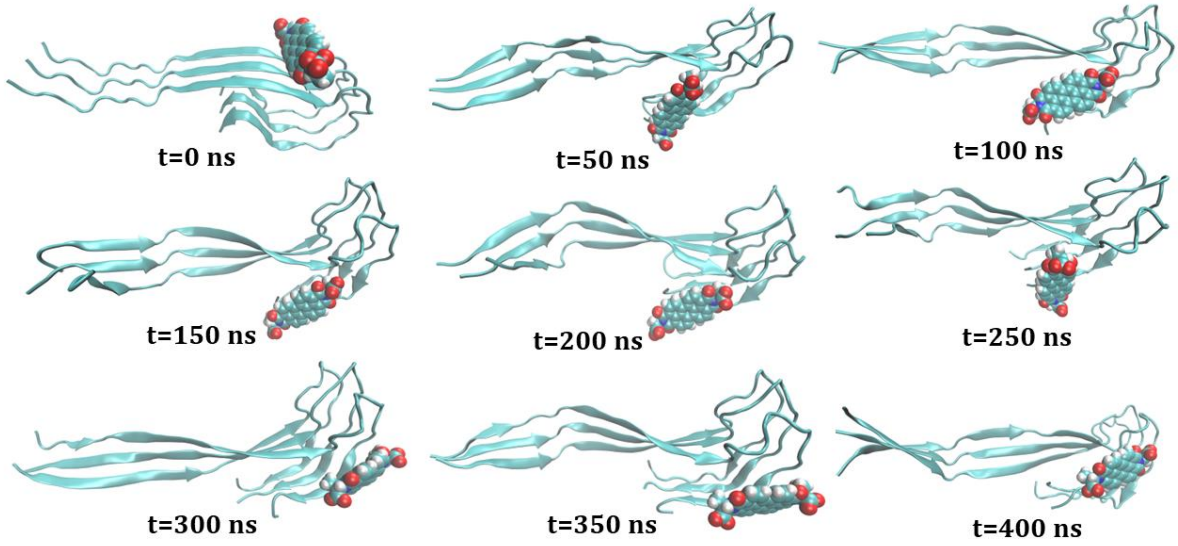

Figure 7.7. Some snapshots from the MD simulations representing the structures of the Aβ40-PDI-ALA of the A2 system collected at different times.

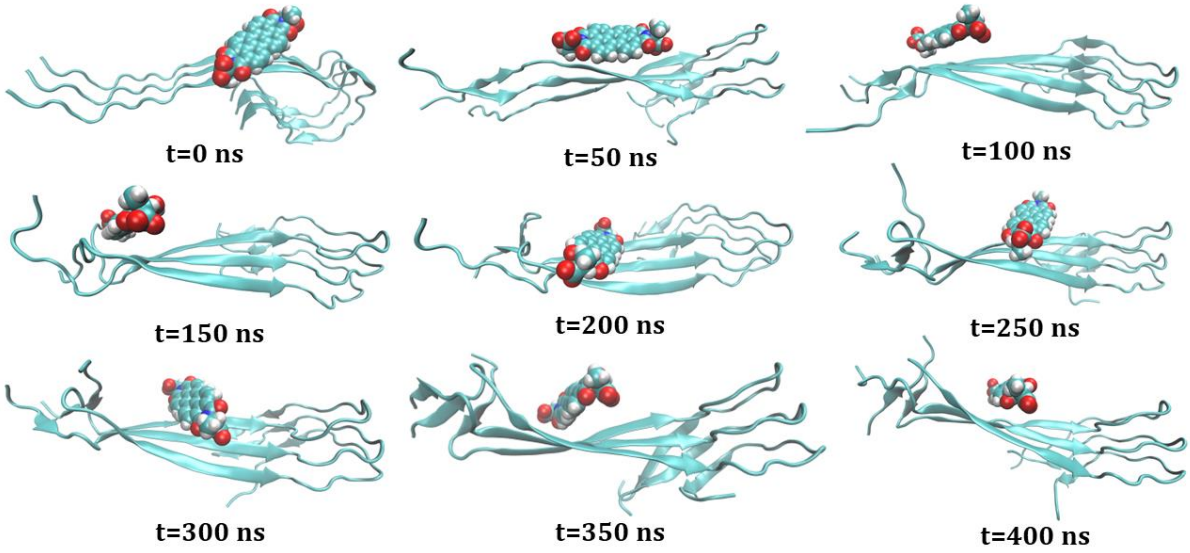

Figure 7.8. Some snapshots from the MD simulations representing the structures of the Aβ40-PDI-ALA of the A8 system collected at different times.

7.3.4.2. Molecular Dynamics Simulations Studies of PDI-PHE with Aβ40 Fibril

Likewise, in the PDI-ALA system, we have selected five docked poses, namely P1, P2, P3, and P5, for the Aβ40-PDI-PHE to perform the MD simulations studies. The structural changes of the Aβ40 protein in P1, P2, P3, P5, and Aβ40 in water are investigated by assessing the Cα-RMSD values. The comparison of Cα-RMSD values of the Aβ40 protein is displayed in Figure 7.9. In the P1 docked conformation, the Cα-RMSD values of Aβ40 reached the average value of 1 nm during the initial 150 ns, then slightly increased and fluctuated and touched the maximum peak of 1.2 nm at around 360 ns (Figure 7.9a). Gradually decreased and maintained stability. This variation in the Cα-RMSD value can be correlated with the structural disruption of Aβ40 fibril (Figure 7. 10). The structures of the Aβ40-PDI-PHE extracted at different times for the P1 system obtained from the 400 ns simulations are presented in Figure 7.10. Over the first 150 ns, PDI-PHE was localized within the β-sheet region-1 of the protein (Figure 7.10). Subsequently, it initiated a transition, shifting towards the connecting region, Aβ40, which can be observed in the configuration of Aβ40-PDI-PHE at times 200 ns to 400 ns (Figure 7.10). At the same time, the disruption of chains A, B, and C in the connecting region of the Aβ40 protein was observed. This movement can be correlated with the slight increase in the Cα-RMSD value after 150 ns (Figure 7.9a).

In the case of the P2 docked pose, the Cα-RMSD value increased and reached approximately 1.1 nm during the initial 1 ns (Figure 7.9b), then slightly fluctuated and remained stable in the

remaining simulation time. From Figure 7.11, we observed that at t = 0 ns, PDI-PHE was bound on the chain C region of the Aβ40. After 50 ns, it started closer toward the connecting region of the Aβ40, and a slight disruption in the structure of Aβ40 was found.

In docked pose P3, the Cα-RMSD value of Aβ40 is almost equal to the Cα-RMSD value of Aβ40 in water (Figure 7.9c) for the first 165 ns. Afterward, a slight elevation in the Cα-RMSD value was maintained and stable during the simulation. Further, we observed that PDI-PHE localized on the β-sheet region of Aβ40 throughout the simulation (Figure 7.12).

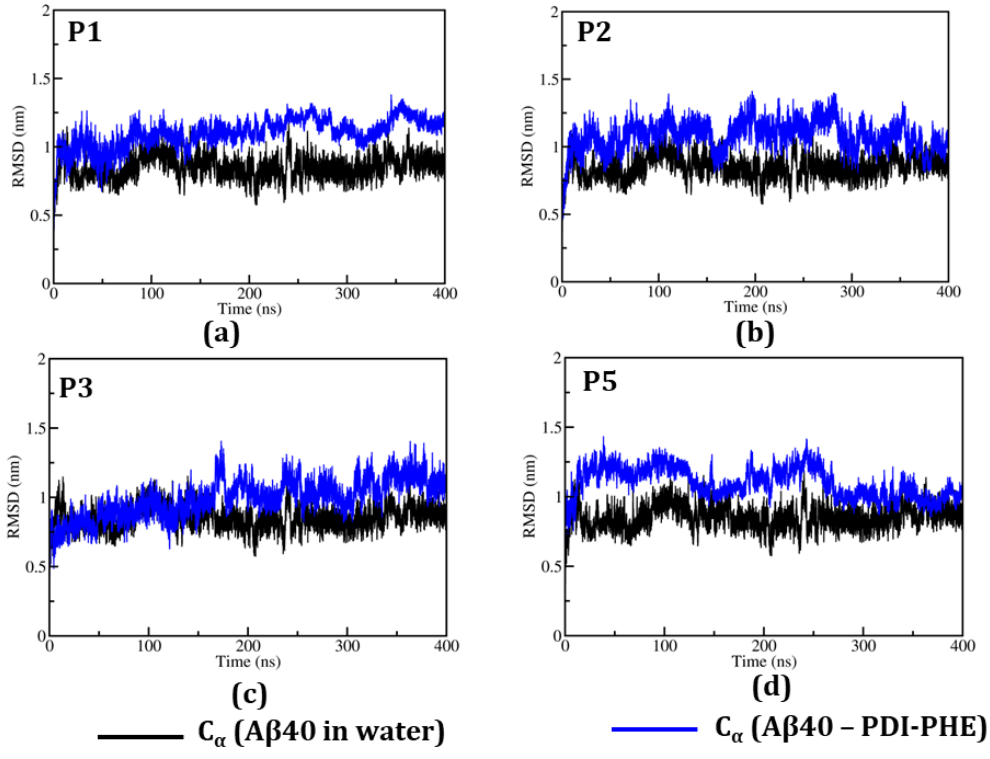

Figure 7.9. Cα-RMSD of Aβ40 fibril in the absence and presence of PDI-PHE; (a) Cα-RMSD of Aβ40 in docked pose P1; (b) Cα-RMSD of Aβ40 in docked pose P2; (c) Cα-RMSD of Aβ40 in docked pose P3; and (d) Cα-RMSD of Aβ40 in docked pose P5.

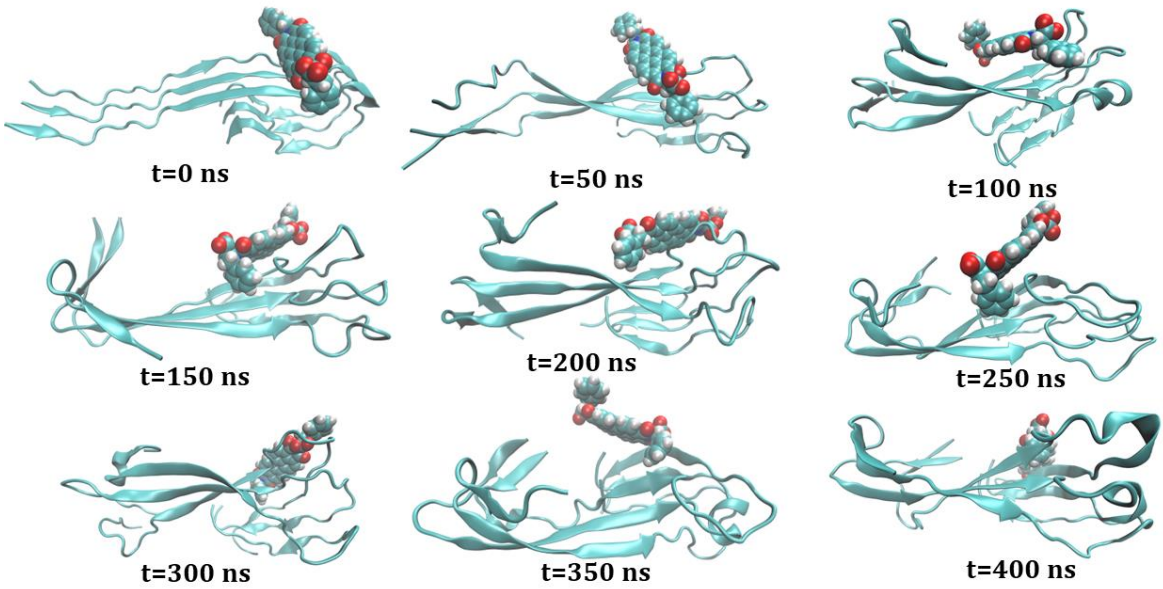

Figure 7.10. Some snapshots from the MD simulations representing the structures of the Aβ40-PDI-PHE of the P1 system collected at different times.

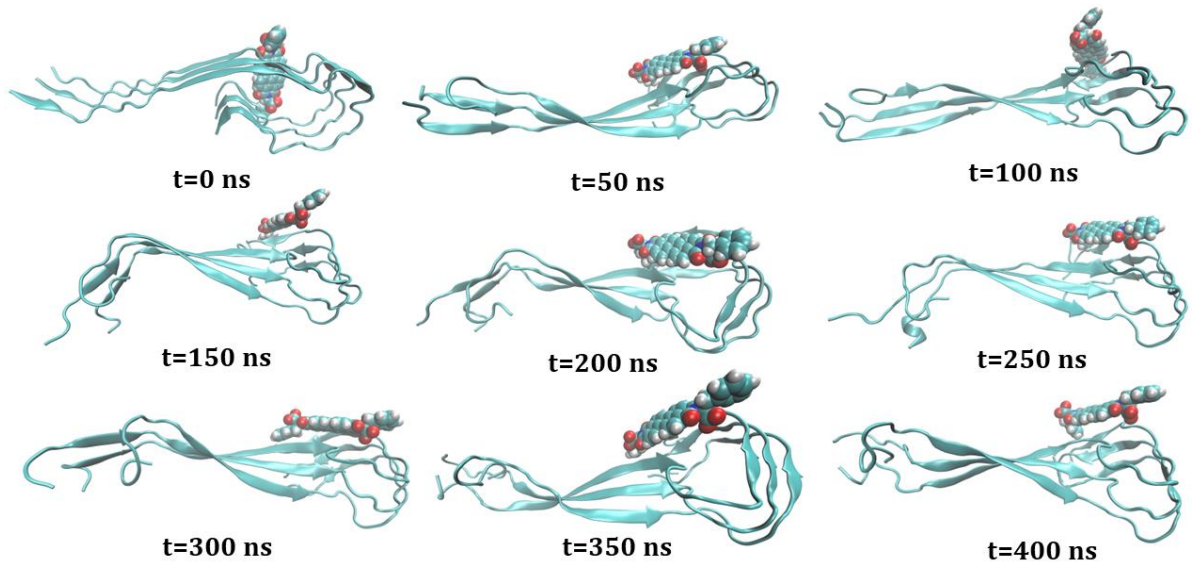

Figure 7.11. Some snapshots from the MD simulations representing the structures of the Aβ40-PDI-PHE of the P2 system collected at different times.

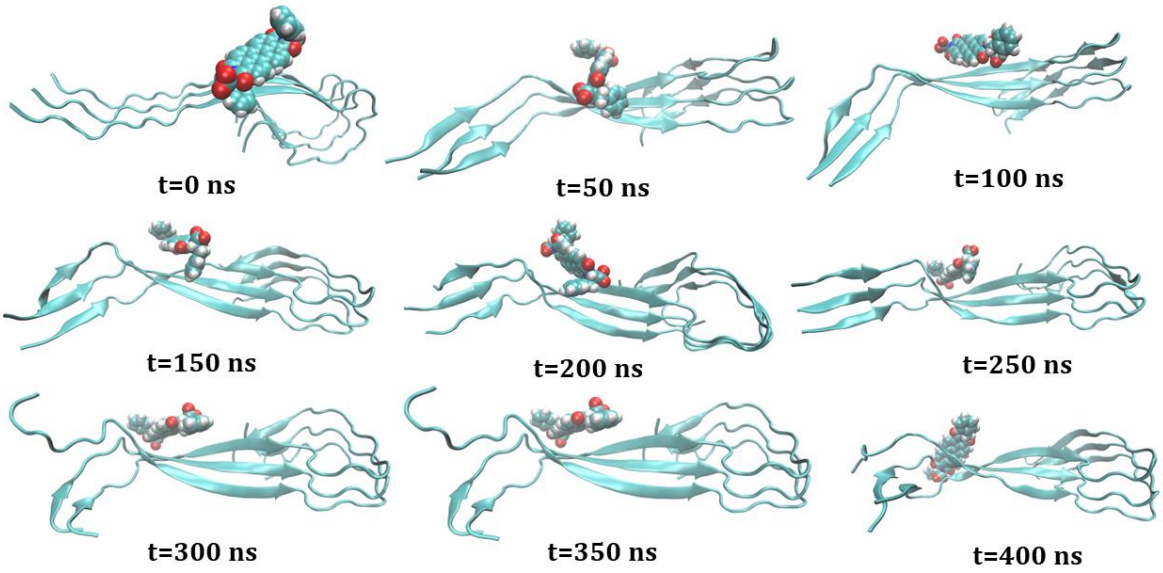

Figure 7.12. Some snapshots from the MD simulations representing the structures of the Aβ40-PDI-PHE of the P3 system collected at different times.

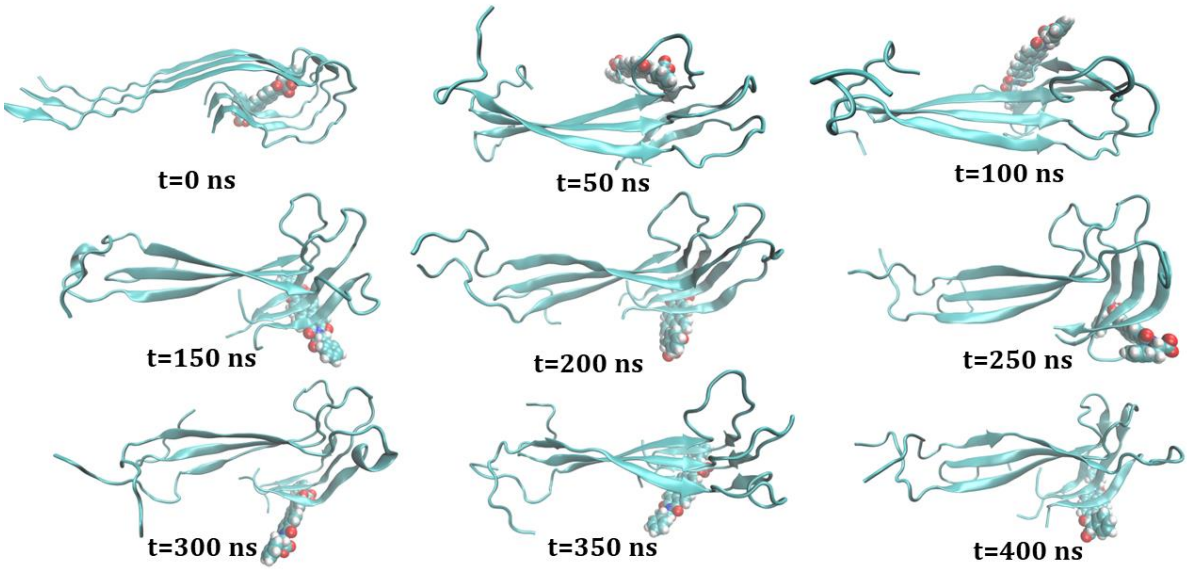

Figure 7.13. Some snapshots from the MD simulations representing the structures of the Aβ40-PDI-PHE of the P5 system collected at different times.

In the case of P5, the Cα-RMSD value of Aβ40 is increased sharply to approximately 1.2 nm within the initial 40 ns (Figure 7.9d), and it undergoes decreased and further increased to 1.2 nm around 100 ns. Subsequently, we found a decreased in the Cα-RMSD value between the approximate time intervals of 130 ns to 180 ns, suggesting that PDI-PHE is shifting from the core cavity site to the external region of the Aβ40. This shifting can be observed by assessing

the binding location of PDI-PHE on the surface of the Aβ40 at times 100 ns to 400 ns (Figure 7.13). Further, after 270 ns, the Cα-RMSD value of Aβ40 stabilized and maintained equilibrium.

7.3.4.3. Molecular Dynamics Simulations Studies of PDI-TYR with Aβ40 Fibril

The docked poses T1, T2, T6, and T8 (Figure 7.4) were selected to perform the molecular dynamics (MD) simulations studies for 400 ns. The plots of Cα-RMSD value of Aβ40 for these docked poses and comparison with the value of Aβ40 in water are illustrated in Figure 7.14. Meanwhile, the structures of the Aβ40-PDI-TYR extracted at different times for the docked poses T1, T2, T6, and T8 are displayed in Figures 7.15, 7.16, 7.17, and 7.18.

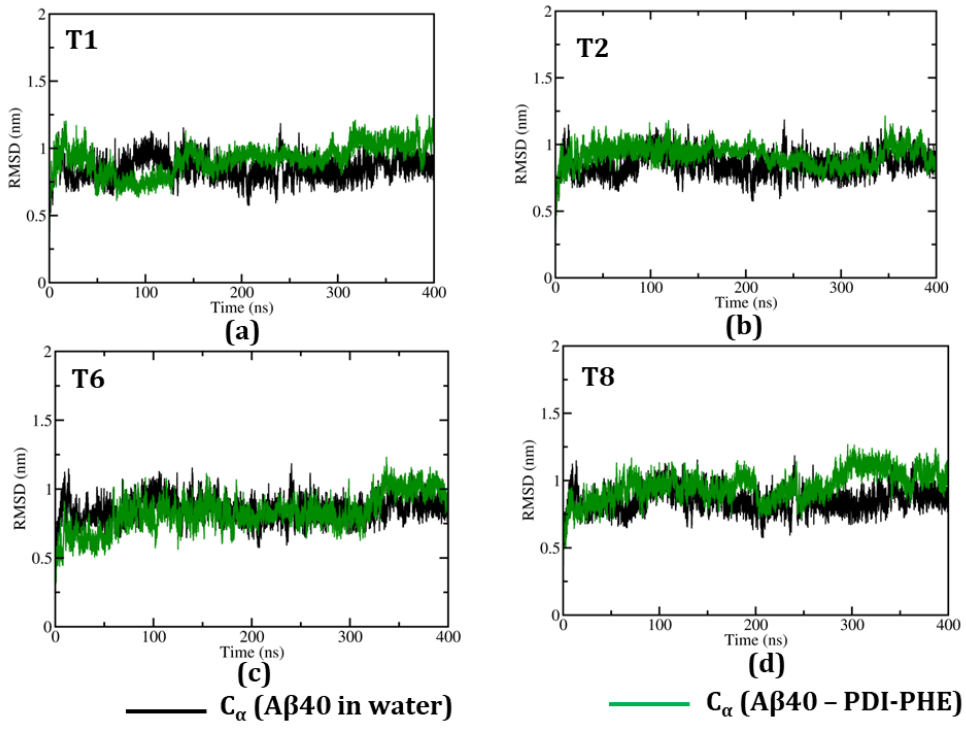

Figure 7.14. Cα-RMSD of Aβ40 fibril in the absence and presence of PDI-TYR; (a) Cα-RMSD of Aβ40 in docked pose T1; (b) Cα-RMSD of Aβ40 in docked pose T2; (c) Cα-RMSD of Aβ40 in docked pose T6; and (d) Cα-RMSD of Aβ40 in docked pose T8.

The Cα-RMSD value of Aβ40 in water closely resembled those of T1, T2, T6, and T8 (Figure 7.14). These results revealed that the disruption impact of PDI-TYR on the structure of Aβ40 is practically negligible. From Figure 7.15, in the T1 docked pose, the PDI-TYR is confined to the chain C region of the Aβ40, and destabilization on the structure of Aβ40 is significantly less. On the other hand, in T2 and T6 docked poses, the PDI-HIS localized on the β-sheet region-1 of the Aβ40 (Figure 7.16 and Figure 7.17). Furthermore, in the T8 docked pose, we

observed during the initial simulation time that the PDI-TYR binds on the β-sheet region-1, and after some time, it moved towards the chain A connecting region of Aβ40. This can be seen from Figure 7.18.

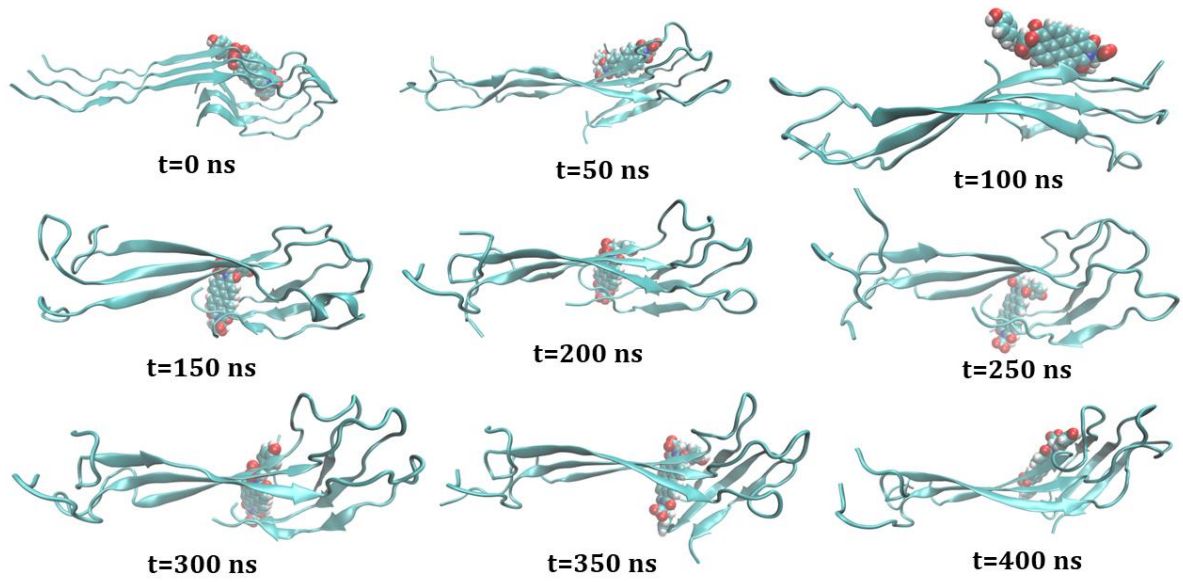

Figure 7.15. Some snapshots from the MD simulations representing the structures of the Aβ40-PDI-TYR of the T1 system collected at different times.

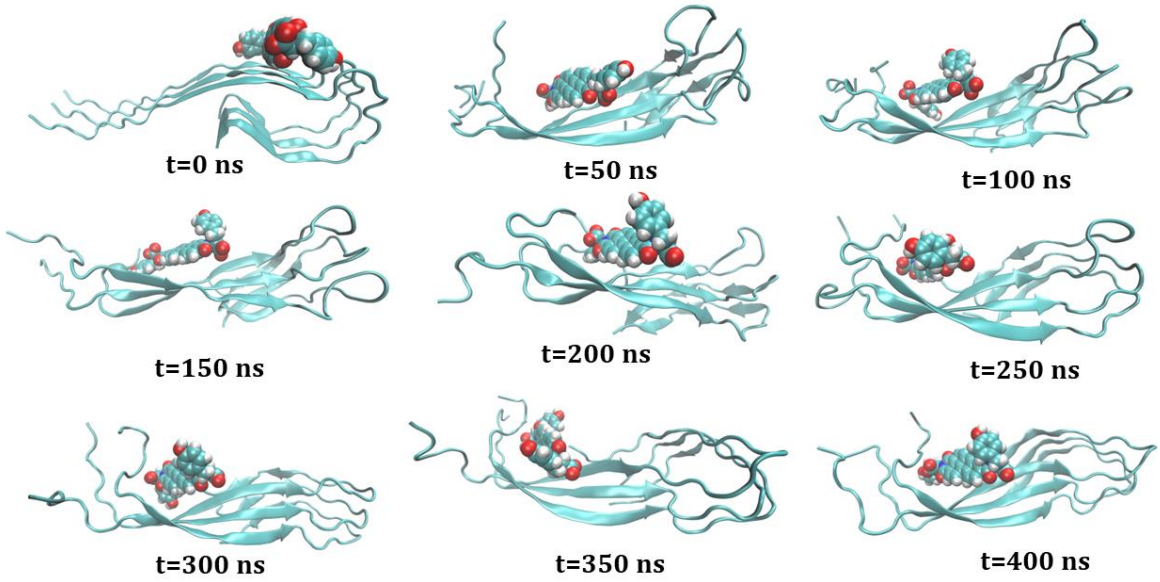

Figure 7.16. Some snapshots from the MD simulations representing the structures of the Aβ40-PDI-TYR of the T2 system collected at different times.

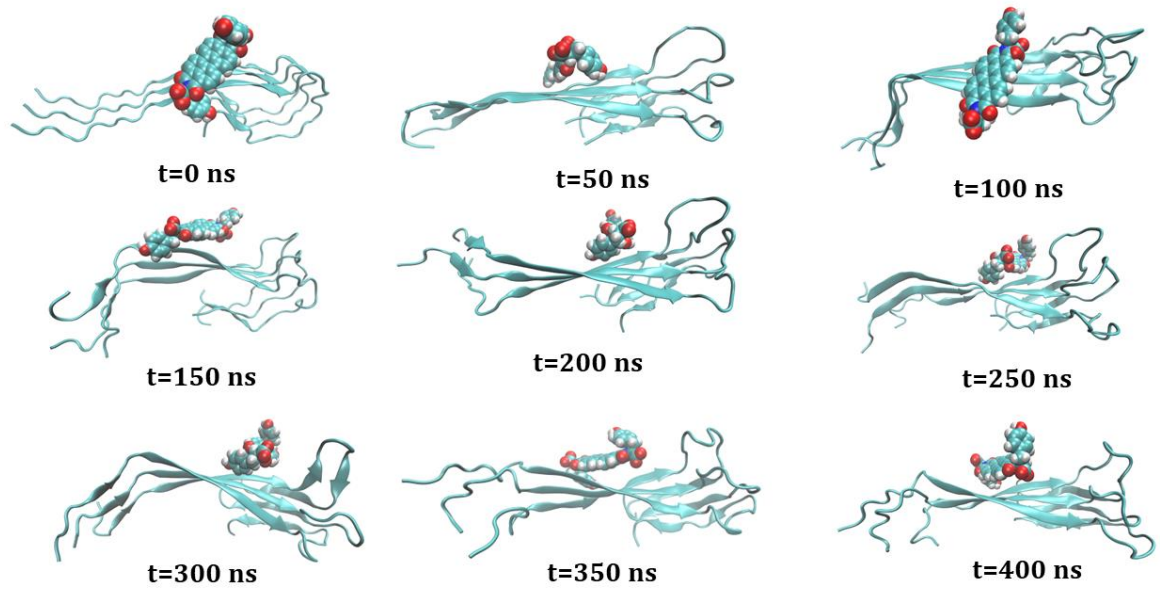

Figure 7.17. Some snapshots from the MD simulations representing the structures of the Aβ40-PDI-TYR of the T6 system collected at different times.

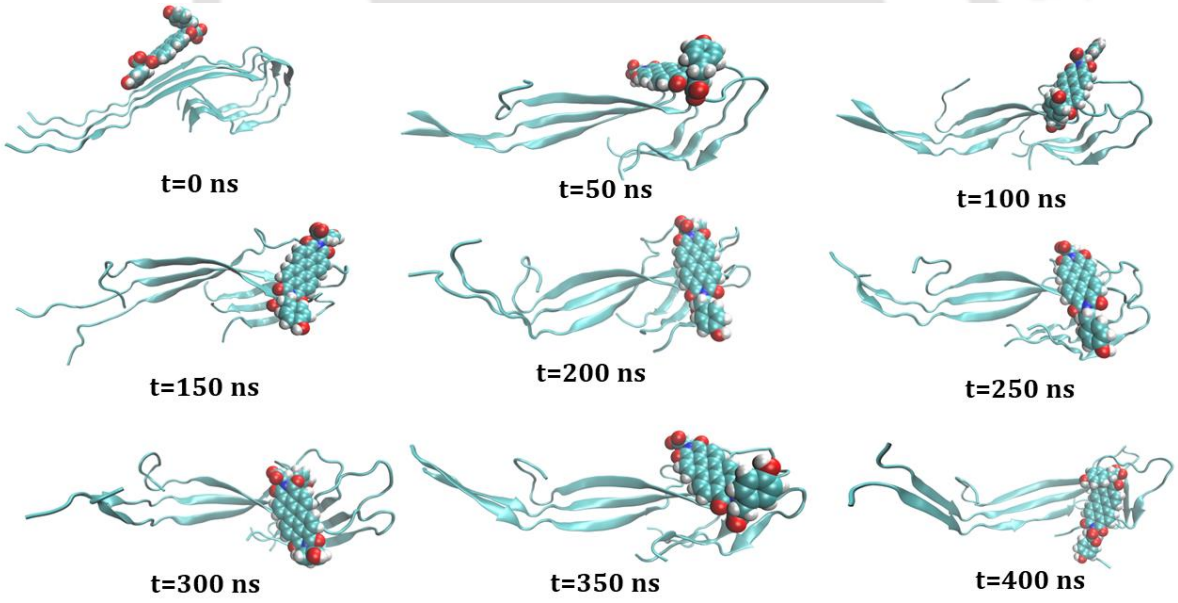

Figure 7.18. Some snapshots from the MD simulations representing the structures of the Aβ40-PDI-TYR of the T8 system collected at different times.

7.3.5. Hydrogen Bonding Interactions

Noncovalent interactions, particularly hydrogen bonding, play an essential role in the stability of proteins. Both theoretical[64] and experimental studies[65] have highlighted the significance of hydrogen bond networks in fortifying the stability of the Aβ40 fibril protein. Moreover, in Aβ40 fibrils, interpeptide hydrogen bonds play a pivotal role in structural stability and aggregations. Therefore, it is necessary to evaluate the quantity of hydrogen bonds in Aβ40 protein, both in the absence and presence of PDI-ALA, PDI-PHE, and PDI-TYR. Figure 7.19 presents the plots depicting the variation of the total number of hydrogen bonds present in Aβ40 vs. time (ns) for the system PDI-ALA, while the remaining systems, PDI-PHE and PDI-TYR, are displayed in Figure E1 and Figure E2 of Appendix-E, respectively.

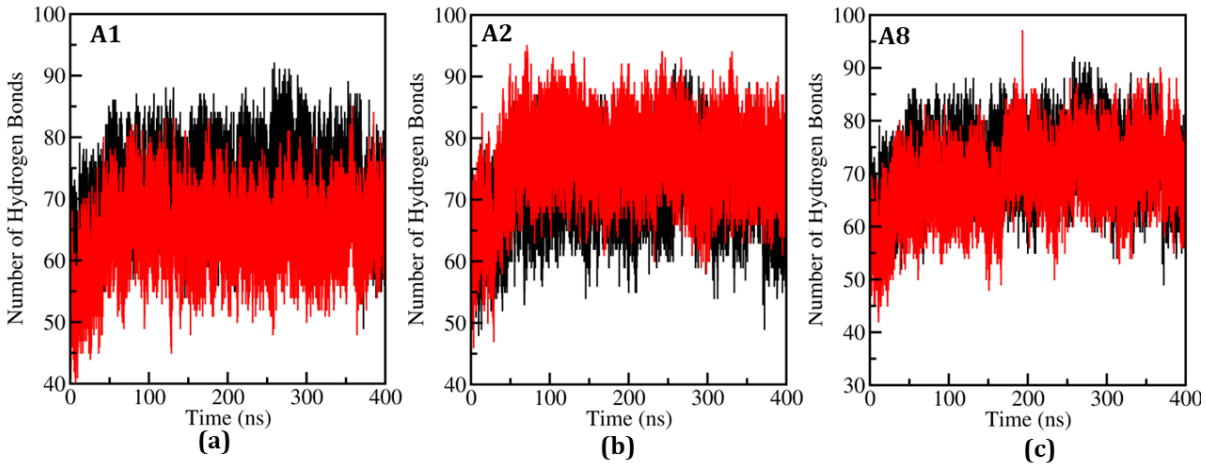

Figure 7.19. (a) Number of hydrogen bonds of Aβ40 in water (black) and Aβ40-PDI-ALA (red) system of docked poses (a) A1, (b) A2, and (c) A8.

From Figure 7.19, we observed that the total number of hydrogen bonds present in Aβ40 of A1 is slightly lower than that of the Aβ40 system in water. However, in the case of A2 and A8 docked poses, there are no significant changes in the number of hydrogen bonds during the simulation time of 400 ns. These findings revealed that the disruption of the structure of the Aβ40 protein due to the presence of PDI-ALA is significantly larger in A1. On the other hand, the Aβ40 structural disruption is less in A2 and A8 docked poses (Figure 7.19). With regard to PDI-PHE, there was no substantial reduction in the number of hydrogen bonds of Aβ40. These results provided that the destabilization effect of PDI-PHE on Aβ40 protein is minimal. The plots illustrating the variation of quantity of hydrogen bonds over simulation time (ns) for the docked poses P1, P2, P3, and P5 can be seen in Figure E1 of Appendix-E.

Furthermore, in the case of PDI-TYR, we observed a reduced number of hydrogen bonds of Aβ40 for the docked poses T1, T2, and T6. However, in the T8 docked pose, the number of hydrogen bonds present in Aβ40 closely resembled to the Aβ40 in water without PDI-TYR. This finding is depicted in Figure E2 of the Appendix-E.

7.3.6. Solvent Accessible Surface Area (SASA) Analysis

To delve deeper into the impact of PDI-ALA, PDI-PHE, and PDI-TYR on the structure of the Aβ40 protein, the SASA value was obtained from the MD trajectory results. Figure 7.20 displays the SASA values of Aβ40 in the absence of ligand, and it is marked with black colour. For the docked poses A1, P5, and T2, which have respective ligands PDI-ALA, PDI-PHE, and PDI-TYR, the SASA value of Aβ40 are denoted by the colours red, blue, and green, respectively. The SASA values for the remaining docked poses are presented in Figure E3, Figure E4, and Figure E5 of Appendix-E. SASA value is linked to the structure of the Aβ protein. The increased in the SASA value indicates the easily accessible of solvent molecule on the surface of the protein and a higher degree of looseness in the structure of the Aβ. From Figure 7.20, we found that the SASA value of Aβ40 in docked poses A1 and T2 increased with time. On the other hand, in the case of the P5 docked complex, which consists of Aβ40 and PDI-TYR, the SASA value increased sharply for the first 50 ns, then gradually decreased and fluctuated. This increase in the SASA value indicates that disrupting the stable structure of the Aβ40 trimer in the presence of ligands.

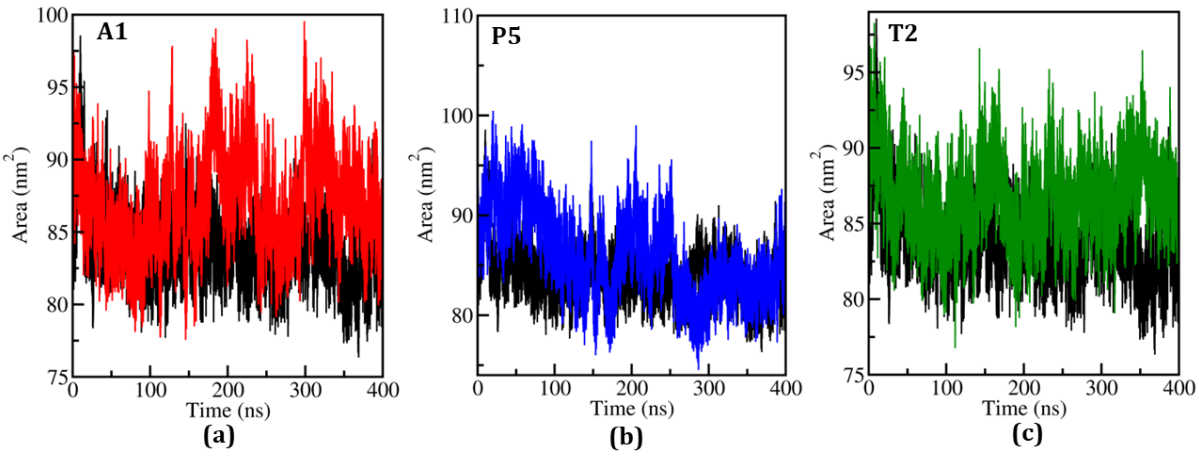

Figure 7.20. Solvent-accessible surface area (SASA) value of Aβ40 in water (black); (a) SASA value of Aβ40 in the presence of PDI-ALA for docked pose A1 (red); (b) SASA value of Aβ40 in the presence of PDI-PHE for the docked pose P5 (blue); and (c) SASA value of Aβ40 in the presence of PDI-TYR for the docked pose T2 (green).

7.3.7. Secondary Structure Analysis

The secondary structure analysis was conducted to explore the contents of β-sheets, coil, and bend of the protein in the Aβ40 in water, A1, P5, and T2. Previous investigations have provided that Aβ fibrils are predominantly composed of β-sheet structures and take a crucial role in the stability of the fibrils and aggregations. So, the investigation of β-sheet content on Aβ40 in the absence and presence of PD-ALA, PDI-PHE, and PDI-TYR is needed. The analysis was performed using a dictionary of the secondary structure of proteins (DSSP) tool. The plot consisting of the profiles of coil, β-sheets, and bend content structure of Aβ40 variation with time for the docked pose A1 is presented in Figure 7.21, while the docked poses P5 and T2 are presented in Figure E6 and Figure E7 of Appendix-E.

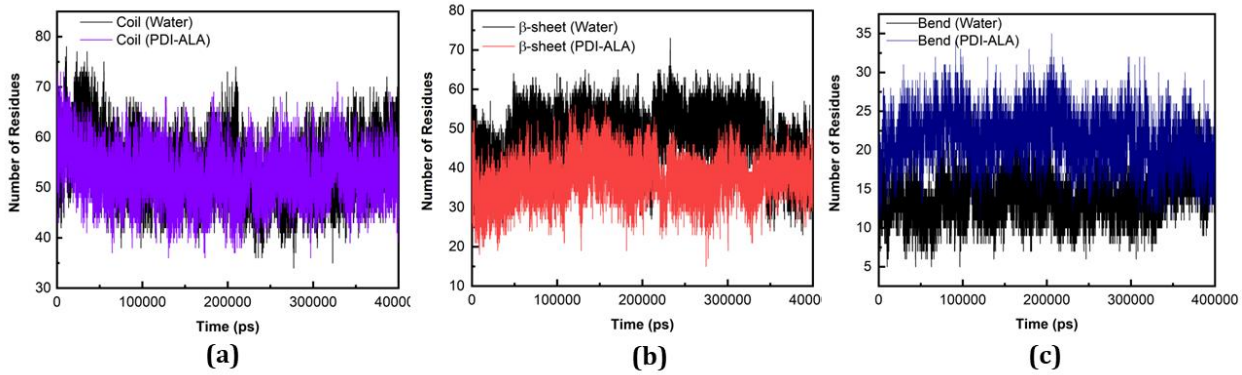

Figure 7.21. Representation of secondary structures of Aβ40-PDI-ALA of docked pose A1 for (a) coil content, (b) β-sheet content, and (c) bend content of protein in Aβ40-water and Aβ40-PDI-ALA.

As we noticed from Figure 7.21a, the changes in the amount of coil content in Aβ40 protein, both in the absence and presence of PDI-ALA, are almost negligible. However, we found that the quantity of β-sheet content in Aβ40 was reduced when the PDI-ALA binds to the protein (Figure 7.21). This result indicates that PDI-ALA accelerates the structural disruption and instability of Aβ40. At the same time, we observed an increased bend content of Aβ40 (Figure 7.21c). Further, this result revealed that the disrupted β-sheet is converted into other secondary structure forms.

7.3.8. Binding Free Energy Analysis using MM/PB(GB)SA method

To enhance our understanding of the interactions between the Aβ40 and considered ligands, we calculated the binding free energy ($\Delta G_{\text{binding}}$) for A1, P5, and T2 systems. The $\Delta G_{\text{binding}}$ for A1, P5, and T2 is calculated by employing the MM/PBSA method, and the results are presented in Table 7.4. The computed $\Delta G_{\text{binding}}$ values for the systems A1, P5, and T2 are -41.25 ± 4.41, -17.74 ± 3.96, and -34.44 ± 8.9, kcal mol^{-1}, respectively. From Table 7.4, among the A1, P5, and T2 systems, we observed that $\Delta G_{\text{binding}}$ value of A1 for the ligand PDI-ALA is relatively higher than that of P5 (PDI-PHE) and T2 (PDI-TYR). Likewise, in our previous investigation of the PDI-HIS ligand, we also found that the van der Waals interaction energy (ΔE_{vdW}) components in the systems A1, P5, and T2 were favourable for binding. On the other hand, the electrostatic interaction (ΔE_{elec}) components were unfavourable for binding. Meanwhile, the contribution of polar (ΔG_{polar}) and non-polar ($\Delta G_{\text{non-polar}}$) terms to the solvation energy (ΔG_{solv}) prefer favourable binding. Furthermore, we also noticed that the contribution of polar (ΔG_{polar}) is more significant than the non-polar ($\Delta G_{\text{non-polar}}$), which can be seen in Table 7.4.

Table 7.4. Binding free energy, $\Delta G_{\text{binding}}$, (in kcal mol^{-1}) of the A1, P5, and T2 docked poses.

	A1	P5	T2
ΔE_{vdW}	-32.57 ± 0.68	-26.76 ± 1.73	-42.83 ± 1.16
ΔE_{elec}	80.60 ± 0.95	133.09 ± 1.98	120.43 ± 7.33
ΔE_{MM}	48.03 ± 1.17	106.33 ± 2.63	77.60 ± 7.42
ΔG_{polar}	-85.22 ± 4.25	-121.17 ± 2.97	-106.44 ± 5.04
$\Delta G_{\text{non-polar}}$	-4.06 ± 0.04	-2.90 ± 0.01	-5.59 ± 0.03
ΔG_{solv}	-89.03 ± 2.8	-124.07 ± 2.97	-160.74 ± 0.80
$\Delta G_{\text{binding}}$	-41.25 ± 4.41	-17.74 ± 3.96	-34.44 ± 8.97

7.3.9. Interaction Analysis between Aβ40 and PDI-ALA, PDI-PHE, PDI-TYR in A1, P5, and T2

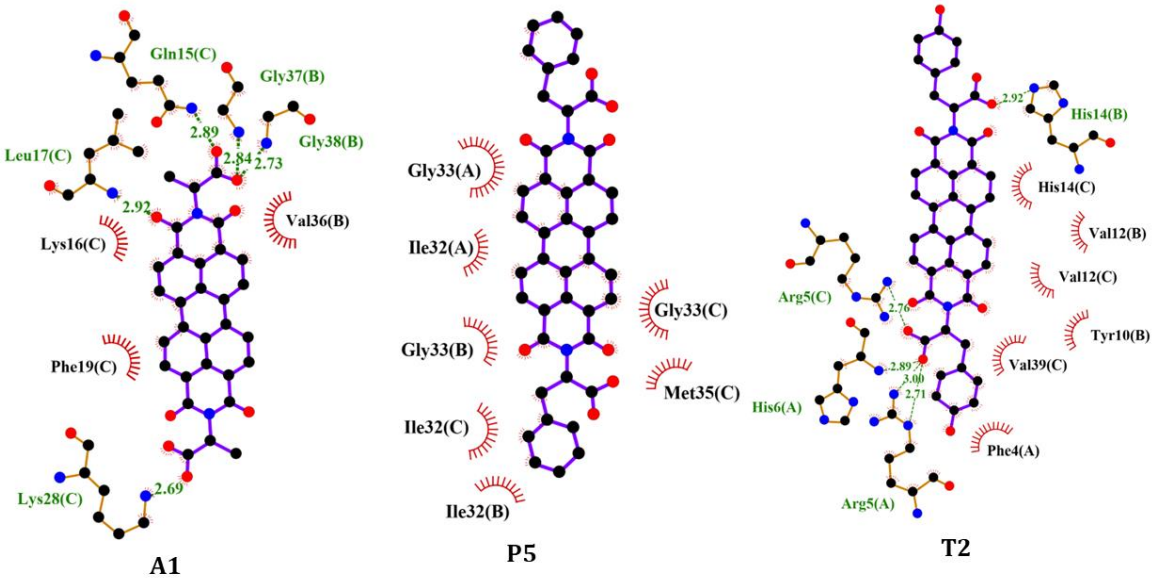

Figure 7.22. Illustration of the interactions between Aβ fibril and ligands PDI-ALA, PDI-PHE, and PDI-TYR at 400 ns for the systems A1, P5, and T2, respectively. The spike near the residues denotes the hydrophobic interactions, and the green line represents the existence of hydrogen bonding interaction (hydrogen bond distance in Å). A, B, and C represent the chains of Aβ fibril.

Using Ligplot plus,[66] depicting the interactions between the Aβ fibril and ligands PDI-ALA, PDI-PHE, and PDI-TYR corresponding to A1, P5, and T2, respectively, are generated. For this evaluation, the Aβ fibril-ligand complex at 400 ns was extracted from the MD trajectory results, and the interactions are illustrated in Figure 6.13. Hydrophobic interactions between the ligands and Aβ fibril were observed in all the systems. Besides this interaction, the hydrogen bonding interactions were also evident in A1 and T2 (Figure 7.22). The residues of Aβ fibril involved in the hydrogen bonding formation with PDI-ALA in A1 are Gln15, Leu17, and Lys28 of chain C and Gly37 and Gly38 of chain B. On the other hand, residues Arg5 and His6 of chain A, Arg5 of chain C, and His14 of chain C participated in the formation of hydrogen bonds with PDI-TYR in T2. Overall, the hydrophobic and hydrogen bonding interactions are the main driving forces of ligands to bind Aβ fibril.

7.4. Conclusions

In this chapter, we explored the modulating impact and nature of interactions of alanine, phenylalanine, and tyrosine substituted perylenediimide (PDI-ALA, PDI-PHE, PHE-TYR) on the Aβ40. Using molecular docking, we have obtained ten docked complexes A1 to A10, P1 to P10, and T1 to T10 for PDI-ALA, PDI-PHE, and PDI-TYR, respectively. We have selected a few docked poses and comprehensively investigated the structural effect and other properties of Aβ40 through molecular dynamics (MD) simulations studies. From the MD results, we found that the disruption in the structure of Aβ40 was highly observed in the docked poses A1, P5, and T2 of PDI-ALA, PDI-PHE, and PDI-TYR, respectively. The binding free energy analysis, utilizing the MM/PB(GB)SA method in conjunction with simulation results, revealed that A2 exhibited the highest binding free energy in comparison with P5 and T2. van der Waals interactions and solvation energy contributions were identified as the primary contributors to the binding of PDI-ALA, PDI-PHE, and PDI-TYR to Aβ40. Our study predicted that hydrophobic and hydrogen bonding interactions are the primary driving forces for ligands to bind Aβ40 fibril. These findings suggest that PDI-ALA, PDI-PHE, and PDI-TYR have a propensity to bind on Aβ40 and disrupt the structure, making it a promising candidate for further exploration in the development of compounds for Alzheimer's disease treatment.

7.5. References

[1] G. Moya-Alvarado, N. Gershoni-Emek, E. Perlson and F. C. Bronfman, *Mol. Cell Proteom.*, 2016, **15**, 409.

[2] M. Prince, A. Wimo, M. Guerchet, G. C. Ali, Y. T. Wu, and M. Prina, *World Alzheimer report 2015. The global impact of dementia: an analysis of prevalence, incidence, cost and trends*. Alzheimer's disease International: London, 2015, (https://www.alzint.org/resource/world-alzheimer-report-2015)

[3] A. Serrano-Pozo, M. P. Frosch, E. Masliah and B. T. Hyman, *Cold Spring Harb. Perspect. Med.*, 2011, **1**, a006189.

[4] A. J. Doig, M. P. del Castillo-Frias, O. Berthoumieu, B. Tarus, J. Nasica-Labouze, F. Sterpone, P. H. Nguyen, N. M. Hooper, P. Faller and P. Derreumaux, *ACS Chem. Neurosci.*, 2017, **8**, 1435.

[5] D. J. Selkoe and J. Hardy, *EMBO Mol. Med.*, 2016, **8**, 595.

[6] G.-F. Chen, T.-H Xu, Y. Yan, Y.-R. Zhou, Y. Jiang, K. Melcher and H. E. Xu, *Acta Pharmacol Sin.*, 2017, **38**, 1205.

[7] M. Ahmed, J. Davis, D. Aucoin, T. Sato, S. Ahuja, S. Aimoto, J. I. Elliott, W. E. Van Nostrand and S. O. Smith, *Nat. Struct. Mol. Biol.*, 2010, **17**, 561.

[8] J. Hardy and D. J. Selkoe, *Science*, 2002, **297**, 353.

[9] D. Puzzo and O. Arancio, *J. Alzheimers Disease*, 2013, **33**, S111.

[10] C. Haass and D. J. Selkoe, *Cell*, 1993, **75**, 1039.

[11] I. M. Ilie and A. Caflisch, *Chem. Rev.*, 2019, **119**, 6956.

[12] A. Dey, R. Bhattacharya, A. Mukherjee and D. K. Pandey, *Biotechnol. Adv.*, 2017, **35**, 178.

[13] P. Williams, A. Sorribas and M. J. R. Howes, *Nat. Prod. Rep.*, 2011, 28, 48.

[14] S. Gupta and A. K. Dasmahapatra, *Phys. Chem. Chem. Phys.*, 2020, **22**, 19643.

[15] L. A. Scrocchi, Y. Chen, S. Waschuk, F. Wang, S. Cheung, A. A. Darabie, J. McLaurin and P. E. Fraser, *J. Mol. Biol.*, 2002, **318**, 697.

[16] V. Villari, R. Tosto, G. Di Natale, A. Sinopoli, M. F. Tomasello, S. Lazzaro, N. Micali and G. Pappalardo, *ChemistrySelect*, 2017, **2**, 9122.

[17] M. A. Findeis, *Curr. Top. Med. Chem.*, 2002, **2**, 417.

[18] H. M. Chan, L. Xiao, K. M. Yeung, S. L. Ho, D. Zhao, W. H. Chan and H. W. Li, *Biomaterials*, 2012, **33**, 4443.

[19] L. Xiao, D. Zhao, W. H. Chan, M. M. Choi and H. W. Li, *Biomaterials*, 2010, **31**, 91.

[20] F. Tavanti, A. Pedone, M. C. Menziani and A. Alexander-Katz, *ACS Chem. Neurosci.*, 2020, **11**, 3153.

[21] L. Lannfelt, K. Blennow, H. Zetterberg, S. Batsman, D. Ames, J. Hrrison, C. L. Masters, S. Targum, A. I. Bush, R. Murdoch, J. Wilson, C. W. Ritchie and P. E. S. Grp, *Lancet Neurol.*, 2008, **7**, 779.

[22] K. Chand, Rajeshwari, E. Candeias, S. M. Cardoso, S. Chaves and M. A. Santos, *Metallomics*, 2018, **10**, 1460.

[23] T. A. Sales, I. G. Prandi, A. A. de Castro, D. H. S. Leal, E. F. F. da Cunha, K. Kuca and T. C. Ramalho, *Int J Mol Sci.*, 2019, **20**, 1829.

[24] R. K. Saini, S. Shuaib, D. Goyal and B. Goyal, *J. Biomol.Struct. Dyn.*, 2019, **37**, 3183.

[25] Y. Wang, D. C. Latshaw and C. K. Hall, *J. Mol. Biol.*, 2017, **429**, 3893.

[26] A. K. Jana and N. Sengupta, *Biophys. Chem.*, 2013, **184**, 108.

[27] J. Luo, S. K. Warmlander, C. H. Yu, K. Muhammad, A. Graslund and J. Pieter Abrahams, *Nanoscale*, 2014, **6**, 6720.

[28] J. Shin, S. Lee and M. Cha, *MedChemComm*, 2017, **8**, 625.

[29] L. Xie, D. Lin, Y. Luo, H. Li, X. Yang and G. Wei, *Biophys. J.*, 2014, **107**, 1930.

[30] W. Zhao, L. Jiang, W. Wang, J. Sang, Q. Sun, Q. Dong, L. Li, F. Lu and F. Liu, *J. Mater. Chem. B*, 2021,**9**, 6902.

[31] L. Zang, Y. Che and J.S. Moore, *Acc. Chem. Res.*, 2008, **41**, 1596.

[32] M. Gryszel, T. Schlossarek, F. Würthner, M. Natali and E. D. Głowack, *ChemPhotoChem*, 2023,**7**, e202300070.

[33] X. Zhang, S. Rehm, M. M. Safont-Sempere, F. Würthner and Vesicular, *Nat. Chem.*, 2009, **1**, 623.

[35] P. Posch, M. Thelakkat and H.W. Schmidt, *Synthetic Met.*, 1999, **102**, 1110.

[36] S. Alibert-Fouet, S. Dardel, H. Bock, M. Oukachmih, S. Archambeau, I. Seguy, P. Jolinat and P. Destruel, *ChemPhysChem*, 2003, **4**, 983.

[37] R. Gerdes, D. Wohrle, W. Spiller, G. Schneider, G. Schnurpfeil and G. Schulz-Ekloff, *J. Photochem. Photobiol. A: Chem.*, 1997, **111**, 65.

[38] Y. Li, X. Zhang and D. Liu, *J. Photochem. Photobiol. C*, 2021, **48**, 100436.

[39] Z. Zhang, Y. Zhu, X. Chen, H. Zhang and J. Wang, *Adv. Mater.*, 2019, **31**, 1806626.

[40] C.-Y. Chen, K. Wang, L-L. Gu and H. Li, *RSC Adv.*, 2017, **7**, 42685.

[41] N. Barooah, P. Karmakar, M. K. Sharanya, M. Mishra, A. C. Bhasikuttan and J. Mohanty, *J. Mater. Chem. B*, 2023, **11**, 9545.

[42] B. Muthuraj, S. R. Chowdhury and P. K. Iyer, *ACS Appl. Mater. Interfaces*, 2015, **7**, 21226.

[43] Y. Zhao and D. G. Truhlar, *Theor. Chem. Acc.*, 2008, **120**, 215.

[44] F. Weigend and R. Ahlrichs, *Phys. Chem. Chem. Phys.*, **2005**, 7, 3297.

[45] M. J. Frisch, G. W. Trucks, H. B. Schlegel, G. E. Scuseria, M. A. Robb, J. R. Cheeseman, G. Scalmani, V. Barone, G. A. Petersson, H. Nakatsuji, X. Li, M. Caricato, A. V. Marenich, J. Bloino, B. G. Janesko, R. Gomperts, B. Mennucci, H. P. Hratchian, J. V. Ortiz, A. F. Izmaylov, J. L. Sonnenberg, D. Williams-Young, F. Ding, F. Lipparini, F. Egidi, J. Goings, B. Peng, A. Petrone, T. Henderson, D. Ranasinghe, V. G. Zakrzewski, J. Gao, N. Rega, G. Zheng, W. Liang, M. Hada, M. Ehara, K. Toyota, R. Fukuda, J. Hasegawa, M. Ishida, T. Nakajima, Y. Honda, O. Kitao, H. Nakai, T. Vreven, K. Throssell, J. A. Montgomery, J. E. Peralta, F. Ogliaro, M. J. Bearpark, J. J. Heyd, E. N. Brothers, K. N. Kudin, V. N. Staroverov, T. A. Keith, R. Kobayashi, J. Normand, K. Raghavachari, A. P. Rendell, J. C. Burant, S. S. Iyengar, J. Tomasi, M. Cossi, J. M. Millam, M. Klene, C. Adamo, R. Cammi, J. W. Ochterski, R. L. Martin, K. Morokuma, O. Farkas, J. B. Foresman and D. J. Fox, Gaussian 16 Revision C.01, Gaussian Inc., Wallingford CT, 2016.

[46] R. Huey, G. M. Morris, A. J. Olson and D. S. Goodsell, *J. Comput. Chem.*, 2007, **28**, 1145.

[47] J.-X. Lu, W. Qiang, W. -M. Yau, C. D. Schwieters, S. C. Meredith and R. Tycko, *Cell*, 2013, **154**, 1257.

[48] F.J. Solis and R. J. B. Wets, *Math. Oper. Res.*, 1981, **6**, 19.

[49] K. Lindorff-Larsen, S. Piana, K. Palmo, P. Maragakis, J. L. Klepeis and R. O. Dror, *Proteins: Struct., Funct.*, Genet., 2010, **78**, 1950.

[50] J. Wang, R. M. Wolf, J. W. Caldwell, P. A. Kollman and D. A Case, *J. Comput. Chem.*, 2004, **25**,1157.

[51] T. Lu, Sobtop: *A Tool of Generating Forcefield Parameters and GROMACS Topology*. Available online: http://sobereva.com/soft/Sobtop

[52] H. J. C. Berendsen, J. R. Grigera and T. P. Straatsma, *J. Phys. Chem.*, 1987, **91**, 6269.

[53] G. Bussi, D. Donadio and M. Parrinello, *J. Chem. Phys.*, 2007, **126**, 014101.

[54] S. Nosé and M. L. Klein, *Mol. Phys.*, 1983, **50**, 1055.

[55] B. Hess, H. Bekker, H. J. Berendsen and J. G. Fraaije, *J. Comput. Chem.*, 1997, **18**, 1463.

[56] T. Darden, D. York and L. Pedersen, *J. Chem. Phys.*, 1993, **98**, 10089.

[57] D. Van Der Spoel, E. Lindahl, B. Hess, G. Groenhof, A. E. Mark and H. J. C. Berendsen, *J. Comput. Chem.*, 2005, **26**, 1701.

[58] E. F. Pettersen, T. D. Goddard, C. C. Huang, G. S. Couch, D. M. Greenblatt, E. C. Meng and T. E. Ferrin, *J. Comput. Chem.*, 2004, **25**, 1605.

[59] W. Humphrey, A. Dalke and K. Schulten, *J. Mol. Graph.*, 1996, **14**, 33.

[60] J. Srinivasan, T. E. Cheatham, P. Cieplak, P. A. Kollman and D. A. Case, *J. Am. Chem. Soc.*, 1998, **120**, 9401.

[61] I. Massova and P. A. Kollman, *Perspect. Drug Discovery Des.*, 2000, **18**, 113.

[62] M. S. Valdés-Tresanco, M. E. Valdés-Tresanco, P. A. Valiente and E. Moreno, *J. Chem. Theory Comput.*, 2021, **17**, 6281.

[63] E. Wang, H. Sun, J. Wang, Z. Wang, H. Liu, J. Z. H. Zhang and T. Hou, *Chem. Rev.*, 2019, **119**, 9478.

[64] J. Zheng, H. Jang, B. Ma, C.-J. Tsai and R. Nussinov, *Biophys. J.*, 2007, **93**, 3046.

[65] M. Sunde, L. C. Serpell, M. Bartlam, P. E. Fraser, M. B. Pepys and C. C. Blake, *J. Mol. Biol.*, 1997, **273**, 729.

[66] R. A. Laskowski and M.B. Swindells, *J. Chem. Inf. Model.*, 2011, **51**, 2778.

Chapter 8

Summary and Conclusions

Noncovalent interactions are widely involved in diverse applications such as supramolecular host-guest interaction, conformational stability of molecular systems, protein-ligand interactions, material science, etc. A few of these interactions are hydrogen bonding, π-π stacking, cation-π, anion-π, etc. Additionally, π-π interaction also served as an electron charge transport system in the host-guest complex. Furthermore, the popularity of noncovalent interactions is also seen in the protein-ligand interactions. One key focus domain involves the binding of inhibitors or drug molecules with amyloid-β (Aβ) fibrils protein. These fibrils are considered the primary cause of the development of Alzheimer's disease (AD). Taking the opportunity of quantum chemical and classical molecular dynamic (MD) methods, computational exploration was conducted to study the noncovalent interactions in supramolecular host-guest systems and protein-ligand systems. The work covered in this thesis is divided into five main parts:

The beginning of this thesis's Chapter 3 is devoted to the investigation of stability and torsional rotational barriers of different conformers of ditopic host 1,6-bis(2,6-bis(benzothiazol-2-yl) pyridine-4-yloxy) hexane (bbh). In addition, the intermolecular interactions present in host-guest complexes formed between bbh and resorcinol guest. The DFT calculation results revealed that a conformer that has intramolecular C-H···N and C-H···S interactions is relatively more stable than others. Through torsional rotation within the bbh system, these intramolecular were vanished. The energy decomposition analysis (EDA) results of the host-guest complexes formed between the bbh and resorcinol guest provided that electrostatic interaction components dominantly contributed to the host-guest interaction. Furthermore, the noncovalent (NCI) analysis confirmed the existence of intermolecular hydrogen bonding and other weak interactions in complexes.

In Chapter 4, utilizing the DFT functional in conjunction with Grimme's dispersion correction, the intermolecular π-π interaction was investigated in the series of host-guest complexes formed between the electron deficient hexacationic cage host (H) and polycyclic aromatic hydrocarbon (PAH) guests namely, naphthalene (G7), anthracene (G2), phenanthrene (G3), pyrene (G4), triphenylene (G5), corannulene (G6), and perylene (G7). Excluding the complex

formed with corannulene (G6) the interaction energy (ΔE) of the remaining complexes showed an increase with the rise in the number of π-electrons of the guest. The abnormal value in the ΔE of the complex formed by G6 may be the existence of the bowl-shaped geometry inside the cavity of the host H. The energy decomposition analysis (EDA) of the complexes unveiled that a major factor in the host-guest binding was contributed from the dispersion interaction term. Furthermore, the conductance measurement showed an increased in the conductance value of H when guest molecules were accommodated inside the cavity of the host. The maximum conductance value was observed in the complex which has perylene (G7) as a guest.

In Chapter 5, noncovalent interactions such as hydrogen bonding and π-π interaction present in the series of 1:1 host-guest complexes formed between the propanediurea-based molecular host and resorcinol guests in which a variety of electron withdrawing and donating were substituted. There are no significant changes in the interaction energy value when the electron-donating groups are substituted. However, the increased in the interaction energy value was observed when the electron-withdrawing groups were substituted on resorcinol.

Chapter 6 explores the impact of structural disruption on the amyloid-β (Aβ) when it interacts with the histidine functionalized perylene diimide (PDI-HIS). The molecular docking and molecular dynamics (MD) simulation results showed that PDI-HIS disrupted the structure of the Aβ40 fibril. The solvent accessible surface area (SASA) value of Aβ40 was found to be increased when the Aβ40 interacted with PDI-HIS. This increased in the SASA value indicates the looseness and conformation changes of Aβ40. Furthermore, in the presence of PDI-HIS, the quantity of hydrogen bonds, and β-sheets content in Aβ40 was found to be reduced. These results showed the disruption and instability of the structure of Aβ40 fibril. Furthermore, the existence of hydrophobic and hydrogen interactions was observed between PDI-HIS and Aβ40.

In Chapter 7, the study focused on three compounds (PDI-ALA, PDI-PHE, and PDI-TYR) which are obtained from PDI by substituting with amino acids namely phenylalanine (PDI-PHE), alanine (ALA), and tyrosine (TYR) to see the modulating effect on the structure of the Aβ40 and interaction involved. Molecular docking and molecular dynamics (MD) simulation results revealed that all the compounds PDI-ALA, PDI-PHE, and PDI-TYR show a disruption effect on the structure of Aβ40 fibril. Similarly, as observed in the PD-HIS system, the overall number of intra and inter chains hydrogen bonds and quantity of β-sheets content of Aβ40 was reduced. The binding free energy results suggest that these compounds have the potential to

bind on Aβ40 protein. Interestingly, PDI-ALA shows the highest binding free energy among the three compounds.

This thesis highlighted the fundamental properties and important applications of noncovalent interactions in the context of host-guest and protein-ligand systems. The work presented in this thesis will contribute to designing the supramolecular host molecule. Further, this thesis's work will also help in the domain of material science for the development of electronic materials composed of supramolecular systems. Furthermore, the study of Aβ40 protein interaction with amino acid functionalized PDI molecules will trigger the finding of drug molecules for AD.

Appendix-A

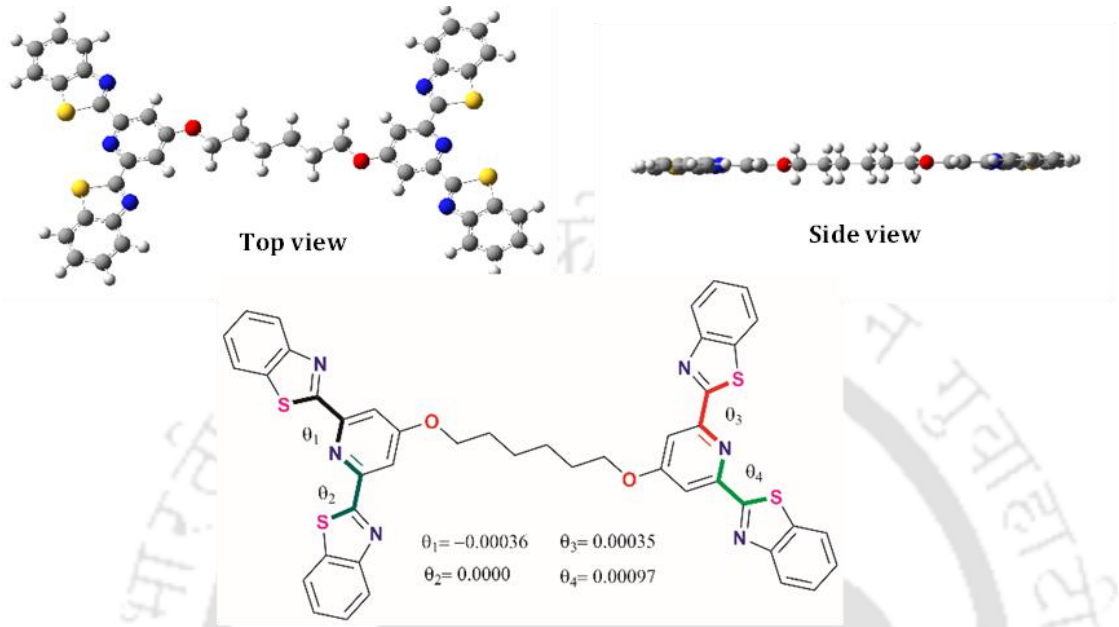

Figure A1. Optimized geometry of the S-N-S|S-N-S conformer showing their torsional angles (θ_1, θ_2, θ_3, and θ_4) values calculated at the B3LYP-D3/6-311++G(d,p) level of theory.

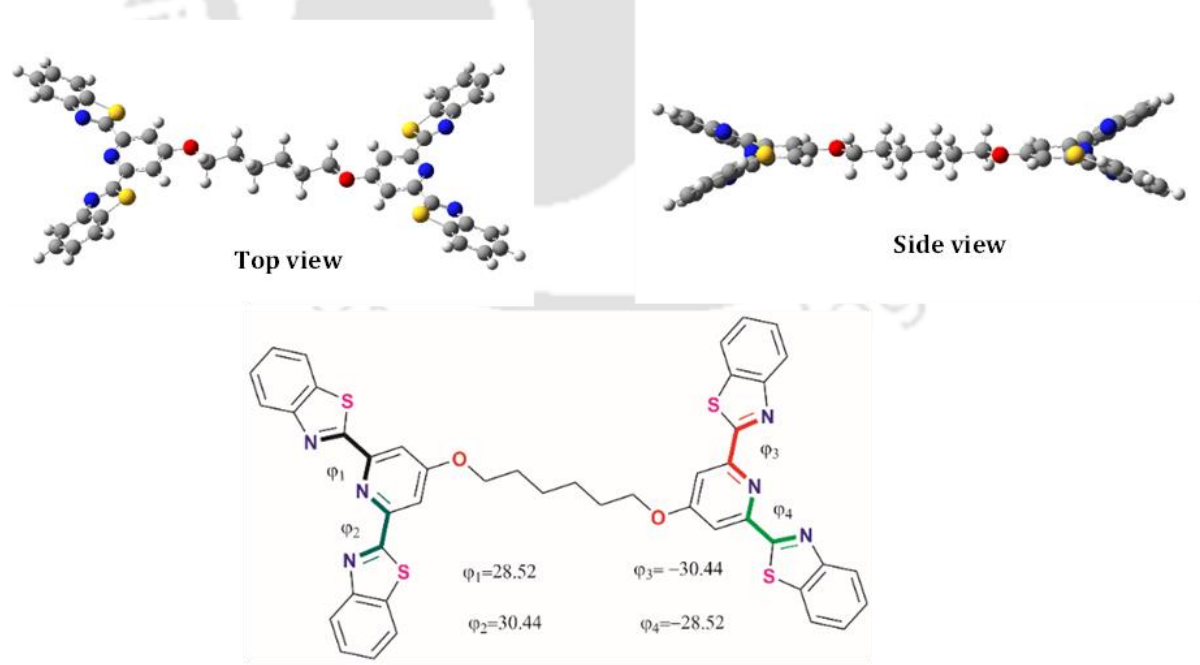

Figure A2. Optimized geometry of the N-N-N|N-N-N conformer showing their torsional angles (φ_1, φ_2, φ_3, and φ_4) values calculated at the B3LYP-D3/6-311++G(d,p) level of theory.

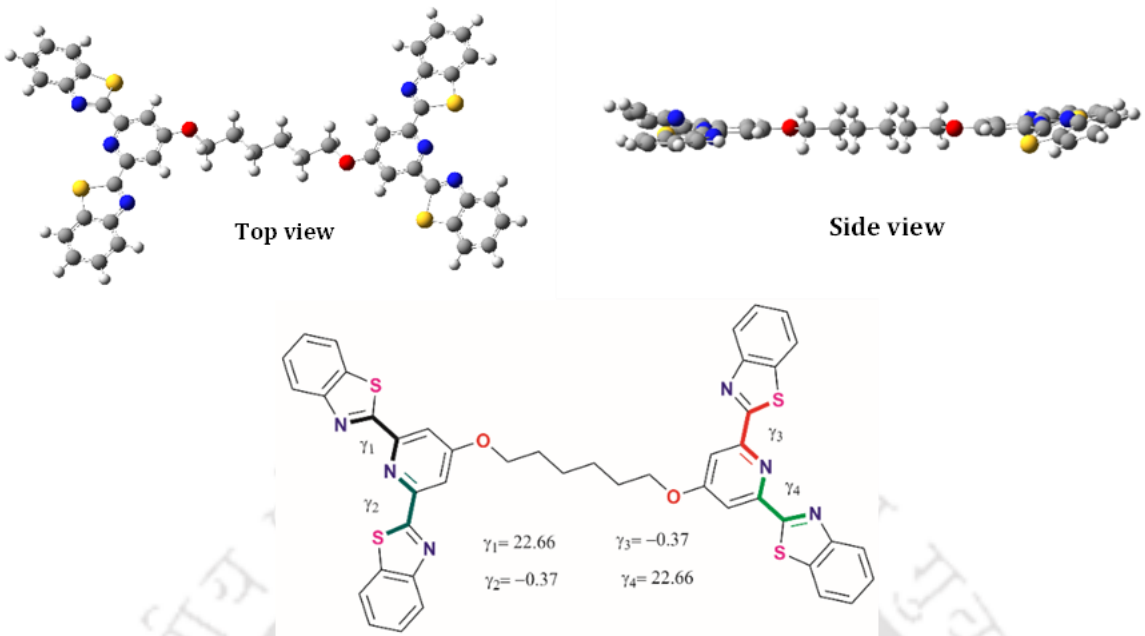

Figure A3. Optimized geometry of the N-N-S|S-N-N conformer showing their torsional angles (γ_1, γ_2, γ_3, and γ_4) values calculated at the B3LYP-D3/6-311++G(d,p) level of theory.

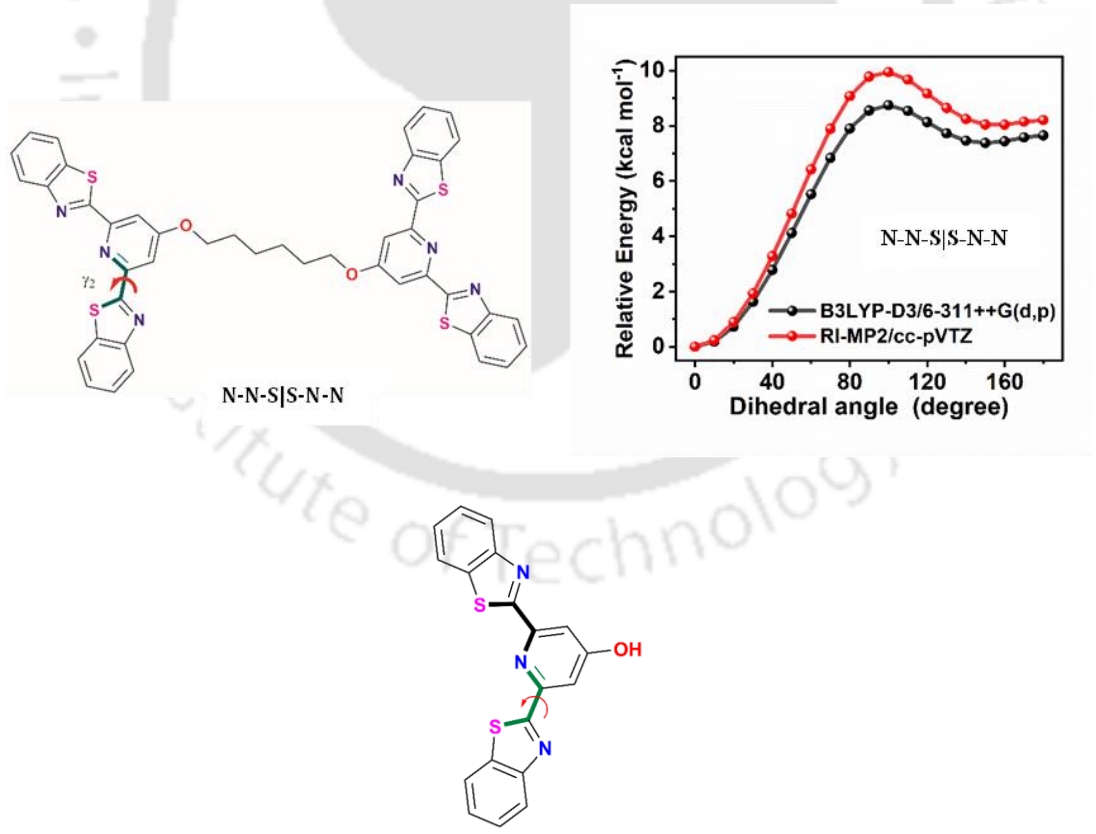

Figure A4. Molecular structure of the S-N-S conformer calculated at the B3LYP-D3/6-311++G(d,p) level of theory.

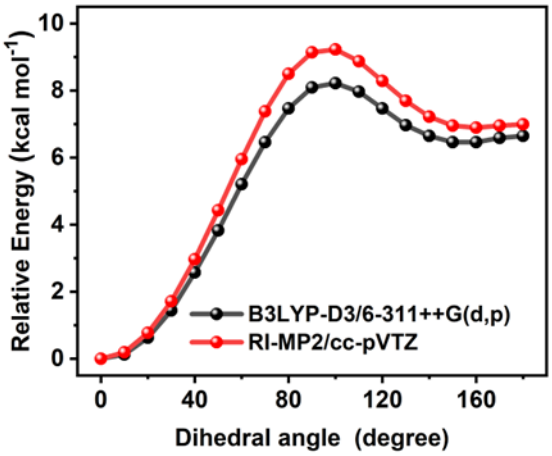

Figure A5. Torsional potential energy surface (PES) of the S-N-S conformer. The relative energy values in kcal mol^{-1}. The RI-MP2/cc-pVTZ //B3LYP-D3/6-311++G(d,p) denotes the single point energy calculation at the RI-MP2/cc-pVTZ to the optimized geometry calculated at the B3LYP-D3/6-311++G(d,p).

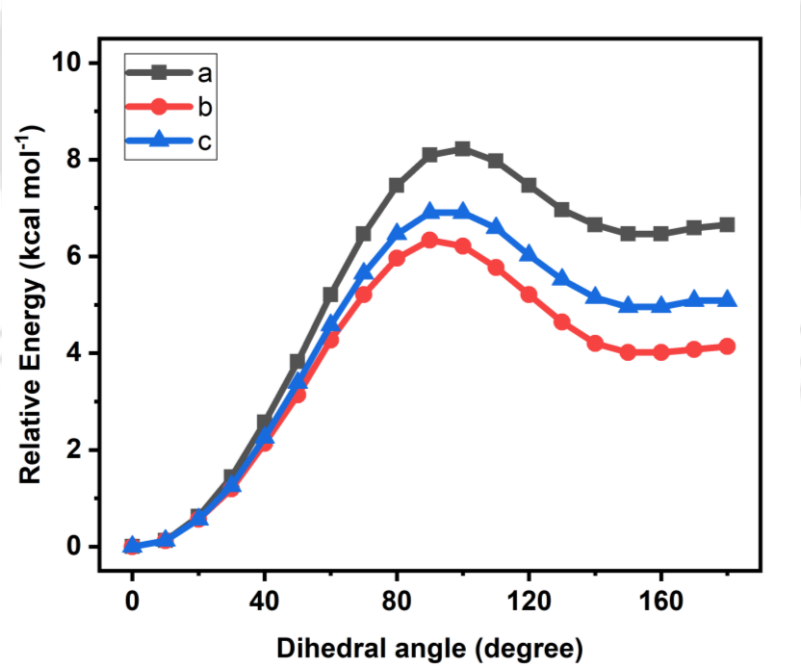

Figure A6. Torsional potential energy surfaces (PESs) of the S-N-S conformer in the (a) gas phase, (b) chloroform, and (**c**) acetonitrile. The relative energy values in kcal mol^{-1} were calculated at the B3LYP-D3/6-311++G(d,p) level of theory.

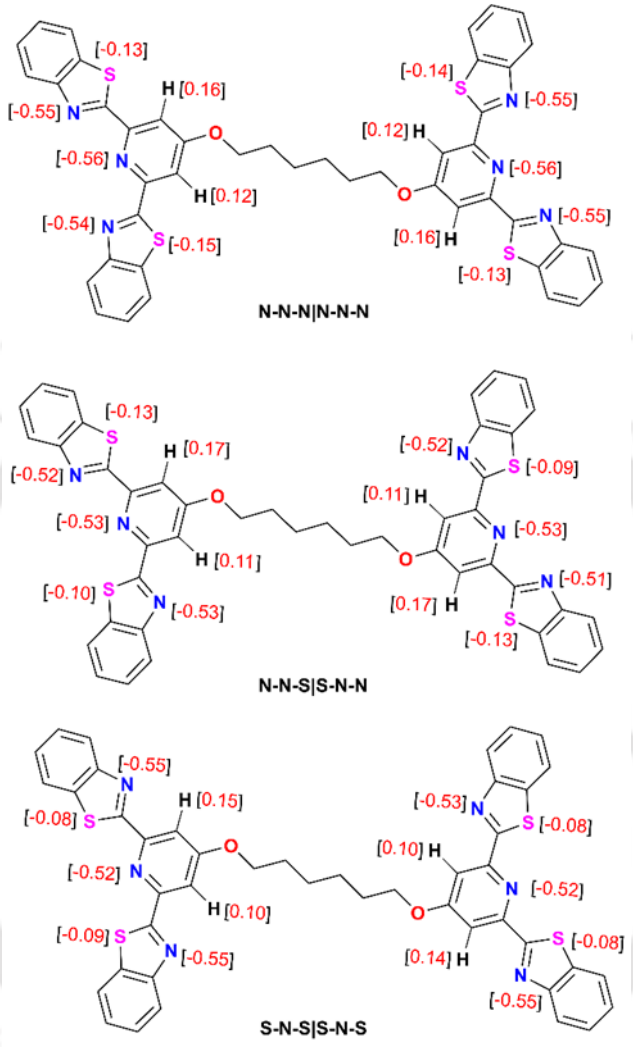

Figure A7. CHelpG charge analysis of conformers N-N-N|N-N-N, S-N-S|S-N-S, and N-N-S|S-N-N calculated at the B3LYP-D3/6-311++G(d,p) level of theory.

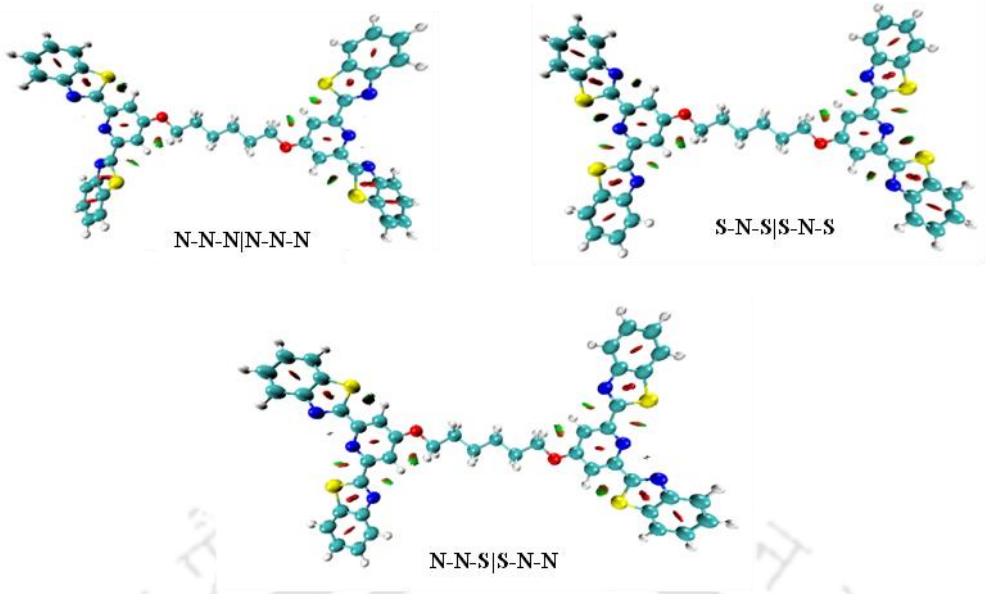

Figure A8. Noncovalent Interactions (NCI) plots of N-N-N|N-N-N, S-N-S|S-N-S, and N-N-S|S-N-N, conformers calculated at the B3LYP-D3/6-311++G(d,p) level of theory.

Interaction Energy [ΔE]

Interaction Energy with counterpoise correction [ΔE (cp)]

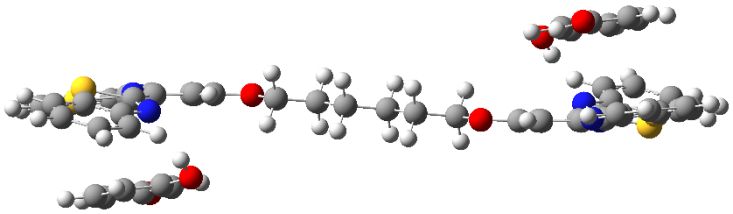

ΔE = -29.64 kcal mol^{-1}

ΔE (cp) = -24.31 kcal mol^{-1}

***trans* (resocrinol:S-N-S|S-N-S:resocrinol)**

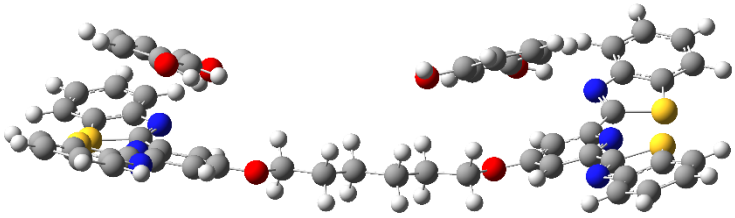

ΔE = -31.34 kcal mol^{-1}

ΔE (cp) = -26.72 kcal mol^{-1}

***cis* (resocrinol:S-N-S|S-N-S:resocrinol)**

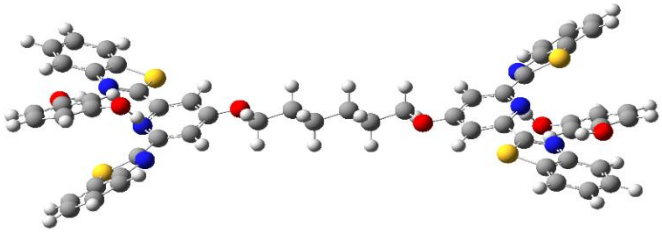

ΔE = -36.75 kcal mol^{-1}

ΔE (cp) = -31.98 kcal mol^{-}

***trans* (resocrinol:N-N-S|S-N-N:resocrinol)**

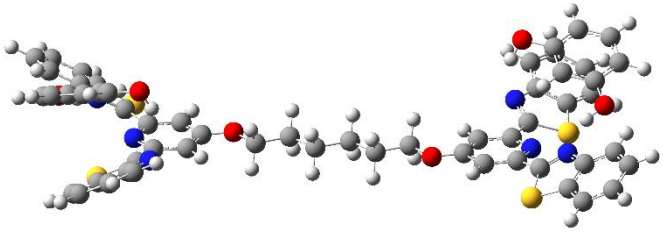

ΔE = -36.70 kcal mol^{-1}

ΔE (cp) = -31.90 kcal mol^{-1}

Figure A9. Binding energies of trimer complexes form between the conformers S-N-S|S-N-S and N-N-S|S-N-N of host bbh with resorcinol guest molecule calculated at the B3LYP-D3/6-311++G(d,p) level of theory.

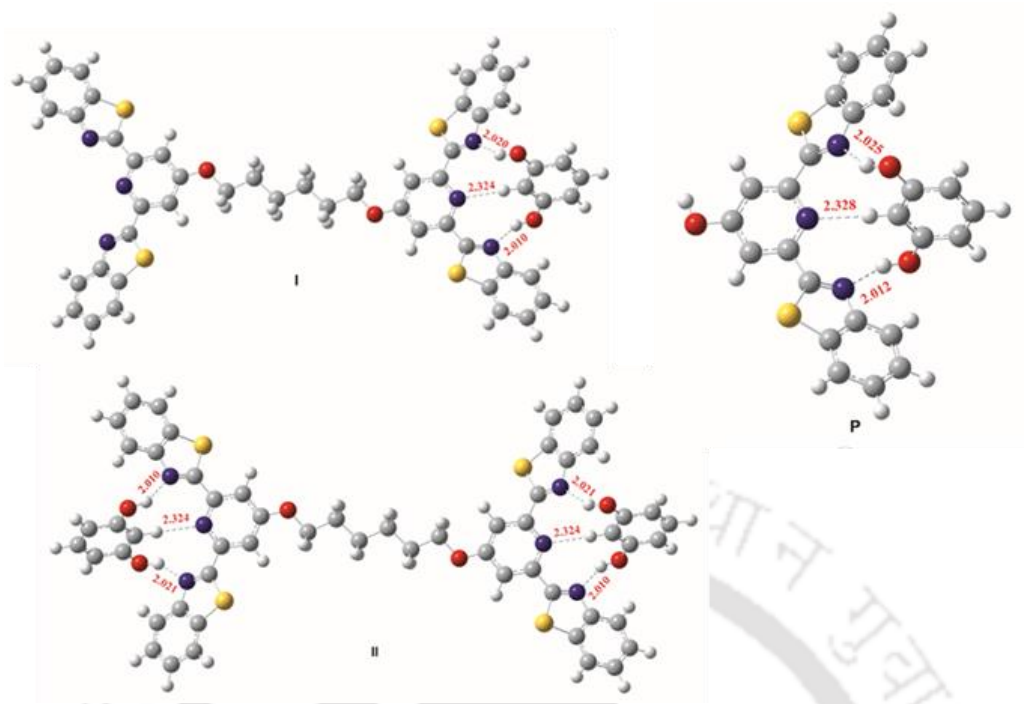

Figure A10. Interatomic distances of complexes I, II, and P calculated at the B3LYP-D3/6-311++G(d,p) level of theory.

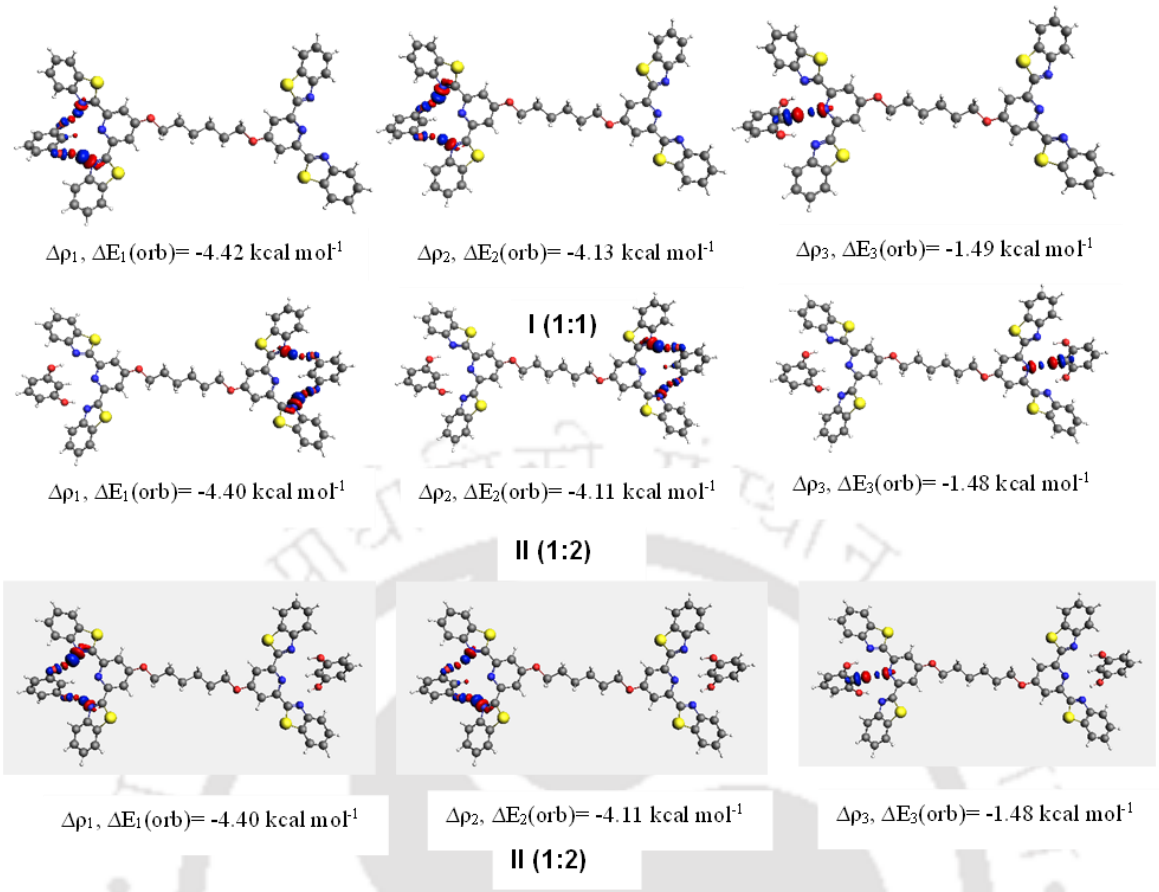

Figure A11. Contour plots (contour value 0.001) of deformation densities $\Delta\rho_1$, $\Delta\rho_2$, and $\Delta\rho_3$ describe the hydrogen bonding interactions of complexes I and II. And also shown their corresponding energy contributions [ΔE_1 (orb), ΔE_2(orb), ΔE_3(orb)] in kcal mol^{-1}.

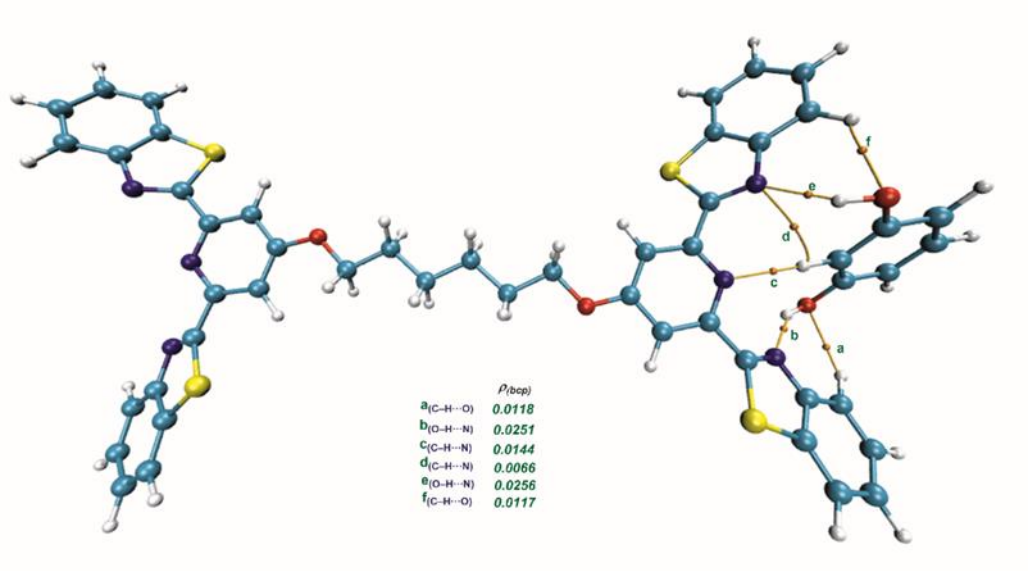

Figure A12. Optimised geometry of dimer complex I and key noncovalent interactions analysis through the AIM formalism calculated at the B3LYP-D3/6-311++G(d,p) level of theory. Major interactions and their corresponding electron densities ρ(r) [au] at the bond critical points (bcps).

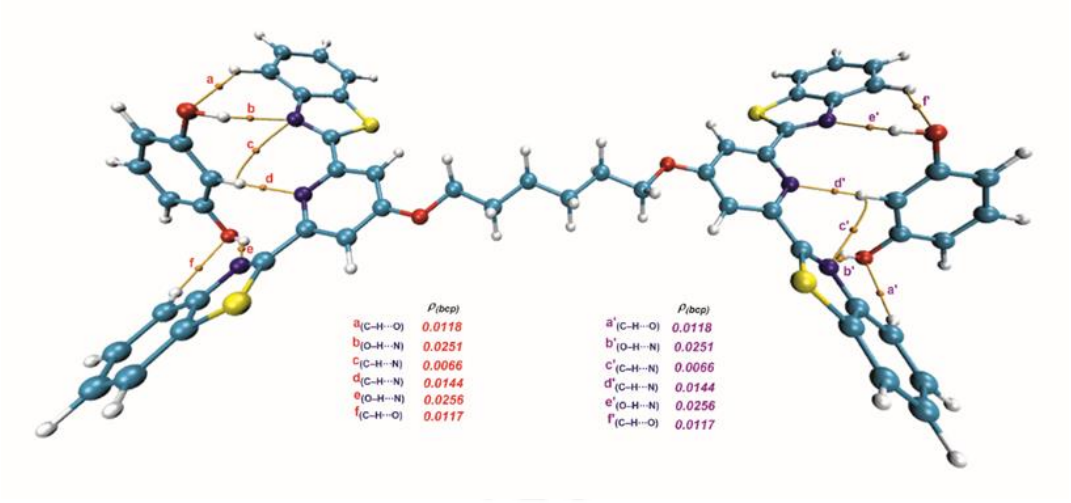

Figure A13. Optimised geometry of dimer complex II and key noncovalent interactions analysis through the AIM formalism calculated at the B3LYP-D3/6-311++G(d,p) level of theory. Major interactions and their corresponding electron densities ρ(r) [au] at the bond critical points (bcps).

Table A1. Torsional potential energy surface (PES) of the S-N-S|S-N-S conformer. The relative energy values in kcal mol^{-1}. The RI-MP2/cc-pVTZ//B3LYP-D3/6-311++G(d,p) denotes the single point energy calculation at the RI-MP2/cc-pVTZ to the optimized geometry calculated at the B3LYP-D3/6-311++G(d,p).

θ_2 (Degrees)	B3LYP-D3/ 6-311++G(d,p)	RI-MP2/cc-pVTZ //B3LYP-D3/6-311++G(d,p)
0	0.00	0.00
10	0.19	0.19
20	0.69	0.77
30	1.51	1.71
40	2.57	2.97
50	3.89	4.43
60	5.21	5.96
70	6.46	7.39
80	7.47	8.51
90	8.09	9.16
100	8.22	9.24
110	7.91	8.87
120	7.40	8.28
130	6.97	7.66
140	6.59	7.18
150	6.46	6.90
160	6.46	6.82
170	6.59	6.89
180	6.65	6.95

Table A2. Torsional potential energy surface (PES) of the N-N-N|N-N-N conformer. The relative energy values in kcal mol^{-1}. The RI-MP2/cc-pVTZ//B3LYP-D3/6-311++G(d,p) denotes the single point energy calculation at RI-MP2/cc-pVTZ to the optimized geometry calculated at the B3LYP-D3/6-311++G(d,p).

ϕ_2 (Degrees)	B3LYP-D3/6-311++G(d,p)	RI-MP2/cc-pVTZ //B3LYP-D3/6-311++G(d,p)
0	7.59	8.22
10	7.53	8.12
20	7.34	7.99
30	7.28	8.00
40	7.34	8.20
50	7.66	8.60
60	8.03	9.11
70	8.47	9.60
80	8.66	9.87
90	8.47	9.72
100	7.91	9.07
110	6.90	7.95
120	5.65	6.50
130	4.27	4.90
140	2.89	3.32
150	1.69	1.94
160	0.75	0.87
170	0.13	0.21
180	0.00	0.00

Table A3. Torsional potential energy surface (PES) of the N-N-S|S-N-N conformer. The relative energy values in kcal mol^{-1}. The RI-MP2/cc-pVTZ //B3LYP-D3/6-311++G(d,p) denotes the single point energy calculation at RI-MP2/cc-pVTZ to the optimized geometry calculated at the B3LYP-D3/6-311++G(d,p).

Υ_2 (Degrees)	B3LYP-D3/6-311++G(d,p)	RI-MP2/cc-pVTZ
0	0.00	0.00
10	0.19	0.24
20	0.73	0.89
30	1.63	1.93
40	2.78	3.28
50	4.12	4.82
60	5.52	6.42
70	6.84	7.90
80	7.90	9.07
90	8.56	9.78
100	8.75	9.95
110	8.54	9.67
120	8.13	9.17
130	7.73	8.65
140	7.46	8.25
150	7.38	8.05
160	7.44	8.04
170	7.58	8.15
180	7.66	8.21

Table A4. Torsional potential energy surface (PES) of the S-N-S conformer. The relative energy values in kcal mol^{-1}. The RI-MP2/cc-pVTZ //B3LYP-D3/6-311++G(d,p) denotes the single point energy calculation at RI-MP2/cc-pVTZ to the optimized geometry calculated at the B3LYP-D3/6-311++G(d,p).

Dihedral Angle (Degree)	B3LYP-D3/6-311++G(d,p)	RI-MP2/cc-pVTZ
0	0.00	0.00
10	0.13	0.19
20	0.63	0.77
30	1.44	1.72
40	2.57	2.97
50	3.83	4.43
60	5.21	5.96
70	6.46	7.38
80	7.47	8.50
90	8.09	9.14
100	8.22	9.23
110	7.97	8.87
120	7.47	8.29
130	6.97	7.69
140	6.65	7.22
150	6.46	6.95
160	6.46	6.89
170	6.59	6.95
180	6.65	6.99

Table A5. Torsional potential energy surface (PES) of the S-N-S conformer in the solvents, acetonitrile and chloroform, calculated at the B3LYP-D3/6-311++G(d,p) level of theory.

Dihedral angle (Degree)	B3LYP-D3/6-311++G(d,p) (Acetonitrile)	B3LYP-D3/6-311++G(d,p) (Chloroform)
0	0.00	0.00
10	0.13	0.13
20	0.56	0.56
30	1.19	1.26
40	2.13	2.26
50	3.14	3.39
60	4.27	4.58
70	5.21	5.65
80	5.96	6.46
90	6.34	6.90
100	6.21	6.90
110	5.77	6.59
120	5.21	6.02
130	4.64	5.52
140	4.20	5.15
150	4.02	4.96
160	4.02	4.96
170	4.08	5.08
180	4.14	5.08

Table A6. Interaction energies (Δ*E*) of complexes I, II, and P without BSSE corrections. All values are in kcal mol^{-1}.

Method	ΔE (I)	ΔE(II)	ΔE(P)
B3LYP-D3/6-311++G(d,p)	-23.57	-47.03	-23.33
PBE0-D3/6-311++G(d,p)	-23.46	-46.89	-23.32
TPSSTPSS-D3/6-311++G(d,p)	-22.88	-45.73	-22.66
M06-2X/6-311++G(d,p)	-21.56	-42.89	-21.22
B3LYP-D3/def2-TZVP	-22.32	-44.57	-22.14
PBE0-D3/def2-TZVP	-21.56	-43.05	-21.41
TPSSTPSS-D3/def2-TZVP	-21.07	-42.11	-20.91
M06-2X/def2-TZVP	-19.20	-38.32	-19.07
B3LYP-D3BJ/6-311++G(d,p)	-23.39	-46.73	-23.18
PBE0-D3BJ/6-311++G(d,p)	-23.25	-46.53	-23.07
TPSSTPSS-D3BJ/6-311++G(d,p)	-22.54	-45.00	-22.28

Table A7. Important noncovalent interactions involved in complex I. The topological parameters were derived through *Atoms-in-Molecules* (AIM) Analysis[i].

	Interaction(s)[ii]	r (Å)	ρ(r)	$\nabla^2\rho(r)$	H(r)	G(r)	V(r)	|V(r)|/G(r)
I	[a]**C—H···O**	2.39	**0.0118**	0.0377	0.0011	0.0083	-0.0071	0.8612
	[b]**O—H···N**	2.01	**0.0251**	0.0780	0.0013	0.0182	-0.0169	0.9295
	[c]**C—H···N**	2.32	**0.0144**	0.0448	0.0019	0.0093	-0.0075	0.8006
	[d]**C—H···N**	2.84	**0.0066**	0.0231	0.0010	0.0047	-0.0037	0.7821
	[e]**O—H···N**	2.02	**0.0256**	0.0792	0.0012	0.0186	-0.0174	0.9362
	[f]**C—H···O**	2.39	**0.0117**	0.0373	0.0011	0.0082	-0.0071	0.8610

[i]ρ(r)= electron density, $\nabla^2\rho(r)$= Laplacian electron density; H(r)=Total electron energy density, G(r)= Kinetic energy density, V(r)= Potential energy density at the bond critical points. [ii]See the bond interactions path in **Figure A12**.

Table A8. Important noncovalent interactions involved in complex II. The topological parameters were derived through *Atoms-in-Molecules* (AIM) Analysis[j].

	Interaction(s)[jj]	r (Å)	ρ(r)	$\nabla^2\rho(r)$	H(r)	G(r)	V(r)	|V(r)|/G(r)
II	[a]**C—H···O**	2.38	**0.0118**	0.0377	0.0011	0.0083	-0.0071	0.8612
	[b]**O—H···N**	2.02	**0.0251**	0.0780	0.0013	0.0182	-0.0169	0.9289
	[c]**C—H···N**	2.83	**0.0066**	0.0231	0.0010	0.0047	-0.0037	0.7823
	[d]**C—H···N**	2.32	**0.0144**	0.0447	0.0019	0.0093	-0.0075	0.8005
	[e]**O—H···N**	2.01	**0.0256**	0.0792	0.0012	0.0186	-0.0174	0.9357
	[f]**C—H···O**	2.39	**0.0117**	0.0374	0.0011	0.0082	-0.0071	0.8610
	[a']**C—H···O**	2.38	**0.0118**	0.0377	0.0011	0.0083	-0.0071	0.8612
	[b']**O—H···N**	2.02	**0.0251**	0.0780	0.0013	0.0182	-0.0169	0.9289
	[c']**C—H···N**	2.83	**0.0066**	0.0231	0.0010	0.0047	-0.0037	0.7823
	[d']**C—H···N**	2.32	**0.0144**	0.0447	0.0019	0.0093	-0.0075	0.8005
	[e']**O—H···N**	2.01	**0.0256**	0.0792	0.0012	0.0186	-0.0174	0.9357
	[f']**C—H···O**	2.39	**0.0117**	0.0374	0.0011	0.0082	-0.0071	0.8610

[j]ρ(r)= electron density, $\nabla^2\rho(r)$= Laplacian electron density; H(r)= Total electron energy density, G(r)= Kinetic energy density, V(r)= Potential energy density at the bond critical points.

[jj] See the bond interactions path in **Figure A13**.

Table A9. Natural Bond Orbital (NBO) results of complexes I and II calculated at the B3LYP-D3/def2-TZVP level of theory.

Complex	Interactions	Donor	Acceptor	Second order perturbation energy of Interactions (kcal mol^{-1})
I	**O—H···N**	Lp(N21)	σ*(H102—O99)	7.73
	C—H···N	Lp(N6)	σ*(H96—C99)	2.45
	O—H···N	Lp(N34)	σ*(H101—O100)	7.26
II	**O—H···N**	Lp(N21)	σ*(H116—O113)	7.69
	C—H···N	Lp(N6)	σ*(H110—C105)	2.44
	O—H···N	Lp(N34)	σ*(H115—O114)	7.23
	O—H···N	Lp(N74)	σ*(H102—O99)	7.69
	C—H···N	Lp(N62)	σ*(H96—C91)	2.44
	O—H···N	Lp(N87)	σ*(H101—O100)	7.23

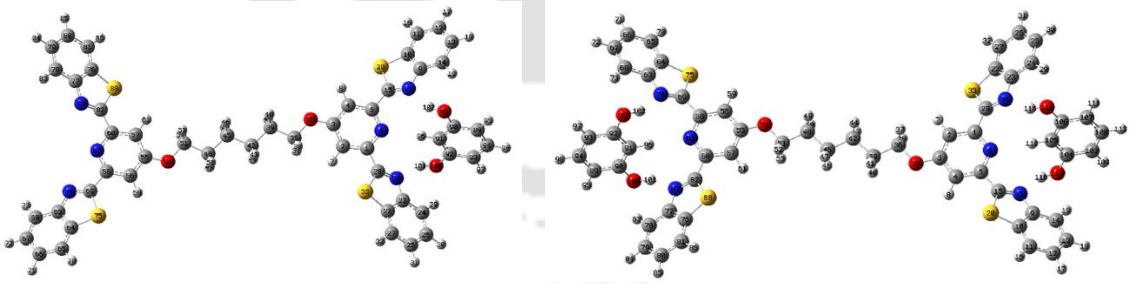

Appendix-B

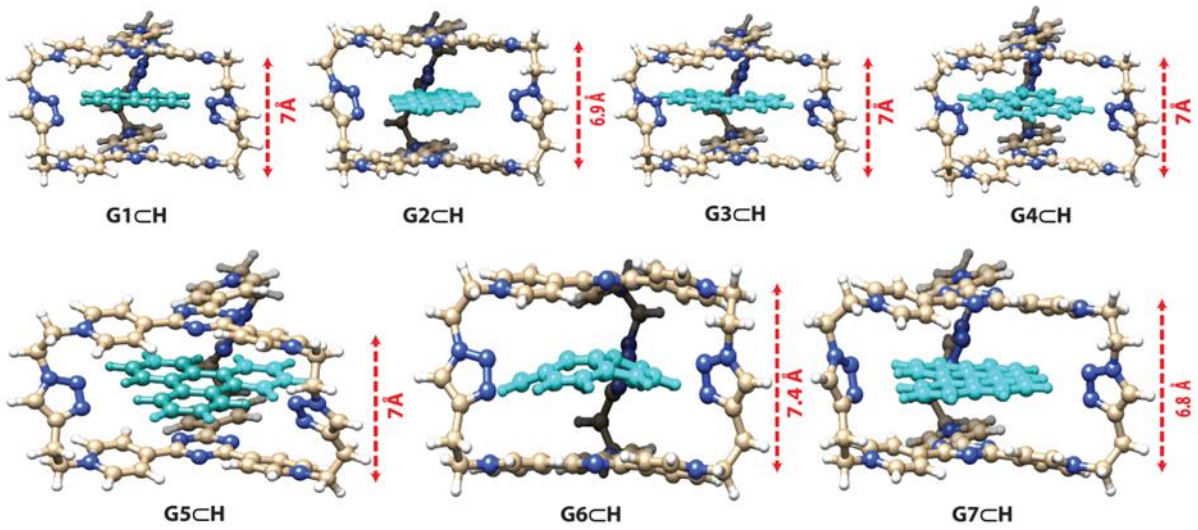

Figure B1. Centroids distances of Host (H) in complexes G1⊂H to G7⊂H calculated at the PBE0-D3BJ/def2-TZVP level of theory.

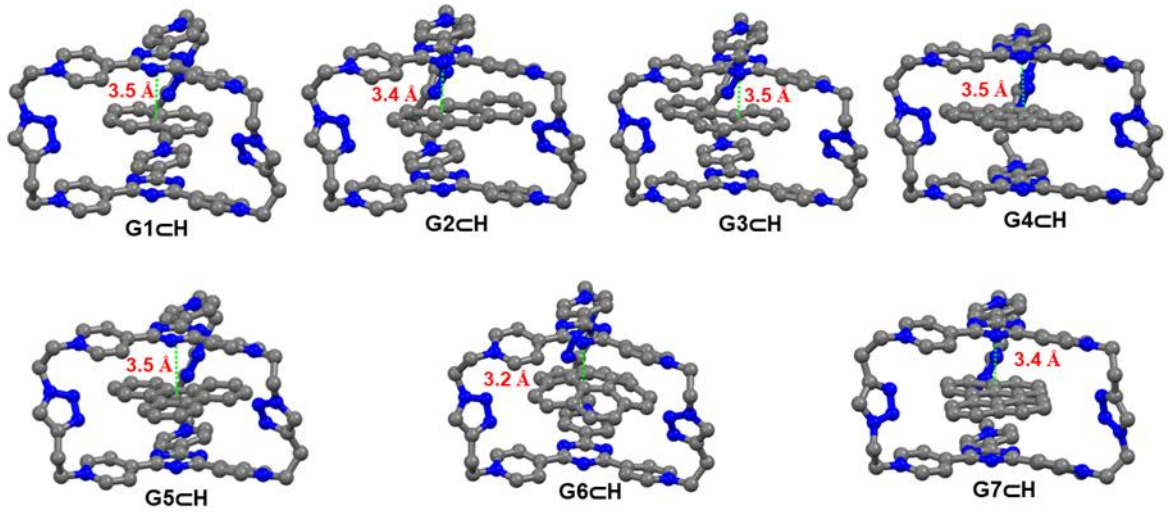

Figure B2. Distances between host and guest in complexes G1⊂H-G7⊂H, calculated at the PBE0-D3BJ/def2-TZVP level of theory.

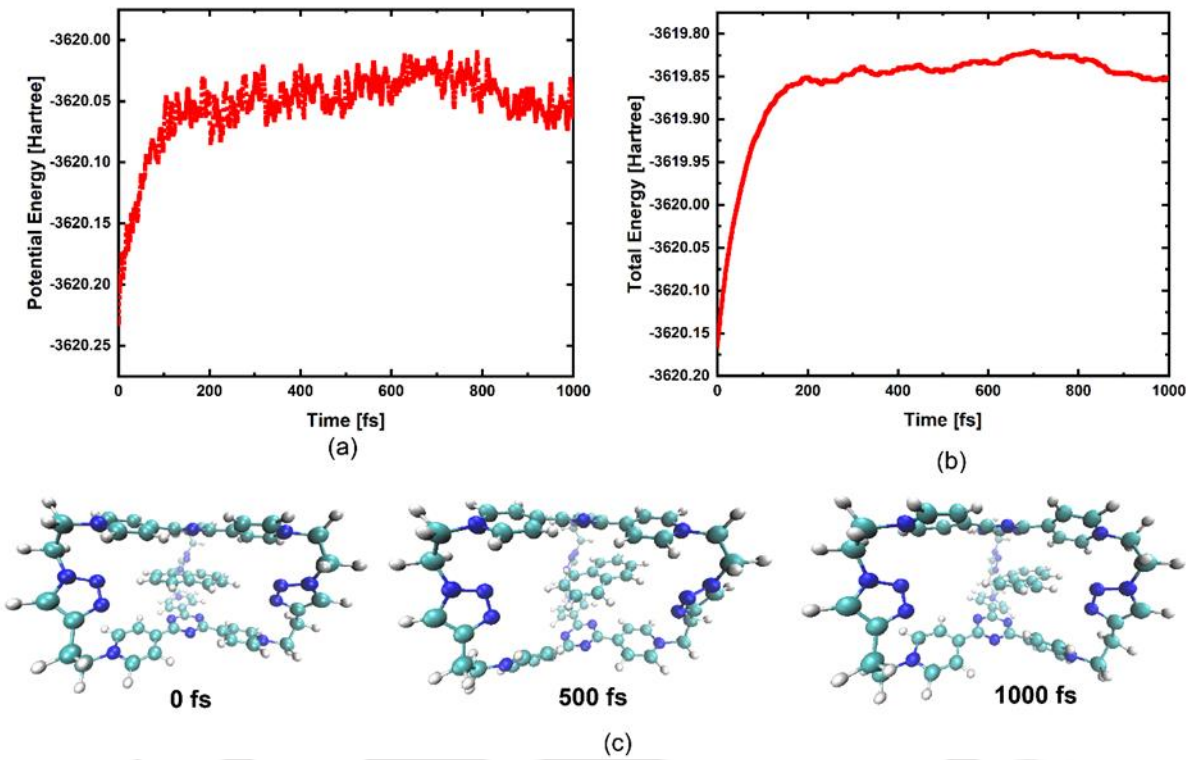

Figure B3. Ab *initio* molecular dynamics simulation of complex (G1⊂H) calculated at the B97-3c/def2-mTZVP level of theory.

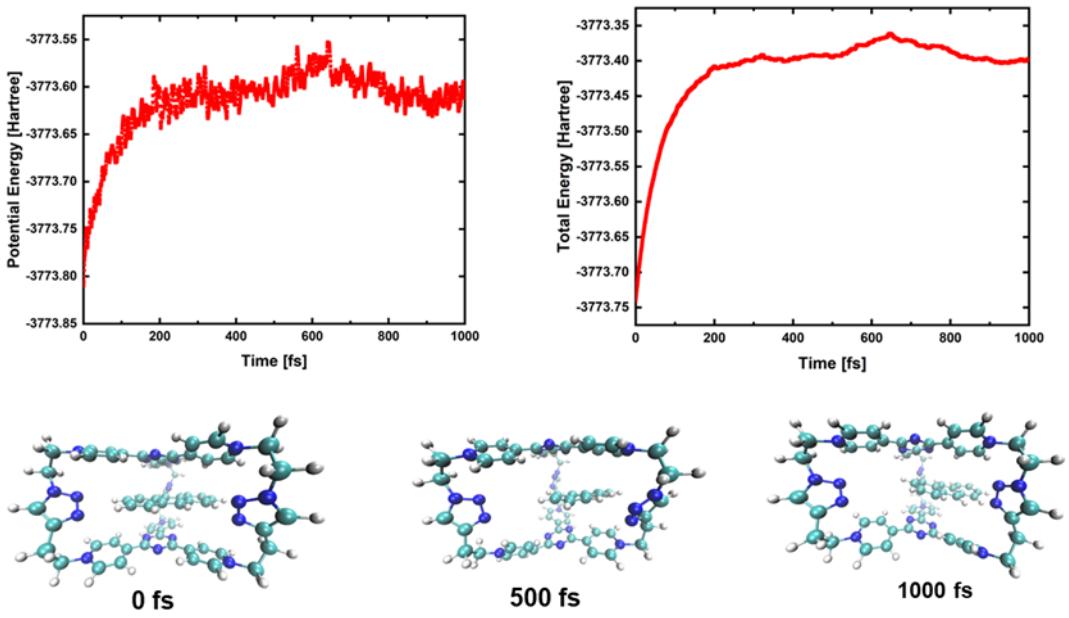

Figure B4. Ab *initio* molecular dynamics simulation of complex (G2⊂H) calculated at the B97-3c/def2-mTZVP level of theory.

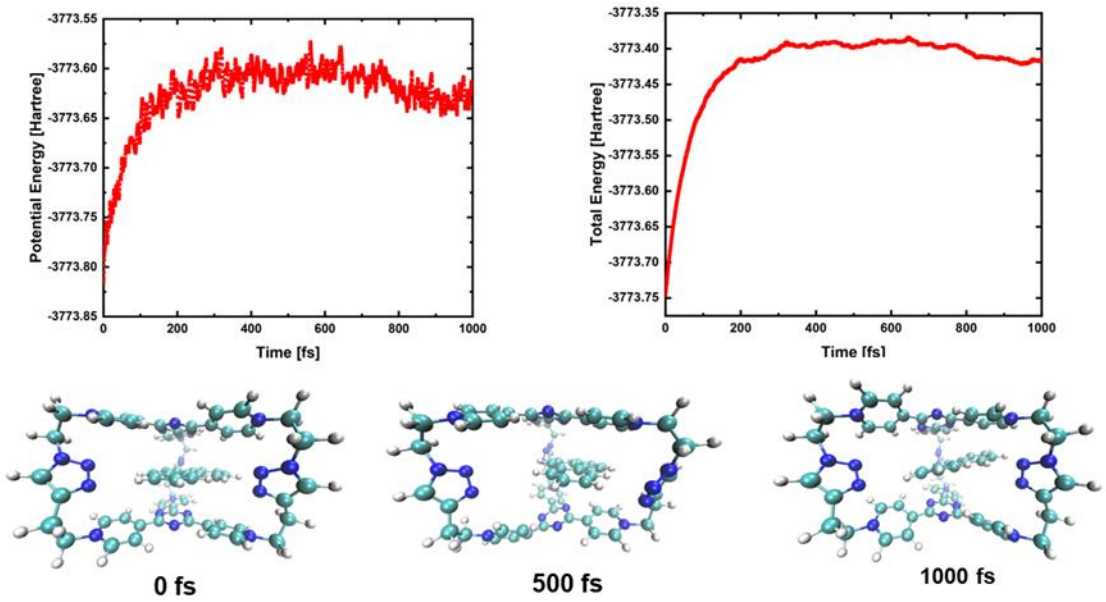

Figure B5. Ab *initio* molecular dynamics simulation of complex (G3⊂H) calculated at the B97-3c/def2-mTZVP level of theory.

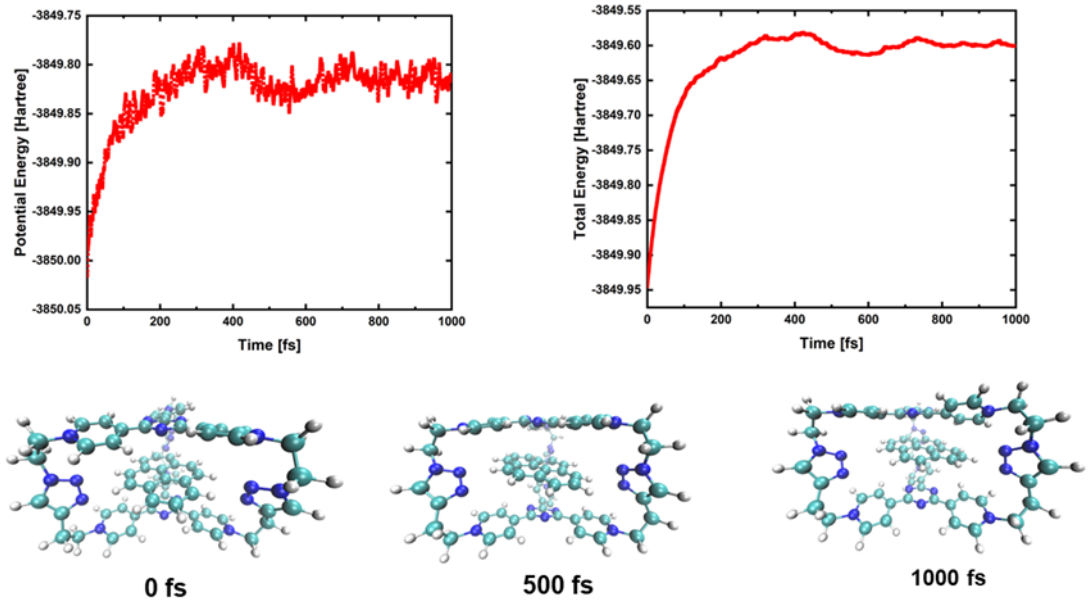

Figure B6. Ab *initio* molecular dynamics simulation of complex (G4⊂H) calculated at the B97-3c/def2-mTZVP level of theory.

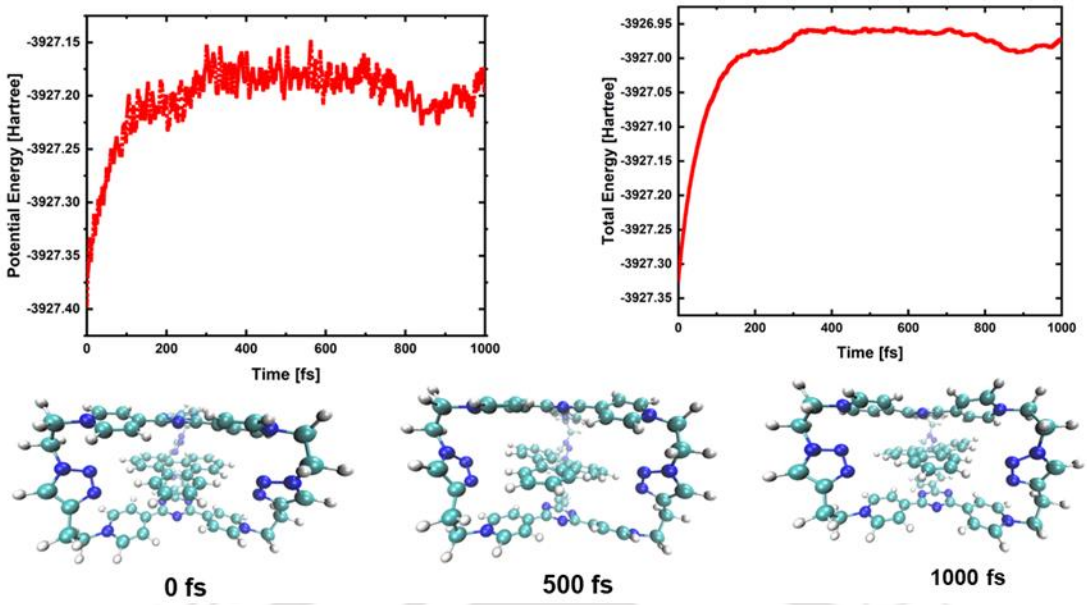

Figure B7. Ab *initio* molecular dynamics simulation of complex (G5⊂H) calculated at the B97-3c/def2-mTZVP level of theory.

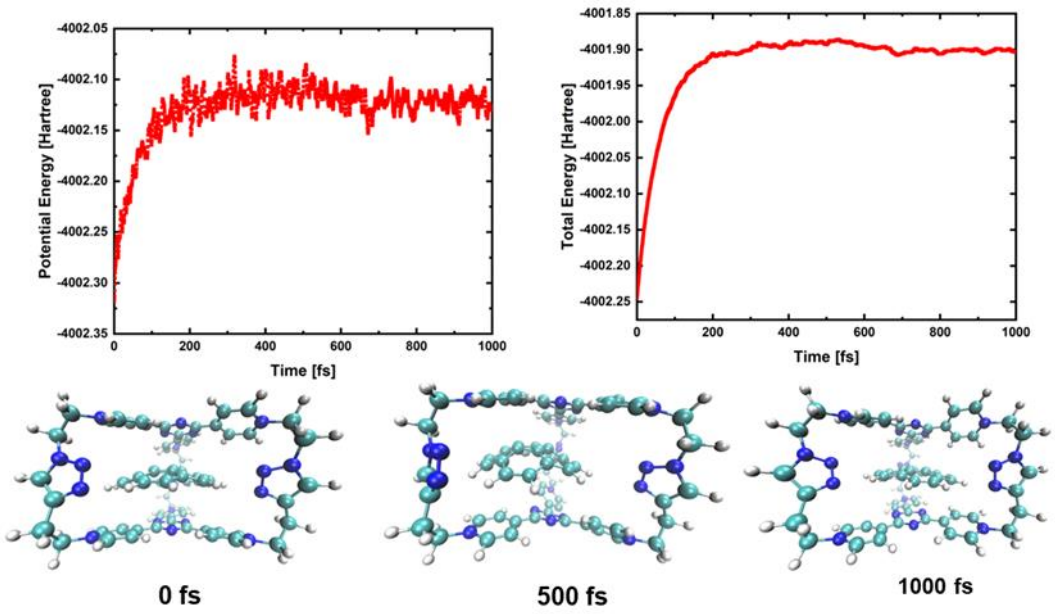

Figure B8. Ab *initio* molecular dynamics simulation of complex (G6⊂H) calculated at the B97-3c/def2-mTZVP level of theory.

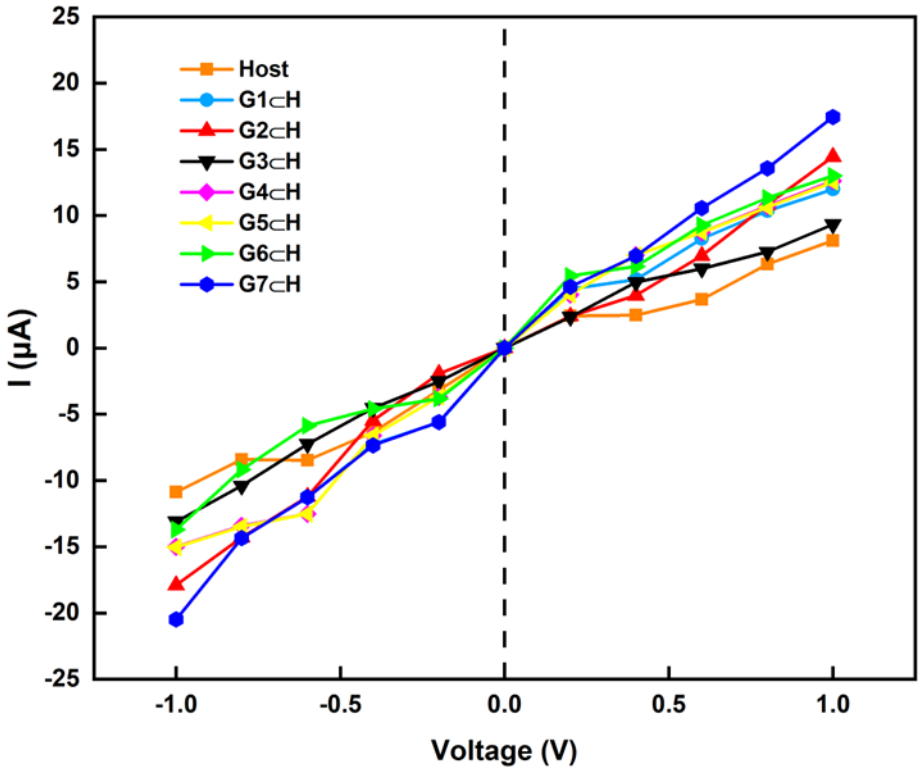

Figure B9. I-V plot of host and host-guest complexes at the reverse and forward bias.

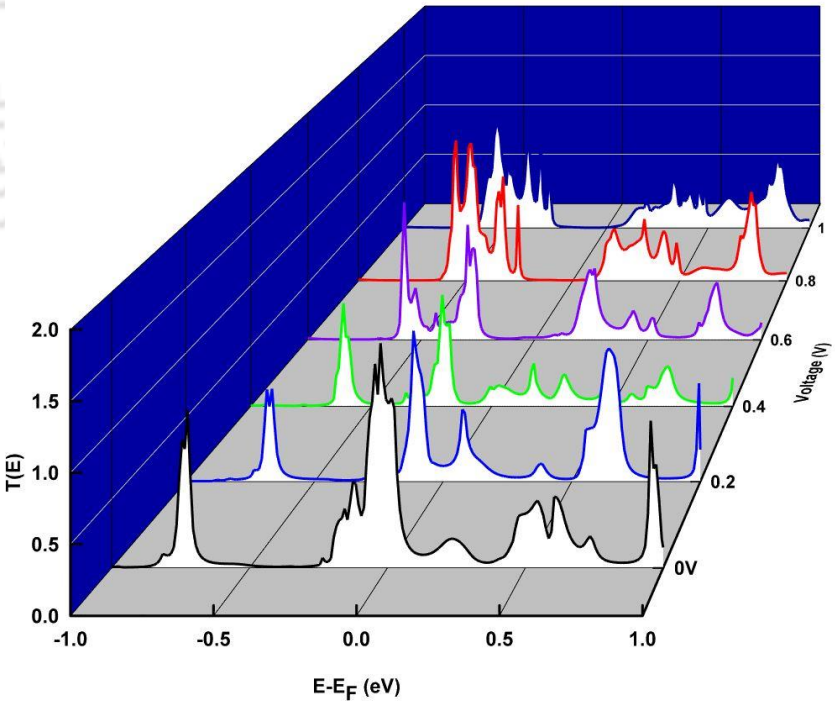

Figure B10. Transmission spectra of the host (H) at voltage -1.0 eV to +1.0 eV.

Table B1. Interaction energy, ΔE (kcal mol^{-1}), of host-guest complexes G1⊂H-G7⊂H, calculated at the PBEh-3c/ def2-mSVP level of theory.

Complexes	ΔE
G1⊂H	-34.02
G2⊂H	-44.02
G3⊂H	-50.42
G4⊂H	-43.14
G5⊂H	-43.38
G6⊂H	-41.00
G7⊂H	-51.96

Table B2. Conductance value and R^2 values of the host and host-guest complexes.

Complexes	Conductance (S)×10^{-5}	R^2-value
H	0.97	0.97
G1⊂H	1.61	0.97
G2⊂H	1.54	0.98
G3⊂H	1.11	0.98
G4⊂H	1.52	0.98
G5⊂H	1.51	0.98
G6⊂H	1.32	0.98
G7⊂H	1.84	0.99

Appendix-C

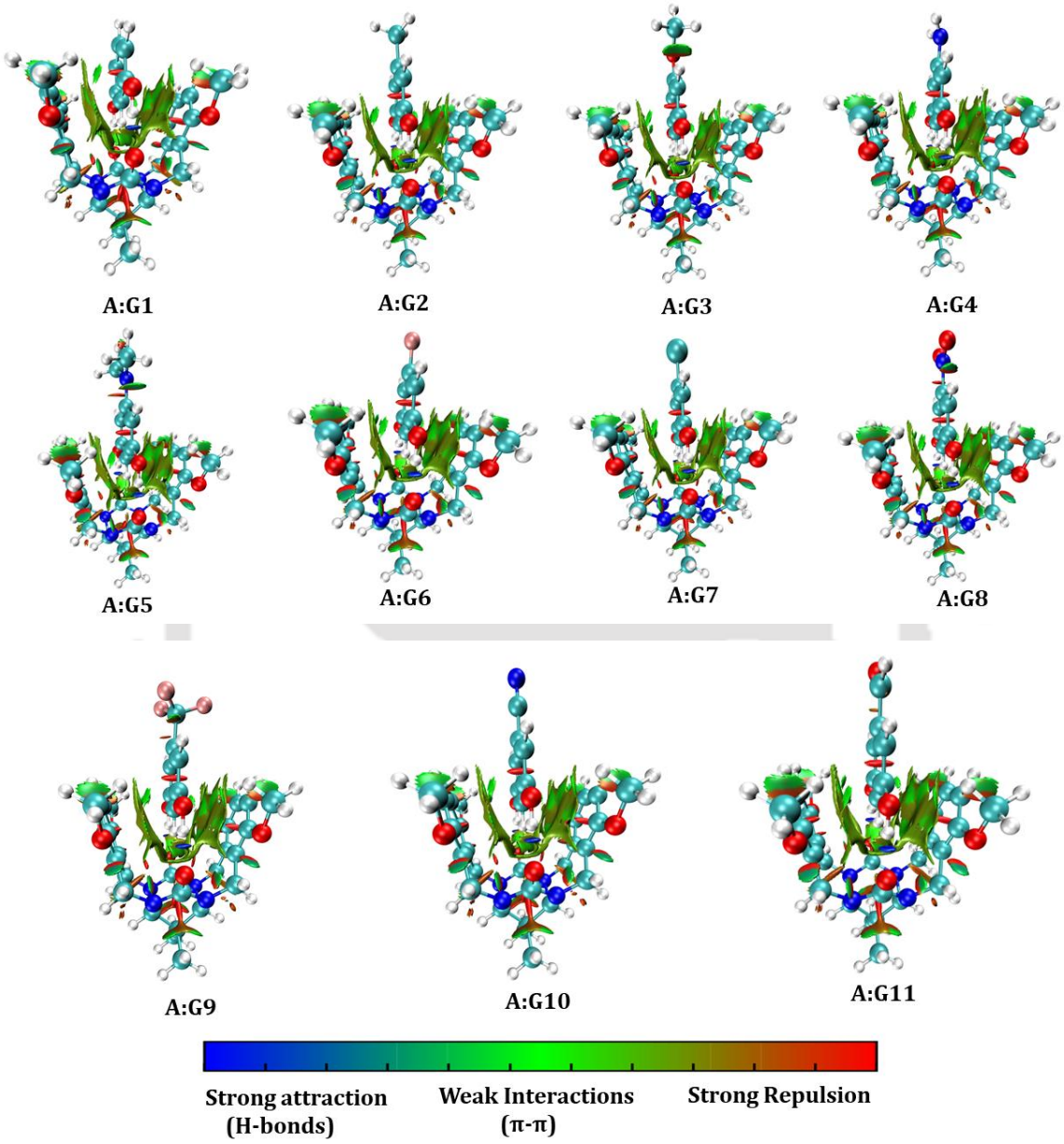

Figure C1. NCI isosurface plots illustrating the noncovalent interactions in host–guest complexes A1:G1 to A1:G11 for Set II.

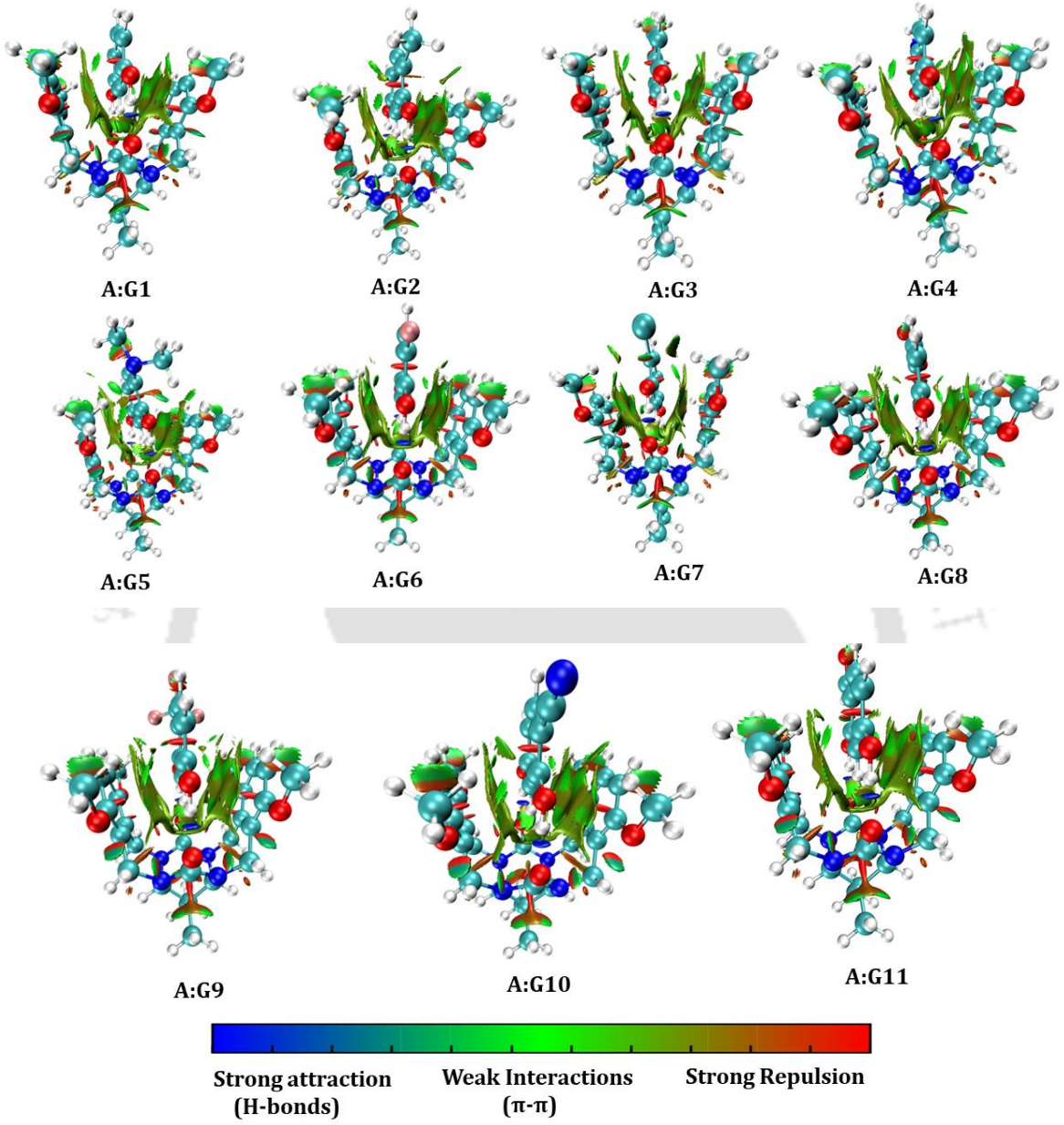

Figure C2. NCI isosurface plots illustrating the noncovalent interactions in host–guest complexes A1:G1 to A1:G11 for Set I.

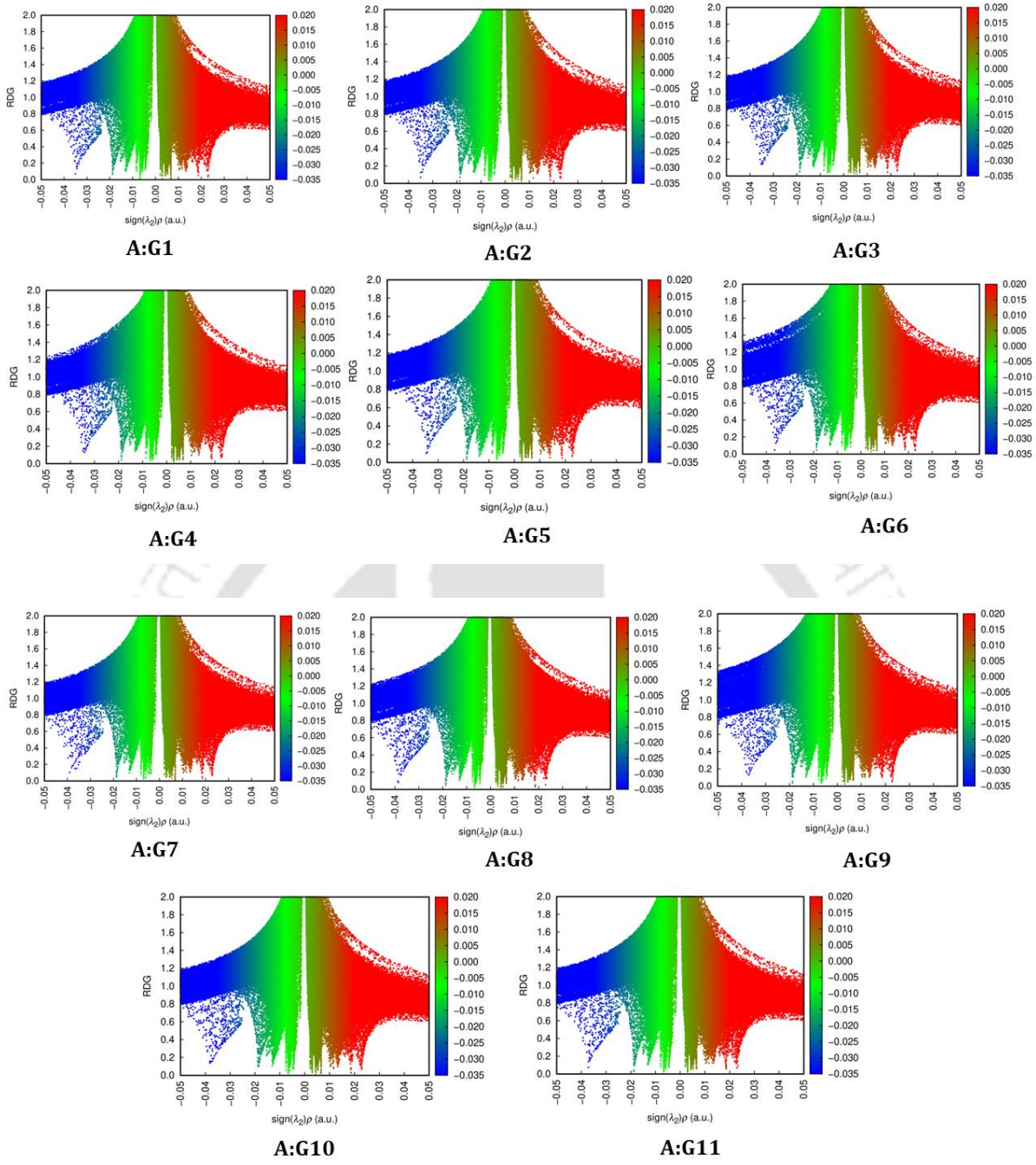

Figure C3. RDG scatter plots of the host–guest complexes A1:G1 to A1:G11 for Set II.

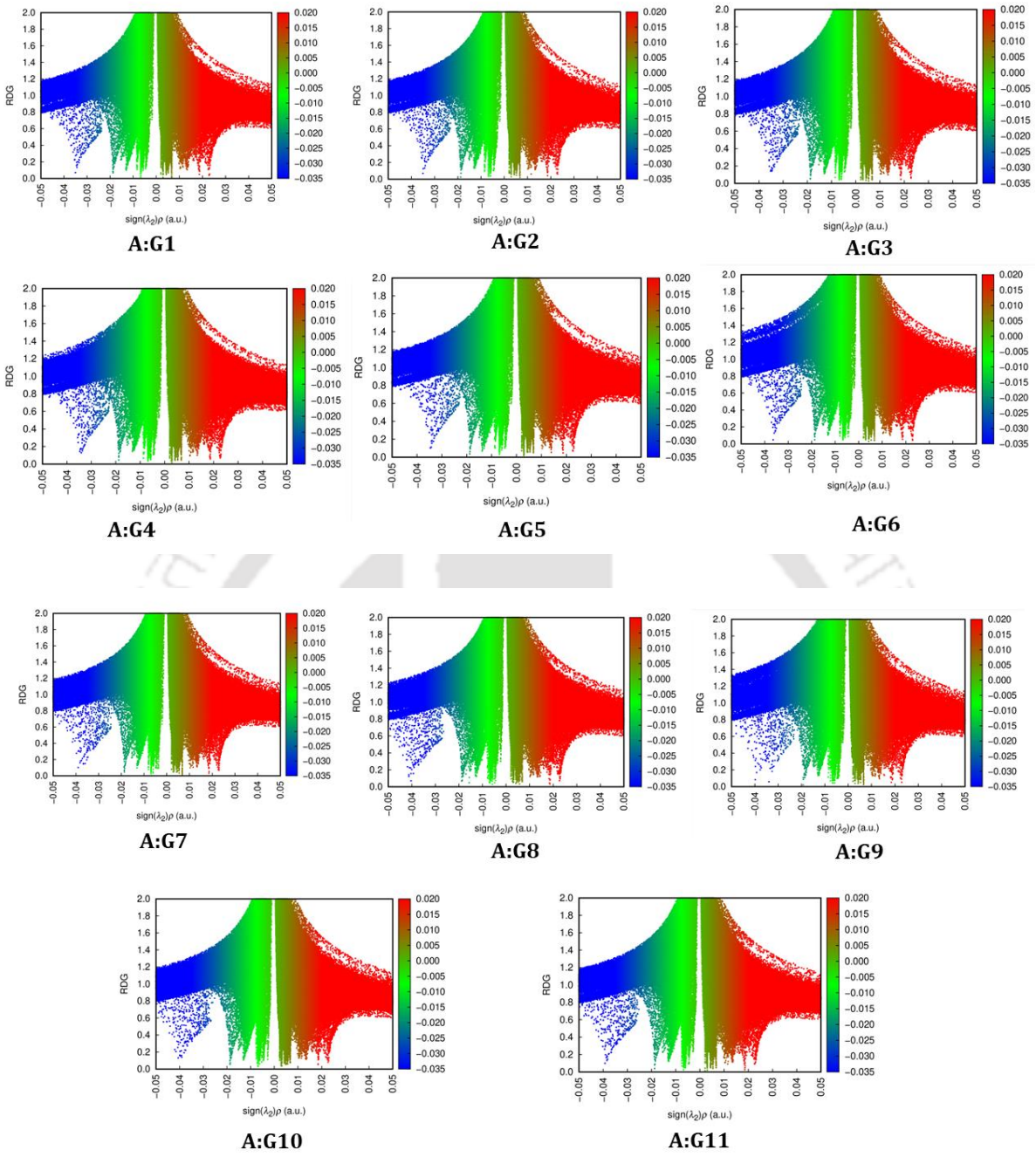

Figure C4. RDG scatter plots of the host–guest complexes A1:G1 to A1:G11 for Set I.

Appendix-D

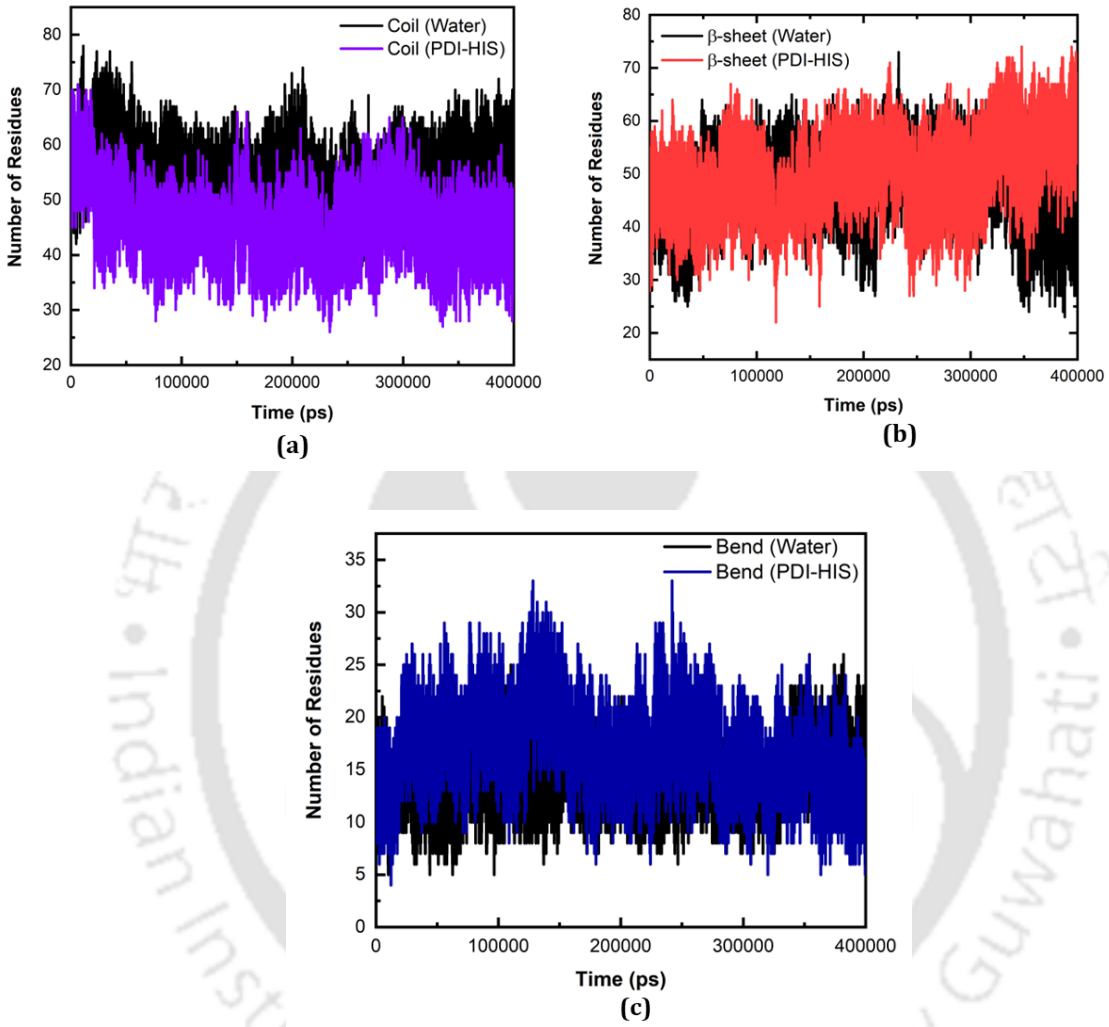

Figure D1. Representation of secondary structures of Aβ40-PDI-HIS of docked pose P1 for (a) coil content, (b) β-sheet content, and (c) bend content, for Aβ40 in water and presence of PDI-HIS.

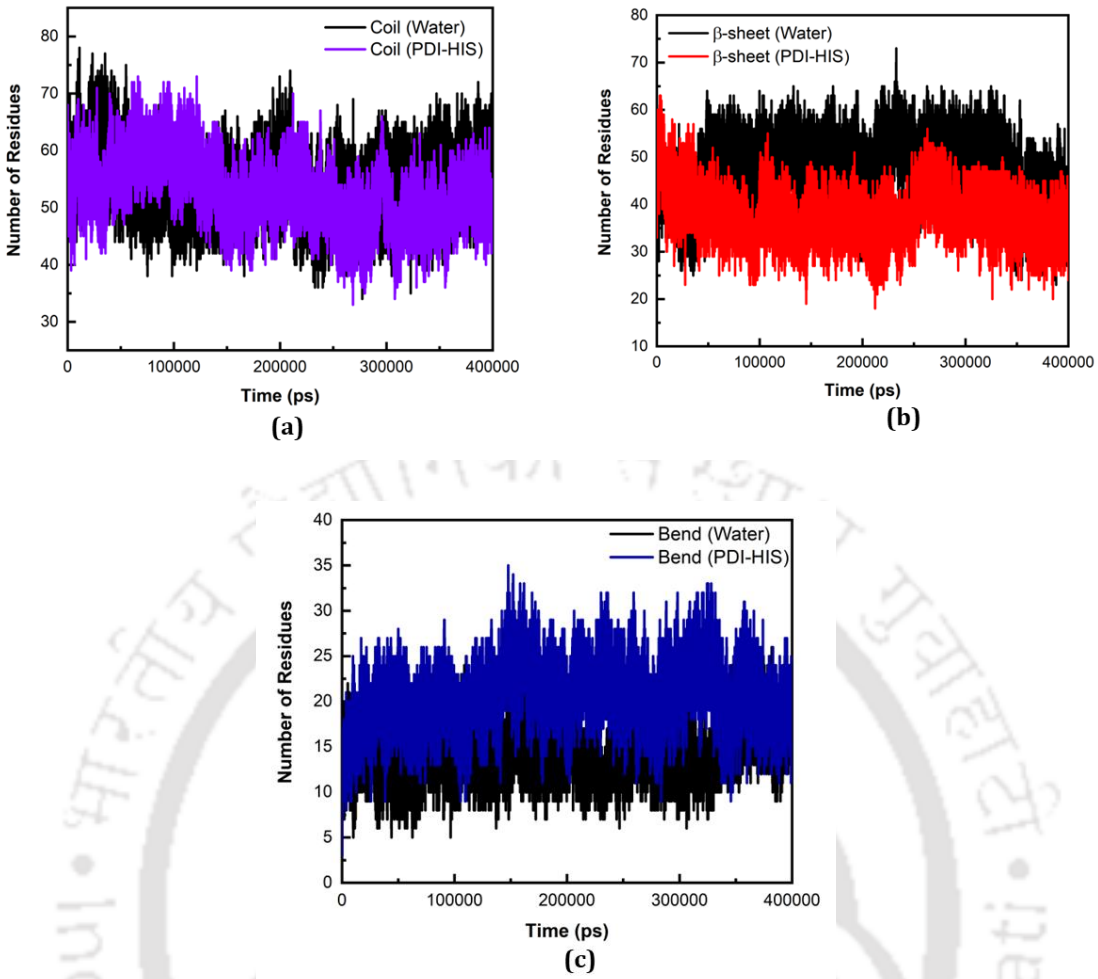

Figure D2. Representation of secondary structures of Aβ40-PDI-HIS of docked pose P5 for (a) coil content, (b) β-sheet content, and (c) bend content, for Aβ40 in water and presence of PDI-HIS.

PDI-HIS (Histidine in ε-form, N-H)

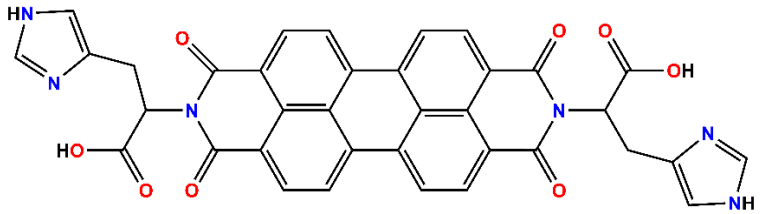

Figure D3. Molecular structure of histidine (HIS) (ε-form, N-H) functionalized perylenediimide (PDI-HIS).

Molecular Docking

The molecular structure of the ε-form histidine functionalized perylenediimide (PDI-HIS) is displayed in **Figure D3**. Using the same protocol as Chapter 6 we performed the electronic structure and molecular docking calculation. The obtained ten docked poses are presented in **Figure D4**.

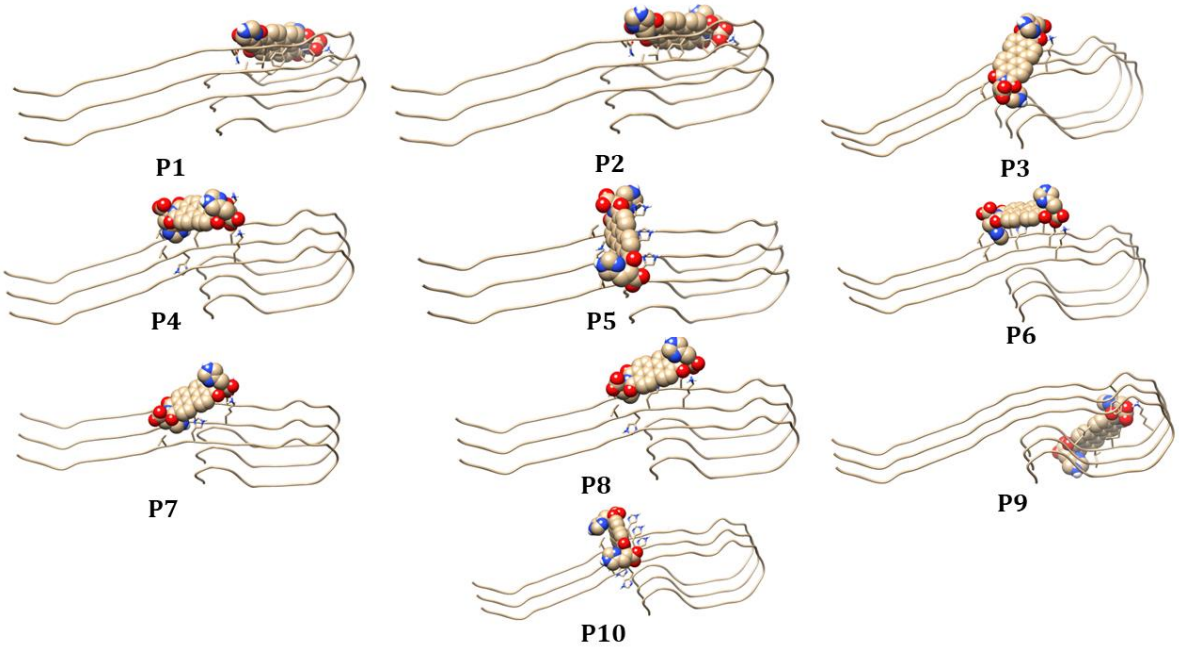

Figure D4. Docked poses P1 to P10 obtained from the molecular docking of PDI-HIS with Aβ40 fibril.

The binding energy (ΔG) of all the docked poses (P1 to P10) and the amino acid residues of Aβ40 fibril involved in the interactions with PDI-HIS are presented in **Table D1**. Out of the

ten docked poses, P1, P3, and P5 were selected to conduct the MD simulation. The same protocol of MD simulation as in Chapter 6 is employed in this analysis.

Table D1. Generated docked poses (P1 to P10) with their binding energy (ΔG) (in kcal mol^{-1}) and residues involved in the interactions.

Docked Pose	Binding Energy, ΔG	Residues involved
P1	−7.11	C (Gln15, Lys16, Leu17, Val18, Phe19, Phe20, Lys28, Ile31, Leu34, Val36)
P2	−6.58	C (Gln15, Lys16, Leu17, Phe19, Phe20, Lys28, Leu34, Val36)
P3	−6.46	A (Val12. His13, His14, Lys16); B (Lys16)
P4	−6.36	A (His14, Lys16); B (Val12, His13, His14, Lys16); C (Val12, His13, His14)
P5	−6.26	A (Val12, His13, His14); B (Val12, His13, His14); C (Val12, His13, His14)
P6	−6.03	A (Lys16); B (Val12, His13, His14, Lys16); C (Val12, His13, His14)
P7	−5.91	A (Val12, His13, His14, Lys16); B (Val12, His13, His14, Lys16,); C (Lys16,)
P8	−5.82	A (His14); B (Val12, His13, His14, Lys16,); C (Val12, His13, His14, Lys16)
P9	−5.55	C (Phe20, Lys28, Ile31, Ile32, Gly33, Leu34)
P10	−5.45	A (Val12, His13, His14); B (Val12, His13, His14); C (Val12, His13, His14)

Molecular Dynamic (MD) Simulations

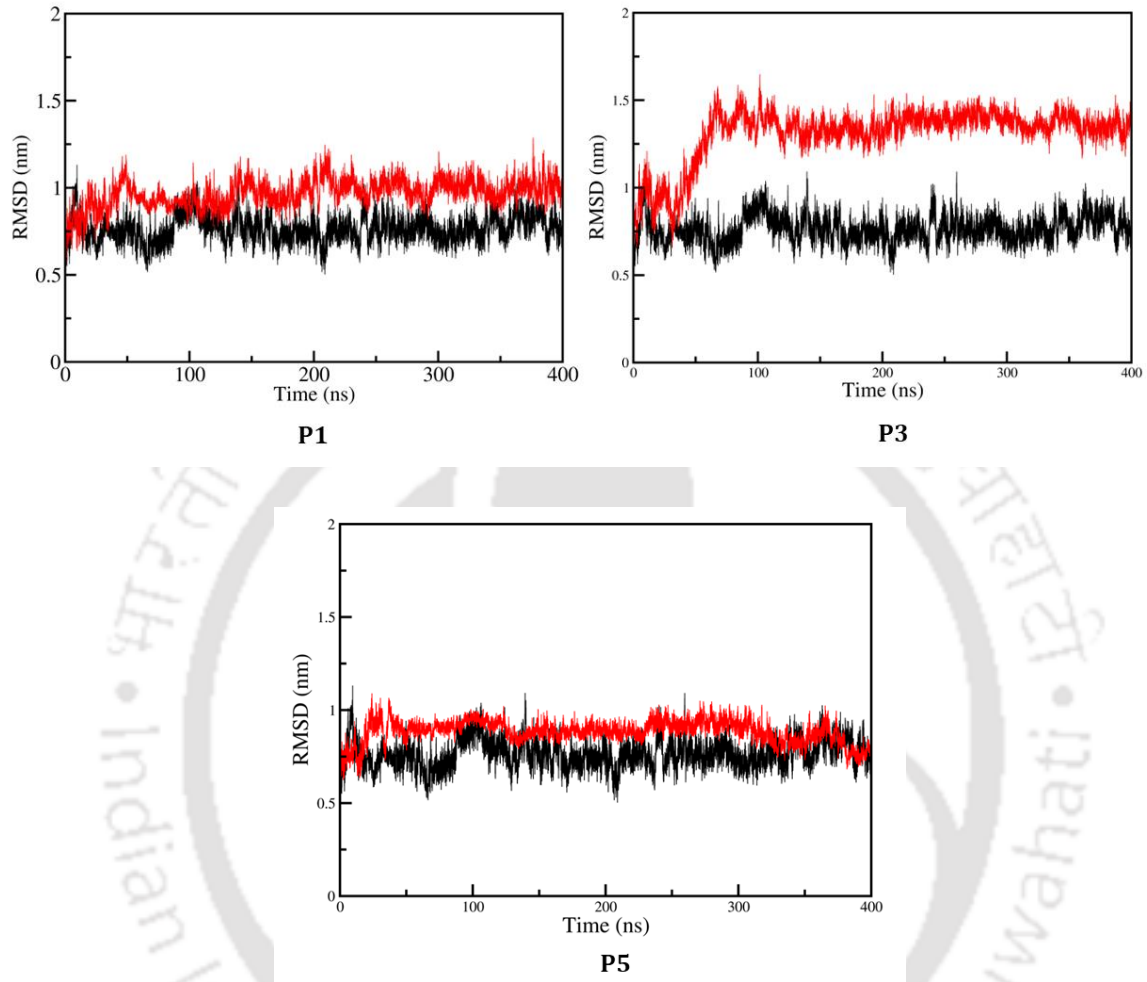

Figure D5. Cα-RMSD of Aβ40 fibril (black) in the absence of PDI-HIS and Cα-RMSD of Aβ40 fibril (red) in the presence of PDI-HIS for the docked poses P1, P3, and P5.

Figure D5 illustrates the comparison of the Cα-RMSD value of Aβ40 fibril in water with the values of P1, P3, and P5 which have PDI-HIS. In P3, the Cα-RMSD value of Aβ40 gradually increased and reached the point of approximately 1.4 nm at around 180 ns, and maintained equilibrium in the remaining time. In P1 and P5, the changes in the deviation of the Cα-RMSD value of Aβ40 fibril is less when compared to the Cα-RMSD value of Aβ1-40 in water. The structure of the Aβ40-PDI-HIS collected at different times for P1, P3, and P5 are presented in **Figure D6**, **Figure D7**, and **Figure D8**, respectively.

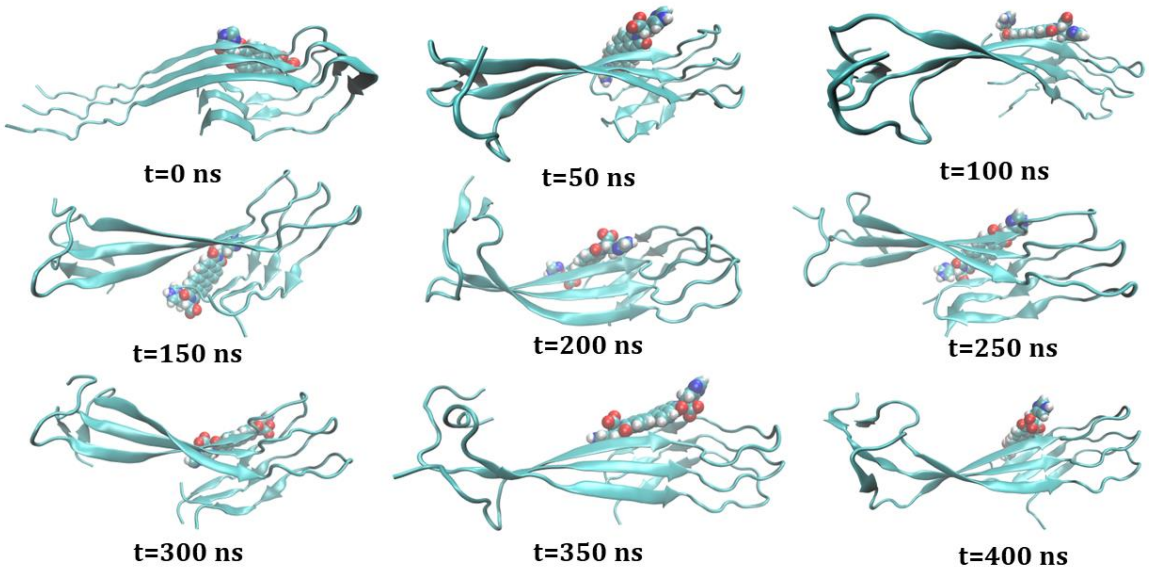

Figure D6. Some snapshots from the MD simulations representing the structures of the Aβ40-PDI-HIS of the P1 system collected at different times.

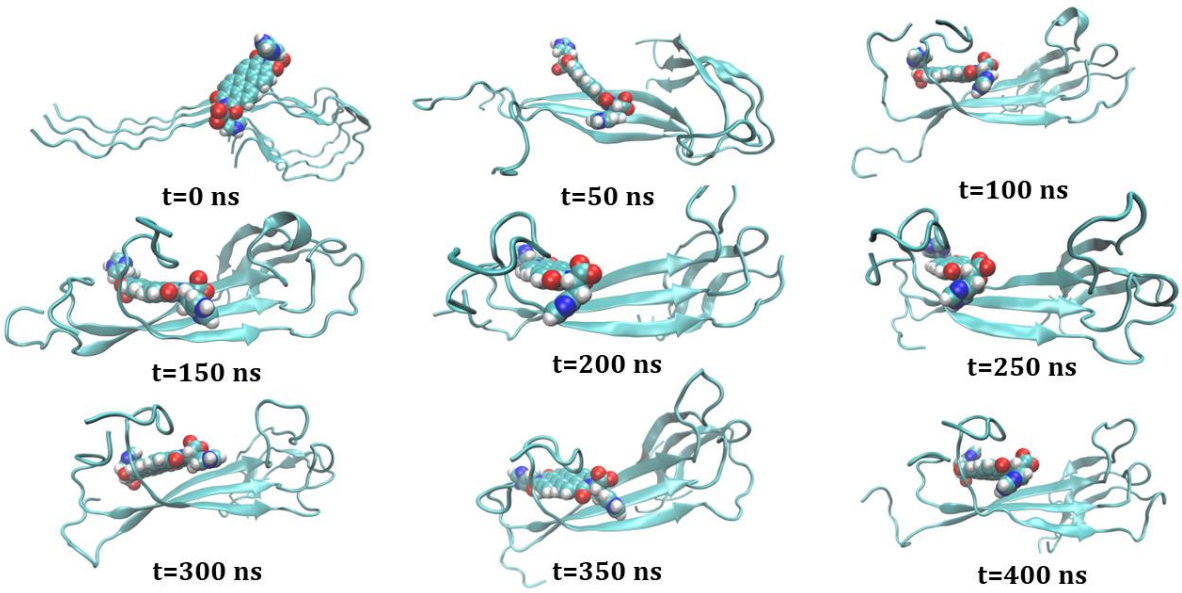

Figure D7. Some snapshots from the MD simulations representing the structures of the Aβ40-PDI-HIS of the P3 system collected at different times.

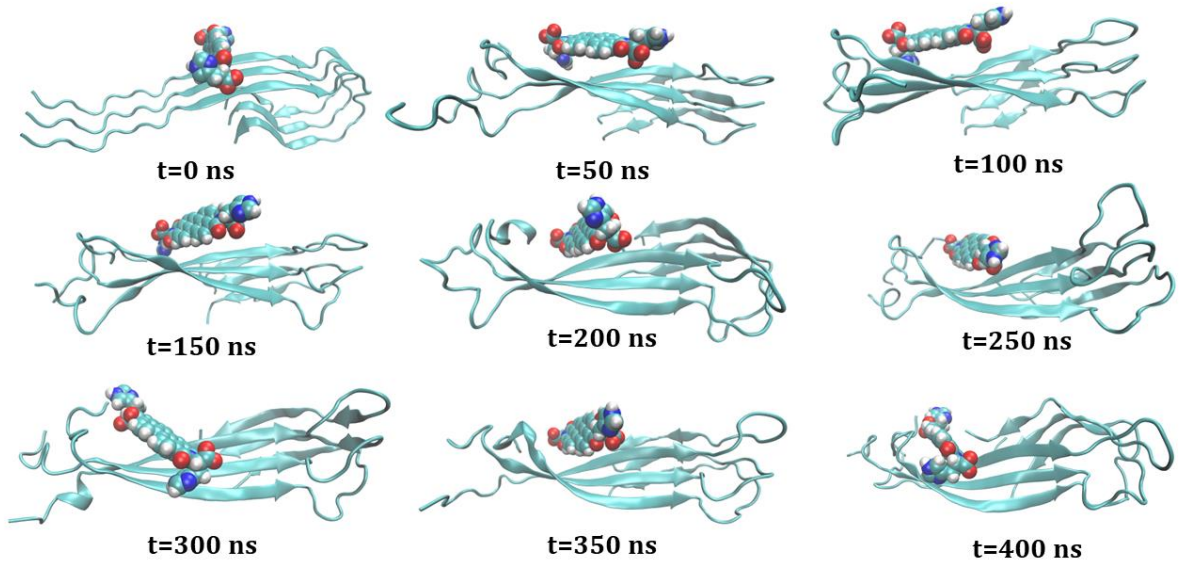

Figure D8. Some snapshots from the MD simulations representing the structures of the Aβ40-PDI-HIS of the P5 system collected at different times.

Hydrogen Bonding Interactions

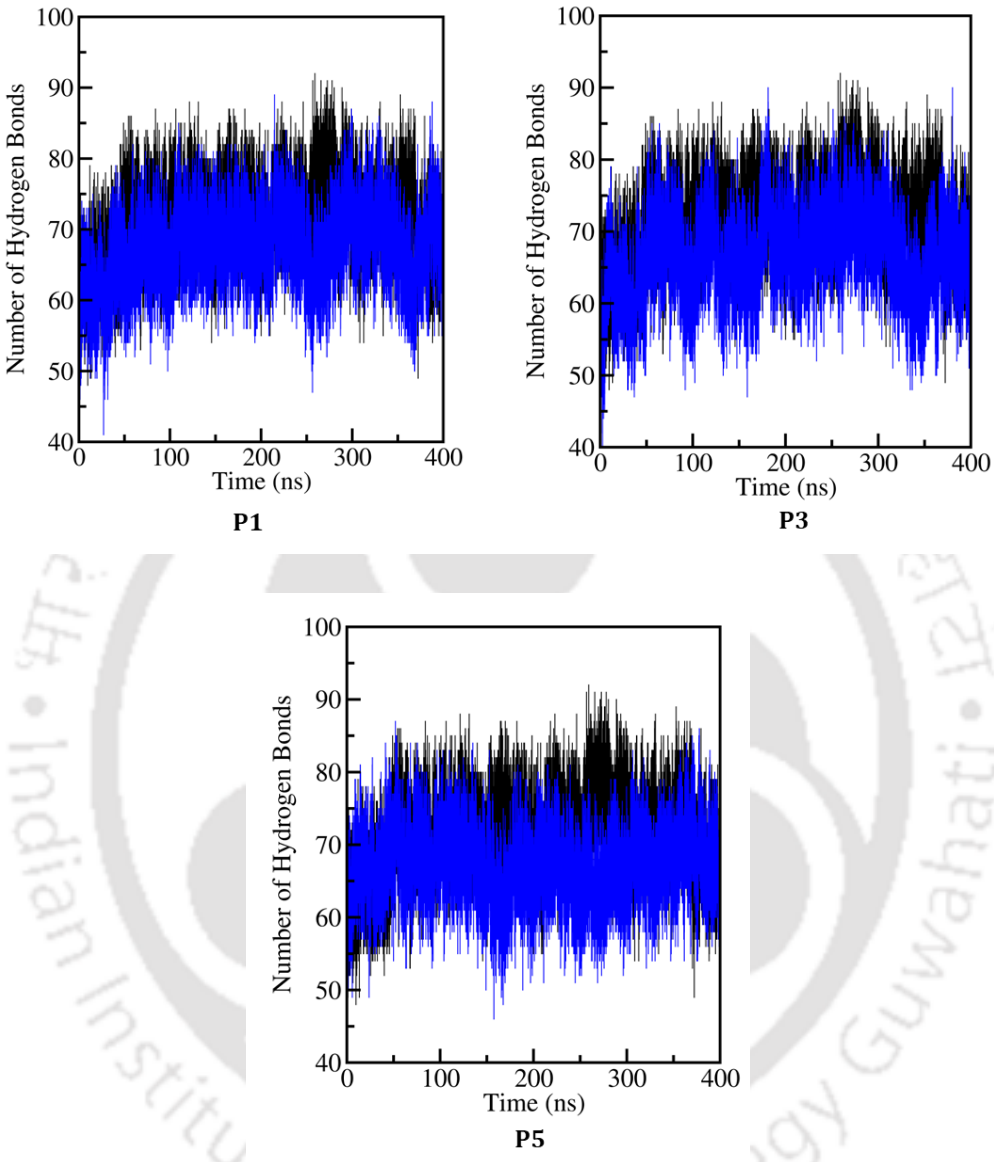

Figure D7. Number of hydrogen bonds of Aβ40 in water (black) and in the presence of PDI-HIS in docked pose P1, P3, P5 (blue).

The quantity of hydrogen bonds present in the Aβ40 is slightly reduced (**Figure D7**) when the PDI-HIS is bind on the protein.

Solvent Accessible Surface Area (SASA) Analysis

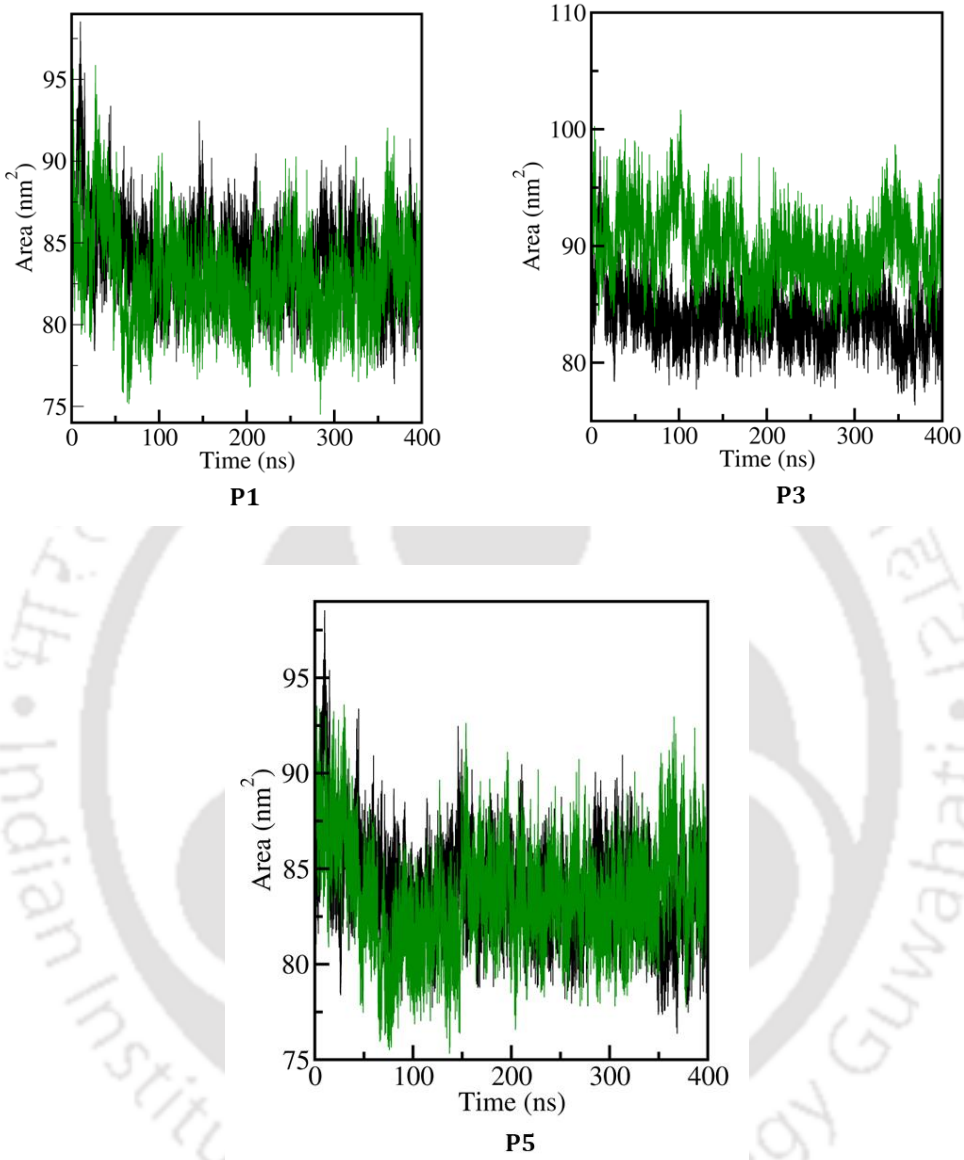

Figure D10. SASA value of Aβ40 in the absence of PDI-HIS (black); SASA value of Aβ40 in P1, P3, and P5 (green).

The increased in the SASA value of Aβ40 was observed in P3 (**Figure D10**). This indicates that the water accessibility on the surface of Aβ40 is increased and the flexibility of the protein increased. However, in the case of P1 and P3 the SASA value showed almost similar pattern with water.

Secondary Structure Analysis

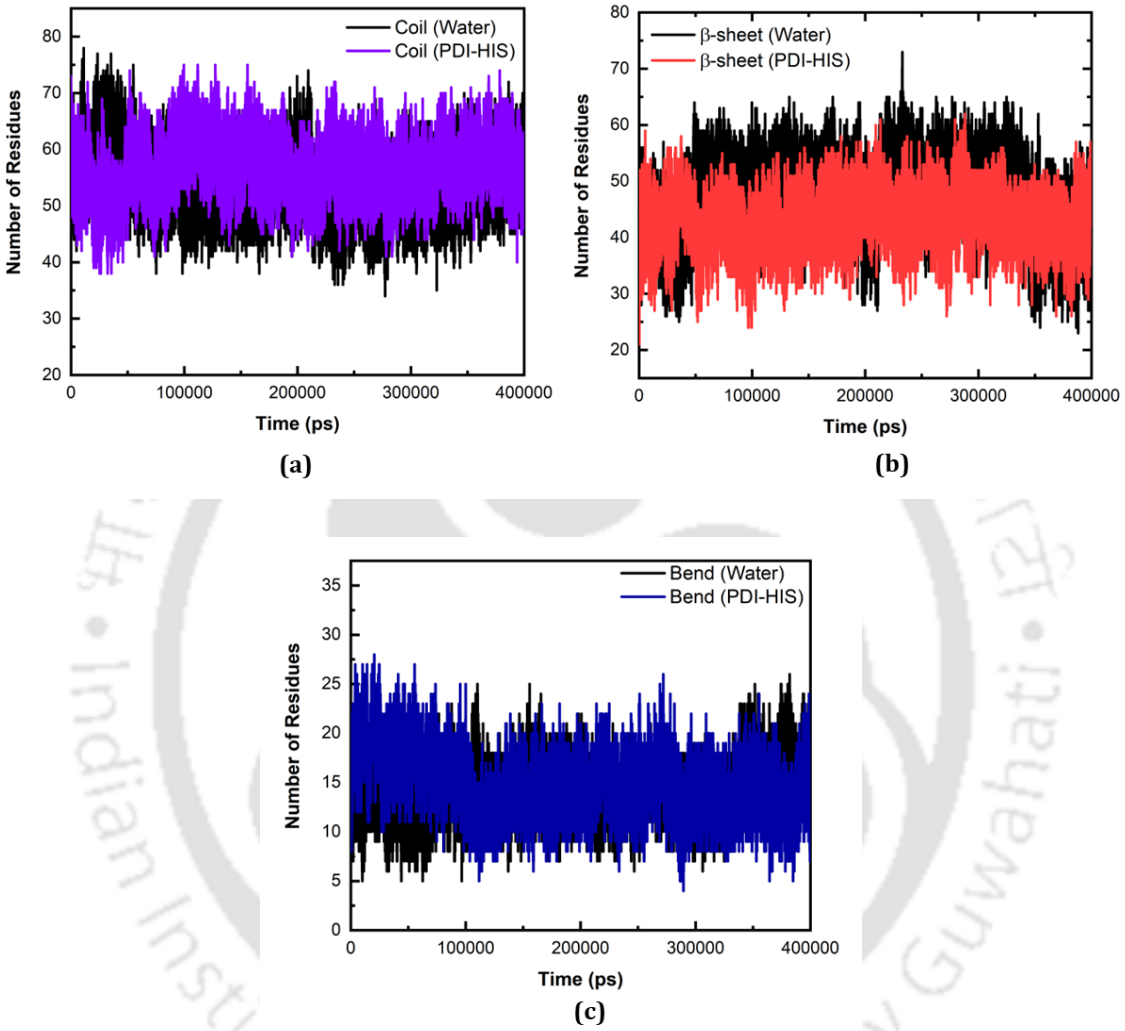

Figure D11. Representation of secondary structures of Aβ40-PDI-HIS of P1 for (a) coil content, (b) β-sheet content, and (c) bend content in Aβ40-water and Aβ40-PDI-HIS.

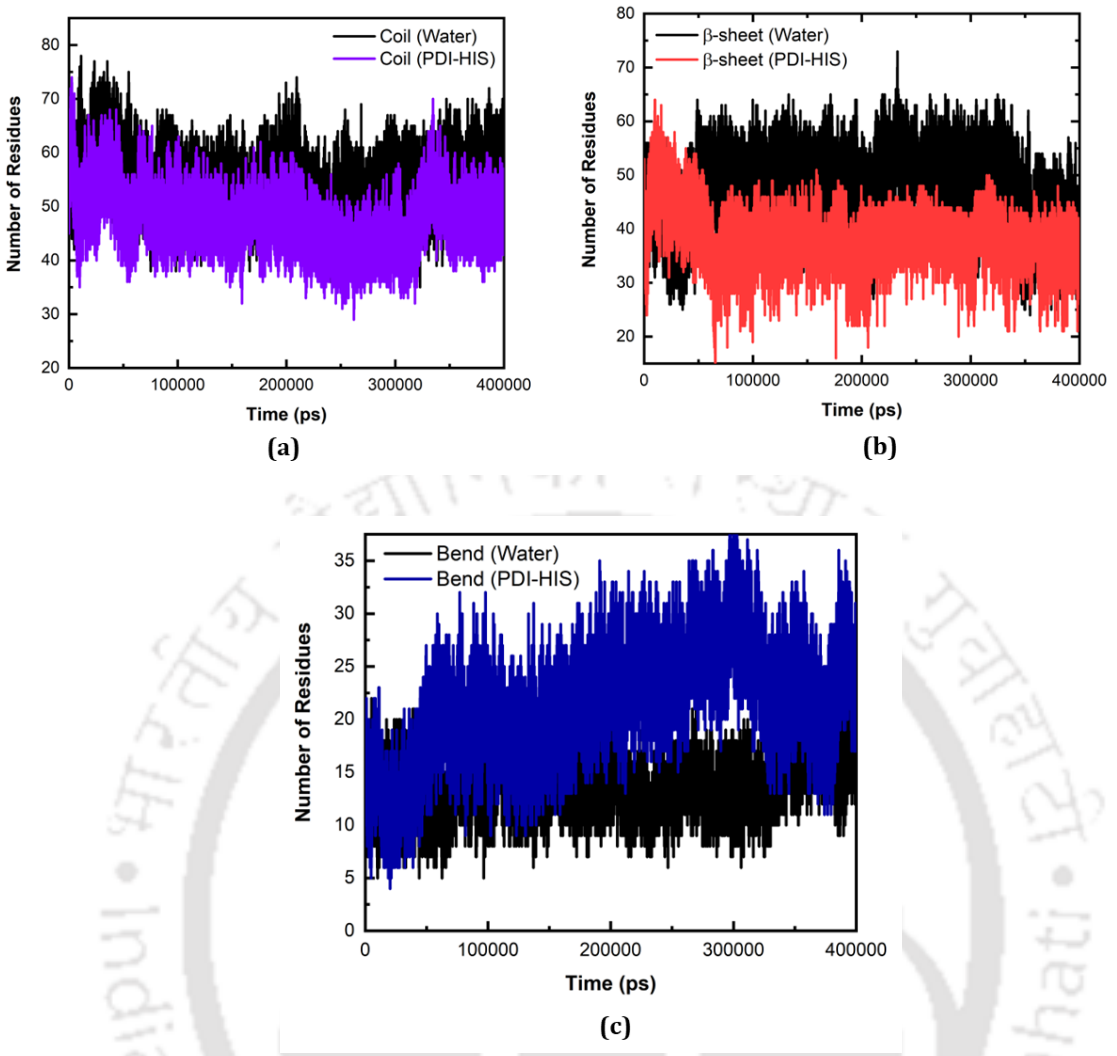

Figure D12. Representation of secondary structures of Aβ40-PDI-HIS of P3 for (a) coil content, (b) β-sheet content, and (c) bend content in Aβ40-water and Aβ40-PDI-HIS.

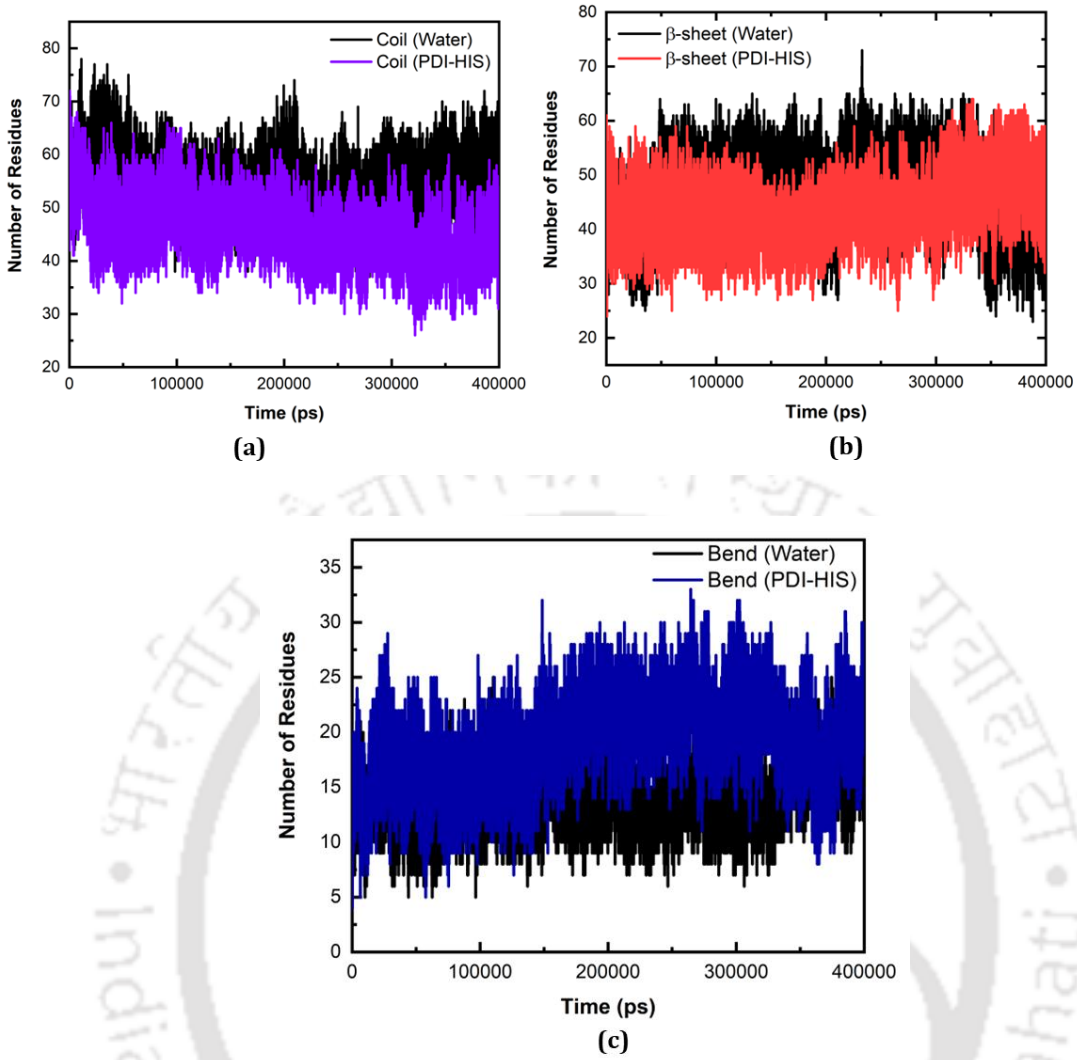

Figure D13. Representation of secondary structures of Aβ40-PDI-HIS of P5 for (a) coil content, (b) β-sheet content, and (c) bend content in Aβ40-water and Aβ40-PDI-HIS.

Secondary structure analysis of Aβ40 for P1, P3, and P5 are presented in **Figure D11**, **Figure D12**, and **Figure D13**, respectively. In P3 and P5, the number of resides exihibited in the coil structure formation is slightly less when compared with P1. On the other hand, the quantity of β-sheet content is significantly reduced in P3 (**Figure D12b**). The impact is very low in the case of P1 and P5. Furthermore, the number of residues involved in the conversion of bend structure in P3 (**Figure D12c**), and P5 (**Figure D13c**) are comparatively larger than P1 (**Figure D11c**). This result indicates that the extent of the disruption effect of PDI-HIS on the structure of the Aβ40 is large in P3.

Binding Free Energy

Table D2. Binding free energy, $\Delta G_{\text{binding}}$, (in kcal mol^{-1}) of P1, P3, and P5 docked poses.

	P1	P3	P5
ΔE_{vdW}	-33.73 ± 1.39	-52.23 ± 1.60	-35.46 ± 0.22
ΔE_{elec}	133.69 ± 1.96	149.14 ± 2.31	117.53 ± 3.20
ΔE_{MM}	99.96 ± 2.40	96.91 ± 2.81	82.07 ± 3.20
ΔG_{polar}	-120.53 ± 5.37	-133.84 ± 1.94	-116.08 ± 1.26
$\Delta G_{\text{non-polar}}$	-3.44 ± 0.04	-6.23 ± 0.03	-4.80 ± 0.06
ΔG_{solv}	-123.96 ± 5.38	-140.07 ± 1.94	-120.88 ± 1.26
$\Delta G_{\text{binding}}$	-24.00 ± 5.89	-43.17 ± 3.41	-38.82 ± 3.44

The $\Delta G_{\text{binding}}$ value (**Table D2**) of P1, P3, and P5 show that PDI-HIS has potential to bind on Aβ40 fibril. Among the selected docked poses, P3 shows the highest $\Delta G_{\text{binding}}$ value.

Interaction Analysis

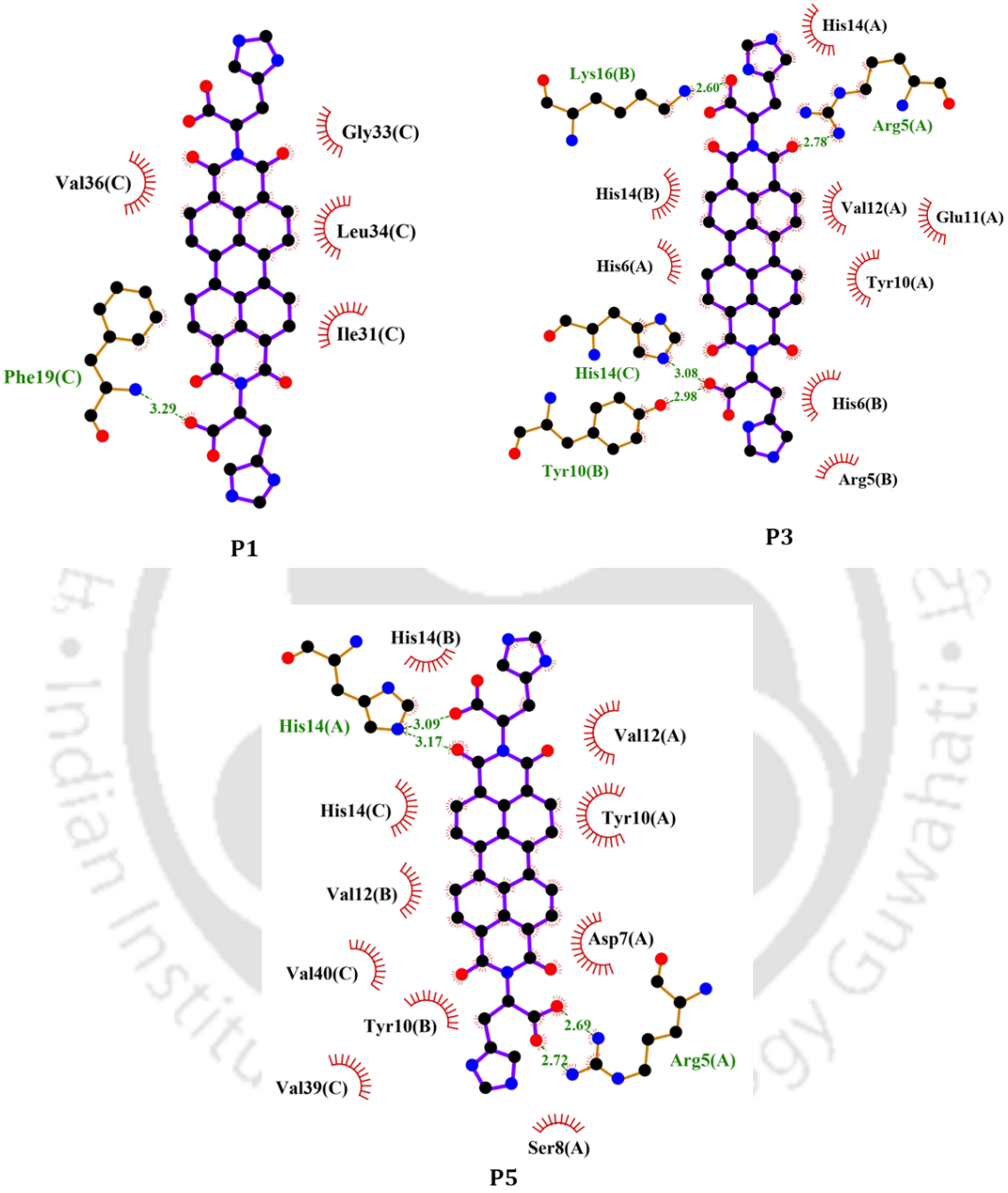

Figure D14. Illustration of the types of interaction form between the Aβ fibril and PDI-HIS at 400 ns for the systems P1, P3, and P5. The spike near the residues denotes the hydrophobic interactions, and the green line represents the existence of hydrogen bonding interaction (hydrogen bond distance in Å). A, B, and C represent the chains of Aβ fibril.

Appendix-E

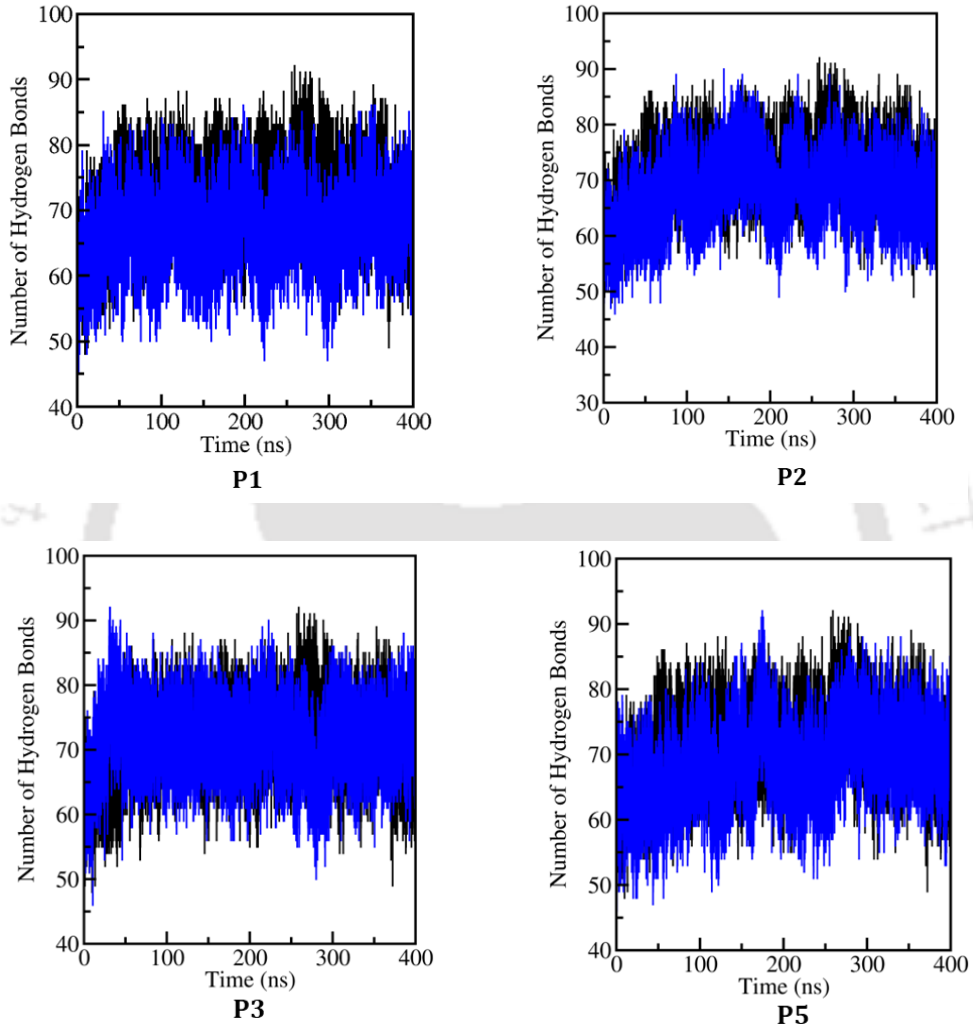

Figure E1. Number of hydrogen bonds of Aβ40 in water (black) and Aβ40-PDI-PHE (blue) for the systems P1, P2, P3, and P5.

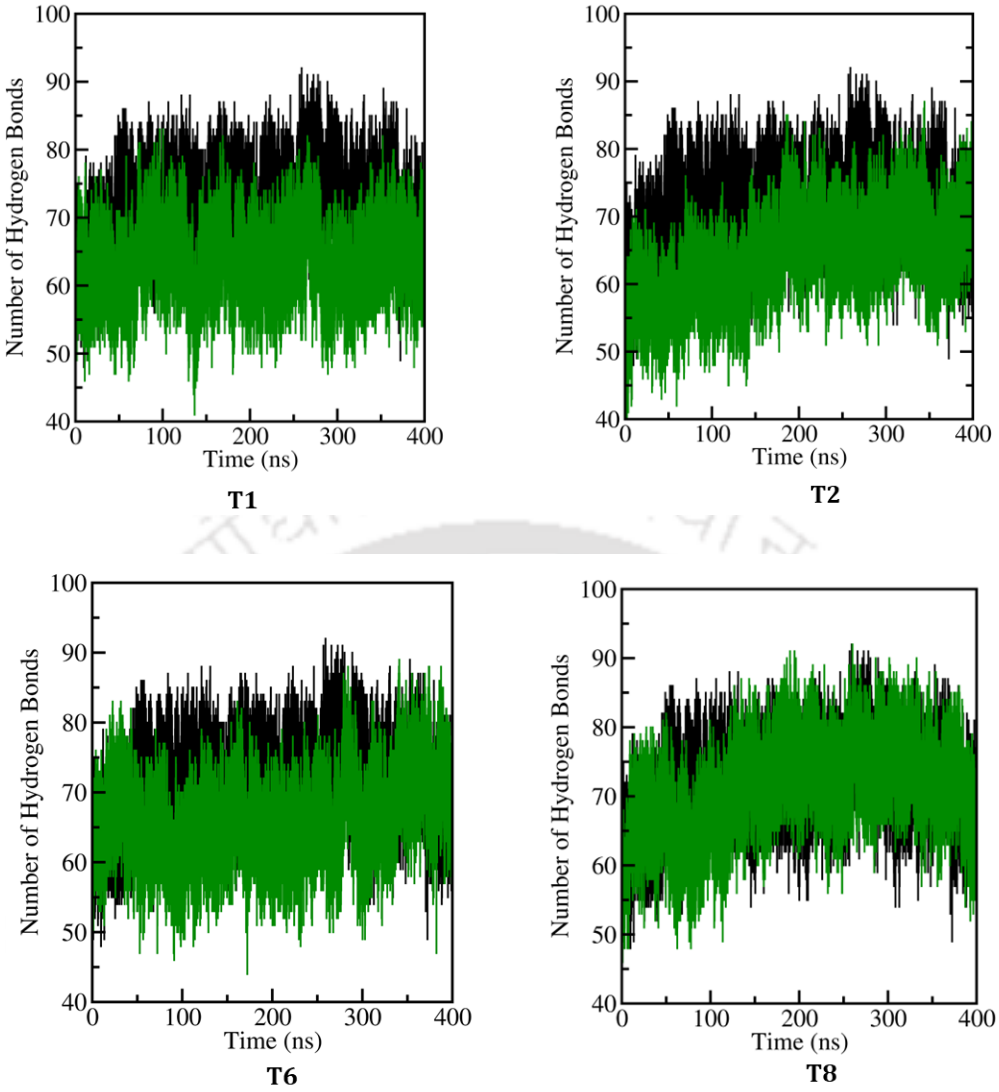

Figure E2. Number of hydrogen bonds of Aβ40 in water (black) and Aβ40-PDI-TYR (green) for the systems T1, T2, T6, and T8.

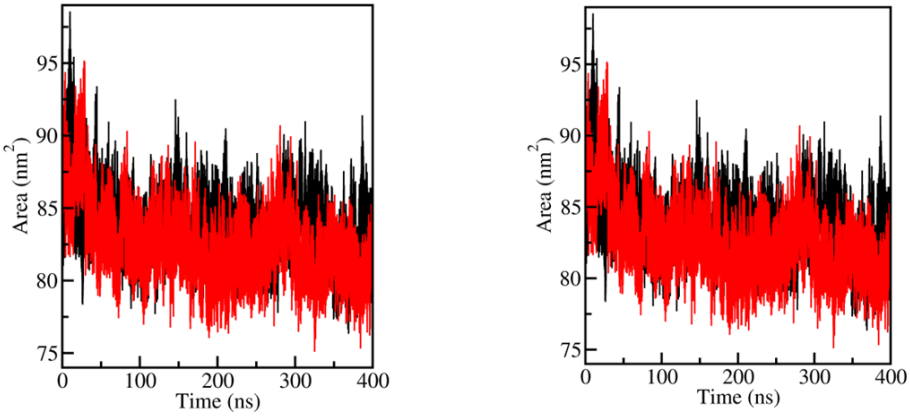

Figure E3. Solvent-accessible surface area (SASA) value of Aβ40 in water (black), SASA value of Aβ40 (red) in the presence of PDI-ALA for docked pose A2 and A8.

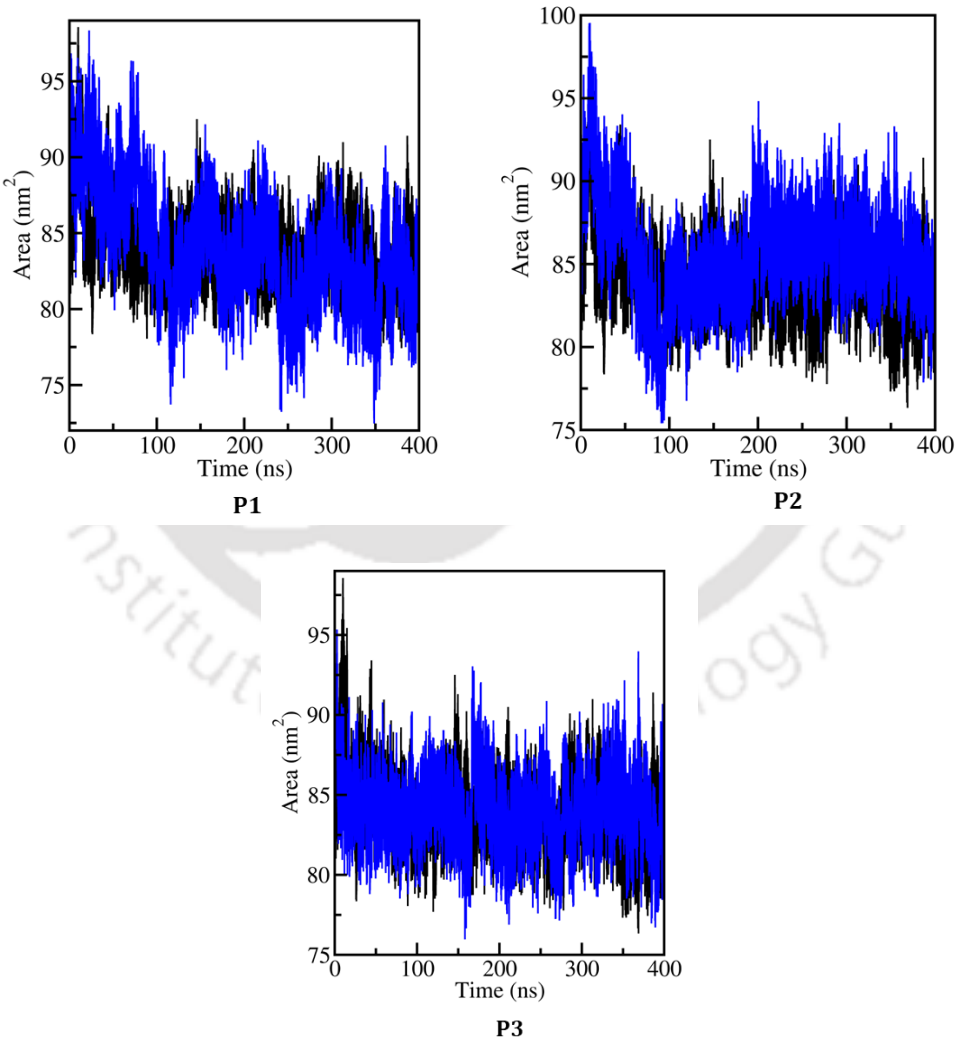

Figure E4. Solvent-accessible surface area (SASA) value of Aβ40 in water (black) and SASA value of Aβ40 (blue) in the presence of PDI-PHE for docked pose P1, P2, and P3

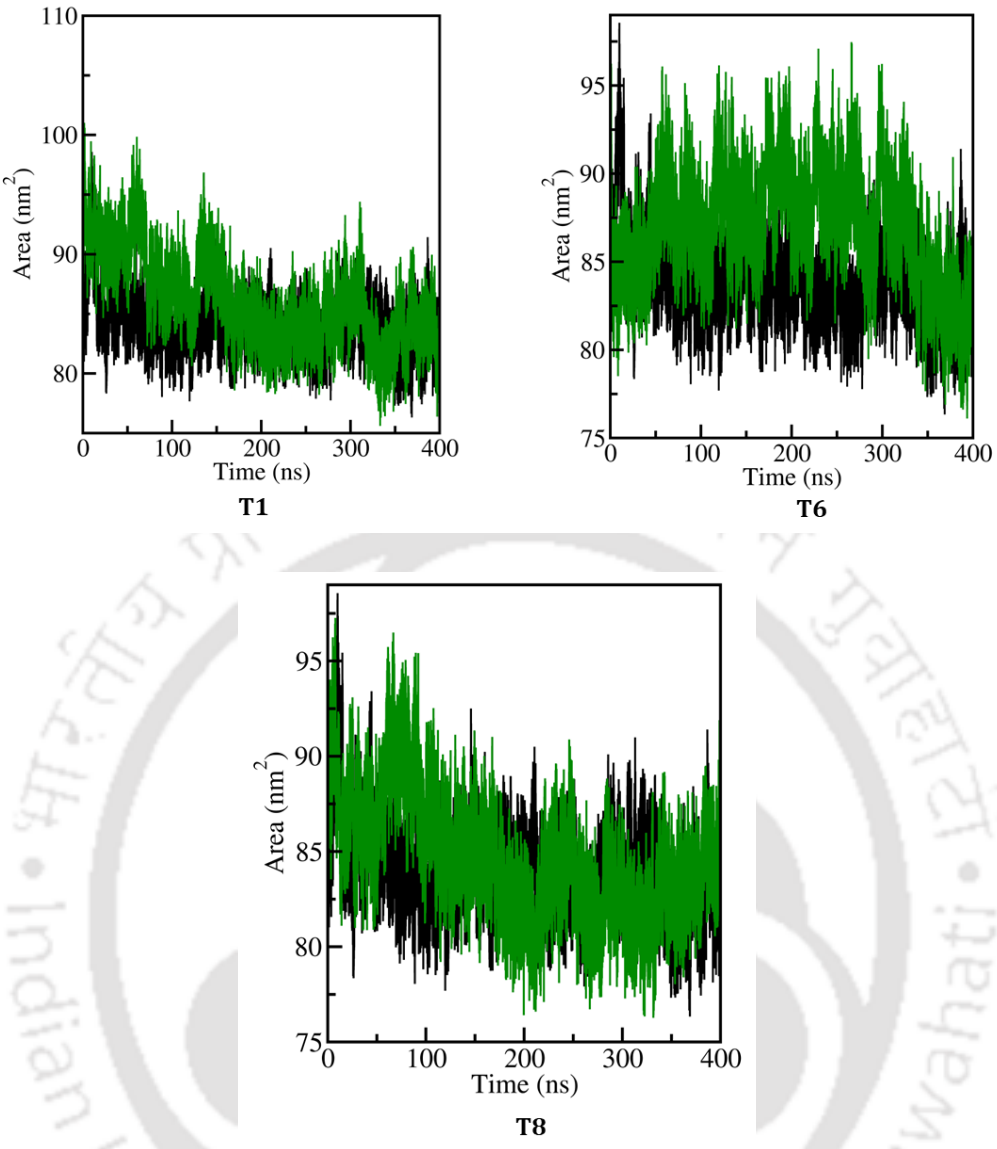

Figure E5. Solvent-accessible surface area (SASA) value of Aβ40 in water (black) and SASA value of Aβ40 (green) in the presence of PDI-TYR for docked pose T1, T6, and T8.

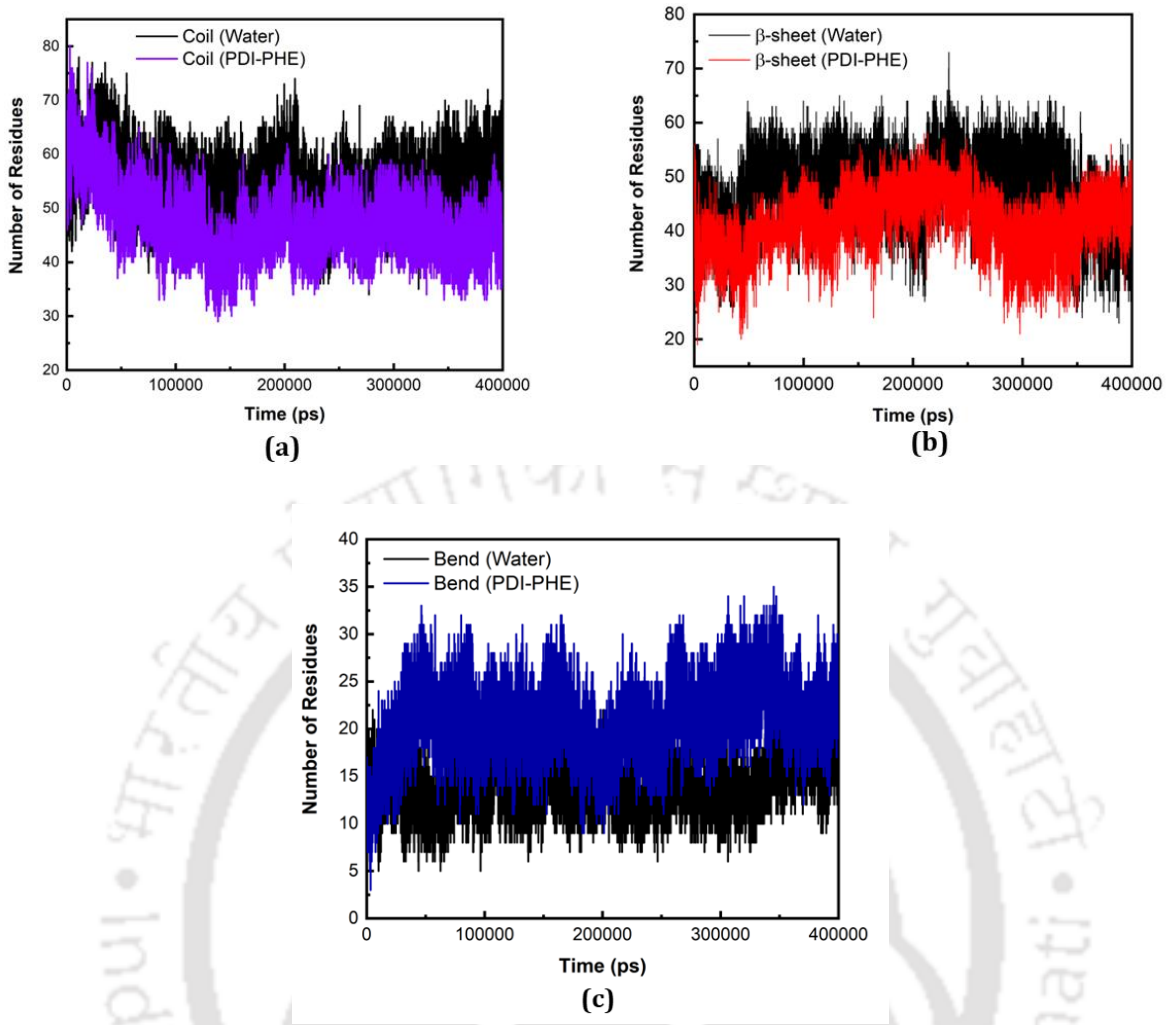

Figure E6. Representation of secondary structures of Aβ40-PDI-PHE of docked pose P5 for (a) coil content, (b) β-sheet content, and (c) bend content of protein in Aβ40-water and Aβ40-PDI-PHE.

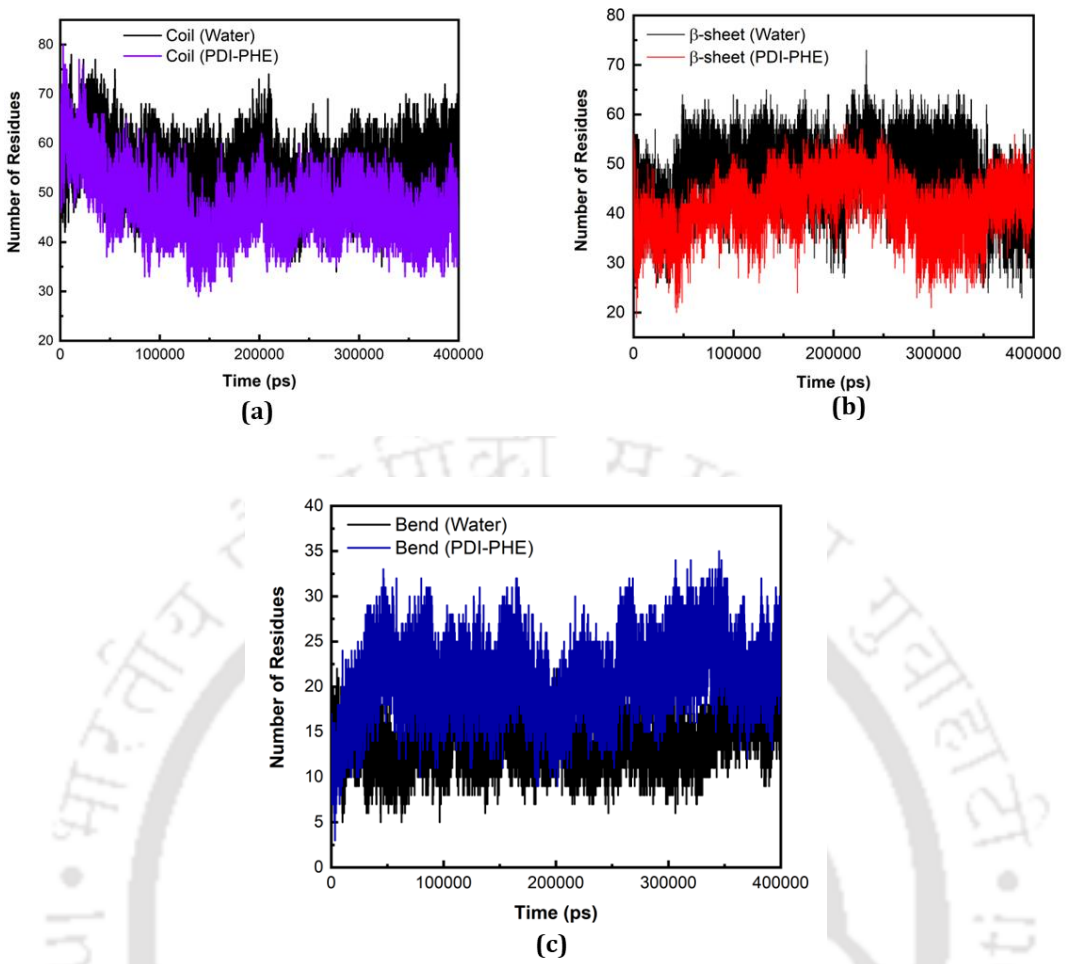

Figure E7. Representation of secondary structures of Aβ40-PDI-TYR of docked pose T2 for (a) coil content, (b) β-sheet content, and (c) bend content of protein in Aβ40-water and Aβ40-PDI-TYR.